AN INVESTIGATION OF THE INTERACTION OF WATER AND OF SATURATED HYDROCARBONS WITH THE (110) SURFACE OF IRIDIUM

Thesis by

Thomas Stephen Wittrig

In Partial Fulfillment of the Requirements

for the Degree of

Doctor of Philosophy

California Institute of Technology

Pasadena, California

1982

(Submitted October 12, 1981)

To my wife, Janis

ACKNOWLEDGMENTS

I would first like to thank my thesis advisor, Henry Weinberg, for his personal support and for the many hours that he spent with me developing ideas and teaching me his approach to science. I would also like to thank my coworkers, Dale Ibbotson and Phil Szuromi. Dale gave a great deal of time to teach me how to do experiments on our system and Phil helped me obtain much of the data that appears in this thesis.

The financial support provided to me by the Fannie and John Hertz Foundation was greatly appreciated. It was a tremendous spiritual boost to be awarded the fellowship. My research was supported by the National Science Foundation.

Finally, I would like to thank my parents, John and Betty Wittrig, without whose love and support I would have never gotten to Cal Tech; and my wife, Janis, without whose love and support I would have never gotten through Cal Tech.

ABSTRACT

The interactions of the reconstructed Ir(110)-(1x2) surface with water and with saturated hydrocarbons have been studied in an ultrahigh vacuum environment. The techniques of thermal desorption mass spectrometry (TDMS), ultrahigh photoelectron spectroscopy (UPS), X-ray photoelectron spectroscopy, contact potential difference measurements and low-energy electron diffraction (LEED) were utilized.

Chapter 2 describes a refinement in the technique for modelling the kinetics of desorption of adsorbed species by an Arrhenius construction. The functional dependence of the energy of desorption and the rate coefficient on the surface coverage are accounted for. An explicit example is provided.

The interaction of water with the Ir(110)-(1x2) surface is discussed in Chapter 3. It is shown that at most, 6% of the adsorbed water dissociates upon adsorption at a temperature of 130 K. Water does dissociate to OH groups when adsorbed on an Ir(110)-(1x2) surface with preadsorbed oxygen. Water exhibits a constant probability of adsorption for all submonolayer coverages. There exist four distinct thermal desorption states of water on the clean Ir(110)-(1x2) surface. A qualitative model is put forth to rationalize the complex thermal desorption behavior.

The remaining chapters describe investigations of the adsorption and reaction of saturated hydrocarbons on Ir(110)-(1x2).

Chapter 4 presents the results of a study of the interaction of cyclopropane and Ir(110). Chapter 5 considers the coadsorption of hydrogen and cyclopropane on Ir(110). Finally, Chapter 6 presents the results of a study of the adsorption and reaction of ethane, propane, isobutane and neopentane on Ir(110). These saturated hydrocarbons dissociated on the surface at some temperature below 130 K. In each case, this dissociation reaction is poisoned by the presence of adsorbed hydrogen on the surface. This leads to the identification of an active site for hydrocarbon dissociation on the surface. As the surface is heated, the carbon remains adsorbed on the surface and the hydrogen desorbs as H_2. For ethane, one thermal desorption peak of H_2 is observed that corresponds to hydrogen adsorbed in β_2 hydrogen adsites on the metal surface. This thermal desorption peak is observed for the remaining hydrocarbons, as well as two other thermal desorption states associated with hydrogen that exists in partially dehydrogenated hydrocarbon fragments present on the surface. No hydrocarbon species other than the one initially adsorbed were observed to desorb from the surface under any of the conditions reported in this work.

TABLE OF CONTENTS

CHAPTER 1:	INTRODUCTION	1
CHAPTER 2:	"ORDER PLOTS" IN THERMAL DESORPTION MASS SPECTROMETRY	10
CHAPTER 3:	THE ADSORPTION OF WATER ON THE RECONSTRUCTED IR(110)-(1x2) SURFACE	15
CHAPTER 4:	THE CHEMISORPTION AND REACTION OF CYCLOPROPANE ON THE (110) SURFACE OF IRIDIUM	20
CHAPTER 5:	THE INTERACTION OF HYDROGEN AND CYCLOPROPANE WITH THE (110) SURFACE OF IRIDIUM	58
CHAPTER 6:	THE INTERACTION OF ETHANE, PROPANE, ISOBUTANE AND NEOPENTANE WITH THE (110) SURFACE OF IRIDIUM	78
CHAPTER 7:	SUMMARY	122
APPENDIX A:	THE CHEMISORPTION OF HYDROGEN ON THE (110) SURFACE OF IRIDIUM	125
APPENDIX B:	THE COADSORPTION OF HYDROGEN AND CARBON MONOXIDE ON THE (110) SURFACE OF IRIDIUM	170
APPENDIX C:	THE CHEMISORPTION OF N_2 ON THE (110) SURFACE OF IRIDIUM	183
APPENDIX D:	THE CHEMISORPTION OF NO ON THE (110) SURFACE OF IRIDIUM	216
APPENDIX E:	THE REDUCTION OF NO WITH D_2 OVER IR(110)	261

CHAPTER 1

INTRODUCTION

Although the process of heterogeneous catalysis is crucial to many sectors of the chemical industry, it remains largely an empirical science. This is primarily due to the fact that methods for obtaining well characterized surfaces and for studying the details of these surfaces routinely have been developed only rather recently. Prior to these developments, studies in the field of heterogeneous catalysis concentrated on the determination of reaction rates over high surface area catalysts at relatively high pressures (i.e. 1 Torr or above). This type of experiment has two major disadvantages. First, reproducibility of the results is poor because many of the parameters that affect catalyst performance are uncontrolled. Some of these factors, for example, might be the exact method for preparing the catalyst, the amount and type of impurities in the reactant stream and the history of the catalyst. The other disadvantage of this type of experiment is that it is exceedingly difficult to determine the details of the reactions (e.g. mechanisms) at the surface. This information, obtained in a well characterized environment, is obviously important if one hopes to deduce more than empirical rate laws.

With the advent of technology for preparing well characterized single crystal metal surfaces in an ultrahigh vacuum environment over the last two decades, several surface-sensitive techniques have emerged to address the detailed mechanistic aspects of surface processes. To cite a few examples, it is now possible with commercial

instrumentation to monitor concentrations of adsorbed species down to 1% of a monolayer, to study electronic distributions and bonding of adsorbed species, and to ascertain surface geometries and adsorption sites.

The disadvantage of studying catalysis in this manner is that in limiting the experimental conditions to those in which the adsorption system is well characterized, one, in general, precludes the study of systems that are closely related to those of commercial interest. However, there are several issues that can be addressed in the ultrahigh vacuum environment that will have fundamental significance in the rational design of real catalysts in the future.

For example, the role of surface geometry in determining catalytic activity and selectivity can be studied by examining model reactions on various orientations of a metal single crystal (1-5). Thus, the identification of specific geometric arrangements of metal atoms (e.g. surface steps) as active sites for reaction may be possible. Surfaces of different metals with the same geometry may be studied in the same manner to investigate the relationship between the electronic structure of the metal and its catalytic properties (1-4).

Another general area that is amenable to investigation in the ultrahigh vacuum environment is the interaction between adsorbed species. Thus, by investigation of the effects of preadsorbed sulfur on surface reactions, one may be able to determine the

fundamental mechanisms of sulfur poisoning of catalytic reactions (6-8). Information concerning the initial stages of coking during catalysis of hydrocarbon reactions may be acquired from studies such as those described in Chapters 4-6 of this work. These types of investigations, although not directly relevant to reaction systems of commercial interest, may suggest strategies for dealing with catalyst poisoning.

Quantitative investigations of competitive adsorption and its effect on surface coverage and reaction rates provide new insight into the interaction between the surface of the catalyst and its environment. For example, the study of the nonreactive coadsorption of two different molecules illustrates explicitly the effects of site competition (App. B) and may even lead to the identification of active catalytic centers on the surface (Chaps. 5 and 6). Investigations of reactive coadsorption systems allow the examination of the coupling between the rates of elementary reactions on the surface (e.g. bond cleavage in reactant molecules and desorption of products) and conditions at the surface (e.g. temperature, partial pressure of reactants and concentration of adsorbed species). Appendix E describes an investigation of this type.

The experimental technique that was utilized most extensively in this work is thermal desorption mass spectrometry (TDMS). It is one of the most versatile techniques available in the ultrahigh

vacuum environment for obtaining information about the general features of a complex adsorption system. The experiment consists of three steps. First, the surface of the crystal is cleaned in some appropriate manner. This is followed by preparation of some adsorbed overlayer. In the simplest case, this step could consist of exposure of the surface to a controlled amount of gas. However, this step can also include adsorption of two or more different gases or heating of the surface at some point during surface preparation. Following this step, the crystal is heated and the atomic mass number (or atomic mass numbers) of the desorbing species of interest are monitored by a mass spectrometer. Provided that the pumping speed in the system is sufficiently high, the partial pressure of the species that is monitored is proportional to the rate of desorption of that species from the surface (9). For all the experiments described in this thesis, the pumping speed is sufficient to satisfy this condition.

Thermal desorption mass spectrometry can provide a wide variety of information concerning surface-adsorbate interactions. The integrated area of the mass spectrometric intensity is proportional to the concentration of adsorbed species on the surface prior to the flash. A series of such spectra as a function of gas exposure provides a determination of the kinetics of adsorption of the adsorbate (e.g. see Chaps. 3 and 4 and Apps. A, B and C). Molecules that are adsorbed at dissimilar geometric sites on the

surfaces may be bound with different energies of adsorption and may, therefore, appear as distinct peaks in the thermal desorption mass spectrum. The integrated area of these thermal desorption peaks can be compared to determine the stoichiometry of the different adsorption sites. This information is useful in development of models of the adsorption site of the adsorbed species.

Investigations of the kinetics of desorption provides a method to determine the energy of the bond between the adsorbed species and the surface. This can be accomplished in practice by performing a series of experiments at various heating rates on a surface with the same initial coverage. The resulting data can be reduced to Arrhenius plots from which the energy of desorption and the rate coefficient may be extracted (10). Chapter 2 of this thesis describes a refinement to the Arrhenius construction that is generally used to describe desorption kinetics.

If the overlayer undergoes reaction on the surface, thermal desorption mass spectrometry can be used to identify the products of the reaction. The appearance of multiple peaks in the thermal desorption mass spectrum of a product or the desorption of two or more different product species allows the identification of different reaction regimes for complex reaction systems on the surface (2-4, 11; see also Chap. 6 and App. D). The use of isotopically labelled reactants may also be useful in studies of this type (4, App. D).

For the investigations described in this thesis, I have used primarily the technique of thermal desorption mass spectrometry to study the interactions of the Ir(110) surface with water and with saturated hydrocarbons. The additional techniques of ultraviolet photoelectron spectroscopy, X-ray photoelectron spectroscopy, low-energy electron diffraction and contact potential difference measurements were also utilized to obtain supplemental information.

The clean Ir(110) surface undergoes reconstruction to a (1x2) LEED pattern (12). The structure of this surface has been determined to be a surface with every other row of atoms missing in the (001) direction (13). The surface may be visualized as a sequence of two-layer deep troughs, the sides of which are formed by two-atom wide (111) terraces. This surface was chosen for study because its highly stepped nature promised to provide new information about the relationship between surface geometry and the interactions between adsorbed molecules and transition metal surfaces.

The interaction of water with the Ir(110)-(1x2) surface is described in Chapter 3. An understanding of the behavior of this adsorption system may provide new insight into such diverse areas as corrosion, the effects of water on catalytic reactions and the microstructure of electrode surfaces in aqueous electrochemical systems.

Chapters 4-6 describe the behavior of saturated hydrocarbons

adsorbed on the Ir(110)-(1x2) surface. Fundamental studies of hydrocarbon-metal surface interactions have obvious practical significance in the field of hydrocarbon catalysis. The mechanistic knowledge gained from such investigations will increasingly enhance our ability to design catalysts that will allow the most efficient use of the world's limited hydrocarbon resources.

References

1. M.-C. Tsai, C.M. Friend and E.L. Muetterties, J. Am. Chem. Soc. (submitted).

2. M.-C. Tsai and E.L. Muetterties, J. Am. Chem. Soc. (submitted)

3. C.M. Friend, J. Stein and E.L. Muetterties, J. Am. Chem. Soc. 103, 767 (1981).

4. E.L. Muetterties, ACS Symp. Ser. 155, 273 (1981).

5. C.E. Smith, J.P. Biberian and G.A. Somorjai, J. Catal. 57, 426 (1979).

6. H.P. Bonzel and R. Ku, J. Chem. Phys. 59, 1641 (1973).

7. T.E. Fischer and S.R. Kelemen, J. Catal. 53, 24 (1977).

8. S.R. Kelemen, T.E. Fischer and J.A. Schwarz, Surface Sci. 81, 440 (1979).

9. J.L. Taylor and W.H. Weinberg, Surface Sci. 78, L508 (1978).

10. J.L. Taylor and W.H. Weinberg, Surface Sci. 78, 259 (1978).

11. J.B. Benziger and R.J. Madix, J. Catal. 65, 49 (1980).

12. K. Christmann and G. Ertl, Z. Naturforsch. 28a, 1144 (1973).

13. C.M. Chan, M.A. Van Hove, W.H. Weinberg and E.D. Williams, Solid State Commun. 30, 47 (1978); Surface Sci. 91, 400 (1980).

CHAPTER 2

"ORDER PLOTS" IN THERMAL DESORPTION MASS SPECTROMETRY

(The text of Chapter 2 consists of an article coauthored with D.E. Ibbotson and W.H. Weinberg that has appeared in Applications of Surface Science 4, 234 (1980).)

Applications of Surface Science 4 (1980) 234–237

"ORDER PLOTS" IN THERMAL DESORPTION MASS SPECTROMETRY ★

T.S. WITTRIG ‡, D.E. IBBOTSON and W.H. WEINBERG ‡
Division of Chemistry and Chemical Engineering, California Institute of Technology, Pasadena, California 91125, USA

Received 11 June 1979
Revised manuscript received 6 August 1979

A common method to determine the rate law for desorption of a gas from a solid surface is to construct order plots derived from thermal desorption experiments. The purpose of this letter is to show that the assumptions on which order plots are based can lead to serious errors in the determined order, and to show how proper corrections can be made.

The starting point of the derivation involves the following expression for the desorption rate,

$$R_d = \nu_d(\theta)\theta^n \exp[-E_d(\theta)/kT] . \tag{1}$$

The order n is assumed to be a constant integer representing the elementary desorption reaction. Logarithmic differentiation of eq. (1) with respect to the fractional surface coverage θ at constant T yields

$$\left(\frac{\partial \ln R_d}{\partial \ln \theta}\right)_T = n + \left(\frac{\partial \ln \nu_d(\theta)}{\partial \ln \theta}\right)_T - \frac{1}{kT}\left(\frac{\partial E_d(\theta)}{\partial \ln \theta}\right)_T . \tag{2}$$

Usually, it is assumed that the last two terms in eq. (2) are zero, and n is equal to the slope for a plot of $\ln R_d$ as function of $\ln \theta$ at constant temperature. However, recent experimental evidence has shown that both rate parameters, E_d and ν_d, can vary strongly with coverage [1,2]. If the terms $(\partial \ln \nu_d/\partial \ln \theta)_T$ and $(\partial E_d/\partial \ln \theta)_T$ are large, the slope of an order plot may not represent the true order of the desorption reaction, n. Furthermore, if the derivatives vary rapidly with coverage, the order plot is not necessarily linear.

To illustrate these effects, recent thermal desorption data of hydrogen on Ir(110) will be considered [3]. Fig. 1 shows the coverage dependence of E_d and ν_d. Saturation coverage (θ = 1) is defined in this case as the coverage resulting from a 300 L

★ Supported by the National Science Foundation (Grant Number DMR77-14976).
‡ Fannie and John Hertz Foundation Predoctoral Fellow.
‡ Camille and Henry Dreyfus Foundation Teacher–Scholar.

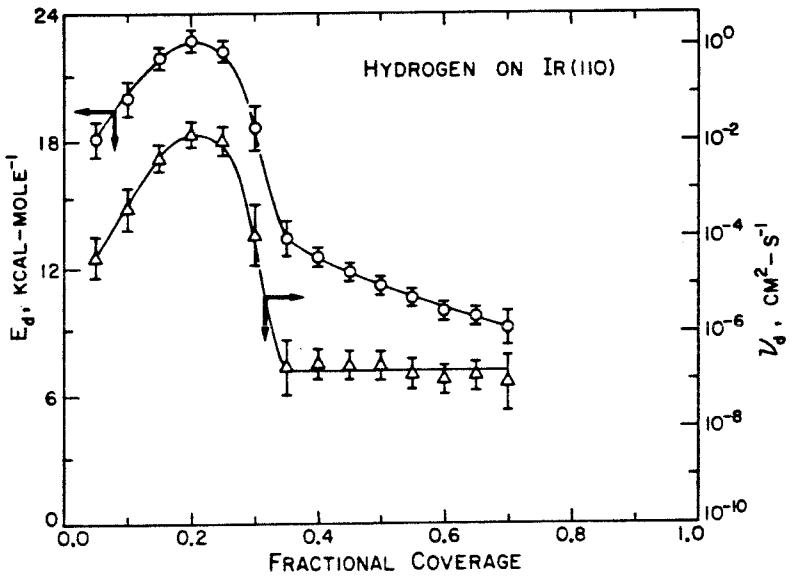

Fig. 1. Activation energy (E_d) and pre-exponential factor (ν_d) for hydrogen desorption from Ir(110) as a function of fractional surface coverage.

exposure of hydrogen to an Ir (110) surface at 130 K. At this coverage, the probability of adsorption of hydrogen is less than 10^{-5}, and higher exposures introduce problems of CO contamination. The values of the parameters were determined by an integral method using variable heating rates [4]. The heating rates were varied from 3 K/s to 110 K/s. This set of experiments was performed twice to enhance the reliability of the results. Further experimental details will be provided in a forthcoming publication [3].

An increase in E_d and ν_d is observed up to a fractional coverage of 0.20. The rapid variation in the rate parameters between coverages of 0.25 and 0.35 is associated with the completion of the low coverage state of hydrogen [3]. At higher coverages, E_d varies approximately linearly with coverage and ν_d varies only weakly with coverage. Fig. 2 illustrates representative order plots for this system. As shown in fig. 2, $(\partial \ln R_d/\partial \ln \theta)_T$ varies strongly with temperature. It is approximately equal to two for $T \geqslant 380$ K, but it is unreasonably large at lower temperatures.

Table 1 compares the slopes of two representative order plots with values calculated using eq. (2) and fig. 1. The coverage was chosen as the logarithmic mean of the coverage extremes in the experimental order plots, although any reasonable coverage choice will give qualitatively similar results. The order n was chosen as two for all coverages since hydrogen adsorbs dissociatively [3].

For $T \geqslant 380$ K both the experimental and calculated values for $(\partial \ln R_d/\partial \ln \theta)_T$ are equal to two, as would be expected from a traditional order plot for dissociative

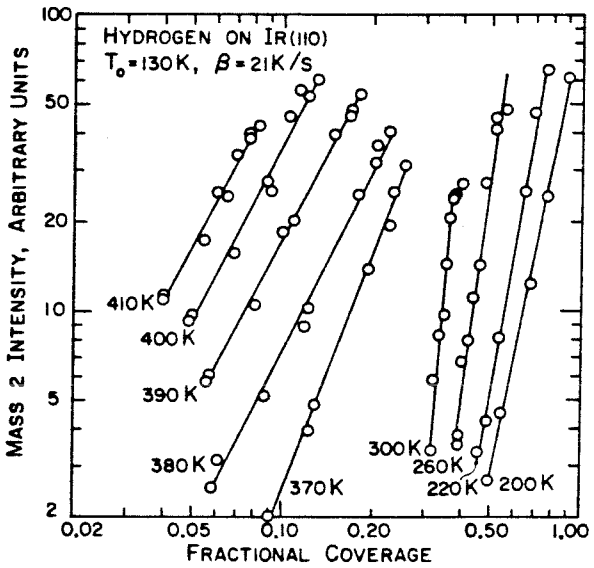

Fig. 2. Traditional order plots for hydrogen desorption from Ir(110) constructed from data in ref. [3].

adsorption. However, the terms $-kT^{-1}(\partial E_d/\partial \ln\theta)_T$ and $(\partial \ln \nu_d/\partial \ln\theta)_T$ in eq. (2), as shown in table 1, are not small but rather cancel one another. This low coverage result may be a general consequence of the so-called compensation effect mentioned in the literature [5,6]. The low temperature result (220 K) in table 1 provides an example of the large error in the measured order from a traditional order plot, where the apparent order $[(\partial \ln R_d/\partial \ln\theta)_T]$ is equal to 6.1. Assuming that $n = 2$, the calculated order using eq. (2), 10 ± 5, agrees with the experimental value. The error limits are large for the calculated $(\partial \ln R_d/\partial \ln\theta)_T$ due to the uncertainty in measuring derivatives in fig. 1. It should be noted in the low temperature case that the deviation of the traditional order plot from yielding an order of two is caused primarily by the observation that $dE_d/d\theta = -10$ kcal-mole^{-1}-monolayer^{-1}

Table 1
Parameters of order plot for H_2 desorption from Ir(110)

T,K	θ	$-\frac{1}{kT}\left(\frac{\partial E_d}{\partial \ln\theta}\right)_T$	$\left(\frac{\partial \ln \nu_d}{\partial \ln\theta}\right)_T$	$\left(\frac{\partial \ln R_d}{\partial \ln\theta}\right)_{T,\text{calc}}$	$\left(\frac{\partial \ln R_d}{\partial \ln\theta}\right)_{T,\text{expt}}$
220	0.58	10.5 ± 4	−2.5 ± 2	10 ± 5	6.1 ± 0.3
390	0.10	−4.6 ± 1.0	4.8 ± 1.0	2.2 ± 1.5	2.0 ± 0.1

for fractional coverages between 0.4 and 0.7. *This value is not unusual when compared to other adsorption systems in the literature* [1,2,7,8].

In conclusion, it has been shown that traditional order plots may lead to errors in the true order of the desorption reaction of the rate parameters for desorption vary with coverage. However, a procedure for correcting the traditional order plots has been developed. A specific example of hydrogen desorption from Ir(110) was discussed for illustration purposes.

References

[1] H. Pfnür, P. Feulner, H.A. Engelhardt and D. Menzel, Chem. Phys. Letters 59 (1978) 481.
[2] J.L. Taylor, D.E. Ibbotson and W.H. Weinberg, J. Chem. Phys. 69 (1978) 4298.
[3] D.E. Ibbotson, T.S. Wittrig and W.H. Weinberg, in preparation.
[4] J.L. Taylor and W.H. Weinberg, Surface Sci. 78 (1978) 259.
[5] G.C. Bond, Catalysis by Metals (Academic Press, New York, 1962).
[6] E. Bauer, F. Bonczek, H. Poppa and G. Todd, Surface Sci. 52 (1975) 237.
[7] K. Christmann, O. Schober, G. Ertl and M. Neumann, J. Chem. Phys. 60 (1974) 4528.
[8] P.A. Thiel, E.D. Williams, J.T. Yates, Jr. and W.H. Weinberg, Surface Sci. 84 (1979) 54.

CHAPTER 3

THE ADSORPTION OF WATER ON THE RECONSTRUCTED IR(110)-(1x2) SURFACE

(The text of Chapter 3 consists of an article coauthored with D.E. Ibbotson and W.H. Weinberg that has appeared in Surface Science 102, 506 (1981).)

Surface Science 102 (1981) 506–517

THE ADSORPTION OF WATER ON THE RECONSTRUCTED Ir(110)-(1 × 2) SURFACE *

T.S. WITTRIG **, D.E. IBBOTSON and W.H. WEINBERG ***
Division of Chemistry and Chemical Engineering, Pasadena, California 91125, USA

Received 12 June 1980; accepted for publication 11 August 1980

The interaction of water with the reconstructed Ir(110)-(1 × 2) surface has been studied with LEED, CPD, XPS and thermal desorption mass spectrometry. It is shown that *at most*, 6% of the adsorbed water dissociates upon adsorption at a temperature of 130 K. Water does dissociate to OH groups when adsorbed on an Ir(110)-(1 × 2) surface with preadsorbed oxygen. Water exhibits a constant sticking coefficient for all submonolayer coverages. There exist four distinct thermal desorption states of water on the clean Ir(110)-(1 × 2) surface. A qualitative model is put forth to rationalize the complex thermal desorption behavior.

1. Introduction

Recently, several ultrahigh vacuum studies of the interaction of water with transition metal surfaces have been carried out [1–5]. There are several reasons for this attention. From a fundamental viewpoint, water is a complex and interesting adsorbate, due partly to strong interadsorbate interactions caused by hydrogen bonding. Also at issue are the questions of whether water dissociates on metal surfaces, and what role the oxygen lone pair plays in the bonding. From a more practical standpoint, detailed knowledge of the interaction of water with metal surfaces has obvious practical applications in such diverse areas as corrosion, effects on catalytic reactions (either as a reactant or modifier) and the microstructure of electrode surfaces.

This study is the first ultrahigh vacuum investigation of water on iridium. The reconstructed Ir(110)-(1 × 2) surface was chosen for this study because it is an "open" surface (not geometrically smooth) with many possible "active" sites. It therefore presents the possibility of observing new, geometry-induced effects.

* Supported by the National Science Foundation under Grant No. CHE77-14976.
** Fannie and John Hertz Foundation Predoctoral Fellow.
*** Camille and Henry Dreyfus Foundation Teacher–Scholar.

2. Experimental procedures

The experiments were performed in an ion-pumped stainless steel bell jar with a base pressure below 2×10^{-10} Torr. Several surface sensitive probes – a quadrupole mass spectrometer, LEED optics, a CPD apparatus, AES and XPS – are contained in the experimental chamber. The XPS and AES are performed in the pulse counting mode with a double pass cylindrical mirror electron energy analyzer. Continuous work function measurements were performed by a retarding potential method described elsewhere [6]. All probes are interfaced to a PDP 11/10 minicomputer [7]. In addition, the system contains a directional beam doser that can be used for introducing adsorbates onto the crystal without backfilling the bell jar. The use of this directional doser allows the creation of an effective pressure at the crystal face that is approximately 100 times greater than the background pressure in the system.

The substrate was cut from a single crystal boule of Ir and was polished on both sides to within 1° of the (110) orientation using standard techniques [8]. Carbon was cleaned from both sides of the crystal through a series of oxidation and reduction cycles. Annealing above 1600 K removed oxygen, calcium and potassium impurities. Details of the cleaning procedure are described elsewhere [9]. The substrate was heated resistively by two 10 mil Ta support wires, and it was cooled conductively by liquid nitrogen. Temperatures were measured with a W/5%Re–W/26%Re thermocouple spotwelded to a 1 mm^2 Ta foil on the back of the Ir crystal. The thermocouple was referenced to an icepoint junction, and temperatures are accurate within ±5 K. The base pressure of water in the UHV system was below 5×10^{-11} Torr. The water was doubly distilled and checked mass spectrometrically for purity. In particular, no O_2 was observed with the mass spectrometer.

3. Low-energy electron diffraction

If a simple termination of the bulk structure is considered, the Ir(110) surface is a series of rows and troughs. However, a clean surface is reconstructed to form a (1 × 2) LEED pattern [10]. Recently, the structure of reconstructed Ir(110) has been determined to be a surface with every other row of surface atoms in the [001] direction missing [11]. The surface may be thought of as (111) microfacets inclined to one another to form a series of troughs that are two layers deep.

Low-energy electron diffraction was performed for water adsorption on this surface at 130 K and room temperature for water coverages up to several monolayers. For this range of conditions, the surface reconstruction was stable. In addition, no additional LEED spots were observed due to scattering by ordered superstructures of the adsorbed water molecules.

4. Thermal desorption mass spectrometry

The thermal desorption mass spectrometry (TDMS) of water on the clean surface was performed using two different methods of exposure. For submonolayer exposures, the adsorbate was introduced into the bell jar through a leak valve. This method allows accurate exposures to be made and exposes the front and the back of the crystal to equal fluxes of adsorbate. However, the use of this technique with water is limited to low exposures due to adsorption on the crystal supports and saturation of the walls of the bell jar which causes subsequently a high partial pressure of water in the system. Therefore, the TDMS of high exposures of water was performed by introducing the adsorbate through the beam doser in the system. This method introduces very little water onto the system walls and minimizes the adsorption of water on the crystal support. The disadvantages of this method for TDMS are that the flux of adsorbate molecules to the front face of the crystal is higher than to the back face, and the exposure is not related in a linear manner to the time of exposure. This latter problem is due to the fact that the flux of water molecules rises gradually over a long period of time from the time the valve is opened. Despite these problems, the TDM spectra obtained by this method give a good qualitative understanding of the thermal desorption characteristics of high coverages of water.

The results of the low coverage TDMS are shown in fig. 1. Three distinct thermal desorption states appear after a one langmuir exposure. As shown in the figure, these states will be referred to as the β, γ_1 and γ_2 states in order of increasing peak temperature.

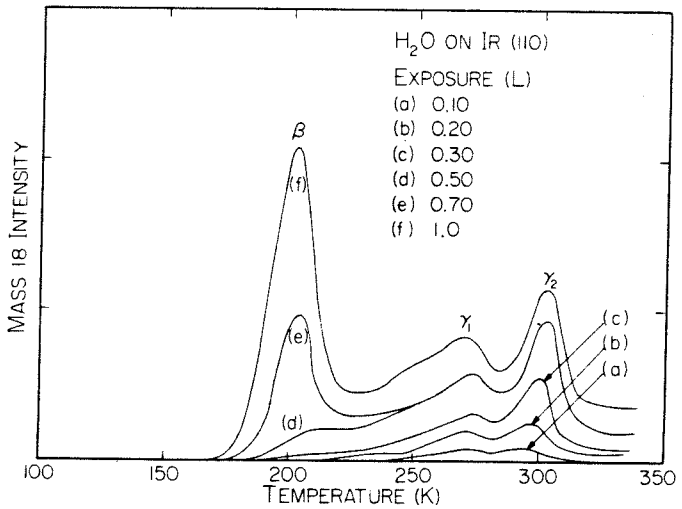

Fig. 1. Thermal desorption mass spectra of submonolayer coverages of water on Ir(110).

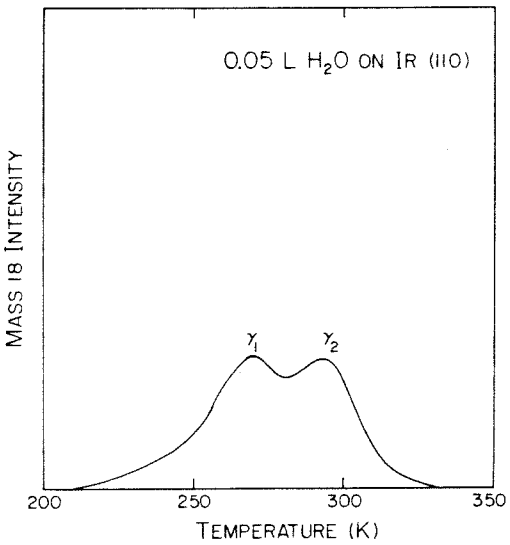

Fig. 2. Thermal desorption mass spectrum of 0.05 L exposure of water on Ir(110).

At exposures below 0.5 L, the only states to appear are the γ states. As shown in fig. 2, both of the γ states are present even at 0.05 L, which was the lowest exposure that was studied. The two states develop with increasing exposure at approximately the same rate. Though uncertainty about the background makes an accurate determination of the relative populations impractical, it appears that the two γ states have approximately equal populations at a saturation exposure of 0.5 L.

Determination of Arrhenius desorption parameters by peak shape analysis was rendered impossible by the unknown shape of the background. However, with the assumption that the Arrhenius preexponential factor, ν_d, falls in the range from 10^{12} to 10^{14} s^{-1}, an analysis following Redhead [12] yields a value for the energy of desorption, E_d, of the γ_1 state of 15.8 ± 1.2 kcal/mole^{-1} and an E_d of 17.5 ± 1.3 kcal/mole^{-1} for the γ_2 state.

At exposures of greater than 0.5 L, the β state begins to populate near 200 K. The β state reaches saturation near 1 L exposure, and, at saturation, its population is approximately the same as that of the combined γ states. Saturation of the β and γ states will be referred to hereafter as one monolayer (ML) coverage. Making use of the assumptions employed above, E_d of the β state is found to be 11.6 ± 0.9 kcal/mole^{-1}.

The relationship between surface coverage and exposure derived from fig. 1 is shown in fig. 3. It reveals that the sticking coefficient for water on Ir(110)-(1 × 2) is constant for all submonolayer coverages. It will be assumed that this sticking coefficient is unity for the following two reasons. First, it is difficult to envision

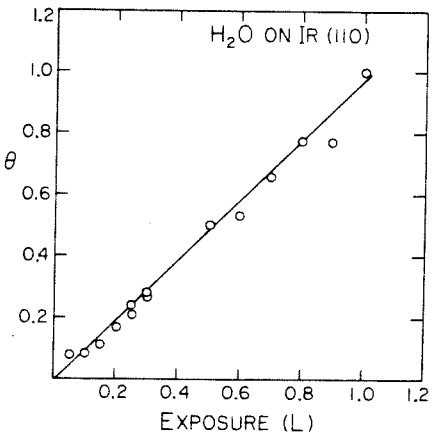

Fig. 3. Water coverage on Ir(110) as a function of exposure.

circumstances in which only a certain constant fraction of water molecules impinging on the surface would desorb irreversibly and additionally that this fraction would show no dependence on surface coverage or conditions. Secondly, with the assumption of a unity sticking coefficient and an impingement flux of 4.5×10^{14} molecules/cm^2 per L (corrected for ion gauge sensitivity), a 1 L saturation exposure corresponds to each molecule occupying one reconstructed unit cell on the surface.

Beginning at 1 L exposure, the multilayer thermal desorption state begins to

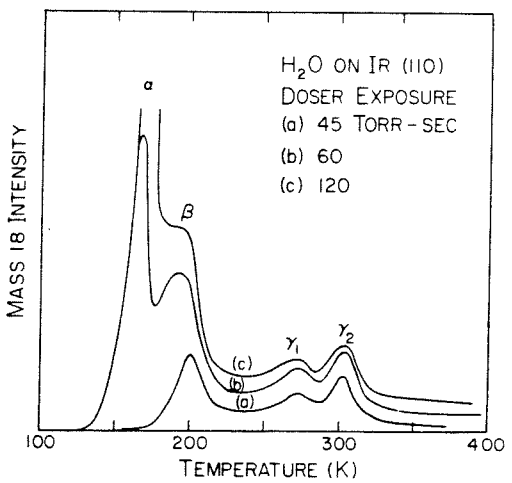

Fig. 4. Thermal desorption mass spectra of high coverages of water on Ir(110).

emerge. This will be referred to as the α state. The development of this state, which apparently grows without limit, was followed by performing doser exposures in conjunction with the TDMS. The results of this experiment are shown in fig. 4. The exposure units shown in the figure are the product of the pressure in the doser storage bulb in Torr and the time that the crystal was exposed to the beam. These units are not related in any simple manner to langmuirs, and they are unique to the geometry of the system. The shape of the desorption from the α state indicates zeroth order desorption. The leading edge is exponential when plotted as a function of $1/T$ and does not depend on initial coverage. In addition, the high temperature edge of the peak indicates a very sharp drop. From an Arrhenius plot of the leading edge of this peak, an E_d of 10 ± 1 kcal/mole^{-1} was calculated. No assumption of the magnitude of ν_d is needed to obtain this value. This value agrees well with that observed previously for multilayers of water on transition metal surfaces [2,3].

Fig. 4 also contains two qualitative features worthy of mention. First, the β state is definitely distinct from the multilayer α state and therefore represents water molecules that are interacting with the metal surface as opposed to those exclusively in an ice matrix. Second, the presence of the β and γ states in the doser TDMS indicates clearly that they are not artifacts due to desorption from the manipulator and crystal supports.

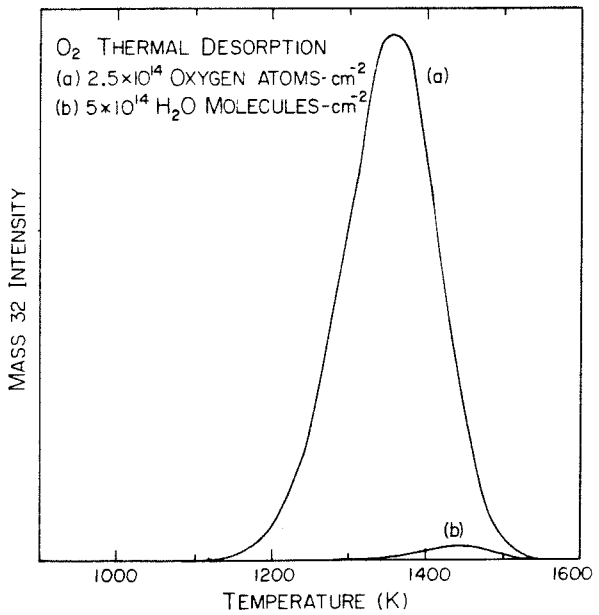

Fig. 5. Oxygen thermal desorption from (a) O_2 adsorbed on Ir(110), and (b) 1 ML H_2O adsorbed on Ir(110).

A series of experiments was also performed to check for residual oxygen left after water had been desorbed thermally from the surface. These experiments were performed to provide information concerning the possible dissociation of water on the surface. The results are presented in fig. 5. A calibration was carried out first by adsorbing 2.5×10^{14} atoms/cm^2 of oxygen on the surface and performing an oxygen TDMS. For an initial coverage of approximately 1 ML of water, a small amount of O_2 desorption was detected. This amount corresponded to the oxygen contained in 3% of a ML of H_2O. It is possible that if the water did dissociate on the surface, some of it might recombine during the thermal desorption. In a separate set of experiments, when deuterium and oxygen were adsorbed on the surface in amounts corresponding to 0.5 ML of water, it was found that only 40% of the reactants left the surface as water, while the remainder desorbed as D_2 and O_2. If it is assumed that all the O_2 in the water adsorption experiment of fig. 5 came from water that dissociated on the surface and also that approximately half of it recombined, then approximately 6% of the water dissociated on the surface. However, this small amount of oxygen could have come from another source (e.g., water dissociating elsewhere and providing oxygen to the surface).

5. Contact potential difference measurements

The work function change ($\Delta\phi$) of the surface plotted as a function of H_2O exposure at 140 K is shown in fig. 6. Since surface coverage is linearly related to exposure, this is equivalent to a $\Delta\phi - \theta$ relationship. The work function decreases in an approximately linear manner throughout the submonolayer coverages to

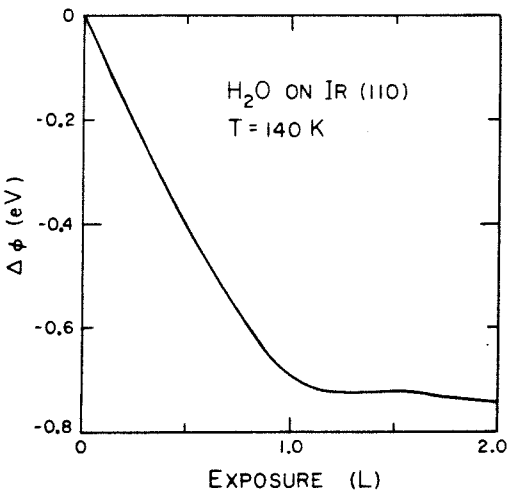

Fig. 6. Work function changes as a function of H_2O exposure on Ir(110).

the work function of ice. The plateau in the multilayer region above 1.0 L continues up to 3 L which was the highest exposure studied. The incremental dipole moment in the submonolayer regime is 0.4 ± 0.1 D per water molecule.

This experiment shows very clearly that only the first langmuir of water interacts directly with the surface, as has already been indicated by the thermal desorption measurements. It also provides further evidence that little, if any, water dissociates on the surface at 140 K, since the adsorbed dissociation products would almost certainly have different dipole moments than the adsorbed water species. If the first monolayer were totally dissociated, this would also be consistent with the observed work function change, but it would not be consistent with the XPS results presented in the next section or with the TDMS results.

6. X-ray photoelectron spectroscopy

The XPS of the oxygen 1s region of water adsorbed on Ir(110) is shown in fig. 7. The coverages shown in the figure are derived from thermal desorption mass spectra performed immediately following the XPS. Since the exposures were carried out with the doser, the coverages are subject to a 20% error. The dominant feature in

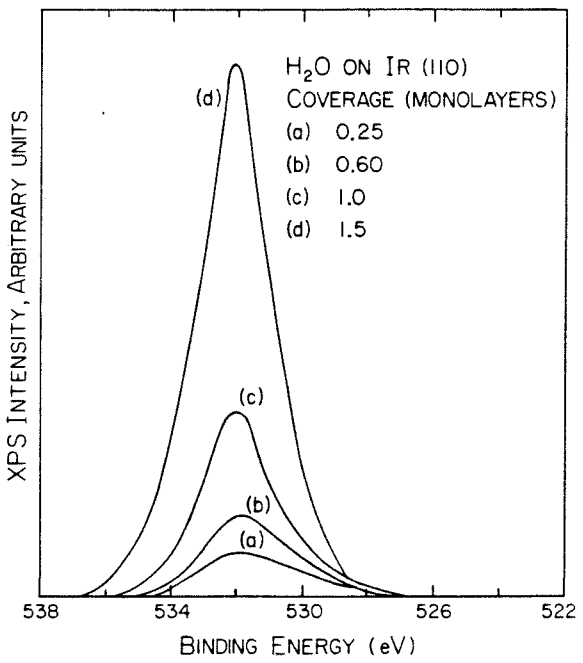

Fig. 7. Oxygen 1s XPS for H_2O on clean Ir(110).

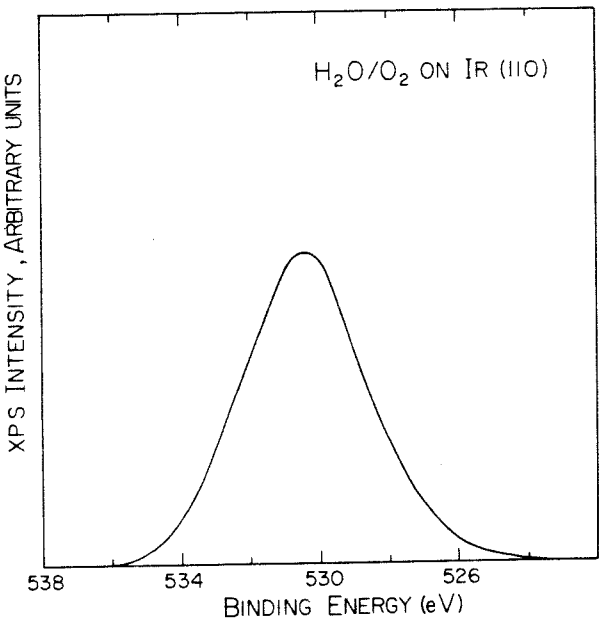

Fig. 8. Oxygen 1s XPS for H_2O on oxygen-covered Ir(110).

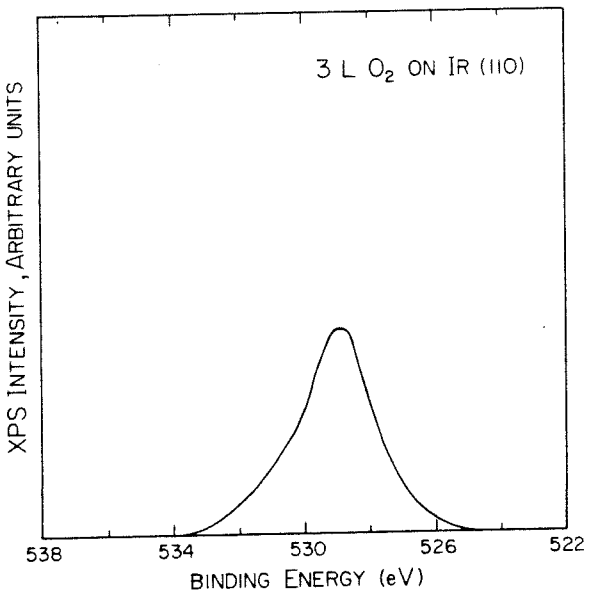

Fig. 9. Oxygen 1s XPS for 3 L O_2 on Ir(110).

these spectra has a binding energy of 532.1 ± 0.2 eV for all coverages from 0.25 to 1.5 ML. This agrees well with the oxygen 1s binding energy of 532.2 ± 0.3 eV observed for nondissociatively adsorbed water on Pt(111) by Fisher and Gland [3]. Since this peak shows no shift or splitting well into the multilayer region, it almost certainly represents nondissociatively adsorbed water. At low coverages, there exists also a small asymmetric broadening to the low binding energy side of the peak. This may represent a small amount of dissociatively adsorbed water on the surface.

Fig. 8 shows the results of adsorbing water on a surface preexposed to oxygen. An amount of water corresponding to one-half monolayer (i.e., 2.5×10^{14} molecules/cm^{-2}) was adsorbed on the surface with an equal concentration of oxygen atoms. The oxygen 1s photoelectron spectrum of the oxygen-covered surface was subtracted from the resulting photoelectron spectrum for clarity. The spectrum exhibits one species with a binding energy of 530.5 ± 0.2 eV. Fisher and Gland have reported a photoelectron spectrum of water on an oxygen-covered Pt(111) surface in which a peak at 530.5 eV was observed [3]. This species has since been shown to be an adsorbed OH species [13].

The oxygen 1s XPS of adsorbed oxygen on Ir(110) is shown in fig. 9 for comparison. The binding energy of this species is 528.8 eV.

7. Discussion

The combined data from XPS, CPD and TDMS indicate that little, if any, water dissociates on the clean surface at an adsorption temperature of 130 K. The XPS of the oxygen 1s binding energy region show mainly a one-peak structure at 532.1 eV throughout the coverage range from 0.25 ML to 1.5 ML, and this peak is associated with nondissociated water molecules. The slight broadening of the peak to low binding energy at low coverages may indicate that a small amount of water does dissociate on the surface. The $\Delta\phi - \theta$ behavior at a temperature of 140 K displays a relatively constant slope throughout the submonolayer region, which implies that there do not exist separate regimes of adsorption at this temperature as would be the case if some appreciable fraction of the water molecules were dissociating. The dissociation of 6% of a monolayer of water indicated by the experimental data of fig. 4 is small but significant. It could either come from a small amount of water dissociated on the surface or, as mentioned previously, from water dissociating elsewhere in the system and depositing oxygen on the surface.

In the interpretation of electron energy loss spectra of water on reconstructed Pt(100) [1], Ibach and Lehwald have proposed a model for water adsorption that may shed some light on the complex thermal desorption behavior observed in this work. At coverages below 0.5 ML, they suggest that water polymers form on the surface through hydrogen-bonding. Due to the constraints of the hydrogen bonds, this would introduce inequivalent types of water molecules on the surface. Above 0.5 ML, they observe a structural change which they attribute to a coalescence of

these separate polymers into an ice-like monolayer. Clustering of water molecules at low coverages is also implied by a recent EELS and LEED study of water on Ru(001) [4].

The ideas above suggest a qualitative picture of what may be occurring on the Ir(110)-(1 × 2) surface. At coverages below 0.5 ML, both of the γ states are present in approximately equal concentrations at all coverages. Furthermore, the peak temperatures shift only slightly with coverage. This would be the expected thermal desorption behavior if water formed small noninteracting clusters on the surface with two inequivalent types of water in the clusters. At coverages above 0.5 ML, the β state would then represent the water molecules that could not participate in the more stable cluster configuration due to steric factors.

It is worthy of mention that thermal desorption states equivalent to the γ states have not previously been observed on transition metal surfaces [2–5]. This is true even of the studies from which the ideas for this model were adopted [1,4]. It may be that the γ states are resolvable here due to the unusually open geometry of this surface.

8. Conclusions

Our conclusions may be summarized as follows:

(1) The amount of water that dissociates upon the adsorption of a monolayer of water on Ir(110)-(1 × 2) at a temperature of 130 K is at most 6% of a monolayer.

(2) When water is adsorbed on an oxygen-covered Ir(110)-(1 × 2) surface, OH groups are formed on the surface.

(3) Water adsorbs on an Ir(110)-(1 × 2) surface at a temperature of 130 K with a constant sticking coefficient throughout the submonolayer regime. This sticking coefficient is assumed to be unity.

(4) Water exhibits four distinct thermal desorption states from the Ir(110)-(1 × 2) surface. The low coverage γ states develop simultaneously up to 0.5 L exposure. The β state evolves for exposures between 0.5 L and 1.0 L. The α state is the multilayer ice state and grows without bound for exposures greater than 1.0 L.

(5) A tentative model has been put forth as a plausible explanation of the complex thermal desorption behavior of this sytem. The γ_1 and γ_2 states in this model represent two differently bound states of water which exist in small clusters of water molecules that are stabilized by hydrogen-bonding. The β state represents water molecules that interact with the surface, but are excluded sterically from joining into the more stable cluster structures.

References

[1] H. Ibach and S. Lehwald, Surface Sci. 91 (1980) 187.

[2] T.E. Madey and J.T. Yates, Jr., Chem. Phys. Letters 51 (1977) 77.

[3] G.B. Fisher and J.L. Gland, Surface Sci., submitted.
[4] P.A. Thiel, F.M. Hoffmann and W.H. Weinberg, in: Proc. 4th Intern. Conf. on Solid Surfaces, Cannes, 1980.
[5] J.J. Zinck and W.H. Weinberg, J. Vacuum Sci. Technol. 17 (1980) 188.
[6] J.L. Taylor and W.H. Weinberg, J. Vacuum Sci. Technol. 15 (1978) 1811.
[7] J.L. Taylor, Ph.D. Thesis, California Institute of Technology, 1978.
[8] C.M. Comrie and W.H. Weinberg, J. Chem. Phys. 64 (1976) 250.
[9] J.L. Taylor, D.E. Ibbotson and W.H. Weinberg, J. Chem. Phys. 69 (1978) 4298.
[10] K. Christmann and G. Ertl, Z. Naturforsch. 28a (1973) 1144.
[11] C.-M. Chan, M.A. Van Hove, W.H. Weinberg and E.D. Williams, Solid State Commun. 30 (1979) 47; Surface Sci. 91 (1980) 440.
[12] P.A. Redhead, Vacuum 12 (1962) 203.
[13] G.B. Fisher and B.A. Sexton, Phys. Rev. Letters 44 (1980) 683.

CHAPTER 4

THE CHEMISORPTION AND REACTION OF CYCLOPROPANE ON THE (110) SURFACE OF IRIDIUM

(The text of Chapter 4 consists of an article coauthored with P.D. Szuromi and W.H. Weinberg that has been submitted to The Journal of Chemical Physics).

Abstract

Thermal desorption mass spectrometry (TDMS), UV photoelectron spectroscopy (UPS), low-energy electron diffraction (LEED) and contact potential difference measurements have been employed to study the interaction of cyclopropane with the reconstructed Ir(110)-(1x2) surface. At an adsorption temperature of 100 K, cyclopropane dissociates on the surface with a reaction probability of 0.87 ± 0.1. This overlayer saturates at a coverage of cyclopropane of (2.1 ± 0.2) x 10^{14} cm^{-2}. Upon further exposure, cyclopropane adsorbs molecularly into two different adsorption sites up to a saturation coverage of 6.6 x 10^{14} cm^{-2}. The parameters of the desorption rate coefficients based upon Arrhenius constructions for low coverages of the two desorption states are E_d = 6.4 ± 1 kcal-$mole^{-1}$ and ν_d = 1.0 x $10^{9 \pm 1}$ sec^{-1}, and E_d = 8.3 ± 1 kcal-$mole^{-1}$ and ν_d = 4.5 x $10^{10 \pm 2}$ sec^{-1}. The work function decreases by 0.5 eV during formation of the dissociated hydrocarbon residue at 100 K and decreases further (a total decrease of 0.7 eV) during the adsorption of molecular cyclopropane.

1. Introduction

The study of the interaction of cyclopropane with transition metal catalysts has long been utilized as a probe of the general nature of hydrocarbon catalysis *(1-10)*. These classical studies over dispersed supported catalysts have addressed such issues as the identity of surface species in hydrocarbon reactions, the role of kinks and steps as active sites, the nature of the hydrocarbon residue that is formed and its role in the mechanism of hydrogenolysis, and the product distribution in the hydrogenolysis reaction. A recent study of cyclopropane adsorption on Ru(001) in ultrahigh vacuum found that cyclopropane adsorbs and desorbs molecularly on this surface and undergoes no further reaction *(11)*. The purpose of this study is to establish a model system for the reaction of a simple hydrocarbon on a well characterized single crystal transition metal surface under ultrahigh vacuum conditions. This model system should make it possible to address some of the issues mentioned above from a fundamental point of view, making use of the array of techniques available in the ultrahigh vacuum environment. Here we consider the dissociative adsorption of cyclopropane on the Ir(110)-(1x2) surface.

2. Experimental Procedures

The experiments were performed in an ion pumped stainless steel belljar that has been described previously *(12,13)*. The base pressure for these experiments was below 2 x 10^{-10} torr of reactive contaminants. The cyclopropane exposures for most of the experiments were carried out with a directional beam doser *(14)*. During dosing, the crystal is approximately 3 mm from the doser face. This provides a beam pressure-to-background pressure ratio of over 100:1. The exposure unit that is employed for the beam doser is torr-second (t-s) and refers to the product of the time of exposure and the pressure in the storage

bulb of the doser. For cyclopropane in this system, 2.5 torr-sec are approximately equivalent to 1 Langmuir.

3. Low-Energy Electron Diffraction

It is well known that the clean surface of Ir(110) reconstructs to form a (1x2) LEED pattern *(15)*. The structure that gives rise to this pattern has been shown to be a surface with every other row of surface atoms missing in the [001] direction *(16)*. Thus, the surface may be pictured as a series of two-layer deep troughs, the sides of which are (111) microfacets as is shown in Fig. 1. A reconstructed unit cell is shown as a dashed rectangle in the top view. In addition, the comparative scale of the cyclopropane molecule is shown to the right of the top view.

For all the conditions reported in this study, no long-range ordering of either the cyclopropane or its decomposition products was observed with LEED. Additionally, the (1x2) substrate beams were always present, indicating the stability of the surface reconstruction under these conditions.

4. Ultraviolet Photoelectron Spectroscopy

Figure 2 illustrates a series of UP spectra for various exposures of cyclopropane to Ir(110) at 100 K. For a 4 t-s exposure, there is a broad background in the region of binding energy below 4 eV. On this background, there are observable peaks at approximately 6 eV and 9 eV. The intensity of these peaks corresponds to approximately 2% of the total intensity. Adsorbate peak intensity is defined here as the height of the peak above the background on which the peak appears. For higher exposures, the two peaks observed in the 4 t-s spectrum as well as one near 4 eV become much more intense. At an exposure of 6

t-s, they constitute approximately 10% of the total intensity, and at 15 t-s exposure, they make up fully one-third of the intensity. Exposures greater than 15 t-s cause no further change in the UP spectrum.

The electronic levels of gas phase cyclopropane *(17)* are indicated [as (e)] above spectrum (d) in Fig. 2 with a static shift to account for relaxation effects. This illustrates that at saturation the predominant species on the surface is molecular cyclopropane.

5. Thermal Desorption Mass Spectrometry

For cyclopropane exposures below 5 t-s, hydrogen and cyclopropane both appear in the thermal desorption mass spectrum. No other hydrocarbons appear in observable quantities as desorption products for any of the conditions reported in this study. Furthermore, the only atomic species remaining on the surface at 800 K is carbon. This fact was ascertained in the following manner. The surface was exposed to 10 t-s of cyclopropane, heated to 800 K and cooled to below room temperature. Subsequently, 5 L of O_2 was adsorbed, and the surface was heated while monitoring H_2, H_2O, CO and CO_2 mass spectrometrically. There was no detectable desorption of H_2 or H_2O in this experiment. Approximately half of the carbon on the surface desorbed as CO and approximately 10% desorbed as CO_2. All the carbon could be removed by heating the surface in oxygen.

Figure 3 shows a series of H_2 thermal desorption mass spectra for various exposures of cyclopropane. In these experiments, the exposures were made through a leak valve in order to obtain an accurate calibration of the flux of the beam doser as well as a reliable comparison of integrated peak areas with peak areas of H_2 thermal desorption from a hydrogen-covered surface. Since an

accurate coverage calibration for hydrogen on Ir(110) is known *(12)*, it is possible to obtain an accurate absolute measure of the number of cyclopropane molecules that decompose as a function of cyclopropane exposure. If we define the reaction probability as the probability that any molecule that encounters the surface will eventually dissociate into H_2(g) and C(a) upon heating, the hydrogen thermal desorption yield is proportional to the cyclopropane reaction probability. As shown in Fig. 4, the reaction probability for a cyclopropane molecule is constant up to a saturation coverage equivalent to $(2.1 \pm 0.2) \times 10^{14}$ molecules-cm^{-2}. This coverage corresponds approximately to one dissociated cyclopropane molecule per 2.5 reconstructed unit cells. Saturation occurs at an exposure of 1.7 L or about 4 t-s. The slope of the line in Fig. 4 indicates that the reaction probability is 0.87 ± 0.10.

It is apparent from the foregoing that a large fraction of the initial cyclopropane to encounter the surface dissociates. The UPS results suggest that the dissociation occurs even at temperatures as low as 100 K. In any case, the dissociation must be complete below 150 K because no molecular cyclopropane remains on the surface above 150 K. The layer of dissociated cyclopropane will hereafter be referred to as the hydrocarbon residue.

Thermal desorption of small amounts of cyclopropane is also observed in this exposure regime ($\leq$ 4 t-s) as is illustrated in Fig. 5. In this adsorption regime, the total desorbed cyclopropane represents less than 15% of the adsorbed cyclopropane. This thermal desorption feature will be referred to as the α thermal desorption state. The relationship between cyclopropane coverage and exposure is shown in Fig. 6. The solid line represents the function

$$\Theta_\Delta = C_1 \varepsilon_\Delta^2 + C_2 \qquad (1)$$

where Θ_Δ is the coverage of cyclopropane in cm^{-2}, ε_Δ is the exposure in t-s, C_1 =

4.62×10^{12} $(t\text{-}s)^{-2}$ cm^{-2}, and $C_2 = 2.0 \times 10^{12}$ cm^{-2}. The nonzero intercept is equivalent to less than 0.3% of saturation coverage of cyclopropane on this surface.

This rather unusual variation of coverage with exposure for nondissociative adsorption might be explained in the following way. If the sites onto which the "α cyclopropane molecules" adsorb are formed by the dissociation of an isolated cyclopropane molecule and if the probability of adsorption of cyclopropane on these sites is a constant, then the rate of increase in the population of the α-state should be proportional to the amount of residue, i.e.

$$\frac{d\Theta_\Delta}{d\varepsilon_\Delta} \propto \Theta_r \tag{2}$$

where Θ_r is residue coverage. It has already been shown in Fig. 4 that Θ_r is proportional to ε_Δ. Thus,

$$\frac{d\Theta_\Delta}{d\varepsilon_\Delta} \propto \varepsilon_\Delta \tag{3}$$

Integration of Eq. (3) yields

$$\Theta_\Delta = k_1\varepsilon_\Delta^2 + k_2 \tag{4}$$

which is of the same form as the observed experimental dependence given by Eq. (1). Note that if the formation of an α-adsite required more than one isolated, dissociated cyclopropane molecule (e.g. close proximity of two or more dissociated cyclopropane molecules or residue island formation), the form of Eq. (2) would be different, and the model would not agree with the observed results.

The Arrhenius parameters for the α-desorption state were obtained by the method of variation of heating rate *(18)* using 4 t-s exposures. The Arrhenius plot obtained in this way is shown in Fig. 7 and corresponds to the coverage at which the desorption rate is a maximum. Assuming that the rate of desorption

is first order, the parameters of the desorption rate coefficient are $E_d = 6.4 \pm 1$ kcal-mole^{-1} and $\nu_d = 1.0 \times 10^{9 \pm 1}$ sec^{-1}.

For cyclopropane exposures greater than 4 t-s, a new thermal desorption state begins to populate in addition to the α-state. As shown in spectrum (b) of Fig. 8, this state is labelled the β-state. Two- state thermal desorption mass spectra occur for all exposures between 5 t-s and 20 t-s, which is saturation at 100 K. As shown in Fig. 8, for exposures of 10 t-s or less, the temperature of the desorption maximum of the β-state decreases with increasing coverage, whereas the desorption maximum of the α-state remains constant at approximately 130 K. For exposures greater than 10 t-s, there are still two distinct features in the thermal desorption mass spectrum. However, the feature with a peak maximum of 130 K appears at a higher temperature than the other peak. The low temperature thermal desorption feature which is evident in Figs. 8(e) and 8(f) appears to represent a structure other than adsorption into the β-adsites based on experiments concerning the adsorption of cyclopropane on the hydrocarbon residue after annealing to 200 K *(19)*.

The coverage-exposure relationship obtained from integrated mass 42 peak areas is shown in Fig. 9. After the initial formation of the residue, the cyclopropane coverage increases linearly with exposure up to at least two-thirds of saturation. The saturation coverage is $(6.6 \pm 1.0) \times 10^{14}$ cm^{-2} as will be demonstrated in the next section. This implies a density of three cyclopropane molecules for every two reconstructed unit cells on the surface. Saturation at an adsorption temperature of 100 K occurs at an exposure of approximately 20 t-s.

The Arrhenius parameters for a low coverage of the β-state of adsorbed cyclopropane were obtained by the variation of heating rate method using a 6

t-s exposure. The resulting Arrhenius plots are presented in Fig. 10 for two different coverages. The coverage for line (a) corresponds to a temperature of approximately 155 K in Fig. 8(b), and for line (b), the corresponding temperature is 145 K. The parameters of the desorption rate coefficient for the low coverage β-state are (a) $E_d = 8.1 \pm 2$ kcal-mole^{-1}, and $\nu_d = 4.7 \times 10^{10 \pm 2}$sec^{-1}; and (b) $E_d = 8.5 \pm 1$ kcal-mole^{-1}, and $\nu_d = 4.4 \times 10^{10 \pm 2}$ sec^{-1}. Since the desorption temperature of the β-state of cyclopropane decreases by at least 20 K with increasing coverage, one would expect that E_d and possibly ν_d depend strongly on surface coverage. This conjecture, however, is not subject to experimental verification due to the overlap of the α- and β-desorption states at higher coverages.

In any case, at low coverage the β-state is bound more strongly to the surface, yet the α-state is the first to begin to populate (during the formation of the residue). Furthermore, after the completion of the residue overlayer, the α- and β-states populate at approximately the same rate as a function of exposure. These facts could imply that the formation of sites for β-adsorption requires the presence of α-cyclopropane on the surface. The results of an experiment performed to test this hypothesis are shown in Fig. 11. Spectrum 11(a) results from a 6 t-s cyclopropane exposure to Ir(110) at 100 K. In 11(b), the exposure was the same as 11(a), but the surface was annealed to 125 K before the thermal desorption experiment was performed. In 11(c), 6 t-s of cyclopropane was exposed to the surface at 135 K. It is immediately apparent from spectra 11(b) and 11(c) that the formation of β-adsites depends only on the completion of the residue overlayer and does not depend on the presence of α-cyclopropane on the surface. This may indicate that the β-adsites are formed by residue island formation or polymerization. This observation demonstrates also that α-cyclopropane and β-cyclopropane are adsorbed at different sites on the surface,

and that these separate features do not result solely from interactions among adsorbed cyclopropane molecules.

6. Cyclopropane Uptake Measurement

The curve shown in Fig. 12 was obtained in the following manner. The beam doser was turned on with cyclopropane in the beam and the crystal facing away from the doser. With the mass spectrometer monitoring mass 42, the crystal was turned immediately to face the doser. As this was done, the mass 42 intensity (I_{42}) decreased to approximately 30% of its original value reflecting the fact that the crystal is "pumping" cyclopropane. As the crystal becomes saturated, I_{42} rises to some equilibrium value $I_{42,\infty}$. The difference $I_{42,\infty} - I_{42}$ is proportional to the probability of adsorption of cyclopropane on the surface as a function of time. It follows that the integral over time of $I_{42,\infty} - I_{42}$ is proportional to the coverage of cyclopropane (dissociated and nondissociated) on the surface at any time.

A comparison of Figs. 4 and 12 permits an approximate determination of the surface coverge of cyclopropane. The rate of adsorption (either dissociative or nondissociative) of cyclopropane onto the clean Ir(110) surface is 85% of the rate of adsorption onto the residue-covered surface. This fact is evident from a comparison of the initial slope of the curve in Fig. 12 with the slope for exposures of greater than 5 t-s and was observed in numerous experiments of this type. The probability of dissociative adsorption for exposures of less than 4 t-s has already been shown to be 0.87 ± 0.1 (cf. Fig. 4 and the associated text). It is was also shown that this reaction probability resulted in a coverage of 2.1×10^{14} dissociated molecules - cm^{-2} after an exposure of 4 t-s. This is equivalent to 5.2×10^{13} molecules - cm^{-2} per t-s of exposure for a reaction probability of 0.87. Therefore, for exposures of greater than 4 t-s, in the region in which the

probability of adsorption of molecular cyclopropane on the residue is unity (see Fig. 12), the incremental addition of molecular cyclopropane to the surface is (6.0 ± 1.0) x 10^{13} molecules - cm^{-2} per t-s. This information allows the assignment of an absolute coverage scale to the ordinates of Figs. 9 and 12. In particular, the saturation coverage of molecular cyclopropane on Ir(110) is (6.6 ± 1.0) x 10^{14} molecules - cm^{-2} (see Fig. 9).

7. Work Function

The work function change for cyclopropane adsorbed on Ir(110) as a function of exposure is shown in Fig. 13. There is a sharp linear decrease to about -0.5 eV over the range of residue formation (0 - 1.7 L), and then a more gradual decrease to a plateau of -0.7 eV as the overlayer saturates. The fact that most of the change in contact potential difference occurs during residue formation is borne out by the UPS results. In Fig. 2(b) (an exposure of 4 t-s), the spectrum is approximately 0.5 eV wider than the spectrum of the clean surface, reflecting a change in work function. The spectra resulting from higher exposures are only slightly wider than that of spectrum 2(b).

8. Conclusions

The conclusions of this study may be summarized as follows:

1. Ultraviolet photoelectron spectroscopy and thermal desorption of H_2 indicate that a layer of hydrocarbon residue results from the exposure of cyclopropane to an Ir(110)-(1x2) reconstructed surface at 100 K. This layer is saturated at (2.1 ± 0.2) x 10^{14} molecules - cm^{-2} for a cyclopropane exposure of 1.7 L. The reaction probability is 0.87 ± 0.1.

2. For exposures of 1.7 L or less, small amounts of molecular cyclopropane

adsorb into the α-thermal desorption state. The variation of cyclopropane coverage with exposure suggests that an α-adsite is formed by the decomposition of an isolated cyclopropane molecule.

3. For cyclopropane exposures greater than 1.7 L, molecular cyclopropane adsorbs on the residue-covered surface with an initial probability of adsorption of unity. The molecular overlayer saturates at a coverage of $(6.6 \pm 1) \times 10^{14}$ molecules - cm^{-2}. Saturation was obtained at 100 K by exposure of the surface to 8 L of cyclopropane. Ultraviolet photoelectron spectroscopy confirmed the existence of molecular cyclopropane on the surface.

4. The Arrhenius parameters of the desorption rate coefficients were measured for low coverages of the α- and β-thermal desorption states. The results are shown in Table 1.

5. The work function decreases linearly during formation of the residue by -0.5 eV. Adsorption of molecular cyclopropane onto the residue results in a further decrease of the work function by -0.2 eV.

References

1. G. C. Bond and J. Sheridan, Trans. Faraday Soc. *48*, 713 (1952).

2. G. C. Bond and J. Turkevich, Trans. Faraday Soc. *50*, 1335 (1954).

3. J. Addy and G. C. Bond, Trans. Faraday Soc. *53*, 368 (1957).

4. J. H. Sinfelt, D. J. C. Yates and W. F. Taylor, J. Phys. Chem. *69*, 1877 (1965).

5. J. R. Anderson and N. R. Avery, J. Catal. *8*, 48 (1967).

6. R. A. Dalla Betta, J. A. Cusumano and J. H. Sinfelt, J. Catal. *19*, 343 (1970).

7. P. H. Otero-Schipper, W. A. Wachter, J. B. Butt, R. L. Burwell, Jr. and J. B. Cohen, J. Catal. *50*, 494 (1977).

8. T. Hattori and R. L. Burwell, Jr., J. Phys. Chem. *83*, 241 (1979).

9. S. Galvagno, J. Schwank and G. Parravano, J. Catal. *61*, 223 (1980).

10. J. H. Sinfelt, Advan. Catal. *23*, 91 (1973).

11. T. E. Madey and J. T. Yates, Jr., Surface Sci. *76*, 397 (1978).

12. D. E. Ibbotson, T. S. Wittrig and W. H. Weinberg, J. Chem. Phys. *72*, 4885 (1980).

13. J. L. Taylor, D. E. Ibbotson and W. H. Weinberg, J. Chem. Phys. *69*, 4298 (1978).

14. D. E. Ibbotson, T. S. Wittrig and W. H. Weinberg, Surface Sci. (in press, 1981).

15. K. Christmann and G. Ertl, Z. Naturforsch *28a*, 1144 (1973).

16. C.-M. Chan, M. A. Van Hove, W. H. Weinberg and E. D. Williams, Solid State Commun. *30*, 47 (1979); Surface Sci. *91*, 440 (1980).

17. G. Bieri, E. Burger, E. Heilbronner and J. P. Maier, Helvetica Chimica Acta *60*, 2213 (1977).

18. J. L. Taylor and W. H. Weinberg, Surface Sci. *78*, 259 (1978).

19. T. S. Wittrig, P. D. Szuromi and W. H. Weinberg, to be published.

Table 1

Arrhenius Parameters for Thermal Desorption of Cyclopropane from Ir(110)

Thermal Desorption State	Coverage, Molecules-cm^{-2}	E_d, kcal/mole	ν_d, sec^{-1}
α	2×10^{13}	6.4 ± 1	$1 \times 10^{9 \pm 1}$
β	2×10^{13}	8.1 ± 2	$4.7 \times 10^{10 \pm 2}$
β	5×10^{13}	8.5 ± 1	$4.7 \times 10^{10 \pm 2}$

Figure Captions

Fig. 1: Schematic view of the missing-row model of the Ir(110)-(1x2) surface. Cross-hatched circles represent top-layer atoms, open circles represent second-layer atoms, and dotted circles represent third- layer atoms. The scale of the cyclopropane molecule is shown also. The carbon atoms would lie at the vertices of the triangle and the projection of the hydrogen pairs onto the plane is shown as the three radiating lines.

Fig. 2: HeI UPS as a function of cyclopropane exposure to the Ir(110)-(1x2) surface.

Fig. 3: Hydrogen thermal desorption as a function of cyclopropane exposure with T_{ads} = 100 K and β = 20 K - sec^{-1}.

Fig. 4: Thermal desorption yield of hydrogen from cyclopropane adsorbed on Ir(110)-(1x2).

Fig. 5: Cyclopropane thermal desorption from Ir(110)-(1x2). The hydrocarbon residue is not saturated for these exposures, and β = 4 K-sec^{-1}.

Fig. 6: Thermal desorption yield of α-cyclopropane for exposures for which the hydrocarbon residue is not complete.

Fig. 7: Arrhenius plot for α-state of cyclopropane determined by the method of variation of heating rate. See Table 1.

Fig. 8: Cyclopropane thermal desorption from Ir(110)-(1x2). For this exposure regime, the hydrocarbon residue is saturated, and β = 4 K - sec^{-1}.

Fig. 9: Thermal desorption yield of cyclopropane from Ir(110)-(1x2). Triangles and circles represent data obtained on different days.

Fig. 10: Arrhenius plots for β-state of cyclopropane determined by the method of variation of heating rate. See Table 1.

Fig. 11: Thermal desorption of cyclopropane after adsorption of 6 t-s under different conditions. Spectrum (a) - Adsorb at 100 K; Spectrum (b) - Adsorb at 100 K and anneal to 130 K for 30 sec; Spectrum (c) - Adsorb at 135 K.

Fig. 12: Continuous measure of cyclopropane coverage as a function of exposure.

Fig. 13: Work function change as a function of cyclopropane exposure to Ir(110)-(1x2).

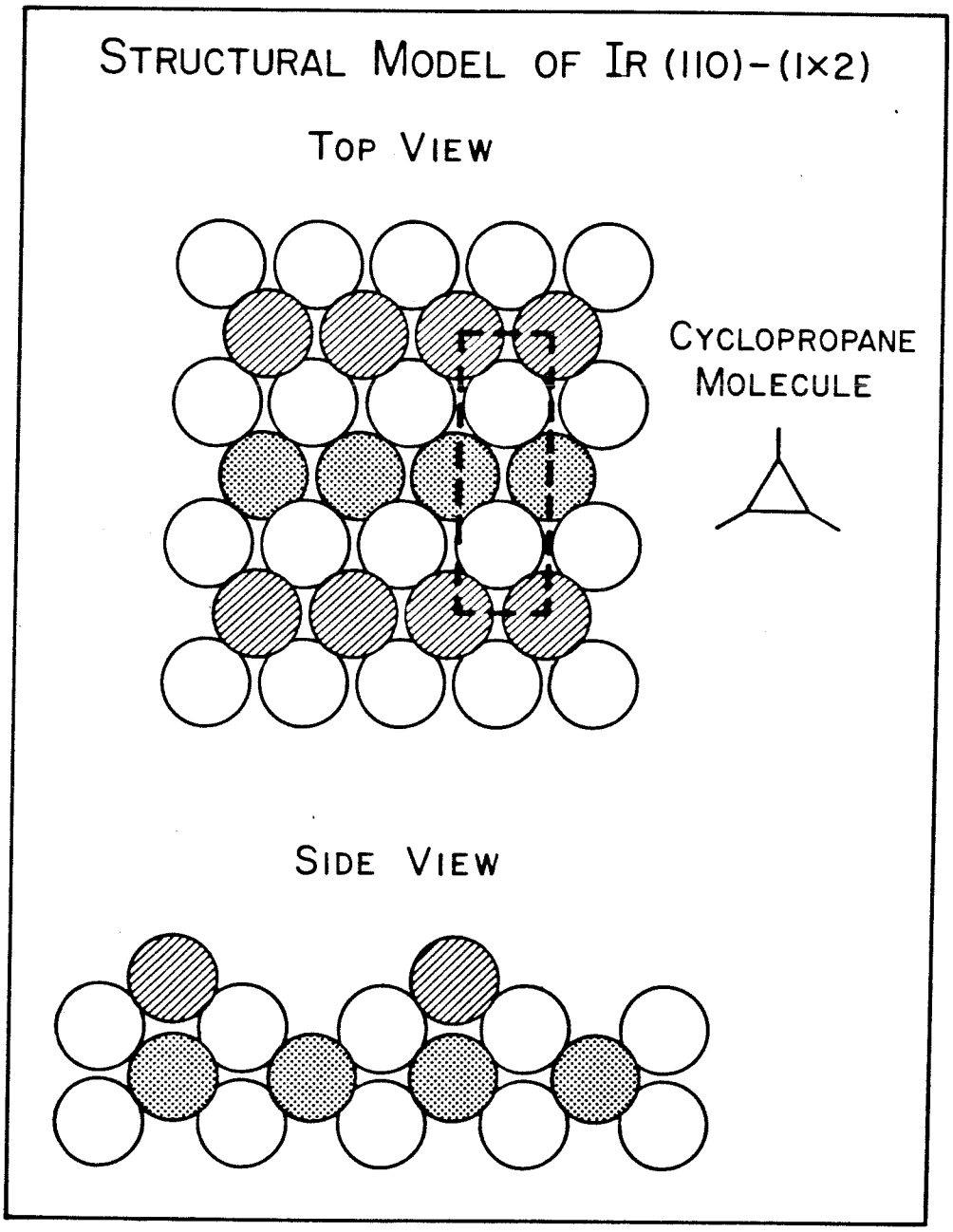
STRUCTURAL MODEL OF IR (110)-(1×2)
TOP VIEW
CYCLOPROPANE
MOLECULE
SIDE VIEW

Fig. 1

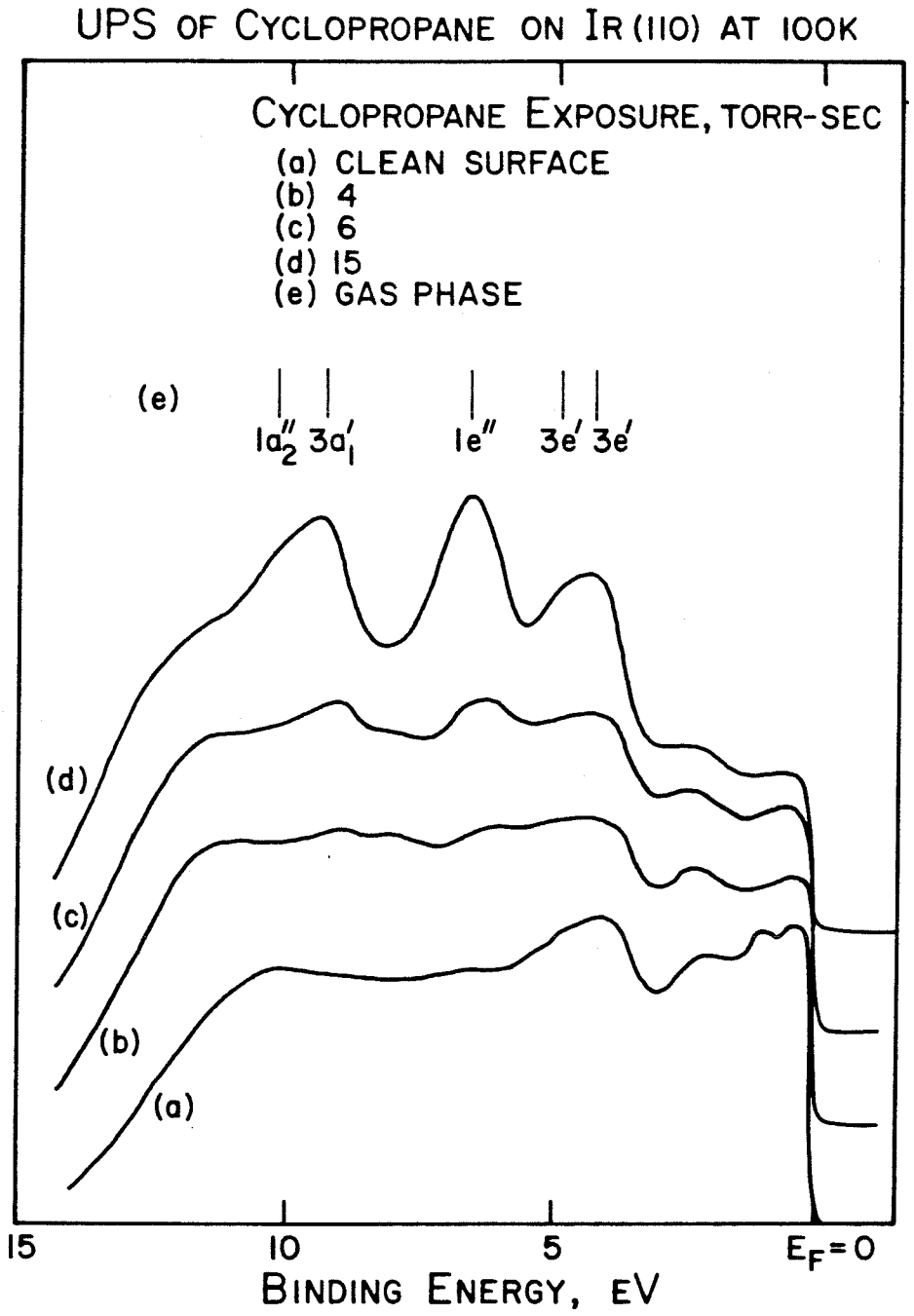
UPS OF CYCLOPROPANE ON IR(110) AT 100K
CYCLOPROPANE EXPOSURE, TORR-SEC
(a) CLEAN SURFACE
(b) 4
(c) 6
(d) 15
(e) GAS PHASE
(e)
$1a_2''$ $3a_1'$
$1e''$
$3e'$ $3e'$
(d)
(c)
(b)
(a)
15
10
5
$E_F = 0$
BINDING ENERGY, eV

Fig. 2

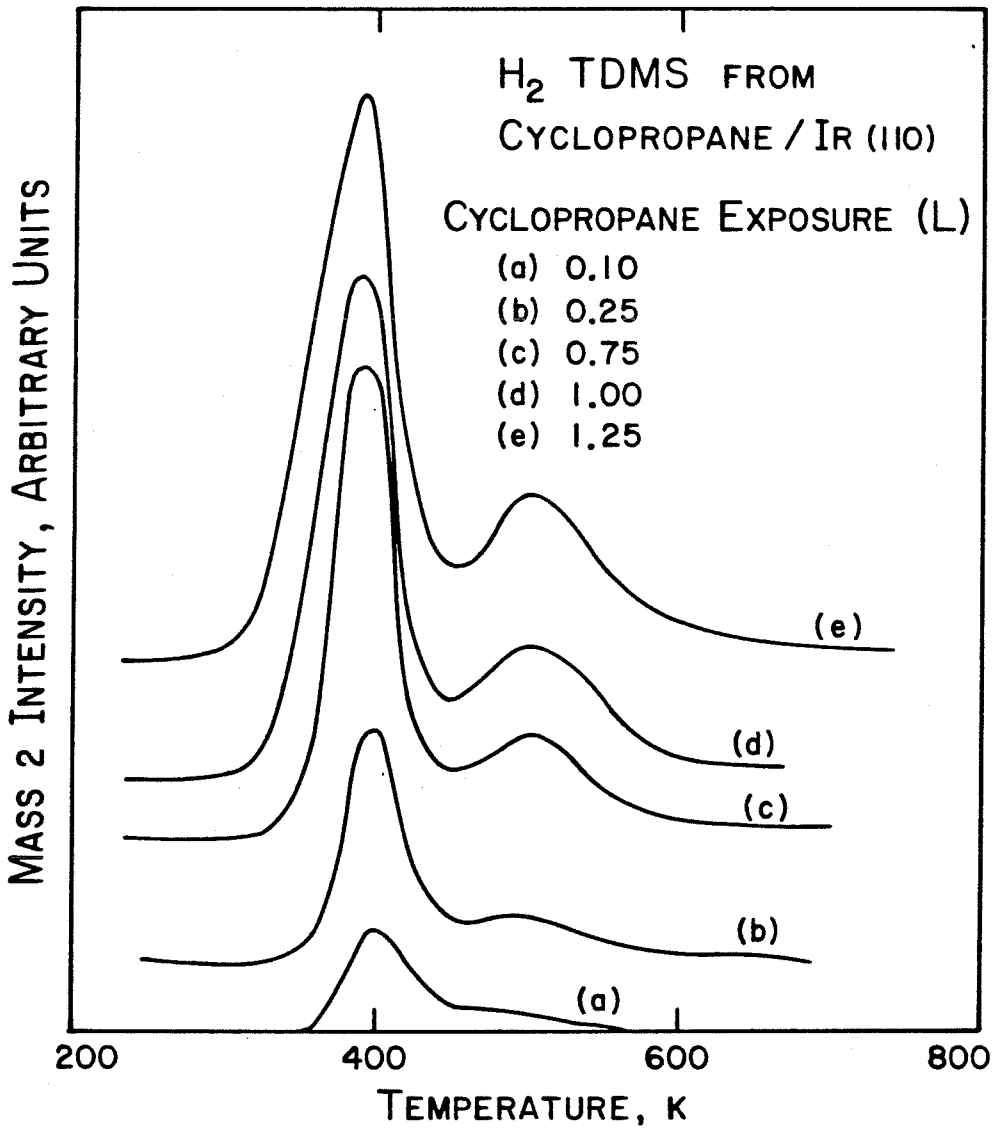
H2 TDMS FROM
CYCLOPROPANE / IR (110)
CYCLOPROPANE EXPOSURE (L)
(a) 0.10
(b) 0.25
(c) 0.75
(d) 1.00
(e) 1.25
(e)
(d)
(c)
(b)
(a)
MASS 2 INTENSITY, ARBITRARY UNITS
200
400
600
800
TEMPERATURE, K

Fig.3

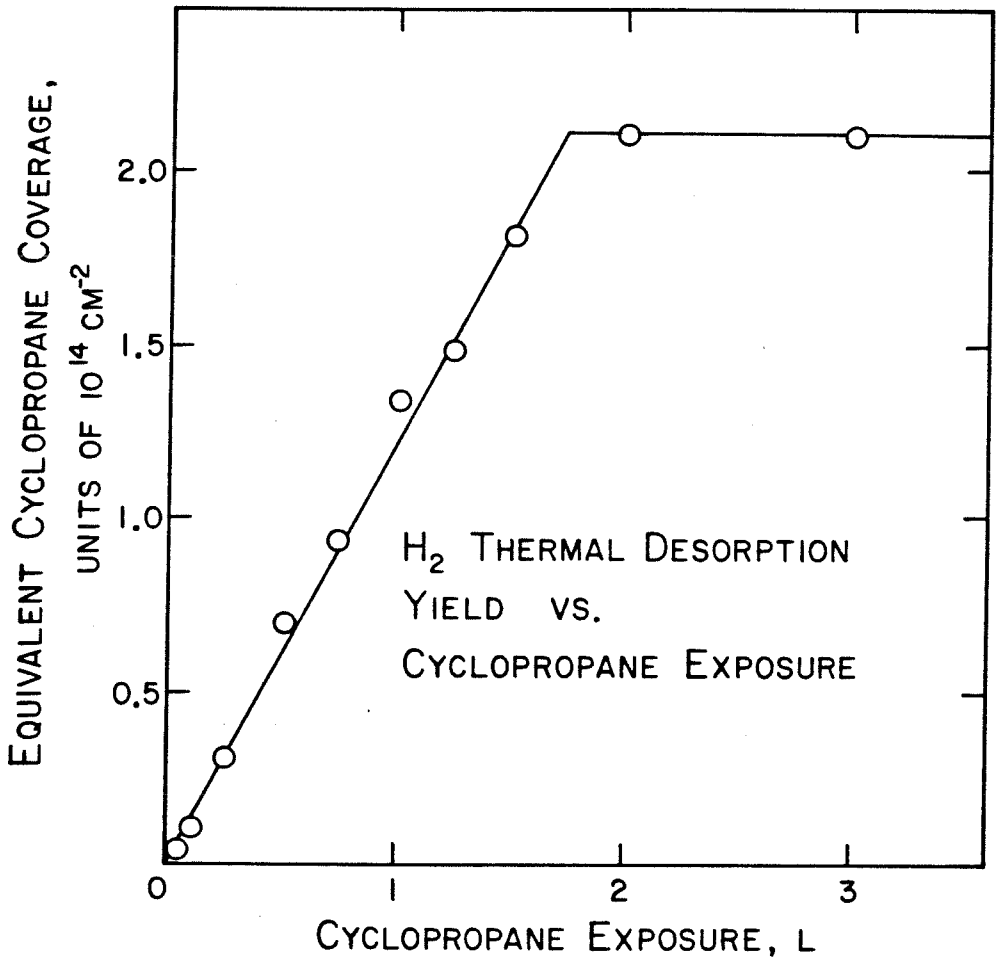
EQUIVALENT CYCLOPROPANE COVERAGE, UNITS OF 10^{14} CM^{-2}
2.0
1.5
1.0
0.5
0
1
2
3
CYCLOPROPANE EXPOSURE, L
H_2 THERMAL DESORPTION
YIELD VS.
CYCLOPROPANE EXPOSURE

Fig. 4

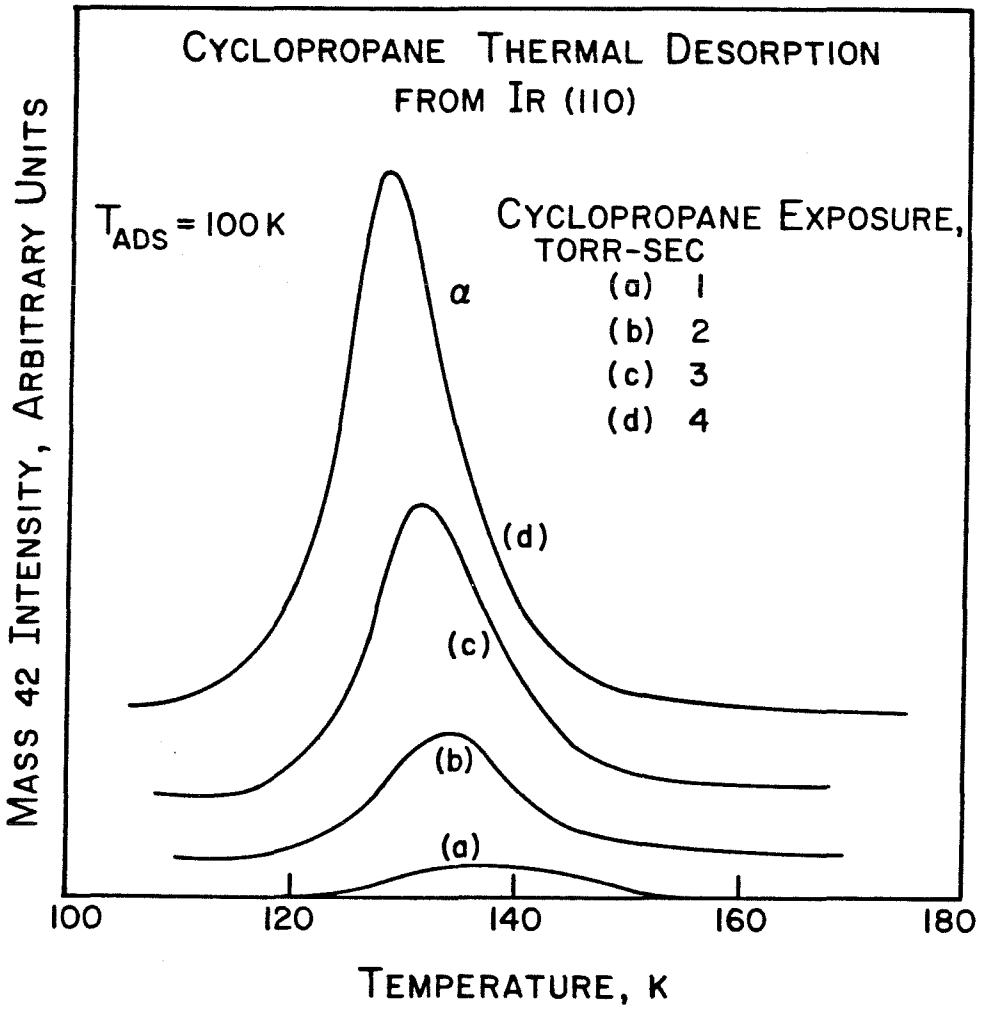
CYCLOPROPANE THERMAL DESORPTION
FROM IR (110)
T_{ADS} = 100 K
CYCLOPROPANE EXPOSURE,
TORR-SEC
(a) 1
(b) 2
(c) 3
(d) 4
α
(d)
(c)
(b)
(a)
MASS 42 INTENSITY, ARBITRARY UNITS
100
120
140
160
180
TEMPERATURE, K

Fig. 5

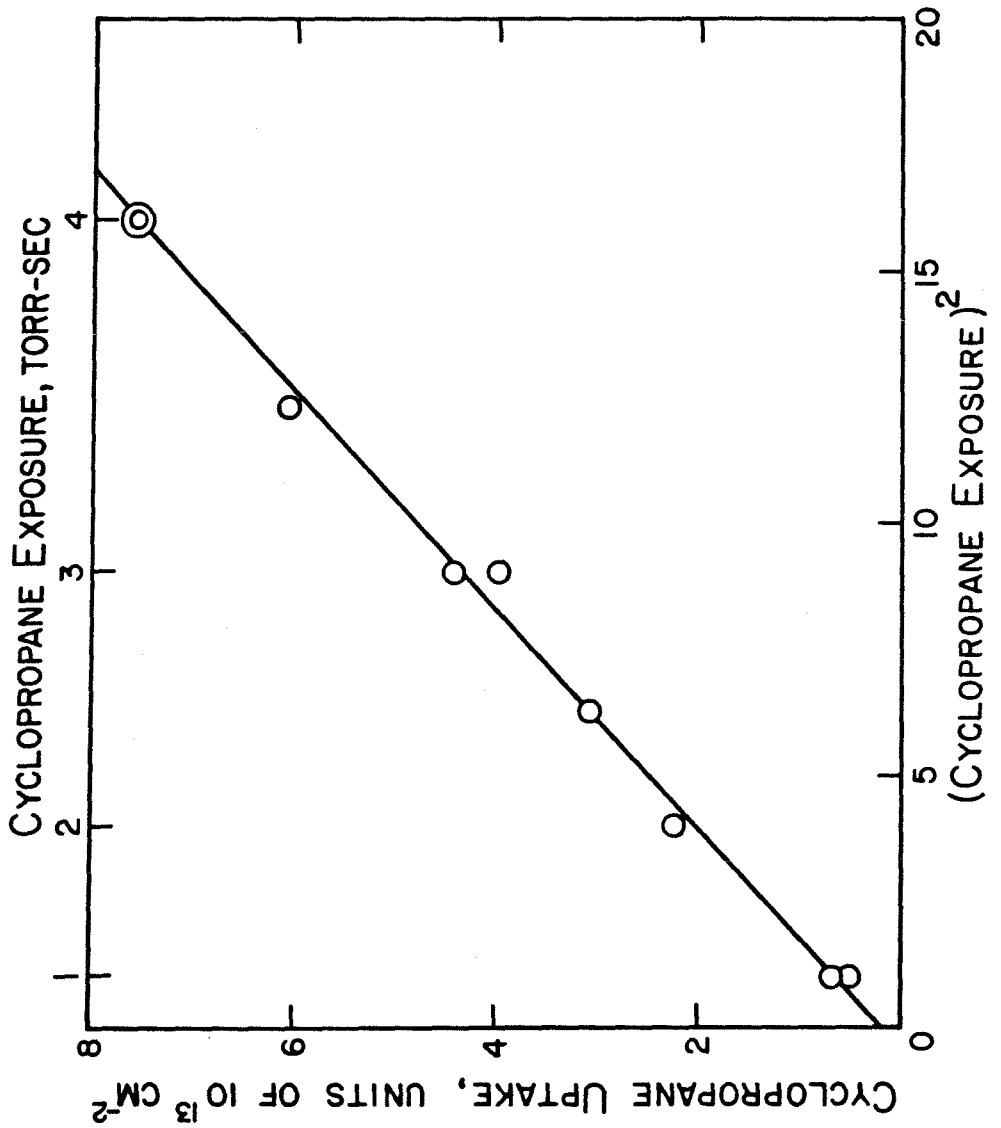
CYCLOPROPANE UPTAKE, UNITS OF 10^{13} CM^{-2}
0
2
4
6
8
CYCLOPROPANE EXPOSURE, TORR-SEC
1
2
3
4
(CYCLOPROPANE EXPOSURE)^2
0
5
10
15
20

Fig. 6

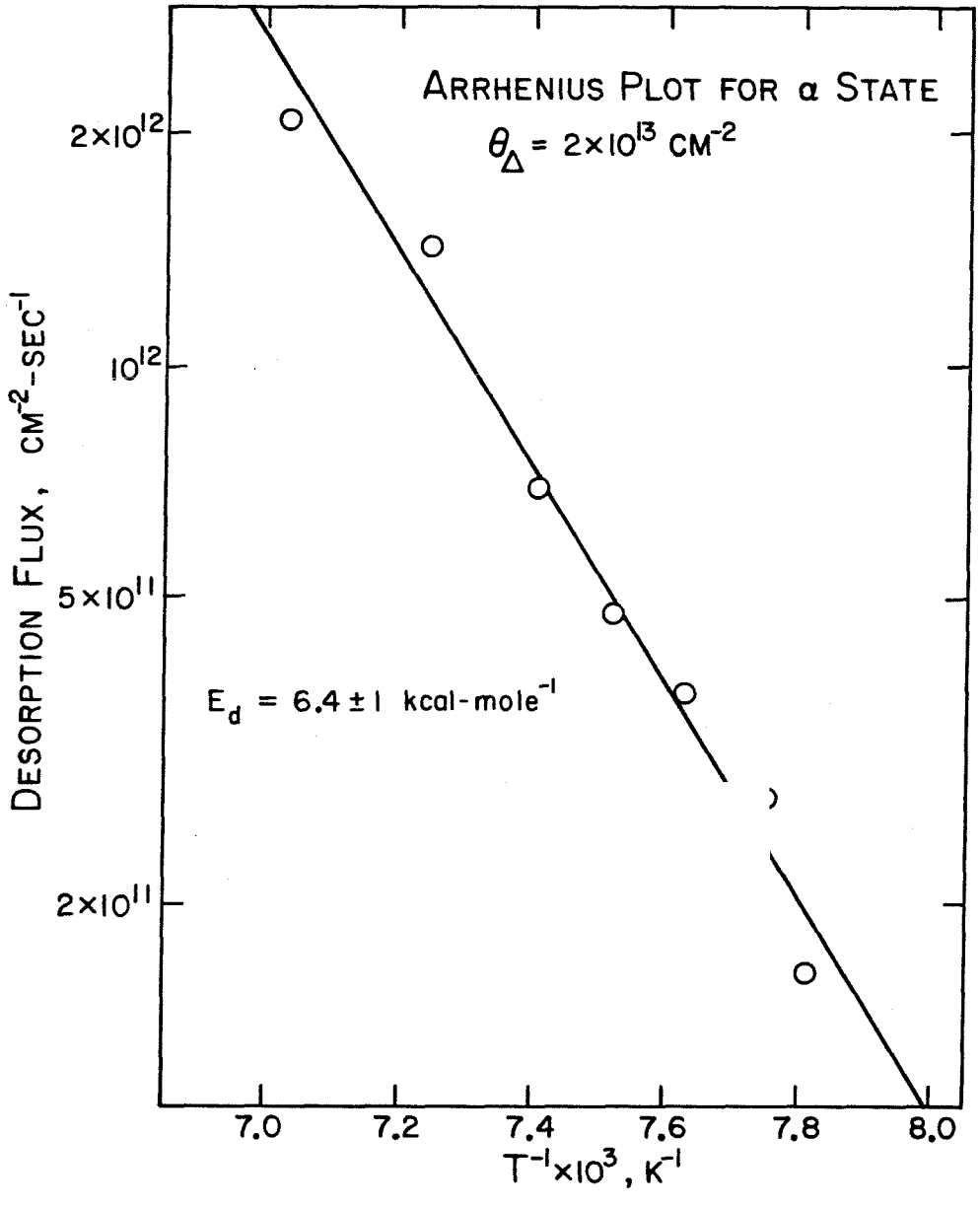
ARRHENIUS PLOT FOR α STATE
$\theta_\Delta = 2\times10^{13}$ CM^{-2}
$E_d = 6.4 \pm 1$ kcal-mole^{-1}
DESORPTION FLUX, CM^{-2}-SEC^{-1}
2×10^{12}
10^{12}
5×10^{11}
2×10^{11}
7.0
7.2
7.4
7.6
7.8
8.0
$T^{-1}\times10^3$, K^{-1}

Fig. 7

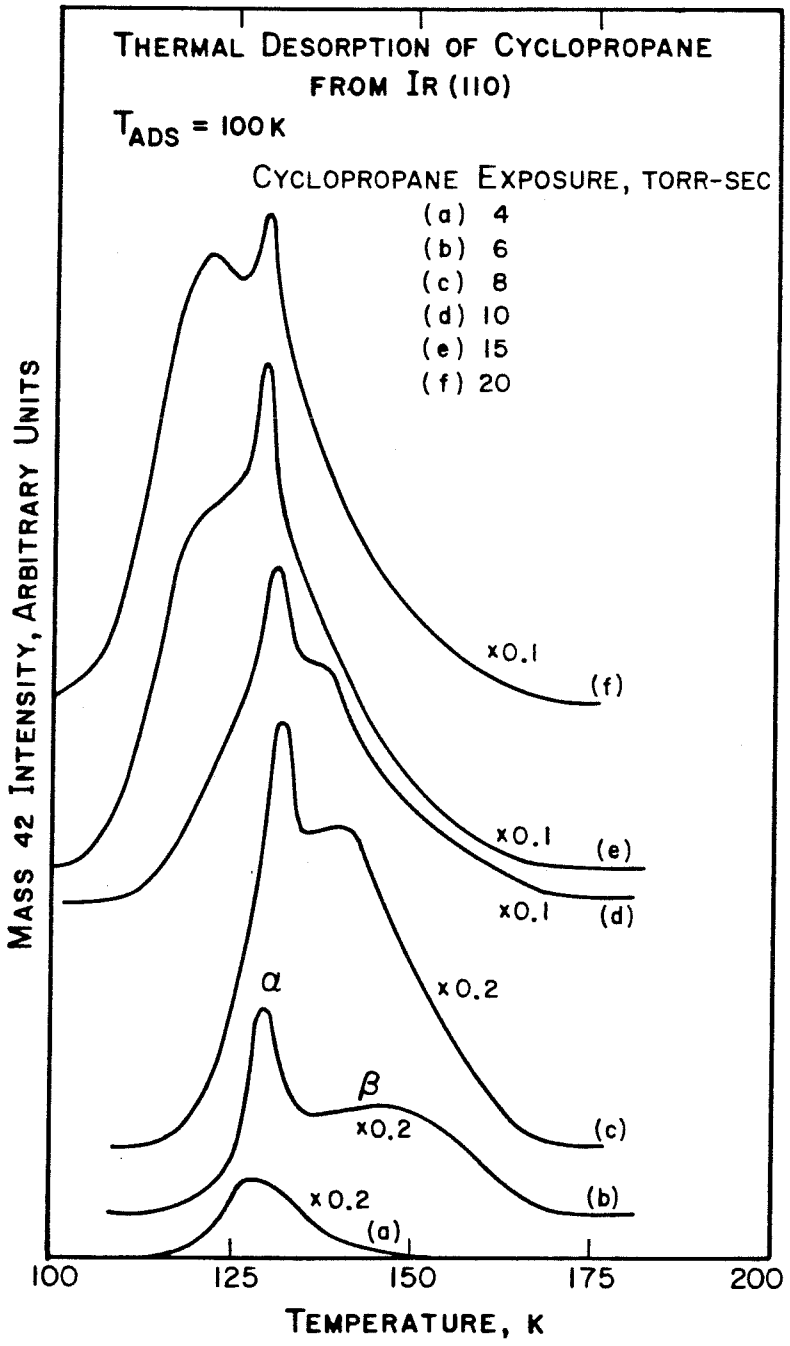
THERMAL DESORPTION OF CYCLOPROPANE
FROM IR (110)
T_{ADS} = 100 K
CYCLOPROPANE EXPOSURE, TORR-SEC
(a) 4
(b) 6
(c) 8
(d) 10
(e) 15
(f) 20
MASS 42 INTENSITY, ARBITRARY UNITS
x0.1
(f)
x0.1
(e)
x0.1
(d)
α
x0.2
β
x0.2
(c)
x0.2
(b)
(a)
100
125
150
175
200
TEMPERATURE, K

Fig. 8

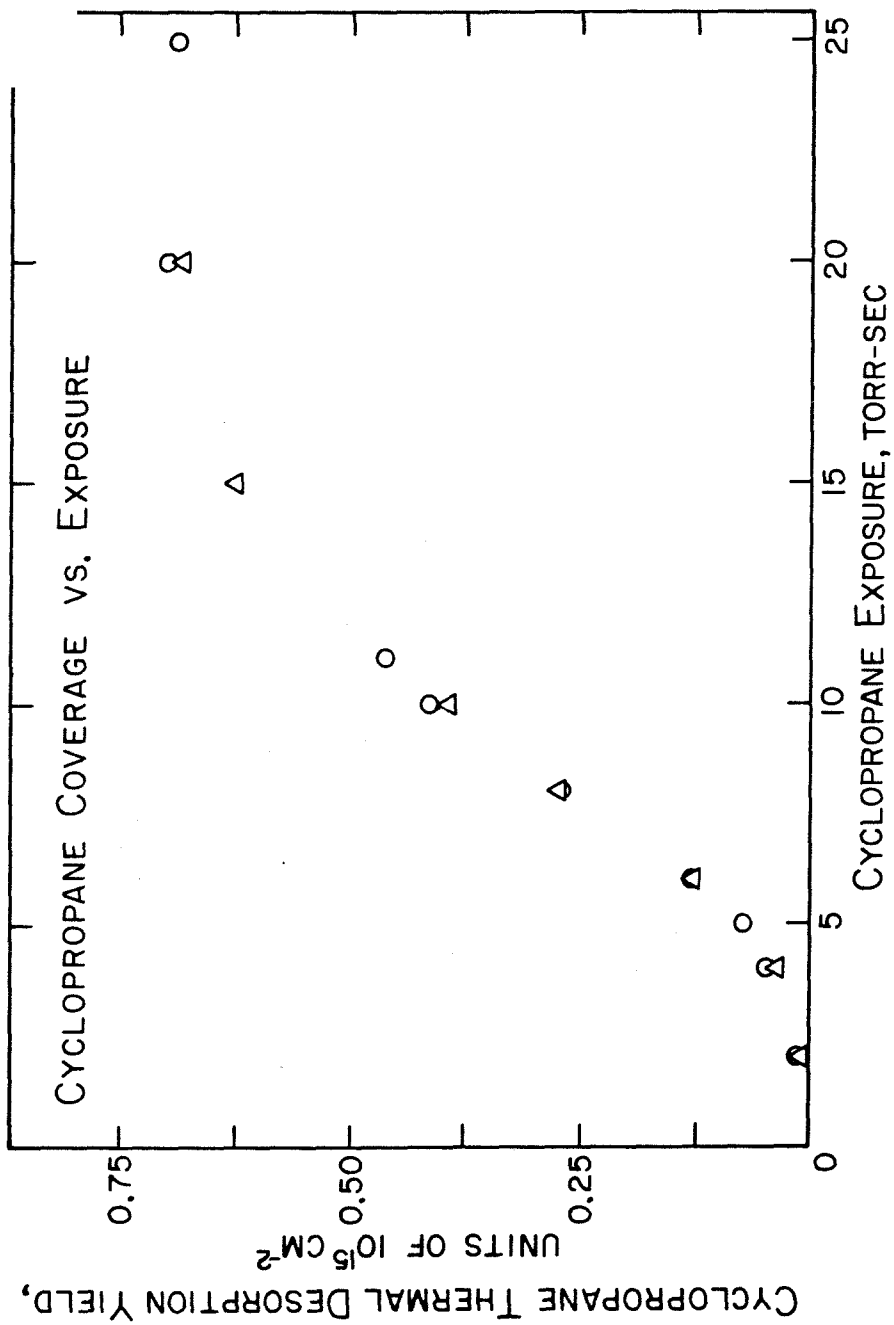
CYCLOPROPANE COVERAGE VS. EXPOSURE
CYCLOPROPANE THERMAL DESORPTION YIELD, UNITS OF 10^{15} CM^{-2}
CYCLOPROPANE EXPOSURE, TORR-SEC
0.75
0.50
0.25
0
5
10
15
20
25

Fig. 9

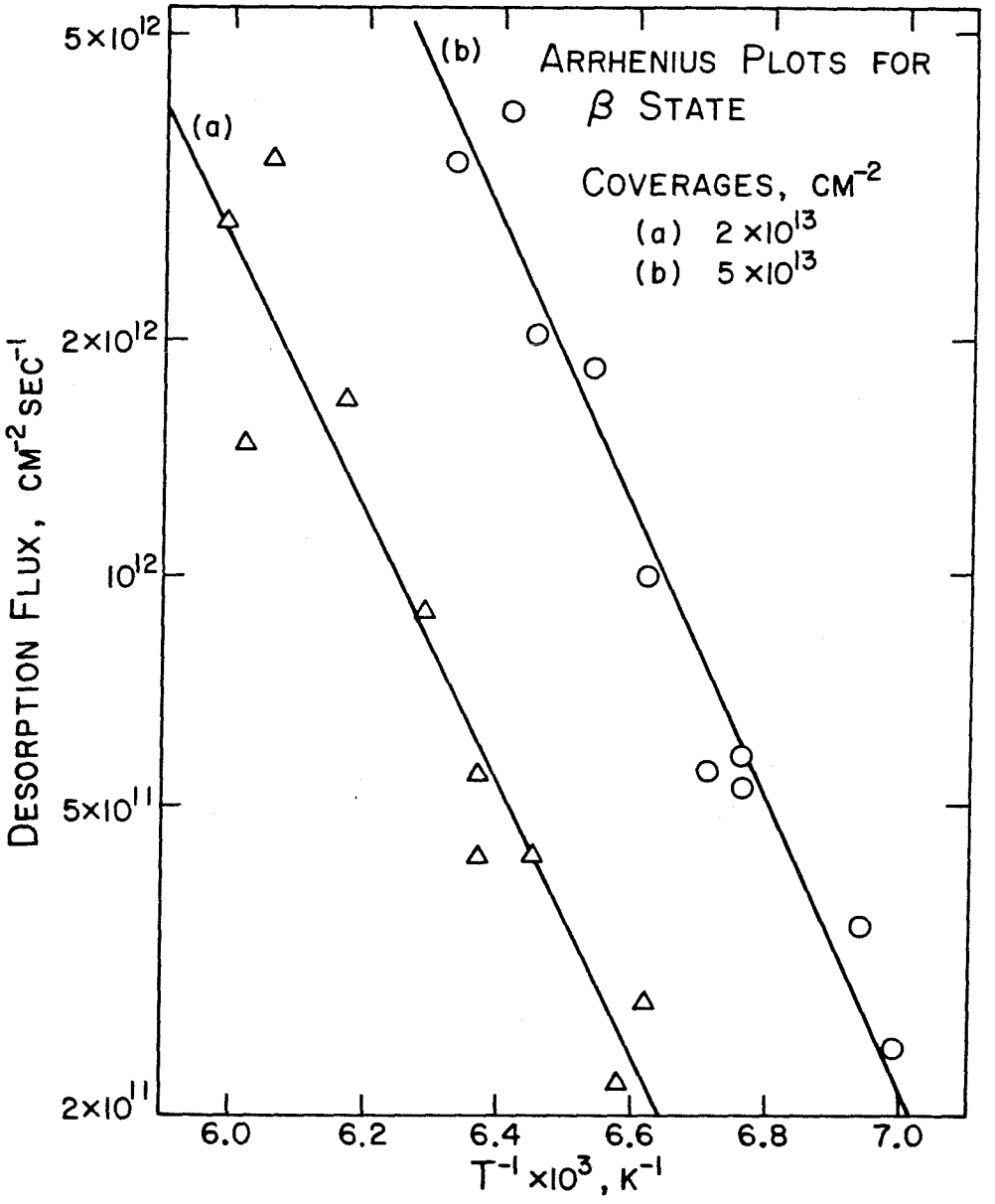
ARRHENIUS PLOTS FOR
β STATE
COVERAGES, CM⁻²
(a) 2×10¹³
(b) 5×10¹³
(a)
(b)
DESORPTION FLUX, CM⁻² SEC⁻¹
5×10¹²
2×10¹²
10¹²
5×10¹¹
2×10¹¹
6.0
6.2
6.4
6.6
6.8
7.0
T⁻¹ ×10³, K⁻¹

Fig. 10

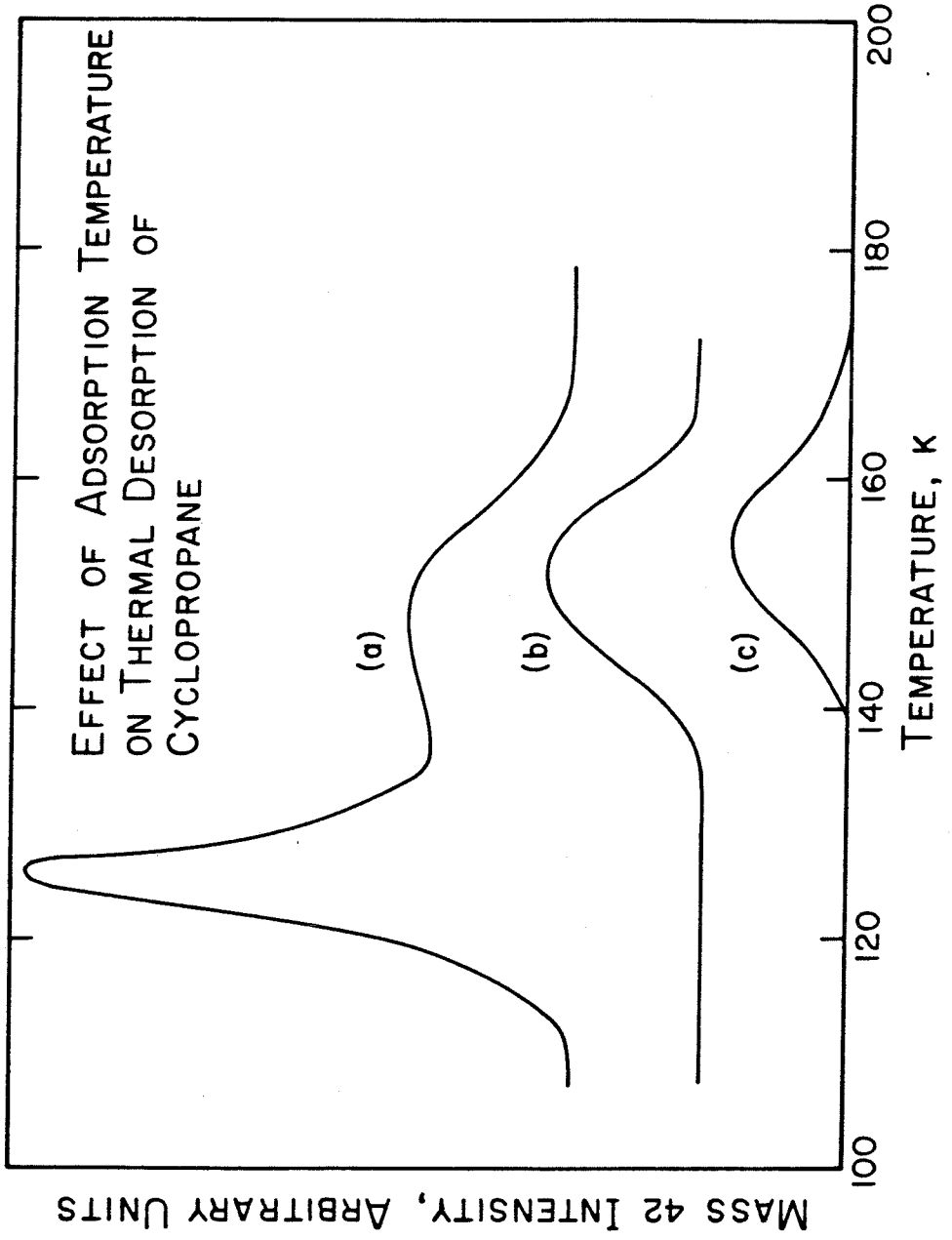
EFFECT OF ADSORPTION TEMPERATURE
ON THERMAL DESORPTION OF
CYCLOPROPANE
(a)
(b)
(c)
100
120
140
160
180
200
TEMPERATURE, K
MASS 42 INTENSITY, ARBITRARY UNITS

Fig. 11

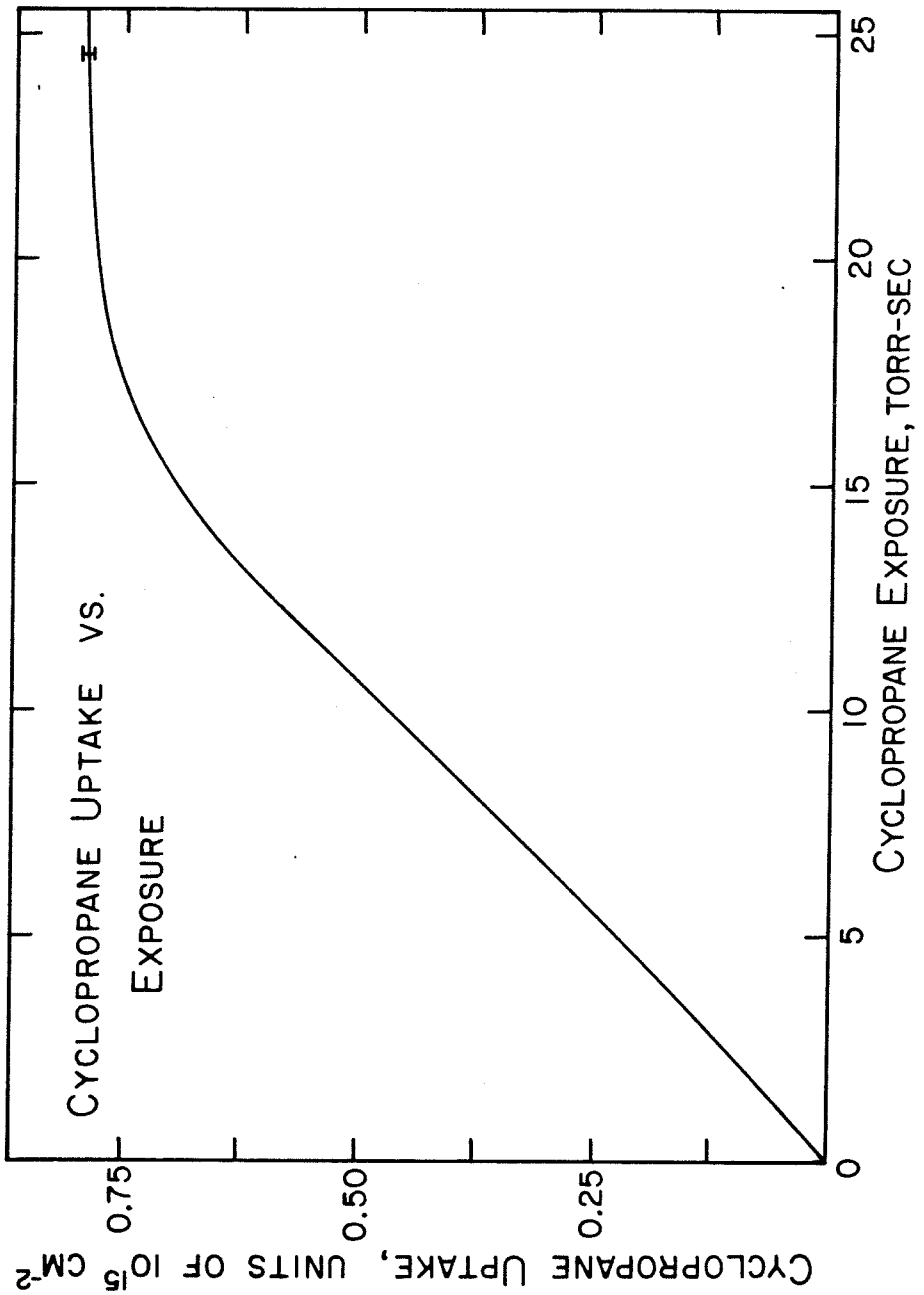
CYCLOPROPANE UPTAKE VS.
EXPOSURE
CYCLOPROPANE UPTAKE, UNITS OF 10^{15} CM^{-2}
0.25
0.50
0.75
0
5
10
15
20
25
CYCLOPROPANE EXPOSURE, TORR-SEC

Fig. 12

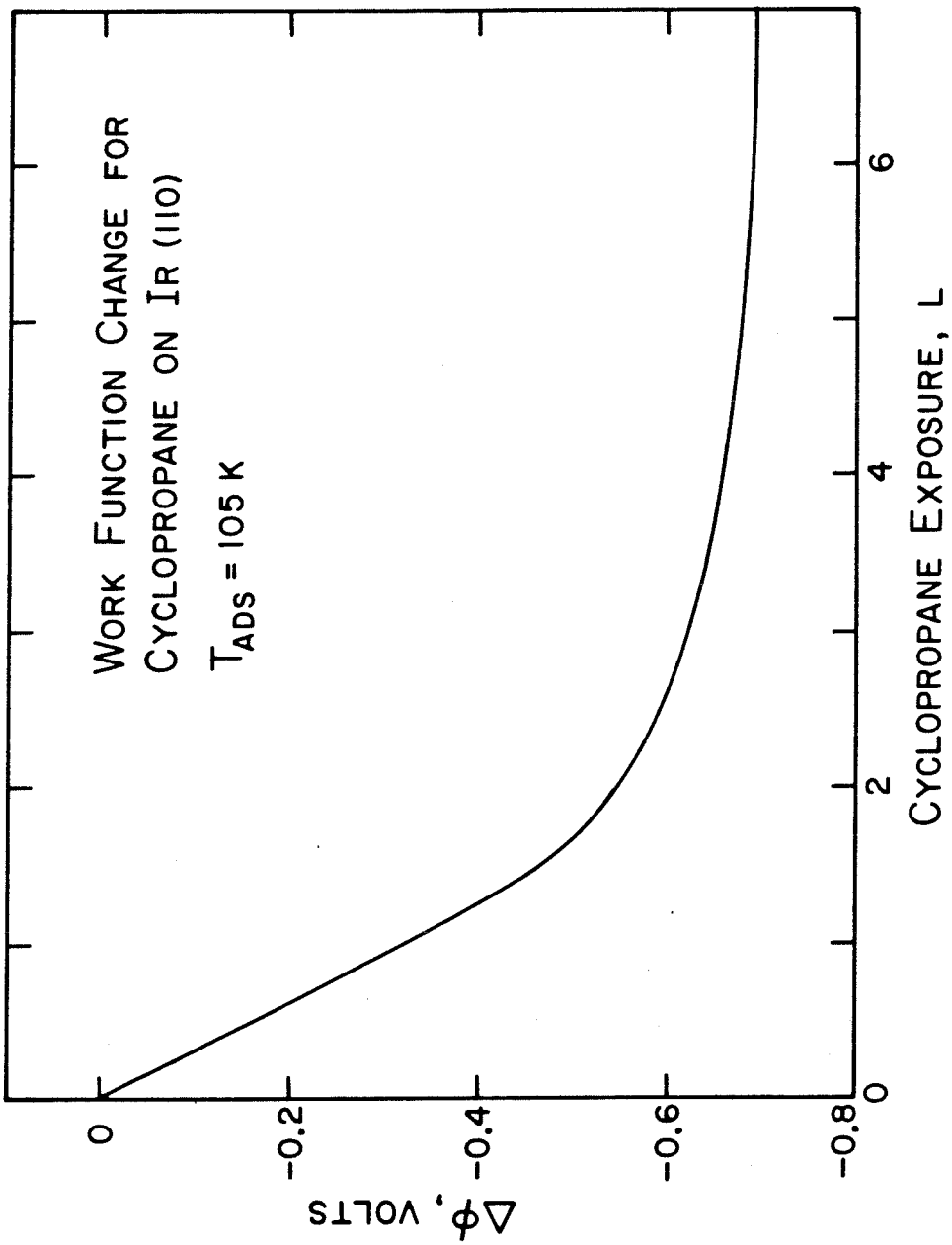
WORK FUNCTION CHANGE FOR
CYCLOPROPANE ON IR (110)
T_{ADS} = 105 K
Δφ, VOLTS
0
-0.2
-0.4
-0.6
-0.8
0
2
4
6
CYCLOPROPANE EXPOSURE, L

Fig. 13

CHAPTER 5

THE INTERACTION OF HYDROGEN AND CYCLOPROPANE WITH THE (110) SURFACE OF IRIDIUM

(The text of Chapter 5 consists of an article coauthored with P.D. Szuromi and W.H. Weinberg that has been submitted to Surface Science.)

Abstract

The interaction of cyclopropane with hydrogen and the residue resulting from the decomposition of the former on the reconstructed Ir(110)-(1x2) surface has been studied with thermal desorption mass spectrometry. Although hydrogen will not adsorb onto the saturated overlayer of dissociatively adsorbed cyclopropane, the preadsorption of hydrogen into the β_2 adstate inhibits the decomposition of cyclopropane on the surface. Desorption of the hydrogen from the saturated overlayer of the dissociatively adsorbed cyclopropane partially regenerates the reactivity of the surface.

1. Introduction

The study of the interactions of saturated hydrocarbons with transition metal surfaces is important because of the insight it may provide into the general mechanisms of hydrocarbon reactions on metal surfaces that may be of industrial importance. There have been several recent ultrahigh vacuum studies of the dehydrogenation of cyclohexane to form benzene **(1-3)**. Other studies of the *nonreactive* interaction of saturated hydrocarbons with surfaces of transition metals include LEED studies of the *nondissociative* adsorption of straight-chain paraffins on Pt(111) and Ag(111) **(4)**, EELS and UPS studies of cyclopropane and cyclohexane adsorbed molecularly on Ru(001) **(5)** and an ESDIAD study of the *nondissociative* adsorption of ethane, cyclopropane and cyclohexane on Ru(001) **(6)**.

In a recently completed study in this laboratory, it was shown that exposure of the clean Ir(110)-(1x2) surface to cyclopropane at 100 K results in the formation of an overlayer of hydrocarbon fragments on the surface **(7)**. A surface prepared in this manner yields the hydrogen thermal desorption spectrum shown in Fig. 1(a). The only **hydrocarbon** that desorbs is molecular cyclopropane below 150 K. The thermal desorption spectrum of a saturation coverage of hydrogen on the clean Ir(110)-(1x2) surface is shown in Fig. 1(b) for comparison **(8)**. As indicated in this figure, there are two peaks referred to as the β_1 (low temperature) and β_2 (high temperature) thermal desorption states. The β_2 state populates according to first-order adsorption kinetics with an initial probability of adsorption of unity. Saturation of the β_2 state occurs after an exposure of 0.35 L of H_2.

The low temperature hydrogen desorption state from the cyclopropane residue has been labelled the β_2' state as indicated in Fig. 1(a). The similarity in

intensity and temperature of desorption of this thermal desorption peak compared to the β_2 peak of hydrogen after adsorption of H_2 is taken as evidence to support the proposition that hydrogen desorbing from the β_2' state is bonded in hydrogen-iridium sites that are closely related to the β_2 adsorption sites of hydrogen on the clean surface. The γ thermal desorption state represents hydrogen that is more strongly bound to the surface than hydrogen on clean Ir(110). It is well known from spectroscopic studies of unsaturated hydrocarbons on transition metals that hydrocarbon fragments exist on these surfaces even after partial dehydrogenation **(9,10)**. The γ thermal desorption state represents hydrogen evolution from such fragments on the Ir(110) surface.

This paper describes measurements concerning the interaction of cyclopropane, the hydrocarbon residue derived from the dissociative chemisorption of cyclopropane, and hydrogen on the Ir(110)-(1x2) surface. The adsorption of hydrogen onto a preadsorbed overlayer of cyclopropane and the adsorption of cyclopropane onto preadsorbed overlayers of hydrogen were investigated, as well as the adsorption of both hydrogen and cyclopropane onto the hydrocarbon residue under various conditions.

2. Experimental Procedures

The experiments were performed in an ion pumped stainless steel belljar that has been described previously **(8,11)**. The base pressure of the belljar was below 2×10^{-10} Torr of reactive contaminants. The cyclopropane exposures were carried out with a directional beam doser consisting of a multichannel array of capillaries **(12)**. During dosing, the crystal is positioned approximately 3 mm from the doser face. This provides a beam pressure-to-background pressure ratio of over 100:1. The unit of exposure that is employed for the beam doser is Torr-s and refers to the product of the time of exposure and the pressure in the

storage bulb of the doser. The storage bulb supplies gas through a capillary to the doser head leading into the vacuum system. Therefore, the flux of gas into the vacuum system is proportional to the pressure in the storage bulb. For cyclopropane in this system, 2.5 Torr-s are approximately equivalent to an exposure of 1 Langmuir in the ultrahigh vacuum system.

The crystal was cleaned between thermal desorption experiments by exposure to 10^{-7} Torr of O_2 for two min at a crystal temperature of 900 K, followed by flashing to 1600 K to desorb the oxygen. This procedure reproducibly yielded a reconstructed Ir(110)-(1x2) surface but was free of oxygen or carbon impurities.

The hydrogen used in this investigation was Matheson research purity (99.9999%). The cyclopropane was obtained from Linde, and the minimum purity was 99%. The cyclopropane was purified further by cryogenic distillation. Both gases were checked mass spectrometrically for purity after admission into ultrahigh vacuum system.

3. Results and Discussion

3.1 Adsorption of H_2 on the Cyclopropane Residue

The results of one of several experiments to determine the kinetics of adsorption of H_2 onto the saturated residue of cyclopropane are shown in Fig. 2. A saturated overlayer of the hydrocarbon residue was prepared by exposing the clean surface to 10 Torr-s of cyclopropane at 100 K, and subsequently annealing the surface to 200 K. An exposure of 10 Torr-s ensured that the residue state was saturated, and the anneal cycle desorbed all reversibly adsorbed molecular cyclopropane. The thermal desorption spectrum shown in Fig. 2(b) results from exposing 2 L of H_2 to a saturated overlayer of the hydrocarbon residue. The two spectra are identical, indicating that the probability of adsorption of H_2 on the

saturated hydrocarbon residue is below 10^{-3}. In particular, the β_1 adsorption sites of hydrogen available on the clean surface are poisoned by the presence of the hydrocarbon residue [cf. Fig. 1(b)].

3.2 Cyclopropane Adsorbed on Preadsorbed Hydrogen

On the other hand, if hydrogen is adsorbed prior to the adsorption of cyclopropane, the reactivity of the surface for the dissociation of cyclopropane is decreased. Here, the reactivity of the surface is defined as the total amount of cyclopropane that is adsorbed dissociatively on the surface, and it was measured by the following procedure. The thermal desorption yield of molecular cyclopropane (mass 42) is shown in Fig. 3 as a function of cyclopropane exposure to the clean surface **(7)**. After an induction period of 4 Torr-s, the yield exhibits a linear rise with increasing exposure. The magnitude of the induction period (defined here as the magnitude of the x-intercept of the line shown in Fig. 3) can be used as a measure of the amount of cyclopropane that dissociates on the surface. For example, if no cyclopropane were to dissociate on the surface, the x-intercept would be the origin. The reactivity of the surface for the dissociative chemisorption of cyclopropane was measured for various precoverages of hydrogen in the β_2 state. The results of these measurements are presented in Fig. 4. The probability of adsorption of molecular cyclopropane on the residue (proportional to the slopes of the lines in Fig. 4) remains constant for the various precoverages of hydrogen. However, the reactivity of the surface for the dissociation of cyclopropane (proportional to the x-intercepts of the lines in Fig. 4) decreases linearly with increasing population of the β_2 adstate of hydrogen. This is shown more clearly in Fig. 5, in which the (normalized) fractional coverage of the dissociatively chemisorbed cyclopropane is shown as a function of the fractional coverage of hydrogen in the β_2 adstate.

It should be noted that saturation of the β_2 adstate of hydrogen corresponds to only 1/3 of saturation coverage of hydrogen on the surface at 100 K, and hence a substantial fraction of the iridium surface remains exposed. This fact, together with the observed linear dependence of the probability of dissociative chemisorption on the availability of β_2 adsites, indicates that the β_2 adsites of hydrogen are essential for the decomposition of cyclopropane on the Ir(110) surface. The residual activity (10% of that on the clean surface) that is apparent in Fig. 5 when the β_2 adstate is saturated with hydrogen is probably due to imperfections on the surface which cannot be poisoned completely by the presence of hydrogen.

For the adsorption of cyclopropane onto surfaces with small fractional precoverages of deuterium, there was no observed desorption of mass 43 in the region of molecular cyclopropane desorption. Thus, there is no exchange between deuterium in the β_2 adstate and hydrogen in molecularly adsorbed cyclopropane. This is a further indication that the surface is not effective for C-H bond activation after the residue state is saturated.

3.3 Adsorption of Hydrogen on the Dehydrogenated Residue

In previous work, it was determined that heating a surface on which cyclopropane was adsorbed to 700 K resulted in complete desorption of the hydrogen with no removal of the carbon from the surface **(7)**. A surface prepared in this manner (with a saturation coverage of the dissociated cyclopropane present initially) will henceforth be referred to as the dehydrogenated residue (DHR). If the DHR is exposed to 20 L of H_2, the thermal desorption spectrum of H_2 exhibits one peak in the range of tempeature suggestive of the β_2 adstate as shown in Fig. 6(b). The thermal desorption spectrum resulting from an exposure of 20 L of H_2 to the clean Ir(110) surface is shown for comparison in Fig. 6(a).

Saturation of the β_2' sites [cf. Fig. 1(a)] available in the presence of the DHR corresponds to 60% of the saturation level of β_2 hydrogen on the clean surface as determined by a comparison of Fig. 6(a) with Fig. 6(b). This indicates that 40% of the sites are poisoned by carbon on the surface. In addition, as is clear from Fig. 6(b), no β_1 adsorption sites are available on the DHR.

The DHR becomes saturated with hydrogen after an exposure of 1 L. Such a surface will be referred to as the hydrogen-treated carbon residue (HTCR). As may be seen in Fig. 7, the hydrogen obeys first-order adsorption kinetics rather than the second-order kinetics usually associated with dissociative adsorption. This unusual behavior is also observed for the adsorption of H_2 into the β_2 adstate on the clean Ir(110) surface. This information is a further indication that the hydrogen adsorbed onto the DHR is adsorbed into sites very similar to the β_2 sites occupied by hydrogen on the clean surface. It should be mentioned, however, that the data of Fig. 7 imply an initial probability of adsorption of H_2 on the DHR of 0.5 ± 0.1 as opposed to a value of unity on the clean surface. However, if the part of the surface that is poisoned for hydrogen adsorption by adsorbed carbon is taken into account, this lower probability for the adsorption of hydrogen is the expected result.

The absence of a γ peak near 500 K in Fig. 6(b) indicates that C-H bonds are not reformed by adsorbing hydrogen onto the DHR. Further evidence of the lack of reactivity of the adsorbed carbon with hydrogen was obtained by exposing the DHR to 5×10^{-8} Torr of H_2 at 700 K for 4 min. Upon cooling and reexposure of this surface to 1.5 L of H_2, the surface exhibited exactly the same thermal desorption spectrum of H_2 as that shown in Fig. 6(b). If any appreciable ($\gtrsim$ 5%) reaction of the chemisorbed carbon had taken place, it would have been observed as an increase in the intensity of the β_2' thermal desorption state near 400 K. Therefore, the availability of β_2' adsorption sites for hydrogen does not

promote the reaction between hydrogen atoms and the adsorbed carbon under the experimental conditions investigated here.

3.4 Reactivity of Cyclopropane on Treated Surfaces

However, the β_2' sites can act as active centers for the dissociation of cyclopropane. The probability of dissociative chemisorption of cyclopropane was measured for the DHR, the HTCR, and the partially dehydrogenated residue (PDHR). The PDHR was formed by saturating the residue state at 100 K followed by annealing the surface to 425 K. This procedure desorbed the hydrogen from the β_2' sites but left the γ C-H bonds intact (cf. Fig. 1). As mentioned previously, the formation of the DHR left an adsorption state of hydrogen that would accommodate 60% as much β_2' hydrogen as the clean surface. Exposure of the DHR to H_2 to create the HTCR, of course, rendered the β_2' sites unavailable for reaction.

The reactivity of these surfaces for the dissociative adsorption of cyclopropane was measured in the manner described previously. The results are presented in Fig. 8. As shown in this figure, the DHR is 58% as reactive as the clean surface for the dissociation of cyclopropane. This is indistinguishably close to the measured availability of β_2' hydrogen adsorption sites (i.e. 60%). The presence of the C-H bonds in the PDHR does not affect the reactivity greatly. However, the presence of hydrogen atoms in the β_2' sites in the HTCR decreases the reactivity to 15% of the reactivity of the clean surface. This compares well with the 10% reactivity observed for a surface saturated with β_2 hydrogen (cf. Fig. 5). Thus, the reactivity of the surface under these circumstances is again limited by the availability of β_2 hydrogen adsorption sites as active reaction centers.

4. Summary

The results of this study may be summarized as follows:

1. The reactivity of the Ir(110)-(1x2) surface for the dissociation of cyclopropane is determined by the number of β_2 hydrogen adsorption sites available. This implies that H-C bond rupture is the initial step in the dissociation of cyclopropane on the surface.

2. The β_1 adsorption state of hydrogen is poisoned by the presence of the cyclopropane residue on the DHR.

3. Exposure of the DHR to H_2 results in the adsorption of hydrogen into a state very similar to the β_2 hydrogen adsorption state observed on clean Ir(110). This state contains 60% as much hydrogen at saturation as the saturated β_2 state on the clean surface.

4. The chemisorbed carbon in the DHR is not reactive to hydrogen, even at temperatures as high as 700 K. The C-H bonds observed in the γ-state in thermal desorption spectra from a cyclopropane residue are not regenerated upon exposure of the DHR to H_2.

References

1. G. W. Rubloff, H. Luth, J. E. Demuth and W. D. Grobman, J. Catal. **53**, 423 (1978).

2. K. Bhattacharya, J. C. S. Faraday I **76**, 126 (1980).

3. J. E. Demuth, H. Ibach and S. Lehwald, Phys. Rev. Letters **40**, 1044 (1978).

4. L. E. Firment and G. A. Somorjai, J. Chem. Phys. **66**, 2901 (1977); J. Chem. Phys. **69**, 3940 (1978).

5. F. M. Hoffmann, T. E. Felter, P. A. Thiel and W. H. Weinberg, Surface Sci. (submitted); J. Vacuum Sci. Technol. **18**, 651 (1981); J. Chem. Phys. (submitted).

6. T. E. Madey and J. T. Yates, Jr., Surface Sci. **76**, 397 (1978).

7. T. S. Wittrig, P. D. Szuromi and W. H. Weinberg, J. Chem. Phys. (submitted).

8. D. E. Ibbotson, T. S. Wittrig and W. H. Weinberg, J. Chem. Phys. **72**, 4885 (1980).

9. J. B. Benziger and R. J. Madix, J. Catal. **65**, 49 (1980).

10. J. E. Demuth, Chem. Phys. Letters **45**, 12 (1977).

11. J. L. Taylor, D. E. Ibbotson and W. H. Weinberg, J. Chem. Phys. **69**, 4298 (1978).

12. D. E. Ibbotson, T. S. Wittrig and W. H. Weinberg, Surface Sci. **110**, 000 (1981).

Figure Captions

Fig. 1: (a) Hydrogen thermal desorption resulting from 1.7 L exposure of cyclopropane to the clean Ir(110)-(1x2) surface. (b) Hydrogen thermal desorption resulting from 300 L exposure of H_2 to the clean Ir(110)-(1x2) surface.

Fig. 2: (a) Hydrogen thermal desorption from a saturated residue of cyclopropane. (b) Hydrogen thermal desorption from a saturated residue of cyclopropane exposed to 2 L H_2.

Fig. 3: Yield of cyclopropane as a function of exposure of cyclopropane.

Fig. 4: Yield of cyclopropane as a function of exposure to cyclopropane parametric in the preexposure of the surface to hydrogen.

Fig. 5: Surface reactivity as a function of preexposure to hydrogen.

Fig. 6: (a) Hydrogen thermal desorption resulting from an exposure of 20 L of H_2 to the clean surface. (b) Hydrogen thermal desorption resulting from an exposure of 20 L of H_2 to the DHR.

Fig. 7: Hydrogen coverage as a function of exposure to the DHR. The solid line represents first-order adsorption kinetics.

Fig. 8: Yield of cyclopropane as a function of surface pretreatment and exposure to cyclopropane.

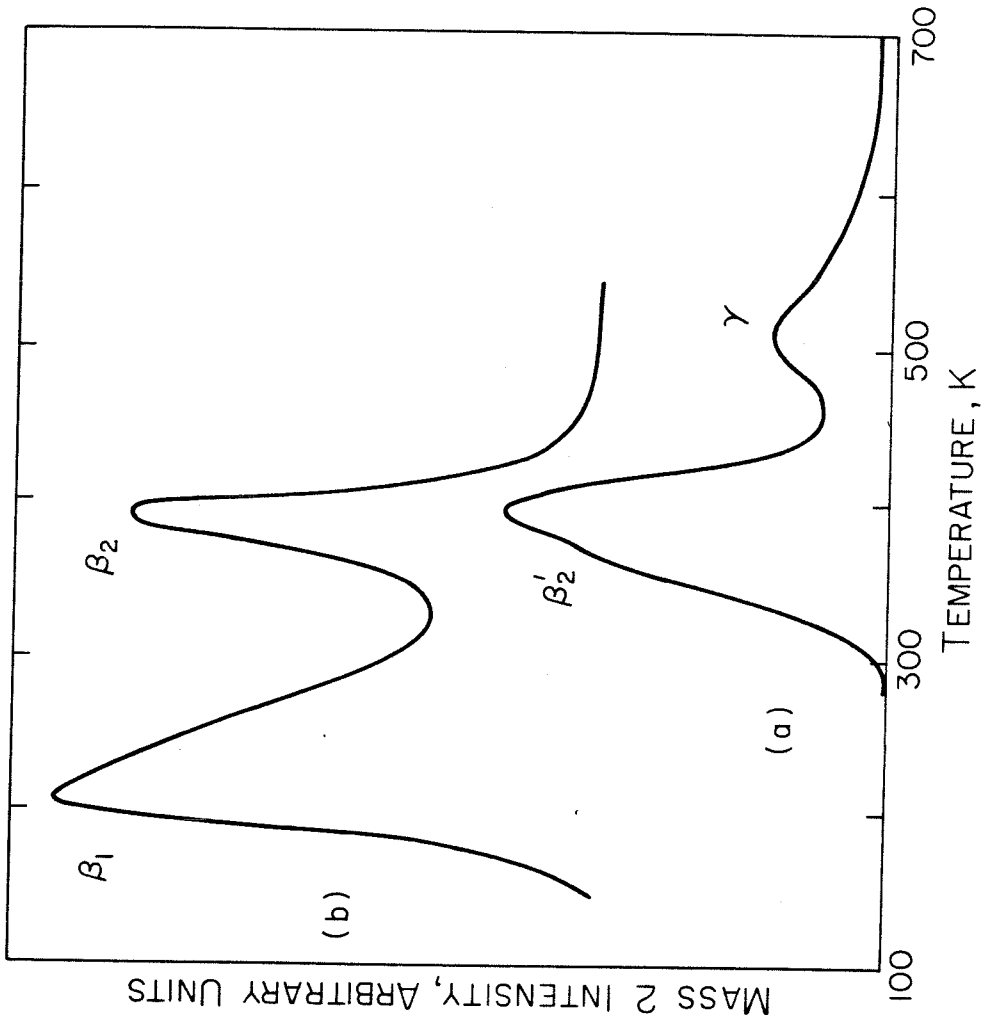
MASS 2 INTENSITY, ARBITRARY UNITS
100
300
500
700
TEMPERATURE, K
(a)
(b)
β_1
β_2
β_2'
γ

Fig. 1

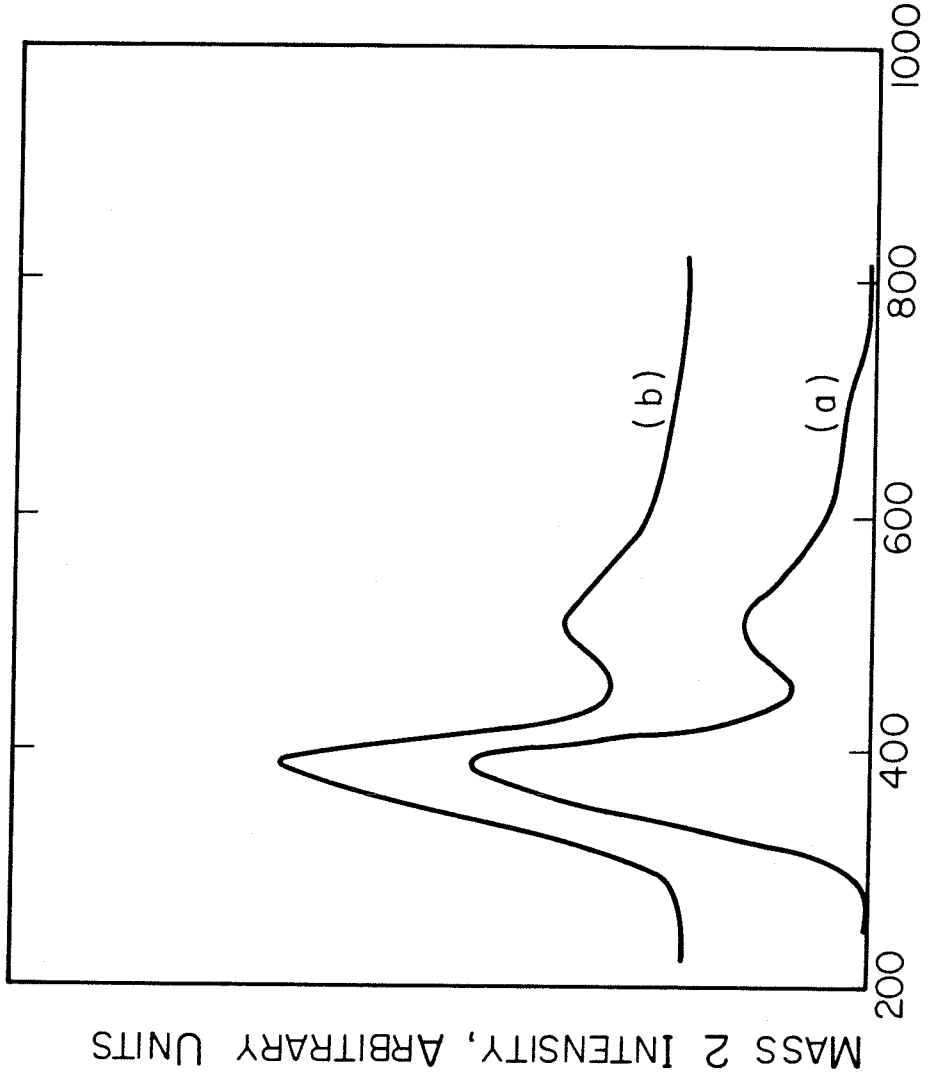
MASS 2 INTENSITY, ARBITRARY UNITS
200
400
600
800
1000
TEMPERATURE, K
(a)
(b)

Fig. 2

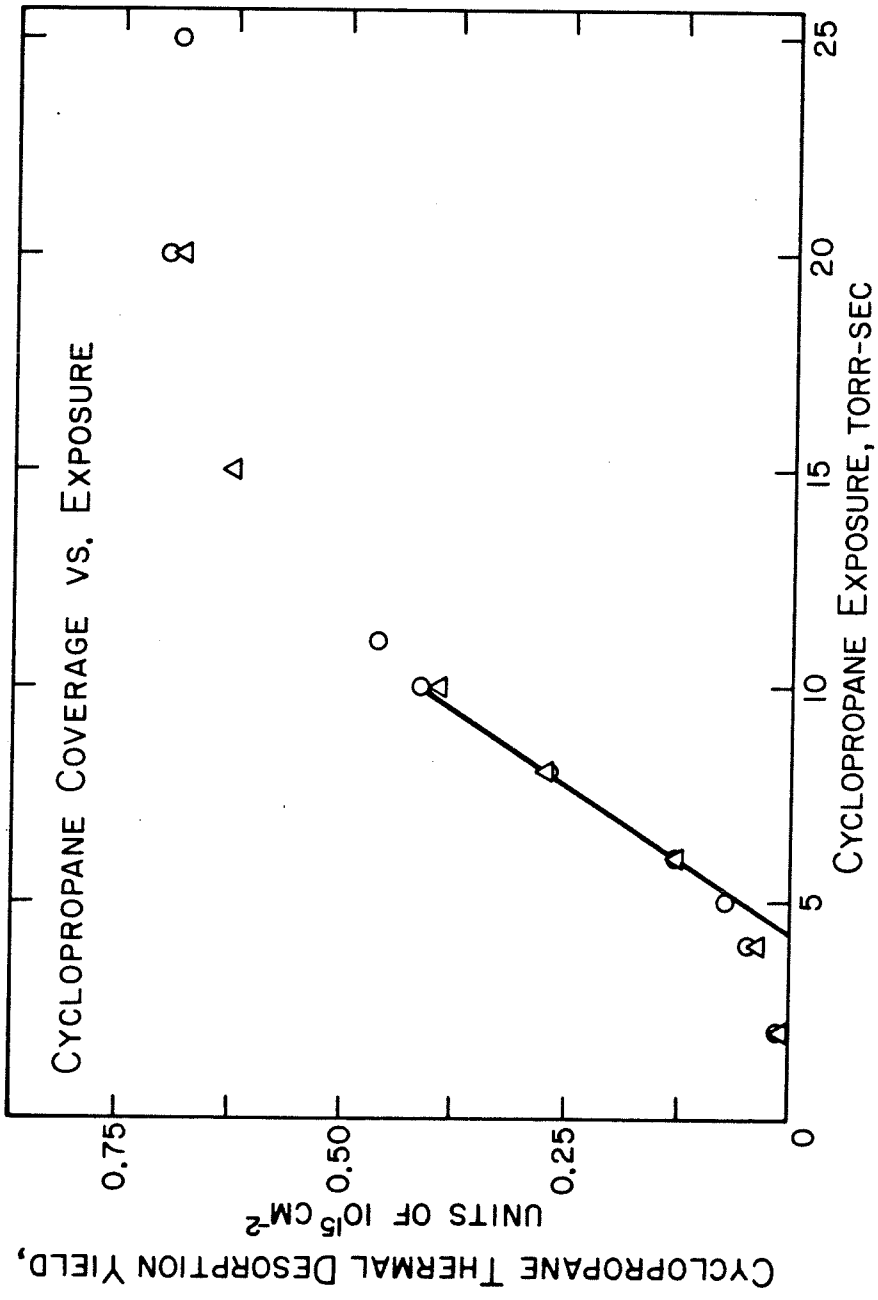
CYCLOPROPANE COVERAGE VS. EXPOSURE
CYCLOPROPANE THERMAL DESORPTION YIELD, UNITS OF 10^{15} CM^{-2}
0.75
0.50
0.25
0
5
10
15
20
25
CYCLOPROPANE EXPOSURE, TORR-SEC

Fig.3

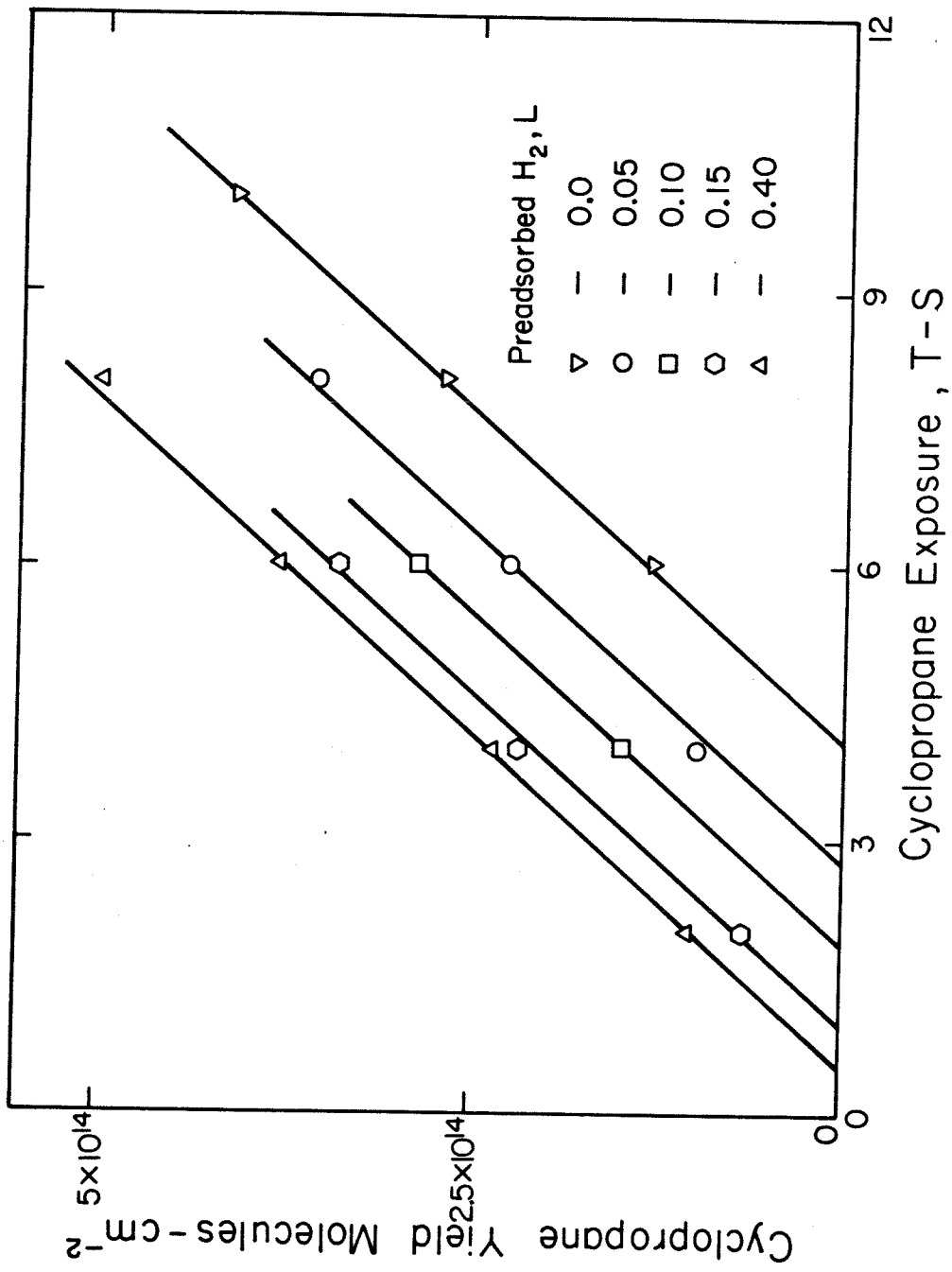
Cyclopropane Yield Molecules - cm⁻²
5x10¹⁴
2.5x10¹⁴
0
0
3
6
9
12
Cyclopropane Exposure, T-S
Preadsorbed H₂, L
0.0
0.05
0.10
0.15
0.40

Fig. 4

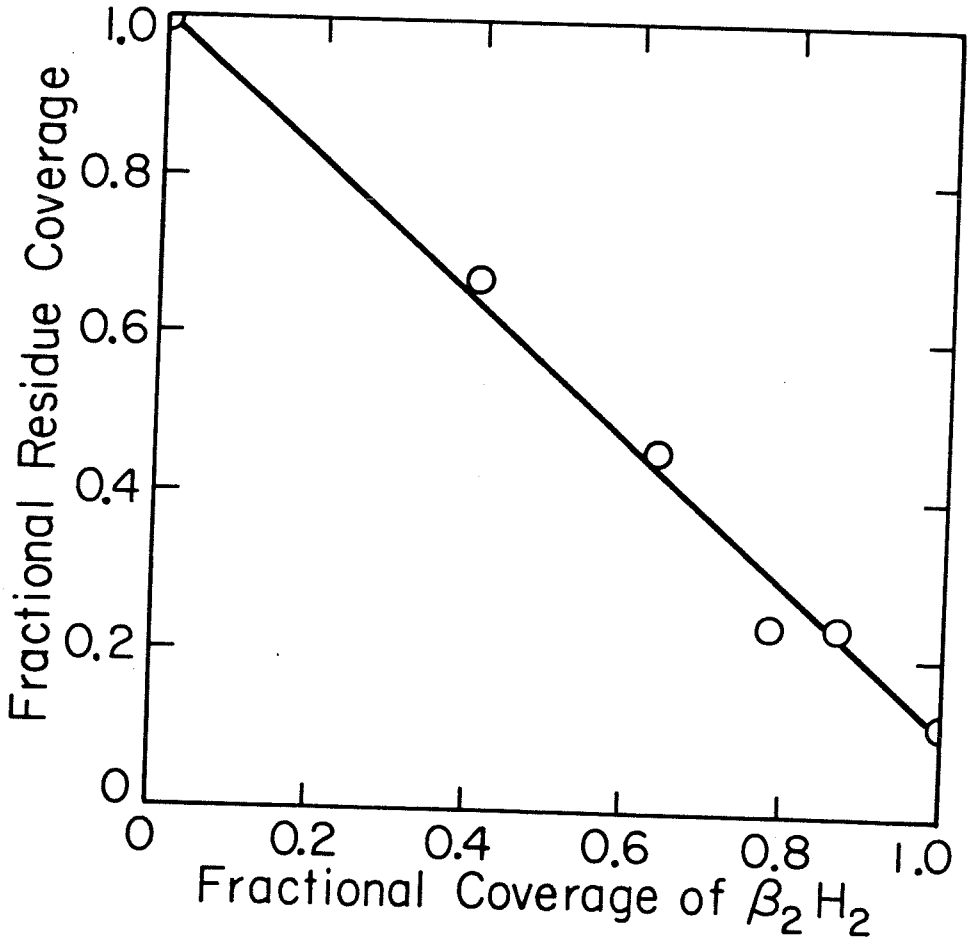
1.0
0.8
0.6
0.4
0.2
0
Fractional Residue Coverage
0
0.2
0.4
0.6
0.8
1.0
Fractional Coverage of $\beta_2 H_2$

Fig.5

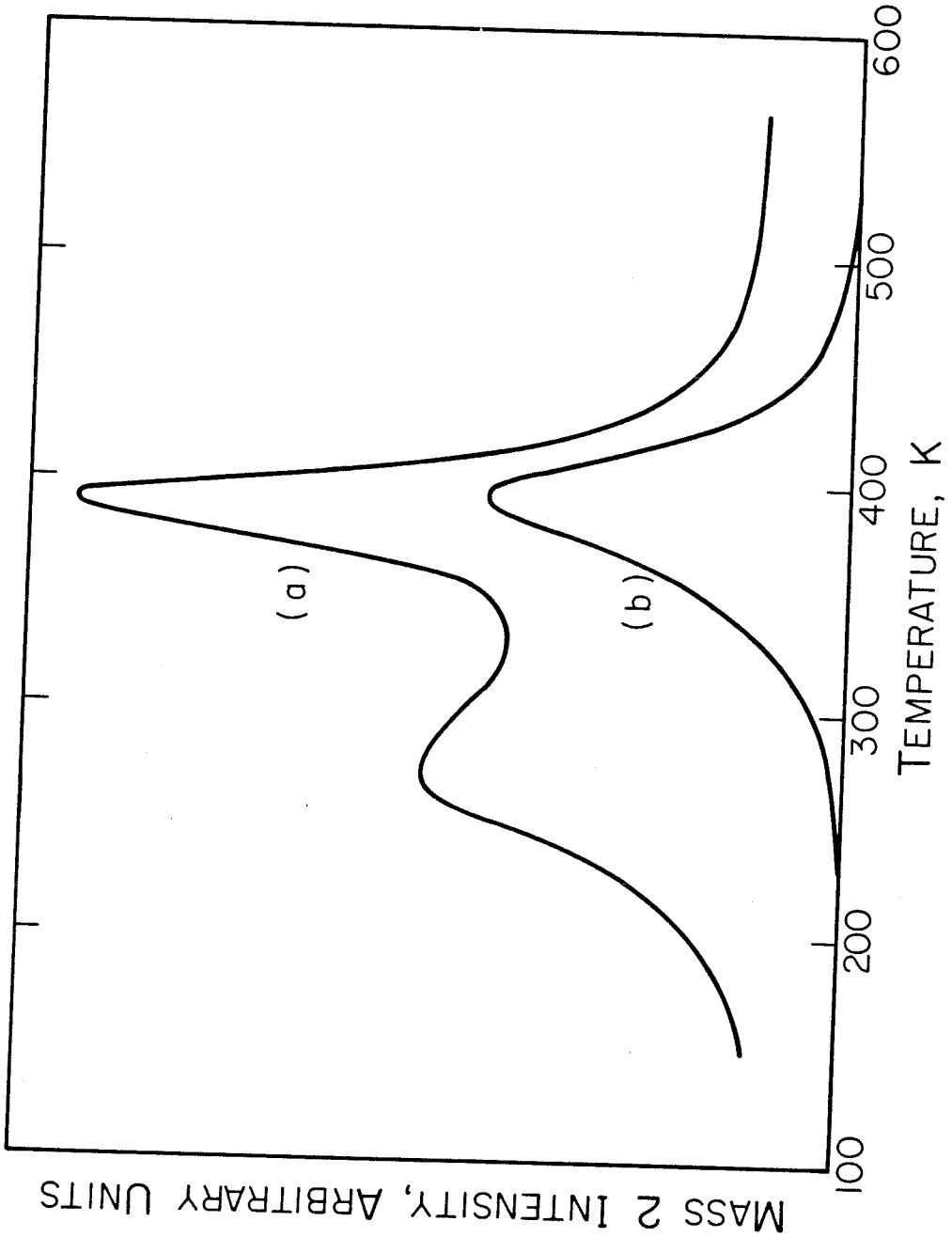
MASS 2 INTENSITY, ARBITRARY UNITS
100
200
300
400
500
600
TEMPERATURE, K
(a)
(b)

Fig. 6

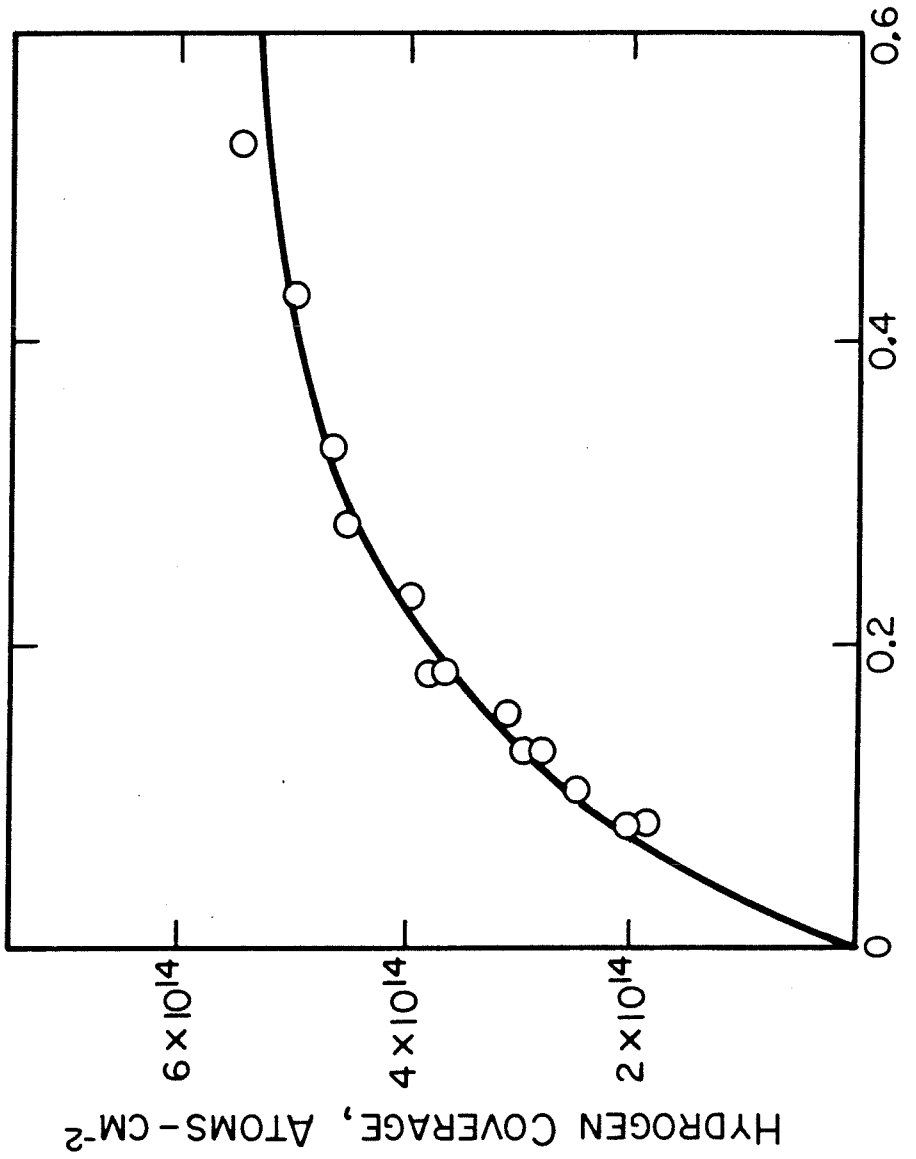
HYDROGEN COVERAGE, ATOMS-CM⁻²
6 x 10¹⁴
4 x 10¹⁴
2 x 10¹⁴
0
0.2
0.4
0.6
H2 EXPOSURE, LANGMUIRS

Fig. 7

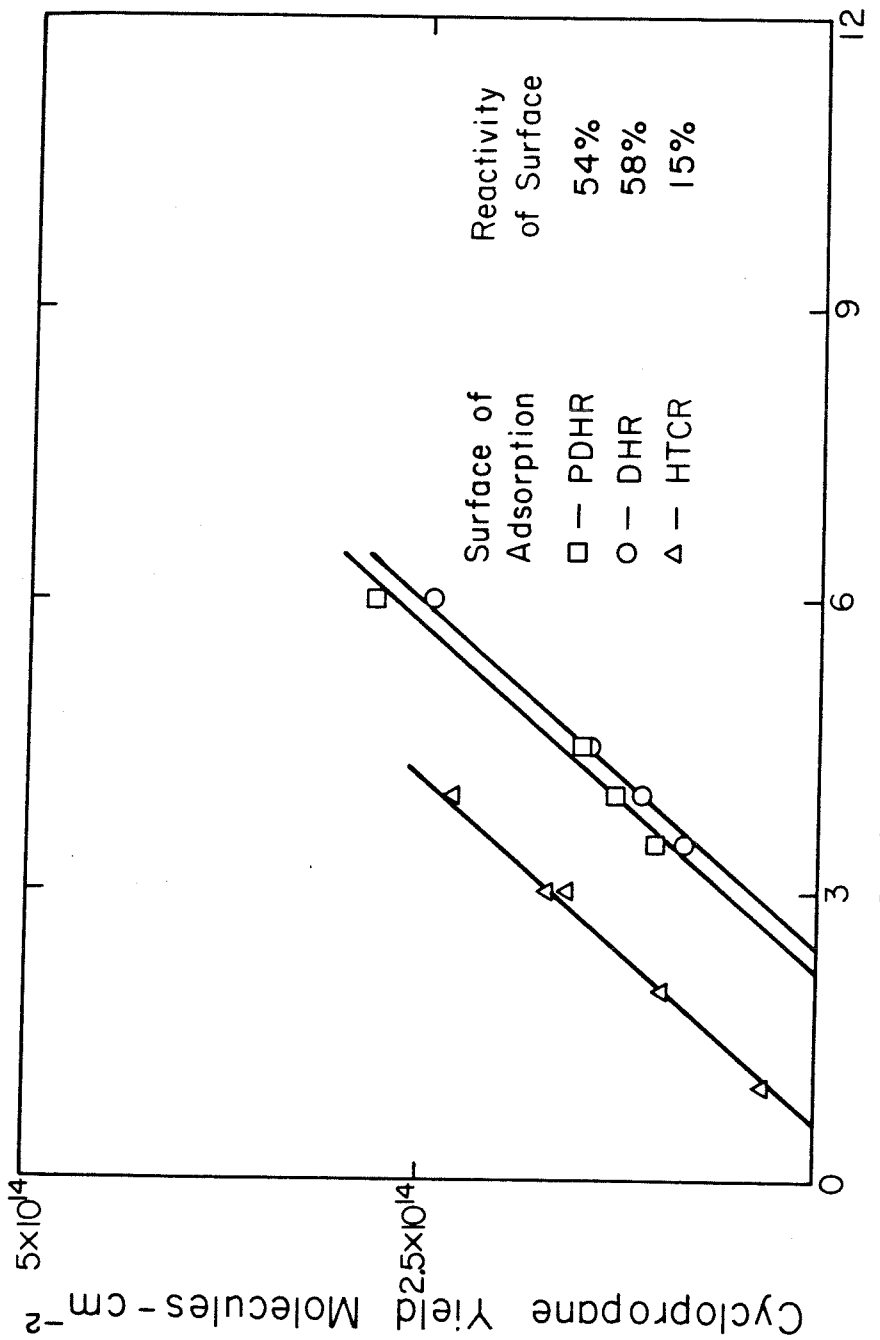
Cyclopropane Yield Molecules - cm⁻²
5x10¹⁴
2.5x10¹⁴
0
3
6
9
12
Cyclopropane Exposure, T - S
Surface of Adsorption
□ — PDHR
○ — DHR
△ — HTCR
Reactivity of Surface
54%
58%
15%

Fig. 8

CHAPTER 6

THE INTERACTION OF ETHANE, PROPANE, ISOBUTANE AND NEOPENTANE WITH THE (110) SURFACE OF IRIDIUM

(The text of Chapter 6 consists of an article coauthored with P.D. Szuromi and W.H. Weinberg that has been submitted to The Journal of Chemical Physics.)

Abstract

The adsorption and reaction of ethane, propane, isobutane and neopentane with the reconstructed Ir (110)-(1x2) surface have been studied with thermal desorption mass spectrometry. As the surface is heated, these hydrocarbons decompose to yield gaseous hydrogen and adsorbed carbon. No hydrocarbons other than the hydrocarbon initially adsorbed was observed to desorb under any of the conditions described in this investigation. The reactivity of the surface for the dissociation of the saturated hydrocarbons is linearly related to the availability of vacant β_2 hydrogen adsites on the surface. Three thermal desorption states of hydrogen, identified as the α, β_2', and γ thermal desorption states, were observed following the dissociation of propane,isobutane and neopentane. The α and γ thermal desorption states are hydrogen molecules desorbing from the surface following the dehydrogenation of hydrocarbon fragments on the surface, and the β_2' thermal desorption state represents hydrogen atoms that are bound to the metal surface in sites that are similar to the β_2 adsites of hydrogen on the clean surface. The thermal desorption of hydrogen following exposure of the surface to ethane exhibits only a β_2' thermal desorption peak.

1. Introduction

A fundamental investigation of the reactions of saturated hydrocarbons on transition metal surfaces is important because it may provide insight into the mechanism of hydrocarbon hydrogenolysis reactions in practical catalytic systems. There have been several recent studies carried out under ultrahigh vacuum conditions concerning the dehydrogenation of cyclohexane to form benzene **(1-4)**. Ultrahigh vacuum investigations of the nonreactive interaction of saturated hydrocarbons with metallic surfaces have included LEED studies of the nondissociative adsorption of straight-chain paraffins on Pt (111) and Ag (111) **(5)**, EELS and UPS studies of cyclopropane and cyclohexane adsorbed molecularly on Ru (001) **(6)** and an ESDIAD study of the nondissociative adsorption of ethane, cyclopropane and cyclohexane of Ru (001) **(7)**.

In a recently completed investigation in this laboratory, the adsorption and decomposition of cyclopropane on the reconstructed Ir(110)-(1x2) surface were examined **(8,9)**. It has since been found that Ir(110)-(1x2) will promote the dissociation of a wide range of saturated hydrocarbons. Of the saturated hydrocarbons that have been investigated (including methane, cyclopropane and those reported in this paper), only methane shows no indication of dissociation on the surface under the conditions that are described in this paper. This paper reports a study of the interactions of a series of hydrocarbons with Ir(110) to ascertain both the similarities and the differences insofar as their interaction with this surface is concerned. These observations may be useful in deducing a more general understanding of the interaction between saturated hydrocarbons and transition metal surfaces.

2. Experimental Procedures

The experiments were performed in an ion-pumped stainless steel belljar that has been described previously **(10,11)**. The base pressure of the belljar was below 2 x 10^{-10} Torr of reactive contaminants. The hydrocarbon exposures were carried out with a directional beam doser consisting of a multichannel array of capillaries **(12)**. During dosing, the crystal was positioned approximately 3 mm from the doser face. This provides a beam pressure-to-background pressure ratio of over 100:1. The unit of exposure that is employed for the beam doser is the Torr-second (Torr-s) and refers to the product of the time of exposure and the pressure in the storage bulb of the doser. The storage bulb supplies gas through a capillary to the doser head leading into the vacuum system. Therefore, the flux of gas into the vacuum system is proportional to the pressure in the storage bulb. For the gases employed in this study, an exposure of 1 Langmuir is approximately equivalent to an exposure of 7 Torr-s for ethane, 3 Torr-s for propane, 4 Torr-s for isobutane and 4 Torr-s for neopentane.

The crystal was cleaned between thermal desorption experiments by exposure to 10^{-7} Torr of O_2 for 1.5-2 min at a crystal temperature of 900 K. This was followed by heating the crystal to 1600 K to desorb the oxygen.

The hydrogen coverage calibration that is used to determine the amount of dissociated hydrocarbon on the surface was determined by titration with oxygen **(10)**. The hydrogen concentration on the surface following an exposure of 0.5 L of H_2 is (7.3 ± 1.0) x 10^{14} molecules-cm^{-2} **(10)**.

With the exception of neopentane, the gases used in this study were obtained from Matheson. The minimum purities quoted were 99.9999% for the hydrogen, 99.0% for the ethane and 99.5% for the propane and isobutane. The neopentane was obtained from Chemtech in Hayward, California and the purity was > 99%. Each of the gases was checked mass spectrometrically for purity and no

extraneous gases were detected by this method.

3. Results

3.1 Thermal Desorption of Hydrogen from Hydrocarbon Overlayers

The thermal desorption mass spectra of hydrogen from saturated overlayers of each of the four hydrocarbons are shown in Fig. 1. Saturation refers here only to the dissociatively adsorbed hydrocarbon and not to the reversibly adsorbed molecular overlayer. The thermal desorption mass spectrum resulting from an exposure of 0.5 L of H_2 to the clean surface is shown in Fig. 1(a) for comparison. An exposure of 0.5 L of H_2 saturates the β_2 adstate of hydrogen on the clean surface **(10)**. The temperature of adsorption for all exposures was 100 K, and all spectra are drawn to the same scale to permit a direct comparison of the amount of hydrogen which desorbs in each case.

The thermal desorption of H_2 resulting from saturation of the residue overlayer after the irreversible adsorption of ethane exhibits a one-peak structure with a maximum rate of desorption at approximately 420 K as shown in Fig 1(b). The area of the peak corresponds to $(1.1 \pm 0.3) \times 10^{14}$ dissociated ethane molecules per cm^2.

In contrast to the single peak resulting from the decomposition of ethane, the thermal desorption of H_2 from the saturated overlayer of the decomposition products of propane, shown in Fig. 1(c), displays a more complicated three-peak structure. Once again, there is a peak in the temperature range ($\sim$ 400 K) that is suggestive of desorption of hydrogen from the β_2 adstate of hydrogen on the clean surface. This thermal desorption state (which appears for all the hydrocarbons investigated in this work) will be referred to as the β_2' thermal desorption state. Also evident in Fig 1(c) is a low-temperature shoulder on the β_2' peak. This state will be defined as the α thermal desorption state. In the region of temperature near 520 K, there is a peak which will be referred to as the γ

thermal desorption state. The temperature range of the γ state indicates that there are hydrogen atoms present on the surface that are more strongly bound than any hydrogen atoms on the clean surface [cf. Fig. 1(a)]. Therefore, the γ state evidently represents hydrogen atoms in highly unsaturated hydrocarbon fragments. This is consistent with the spectroscopic observation of partially dehydrogenated fragments in studies of the interactions of unsaturated hydrocarbons with other transition metals **(13-15)**. The ratio of the combined areas of the α and β_2' peaks to the area of the γ peak is 3.2 ± 0.3. This ratio will be referred to hereafter as R. This value of R indicates that 1.9 ± 0.2 hydrogen atoms in each propane molecule remain in hydrogen-carbon bonds until desorption occurs from the high temperature γ state. The total area of the thermal desorption of hydrogen from the residue overlayer resulting from the irreversible adsorption of propane indicates that (1.1 ± 0.3) x 10^{14} propane molecules dissociate per cm^2 of surface.

The hydrogen thermal desorption from a saturated residue of isobutane, shown in Fig. 1(d), again exhibits three thermal desorption states. The α state is much more well resolved from the β_2' state than it was in the case of propane. The γ thermal desorption state has increased in intensity, signifying the presence of more hydrogen in the hydrocarbon matrix. The value of R for isobutane is 1.7 ± 0.2 which indicates that 3.7 ± 0.2 hydrogen atoms per molecule remain in hydrogen- carbon bonds on the surface. A saturation coverage of (1.1 ± 0.3) x 10^{14} dissociated molecules per cm^2 was determined from the total area under the three thermal desorption peaks of hydrogen.

A saturated overlayer of the decomposition products of neopentane produces the hydrogen thermal desorption spectrum shown in Fig 1(e). The most striking features of this spectrum are that no α state is observed and that the peak at 410 K has approximately twice the intensity as the β_2 thermal desorption state

of hydrogen at saturation on the clean surface [cf. Fig. 1(a)]. This indicates that there are more hydrogen atoms in that state than can be accommodated in β_2-like sites on the surface. These two facts suggest that the thermal desorption peak at 410 K actually represents two adsorbed states of hydrogen that desorb in the same temperature range. Further support for this idea is provided by the fact that the desorption maximum of the peak occurs at 410 K (approximately 10 K higher in temperature than for any of the other hydrocarbons). For neopentane, the value of R is 2.1 ± 0.2 which means that 4.0 ± 0.2 hydrogen atoms remain in hydrogen-carbon bonds in the γ thermal desorption state. The residue saturates at the point at which (1.5 ± 0.3) x 10^{14} neopentane molecules have been dissociated per cm^2 of surface.

Table 1 lists the concentration of each hydrocarbon that will dissociate on the Ir (110) surface as well as the number of hydrogen atoms per molecule that are abstracted from the molecule below 400 K and the number of hydrogen atoms per molecule that remain in the hydrocarbon fragment that gives rise to the γ thermal desorption peak. Since the concentration of hydrocarbon molecules that will dissociate on the surface is relatively independent of the molecule, it is apparently not strongly related to the size of the molecule. The number of hydrogen atoms per molecule that are removed from the molecule below 420 K is also relatively constant. Thus, the concentration of active centers for C-H bond cleavage on the surface to form the hydrocarbon fragment that corresponds to the γ thermal desorption peak is the factor that determines the concentration of dissociated molecules on the surface at saturation.

The development of the thermal desorption spectra as a function of hydrocarbon exposure is shown in Fig. 2. Each quadrant is drawn with a different mass spectrometric intensity scale to facilitate the presentation. As shown in Fig. 2, an exposure of 1 Torr-s of ethane [III(a)] produces a thermal desorption

peak with the same shape and peak temperature as a saturation exposure of 7.5 Torr-s [III(b)]. The β_2' peak temperature for propane, shown in quadrant I of Fig. 2, remains constant at 400 K. However, comparison of the spectra resulting from a 2 Torr-s exposure [I(a)] and a 5 Torr-s saturation exposure [I(b)] indicates that the α shoulder on the β_2' peak does not populate until the β_2' adsite is saturated. For isobutane, in quadrant IV of Fig. 2, this point is illustrated more clearly. The β_2' and γ states are the only states that are populated after an exposue of 2 Torr-s [IV(a)]. Following an exposure of 4 Torr-s [IV(b)], the β_2' state is fully populated, and the α state is beginning to develop. For a saturation exposure of 6 Torr-s [IV(c)], the α state is fully developed, and the γ state has increased in intensity as well. Note that the peak temperature of the β_2' thermal desorption state remains constant at 395 K. The two thermal desorption peaks of neopentane, quadrant II of Fig. 2, develop simultaneously throughout the entire range of coverage. Following an exposure of 2 Torr-s [II(a)], the β_2' peak temperature is 400 K, which is in the range of the β_2' peak temperatures of ethane, propane and isobutane. However, for the two higher exposures of 5 Torr-s [II(b)] and 8 Torr-s [II(c)], the β_2' peak temperature increases to a value of 410 K. Since it has been observed that the α states of propane and isobutane develop subsequent to saturation of the β_2' state, this observation is consistent with the suggestion that the peak at 410 K for neopentane is composed of contributions from a β_2' adstate and an α adstate.

One observation that is not apparent from visual inspection of Fig. 2 is the fact that the value of R for each of the species, isobutane and neopentane, is a constant (within ± 5%) as a function of coverage. Hence, the stoichiometry of the hydrocarbon fragment represented by the γ thermal desorption state remains constant regardless of the surface coverage. This fact implies that the γ thermal desorption state represents a stable hydrocarbon intermediate on the

surface.

Further proof of this proposition can be gained by the following experiment. If a surface with a saturated overlayer of hydrocarbon residue is annealed to 400 K, then both the α adsites and the β_2' adsites are depopulated. As will be shown later in this section, the β_2' adsites are thus rendered active centers for the dissociation of additional hydrocarbon molecules (i.e. they regain their ability to break H-C bonds). Thus, if the H-C bonds in the hydrocarbon entity corresponding to the γ adstate were unstable to the presence of these active centers, annealing a saturated overlayer of hydrocarbon residue to 400 K should induce a reduction in the γ peak area. This measurement was performed for isobutane and neopentane, and the results are presented in Fig. 3. Thermal desorption spectra of hydrogen resulting from saturation coverages of isobutane and neopentane are shown in I(a) and II(a), respectively, of Fig. 3. The thermal desorption spectra corresponding to the annealed surfaces are shown in I(b) for isobutane and II(b) for neopentane in Fig. 3. The saturated isobutane residue was annealed for 90 seconds at 400 K and the saturated neopentane residue was annealed for 10 seconds at 400 K.

When a surface with a saturated overlayer of hydrocarbon residue is annealed to 400 K, the β_2' sites again become available as active centers for dissociation of hydrocarbon molecules. If such a surface (prepared with isobutane) is cooled to 100 K and reexposed to 8 Torr-s of isobutane, the β_2' thermal desorption state is repopulated and there is an increased intensity in the γ thermal desorption state due to additional dissociative adsorption of isobutane on the surface. This is shown clearly in Fig. 4(a). The thermal desorption spectrum shown in Fig. 4(a) results from preparing the surface represented by Fig. 3 [I(b)] and exposing that surface to 8 Torr-s of isobutane at 100 K. The thermal desorption of hydrogen from a saturated overlayer of isobutane residue is shown in Fig. 4(b)

for comparison. It should be noted that the α thermal desorption state is not regenerated after the irreversible adsorption of additional isobutane.

This experiment illustrates two points. First, the ability of the surface to dissociate adsorbed isobutane is not limited by the availability of sites to form the hydrocarbon fragment which gives rise to the γ thermal desorption state. Also, the activity of the surface for dissociative adsorption of hydrocarbons can be regenerated by depopulation of the β_2' adsites. Thus, the availability of β_2' adsites is the factor that determines the reactivity of the surface for the dissociation of these saturated hydrocarbons.

3.2 Adsorption of Hydrocarbons on Preadsorbed β_2 Hydrogen

There also exists a correlation between reactivity and the availability of β_2 hydrogen adsorption sites on the surface. This can be confirmed by restricting the availability of β_2 sites through adsorption of hydrogen into those sites. Reactivity is defined here as the the total amount of hydrocarbon that will dissociate on the surface. Since, as stated in Section 3.1, the ratio R is constant regardless of coverage, the number of hydrogen atoms per molecule retained in the γ adstate is constant with coverage. Thus, the area of the γ thermal desorption peak is proportional to the number of dissociated molecules on the surface. Therefore, the area of the γ peak at saturation is proportional to the reactivity of the surface. The area of the γ thermal desorption peak is used as a measure of hydrocarbon coverage because the preadsorbed hydrogen adds to the intensity in the temperature range of the α and β_2' thermal desorption peaks.

Representative thermal desorption spectra of hydrogen resulting from saturation exposures of neopentane, isobutane and propane adsorbed on various precoverages of β_2 hydrogen are shown in Figs. 5(I), 5(II) and 5(III), respectively. The adsorption of any one of these hydrocarbon molecules onto a

surface saturated with β_2 hydrogen [shown as spectrum (c) in each section of Fig. 5], results in a spectrum that corresponds exactly to thermal desorption from a surface saturated with β_2 hydrogen (note that each section of Fig. 5 is drawn with a different mass spectrometric intensity scale). In particular, no desorption from the γ state is observed for these spectra, indicating no dissociative adsorption of these saturated hydrocarbons occurs on the surface when the β_2 adstate is saturated with hydrogen. Spectrum (b) in each section of Fig. 5 corresponds to hydrogen thermal desorption after a saturation exposure of each hydrocarbon to a surface that was previously exposed to 0.05 L of H_2 (corresponding to 38% of saturation of the β_2 adstate). A γ thermal desorption peak is observed under these conditions, but it is less intense than those measured after the corresponding exposure of hydrocarbon to the clean surface shown in spectrum (a) of each section of Fig. 5.

The reactivity of the surface for hydrocarbon decomposition (plotted as the normalized population of the γ adstate at saturation) is shown in Fig. 6 as a function of the fractional precoverage of hydrogen in the β_2 adsites. This figure indicates clearly that the ability of the surface to dissociate saturated hydrocarbon molecules is linearly related to the number of β_2 hydogen adsorption sites available on the surface. This provides further evidence that the β_2' thermal desorption state observed for all of these hydrocarbons adsorbed on Ir(110) represents hydrogen atoms that have been abstracted from H-C bonds and are bonded to metal-hydrogen sites similar to the β_2 adsites of hydrogen on the clean surface.

If 0.05 L of deuterium is adsorbed into the β_2 adsites prior to the adsorption of a saturation exposure of isobutane, the subsequent thermal desorption spectrum of HD, shown in Fig. 7, indicates intensity in all three thermal desorption states (i.e. α, β_2' and γ). *This result proves incisively that the hydrogen atoms in*

the hydrocarbon fragment, represented by the γ thermal desorption state, exchange with hydrogen atoms in the β_2 adstate. This is in spite of the fact that the γ adstate is stable in the presence of unpopulated β_2 adsites.

3.3 Annealed Residues of Isobutane

A saturated overlayer of hydrocarbon residue that is heated to 800 K retains no hydrogen, and the carbon overlayer thus obtained will be referred to as the dehydrogenated residue (DHR). The hydrogen thermal desorption spectrum corresponding to exposure of 20 L of H_2 to the isobutane DHR is shown in Fig. 8(b). The hydrogen thermal desorption spectrum after an exposure of 20 L of H_2 to the clean Ir(110) surface is shown in Fig. 8(a) for comparison. Note that the adsorption of hydrogen into β_1 adsites is blocked by the presence of the carbon residue. Furthermore, the γ adstates (corresponding to the formation of C-H bonds) are not repopulated by exposure to hydrogen.

A series of experiments was performed in which a saturation exposure of isobutane was adsorbed on the surface, the surface was subsequently flashed to 200 K, and then cooled to 100 K. This procedure was repeated a total of four times, and the results are shown in Fig. 9. The hydrogen thermal desorption spectrum of hydrogen that follows an exposure of 8 Torr-s of isobutane to the clean Ir(110) surface is shown in Fig. 9(a). The thermal desorption spectrum of hydrogen following an exposure of 8 Torr-s of isobutane to the DHR formed in the experiment of Fig. 9(a) is shown in Fig. 9(b). Figures 9(c) and 9(d) follow in the same manner. The active centers for dissociation of isobutane molecules are progressively blocked by the accumulation of adsorbed carbon on the surface. The (normalized) extent of reaction of isobutane (proportional to H_2 thermal desorption area) is tabulated for each experiment in Fig. 9. The amount of isobutane that dissociates on the surface is reduced by approximately 40% for

each iteration. If the assumption is made that this trend will persist, an estimate of the total number of isobutane molecules that it is possible to dissociate on the surface can be obtained from the product of the infinite series $\sum_{n=0}^{\infty}$ (0.6 ± 0.03) and the concentration of isobutane represented by Fig. 9(a) [i.e. (1.1 ± 0.3) x 10^{14} cm^{-2}]. This number is (2.8 ± 0.8) x 10^{14} cm^{-2}. Thus, a coverage of approximately (1.1 ± 0.3) x 10^{15} carbon atoms per cm^2 of surface is sufficient to poison the dissociation of isobutane on the surface.

The number of hydrogen atoms per molecule in the γ hydrocarbon fragment (as computed from the ratio R) remains in the range 3.7 ± 0.2 for spectra 9(b) and 9(c). The deconvolution method used to determine R was not practical for spectrum 9(d). Thus, the stoichiometry of the stable γ intermediate is not affected by the presence of adsorbed carbon on the surface.

The formation of the α hydrogen adstate is apparently blocked by adsorbed carbon. As shown in Fig. 9, the α thermal desorption peak does not appear for isobutane adsorption onto a surface containing adsorbed carbon.

In order to probe the nature of the α thermal desorption state, an attempt was made to regenerate it following the mildest pretreatment of the isobutane residue that would depopulate it completely. Specifically, a surface that had been exposed to 8 Torr-s of isobutane (saturation exposure) was heated to 320 K. This creates an overlayer that yields the hydrogen thermal desorption spectrum shown in Fig. 10(a). This surface will be referred to in this paper as the partially dehydrogenated residue (PDR).

Exposure of the PDR to 6 Torr-s of isobutane at 100 K results in the thermal desorption spectrum of hydrogen shown in Fig. 10(b). This spectrum is identical to the spectrum of Fig. 10(a), indicating that no further dissociative adsorption occurs upon exposure of isobutane to the PDR. *Thus, the α adstate does not*

serve as an active center for dissociative adsorption of isobutane under these conditions.

The thermal desorption spectrum of hydrogen following an exposure of 5 L of H_2 to the PDR is shown in Fig. 10(c). A slight broadening on the low-temperature side of the β_2' peak has occurred. This is probably due to the adsorption of hydrogen into a small concentration of β_1 hydrogen adsites (< 5% of the concentration of β_1 adsites on the clean surface). However, as before, there is no peak near 320 K which would be expected for desorption from the α adstate. Thus, the α adsite is not repopulated by exposure of H_2 to the PDR.

An attempt was made to adsorb hydrogen into the α adstate on which the α adstate was not saturated. Such a surface was prepared by the adsorption of 3.5 Torr-s of isobutane at 100 K. The thermal desorption spectrum of hydrogen from this surface is shown in Fig. 11(a). It is apparent from inspection of this thermal desorption spectrum that the α thermal desorption peak has just begun to develop at this exposure. The thermal desorption spectrum that results from an exposure of 4 L of H_2 to the surface following an exposure to 3.5 Torr-s of isobutane is shown in Fig. 11(b). There is some additional intensity in the region of desorption of the α state, but the peak temperature is 300 K which is indicative of hydrogen adsorbed in β_1 hydrogen adsites. By comparison, the peak temperature of the α thermal desorption state is 320 K. Indeed, on a surface that is not saturated with hydrocarbon residue, it would be expected that some β_1 adsites would be available. Thus, it appears that the α thermal desorption state is not populated by postexposure to hydrogen in this case either.

3.4 Postadsorption of Hydrogen on the Hydrocarbon Overlayers

A far more interesting feature of Fig. 11(b) is the loss of approximately 60% of the intensity in the γ thermal desorption state relative to Fig. 11(a). This result

indicates that exposing the surface to hydrogen *at 100 K* has caused hydrogen that would otherwise have been evolved from the γ adstate to desorb as hydrogen in a hydrocarbon molecule.

This proposition is proved incisively by the experiment represented in Fig. 12. The thermal desorption spectra in Sections I, II and III of Fig. 12 correspond to a major cracking fragment of propane, isobutane and neopentane, respectively. Spectra (a) are the result of an exposure of hydrogen to an overlayer of each hydrocarbon that corresponds to a coverage at which the hydrogen thermal desorption is not saturated. Spectra (b) are "blank" mesurements in which the same amount of hydrocabon was exposed to the surface, but no hydrogen was adsorbed onto it. Inspection of Fig. 12 shows clearly that postadsorption of hydrogen at 100 K induces the desorption of the molecular hydrocarbon from the surface upon heating. The analogous experiment for ethane is shown on a different temperature scale in Fig. 13. The mass spectrometric cracking patterns of the desorbing hydrocarbons match the cracking patterns of the hydrocarbon initially adsorbed in each case. The sensitivity of this analysis is sufficiently high to establish that at least 90% (and possibly all) of the desorbing hydrocarbon molecules correspond in each case to that hydrocarbon adsorbed initially.

If deuterium is postadsorbed onto the hydrocarbon overlayers rather than hydrogen, *there is no exchange of deuterium into the C-H bonds of the desorbing hydrocarbons*. This H-D exchange would be expected if dissociative adsorption of the parent hydrocarbon had occurred at 100 K and the adsorption of $H_2(D_2)$ were causing regeneration of the parent hydrocarbon.

Thus, it is apparent that adsorption of these saturated hydrocarbons on the Ir(110) surface at 100 K results in an overlayer in which at least some of the

molecules that will undergo dissociation retain their molecular identity. The postadsorbed hydrogen is displacing these associatively adsorbed molecules from the vicinity of active centers on which they would otherwise dissociate at higher temperatures.

The temperatures at which the dissociation takes place are below the temperatures at which reversibly adsorbed molecules desorb from the surface. All reversibly adsorbed ethane is desorbed upon warming the surface to 130 K. The corresponding temperatures for propane, isobutane and neopentane are 160 K, 170 K and 180 K, respectively. If, for any of these hydrocarbons, the adsorbed overlayer is heated to 130 K, recooled, and then exposed to hydrogen, no displacement of the hydrocarbon takes place. Thus, at some temperature between 100 K and 130 K, the adsorbed hydrocarbon molecules undergo a transformation (probably partial dehydrogenation) which renders them irreversibly adsorbed.

3.5 The Effect of Postadsorbed Co on Adsorbed Isobutane and Neopentane

It was established in an earlier investigation of the coadsorption of H_2 and CO on Ir(110) that CO which is adsorbed onto an overlayer of β_2 hydrogen displaces the hydrogen atoms from β_2 to β_1 adsites **(16)**. Thus, it would be expected that CO would also be effective in displacing associatively adsorbed hydrocarbon molecules from the vicinity of β_2' dissociation sites on the surface. This expectation is borne out as shown explicitly for isobutane and neopentane in Fig. 14. Thermal desorption spectra I(b) and II(b) in Fig. 14 correspond to the desorption of hydrogen from overlayers of isobutane and neopentane, respectively, onto which CO was adsorbed at 100 K. Spectra I(a) and II(a) represent hydrogen which desorbs from the corresponding hydrocarbon overlayers that were not exposed to CO. Comparison of the two pairs of spectra shows that postexposure

of 2 L of CO reduces the extent of isobutane dissociation by 45% and that of neopentane by 70%. This indicates that CO does indeed displace associatively adsorbed hydrocarbon molecules from the vicinity of the active center for dissociation.

The nature of the lower temperature thermal desorption states is also clarified by these experiments. The displacement by CO of hydrogen adsorbed in the β_2' adstate to a β_1 adstate, analogous to the β_2 to β_1 displacement on the clean surface, occurs for both isobutane and neopentane. Thus, for isobutane [Fig. 14(I)], the thermal desorption peak at 400 K is no longer present, and a peak that desorbs in the range of temperatures ($\sim$ 270 K) suggestive of β_1 desorption appears in the spectrum. Note that this thermal desorption peak is distinguishable from the α peak which has retained its peak temperature at 330 K. This observation illustrates that the α thermal desorption peak does not represent hydrogen adsorbed in β_1-type hydrogen-metal bonds.

For neopentane [Fig. 14(II)], a peak at 270 K again appears in the thermal desorption spectrum of hydrogen following postadsorption of CO at 100 K. The fact that a thermal desorption peak is observed at 400 K is further evidence to support the idea put forward in Section 3.1 that the peak at 410 K in the thermal desorption spectrum of hydrogen after the adsorption and dissociation of neopentane consists of contributions from an α adstate and a β_2' adstate.

Exposures of 5 L of CO and 20 L of CO to a surface that had been preexposed to 2 Torr-s of neopentane resulted in a thermal desorption spectrum of hydrogen corresponding to the dissociation of approximately 10% of that which would have occurred without the CO exposure. This indicates that, at least for neopentane, there is a possibility that some C-H bond cleavage takes place on the surface at 100 K.

4. Discussion

A recent series of articles by Muetterties et al. has explored the concept of C-H-metal three-center two-electron bonds as precursors to C-H bond cleavage in hydrocarbon-metal surface interactions **(4,17-19)**. This type of bonding interaction has been observed in organometallic chemistry [see Ref. (17) and references therein]. Though this type of bonding may occur on many metal surfaces resulting in a weak chemisorption bond, it appears that the further reaction to C-H bond cleavage is facilitated on stepped surfaces **(4,17-19)**.

If a simple termination of the bulk is considered, the Ir(110) surface is a series of rows and troughs. However, the clean surface is reconstructed to form a (1x2) superstructure **(20)**. The structure of this reconstructed surface has been determined to be a surface with every other row of surface atoms missing in the [001] direction **(20)**. Thus, not only are second layer Ir atoms exposed, but third layer atoms under the locations of the missing rows are exposed as well. The surface may be thought of as a series of 2-atom wide (111) terraces inclined at a 90° angle to each other to form 2-layer deep troughs. Consequently, this surface has a high concentration of surface steps.

As shown in Sections 3.2 and 3.4, the β_2 hydrogen adsorption site on the Ir(110) surface acts as a hydrogen-acceptor site to enable hydrogen abstraction from C-H-metal bonds present on the surface. If these sites are blocked by hydrogen adsorption (either before or after adsorption of the hydrocarbon at 100 K), the extent of C-H bond cleavage is reduced.

In Section 3.1, it was shown that the area of the γ thermal desorption peak for propane, isobutane and neopentane represents a constant number of hydrogen atoms per hydrocarbon molecule remaining in C-H bonds at a surface temperature of 400 K, regardless of the surface coverage. It was further shown

that these C-H bonds are stable at 400 K despite the presence of active C-H bondbreaking sites on the surface. These facts prove the existence of stable hydrocarbon fragments on the surface at temperatures above 500 K. The stoichiometry of these fragments is approximately C_3H_2 for propane, C_4H_4 for isobutane, and C_5H_4 for neopentane. No γ hydrocarbon fragment was observed after the irreversible adsorption of ethane. There are, of course, many geometrical arrangements that are consistent with these stoichiometries, so any detailed structure of the γ fragments must await spectroscopic results. However, the absence of a γ hydrocabon fragment for ethane may suggest that the γ fragments for propane, isobutane (2-methylpropane) and neopentane (2,2-dimethylpropane) involve dehydrogenation and bonding of the 1 and 3 carbons of the propane skeleton to the metal in a way that affords some stabilization to the other C-H bonds in the molecule. According to the stoichiometry, these C-H bonds would be fully "protected" in the case of propane and isobutane, but only partially "protected" in the neopentane γ fragment (the stoichimetry is C_5H_4 rather than the predicted C_5H_6). This apparent incongruity could be due to steric crowding between the two methyl groups forcing one of them close enough to the surface to be partially dehydrogenated.

Any explanation of the nature of the α thermal desorption state must account for the following experimental observations:

1. The α state has not begun to be populated until after the β_2' state has reached 80% of its saturation coverage [see Fig. 2(I) and 2(IV)].

2. For a saturated overlayer of isobutane annealed to 320 K to form the PDH, the α adstate is not repopulated upon exposure to H_2 or upon further exposure to isobutane at 100 K (see Fig.10).

3. It does not appear possible to adsorb H_2 into the α adstate of a nonsaturated

overlayer of isobutane (see Fig.11).

4. The α adstate is distinct from the β_1 hydrogen-metal bonding state that exists on the clean surface (see Fig. 14).

5. The stability of the α adstate (i.e. the temperature at which desorption from it occurs) depends on the hydrocarbon from which it is formed (see Figs. 1 and 2).

6. The α adstate is not formed upon exposure of isobutane to the DHR (see Fig. 9).

Observations (2)-(5) indicate that the α adsite is not a H-metal bond, but rather a C-H bond. It is apparent from observation (1) that as the density of the hydrocarbon overlayer increases, sites are created on the surface that possess only enough β_2' hydrogen abstraction sites to partially complete the transformation of the hydrocarbon molecule to the stable γ fragment. Thus, at some temperature below 130 K, a hydrocarbon fragment can be formed that is intermediate in hydrogen content between the parent molecule and the stable γ fragment. Sites apparently exist on the surfaces which will facilitate the transformation of these metastable fragments to the γ fragments, but only at temperatures higher than 130 K. These sites may be, for example, bare Ir sites that do not have the geometry of the β_2 (or β_2') hydrogen adsorption sites; or, in the case of neopentane, they could be β_2' sites that are vacated at 400 K. Upon dehydrogenation of the metastable fragment, the hydrogen recombines and desorbs as the α thermal desorption peak.

Observation (6) indicates that the presence of adsorbed carbon on the surface interferes with the mechanism of α state desorption for isobutane. It may be that the chemisorbed carbon poisons the sites which dehydrogenate the metastable fragment, and the transformation to the γ fragment must await the

depopulation of the β_2' adsites at 400 K. As was pointed out in section 3.3, the stoichiometry of the γ fragment does remain the same even for adsorption onto the carbon- poisoned surfaces. Thus, the dehydrogenation must be completed at some temperature below 450 K.

5. Synopsis

The results of this study may be summarized as follows:

1. The β_2 hydrogen adsorption sites on the clean Ir(110)-(1x2) surface act as active centers for the dissociation of adsorbed, saturated hydrocarbons. Although dissociative adsorption may occur to some extent at 100 K, experiments concerning the coadsorption of H_2 and CO with hydrocarbons indicate that molecular adsorption, followed by dissociation at higher surface temperatures, occurs as well. The dissociation reaction is complete at surface temperatures below 130 K.

2. The γ thermal desorption state observed for propane, isobutane and neopentane represents hydrogen desorbing from hydrocarbon fragments that remain stable in the presence of active centers for C-H bond breaking (i.e., vacant β_2' hydrogen adsites). Deuterium exchange into these C-H bonds does take place. The hydrocarbon fragments have a fixed stoichiometry for each species that does not depend on surface coverage. The stoichiometry of the fragment for propane is approximately C_3H_2, for isobutane is C_4H_4, and for neopentane is C_5H_4.

3. The α thermal desorption state probably represents hydrocarbon fragments that, although partially dehydrogenated, are not in the vicinity of enough vacant β_2' active sites to be able to dehydrogenate fully to stable γ hydrocarbon fragments below 130 K. The completion of this transformation to γ frag-

ments occurs at higher temperatures and is manifested as a thermal desorption peak of hydrogen.

Table I

Species	Hydrocarbon Coverage at Saturation (10^{14} molecules-cm^{-2})	Hydrogen Atoms in γ Fragment (per molecule)	Hydrogen Atoms Desorbed Below 420 K (per molecule)
Ethane	1.1 ± 0.3	0	6
Propane	1.1 ± 0.3	1.9	6.1
Isobutane	1.1 ± 0.3	3.7	6.3
Neopentane	1.5 ± 0.3	3.9	8.1

References

1. G. W. Rubloff, H. Luth, J. E. Demuth and W. D. Grobman, J. Catal. **53**, 423 (1978).

2. A. K. Bhattacharya, J. C. S. Faraday I **76**, 126 (1980).

3. J. E. Demuth, H. Ibach and S. Lehwald, Phys. Rev. Letters **40**, 1044 (1978).

4. M.-C. Tsai, C. M. Friend and E. L. Muetterties, J. Am. Chem. Soc. (submitted).

5. L. E. Firment and G. A. Somorjai, J. Chem. Phys. **66**, 2901 (1977); J. Chem. Phys. **69**, 3940 (1978).

6. F. M. Hoffmann, T. E. Felter, P. A. Thiel and W. H. Weinberg, Surface Sci. (submitted); J. Vac. Sci. Technol. **18**, 651 (1981); Surface Sci. (submitted).

7. T. E. Madey and J. T. Yates, Jr., Surface Sci. **76**, 397 (1978).

8. T. S. Wittrig, P. D. Szuromi and W. H. Weinberg, J. Chem. Phys. (submitted)

9. T. S. Wittrig, P. D. Szuromi and W. H. Weinberg, Surface Sci. (submitted)

10. D. E. Ibbotson, T. S. Wittrig and W. H. Weinberg, J. Chem. Phys. **72**, 4885 (1980).

11. J. L. Taylor, D. E. Ibbotson and W. H. Weinberg, J. Chem. Phys. **69**, 4298 (1978).

12. D. E. Ibbotson, T. S. Wittrig and W. H. Weinberg, Surface Sci. **110**, 000 (1981).

13. J. E. Demuth and D. E. Eastman, Phys. Rev. Letters **32**, 1123 (1974).

14. J. E. Demuth, Chem. Phys. Letters, **45**, 12 (1977).

15. J. B. Benziger and R. J. Madix, J. Catal. **65**, 49 (1980).

16. D. E. Ibbotson, T. S. Wittrig, and W. H. Weinberg, Surface Sci. **97**, 297 (1980).

17. E. L. Muetterties, ACS Symp. Ser. **155**, 273 (1981).

18. C. M. Friend and E. L. Muetterties, J. Am. Chem. Soc. **103**, 773 (1981).

19. M.-C. Tsai and E. L. Muetterties, J. Am. Chem. Soc. (submitted).

20. K. Christmann and G. Ertl, Z. Naturforsch. **28a**, 1144 (1973).

21. C. M. Chan, M. A. Van Hove, W. H. Weinberg and E. D. Williams, Solid State Commun. **30**, 47 (1979); Surface Sci. **91**, 400 (1980).

Figure Captions

Figure 1: Thermal desorption of hydrogen resulting from exposure of the Ir(110) surface to: (a) 0.5 L of H_2; (b) 5 Torr-s of ethane (saturation); (c) 6 Torr-s of propane (saturation); (d) 8 Torr-s of isobutane (saturation); and (e) 10 Torr-s of neopentane (saturation).

Figure 2: Thermal desorption of hydrogen as a function of exposure for: I. Propane, II. Neopentane, III. Ethane, and IV. Isobutane. Exposures are shown adjacent to the corresponding spectrum.

Figure 3: Thermal desorption of hydrogen resulting from: I(a). Exposure of 8 Torr-s of isobutane to the Ir(110) surface at 100 K; I(b). Surface of I(a) annealed to 400 K for 90 sec; II(a). Exposure of 10 Torr-s of neopentane to the Ir(110) surface at 100 K; and II(b). Surface of II(a) annealed to 400 K for 10 sec.

Figure 4: Thermal desorption of hydrogen resulting from:

a. Exposure of the Ir(110) surface to 8 Torr-s of isobutane at 100 K followed by heating the surface to 400 K, recooling to 100 K, and reexposure to 8 Torr-s of isobutane; and

b. Exposure of the Ir(110) surface to 8 Torr-s of isobutane.

Figure 5: Thermal desorption of hydrogen resulting from adsorption of: I. 10 Torr-s of neopentane, II. 8 Torr-s of isobutane, and III. 6 Torr-s of propane onto surfaces prepared in the following manner:

a. Clean Ir(110) surface;

b. Ir(110) surface exposed to 0.05 L of H_2; and

c. Ir(110) surface exposed to 0.50 L of H_2.

Figure 6: Reactivity of surface for hydrocarbon decomposition as a function of the availability of β_2 hydrogen adsorption sites.

Figure 7: Thermal desorption of H_2 and HD following the exposure of 8 Torr-s of isobutane onto a surface that was preexposed to 0.05 L of D_2.

Figure 8: Thermal desorption of hydrogen resulting from exposure of 20 L of H_2 to:

a. The clean Ir(110) surface, and

b. The dehydrogenated isobutane residue.

Figure 9: Thermal desorption of hydrogen resulting from exposure of 8 Torr-s of isobutane at 100 K to:

a. The clean Ir(110) surface;

b. Surface after experiment (a);

c. Surface after experiment (b); and

d. Surface after experiment (c).

Figure 10: Thermal desorption of hydrogen resulting from:

a. Exposure of the clean Ir(110) surface to 8 Torr-s of isobutane, followed by heating to 320 K (i.e. formation of PDR);

b. Exposure at the PDR to 6 Torr-s of isobutane; and

c. Exposure of the PDR to 5 L of H_2.

Figure 11: Thermal desorption of hydrogen resulting from:

a. Exposure of 3.5 Torr-s of isobutane to the Ir(110) surface followed by an exposure of 4 L of H_2 at 100 K; and

b. Exposure of 3.5 Torr-s of isobutane to the Ir(110) surface at 100 K.

Figure 12:

I. Thermal desorption (monitoring mass 43) resulting from:

a. Exposure of the surface to 2 Torr-s of propane followed by an exposure of 2 L of H_2 at 100 K; and

b. Exposure of the surface to 2 Torr-s of propane at 100 K.

II. Thermal desorption (of mass 43) resulting from:

a. Exposure of the surface to 3.5 Torr-s of isobutane followed by an exposure of 0.25 L of H_2 at 100 K; and

b. Exposure of the surface to 3.5 Torr-s of isobutane at 100 K.

III. Thermal desorption (of mass 41) resulting from:

a. Exposure of the surface to 2 Torr-s of neopentane followed by an exposure of 2 L of H_2 at 100 K; and

b. Exposure of the surface to 2 Torr-s of neopentane at 100 K.

Figure 13: Thermal desorption (of mass 30) resulting from:

a. Exposure of the surface to 2 Torr-s of ethane followed by an exposure of 2 L of H_2 at 100 K; and

b. Exposure of the surface to 2 Torr-s of ethane at 100 K.

Figure 14:

I. Thermal desorption of hydrogen resulting from:

a. Exposure of the surface to 3.5 Torr-s of isobutane at 100 K;

and

b. Exposure of the surface to 3.5 Torr-s of isobutane followed by an exposure of 2 L of CO at 100 K.

II. Thermal desorption of hydrogen resulting from:

a. Exposure of the surface to 4 Torr-s of neopentane at 100 K; and

b. Exposure of the surface to 4 Torr-s of neopentane followed by an exposure of 2 L of CO at 100 K.

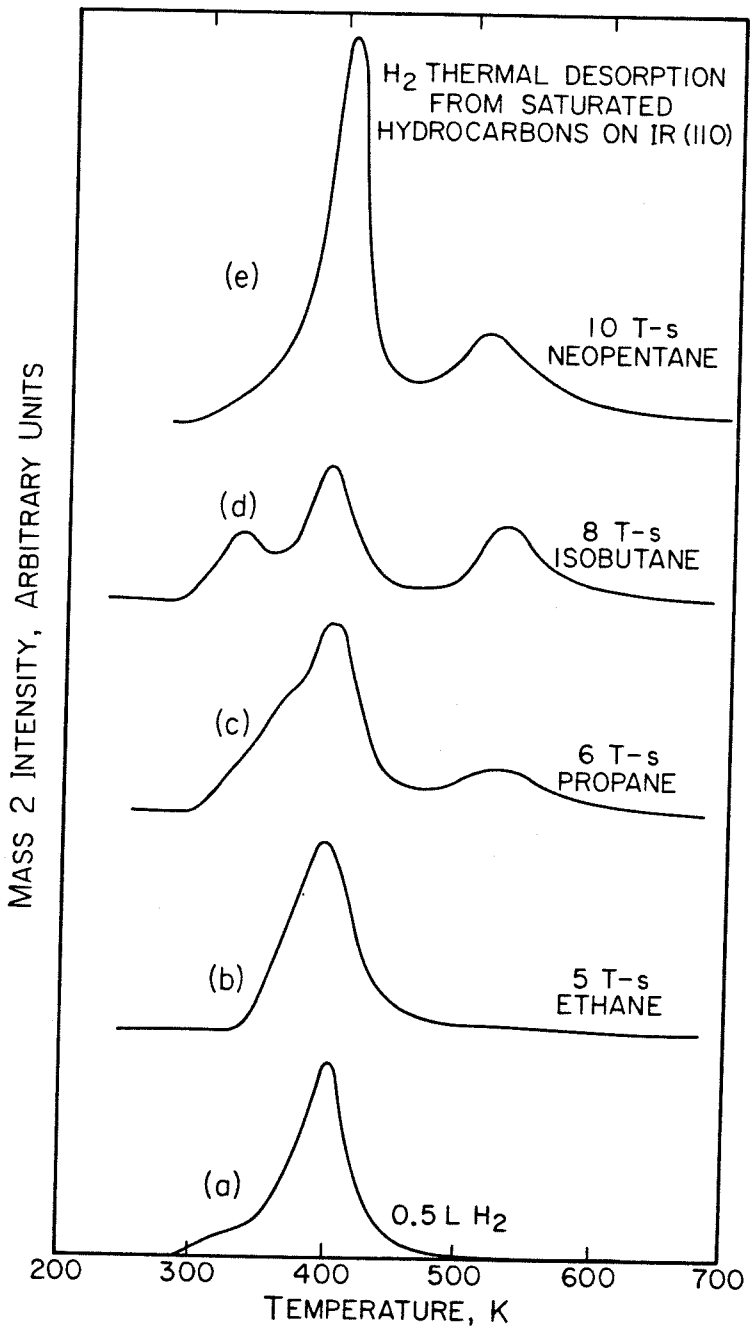
H_2 THERMAL DESORPTION FROM SATURATED HYDROCARBONS ON IR (110)
(e)
10 T-s NEOPENTANE
(d)
8 T-s ISOBUTANE
(c)
6 T-s PROPANE
(b)
5 T-s ETHANE
(a)
0.5 L H_2
MASS 2 INTENSITY, ARBITRARY UNITS
200
300
400
500
600
700
TEMPERATURE, K

Fig. 1

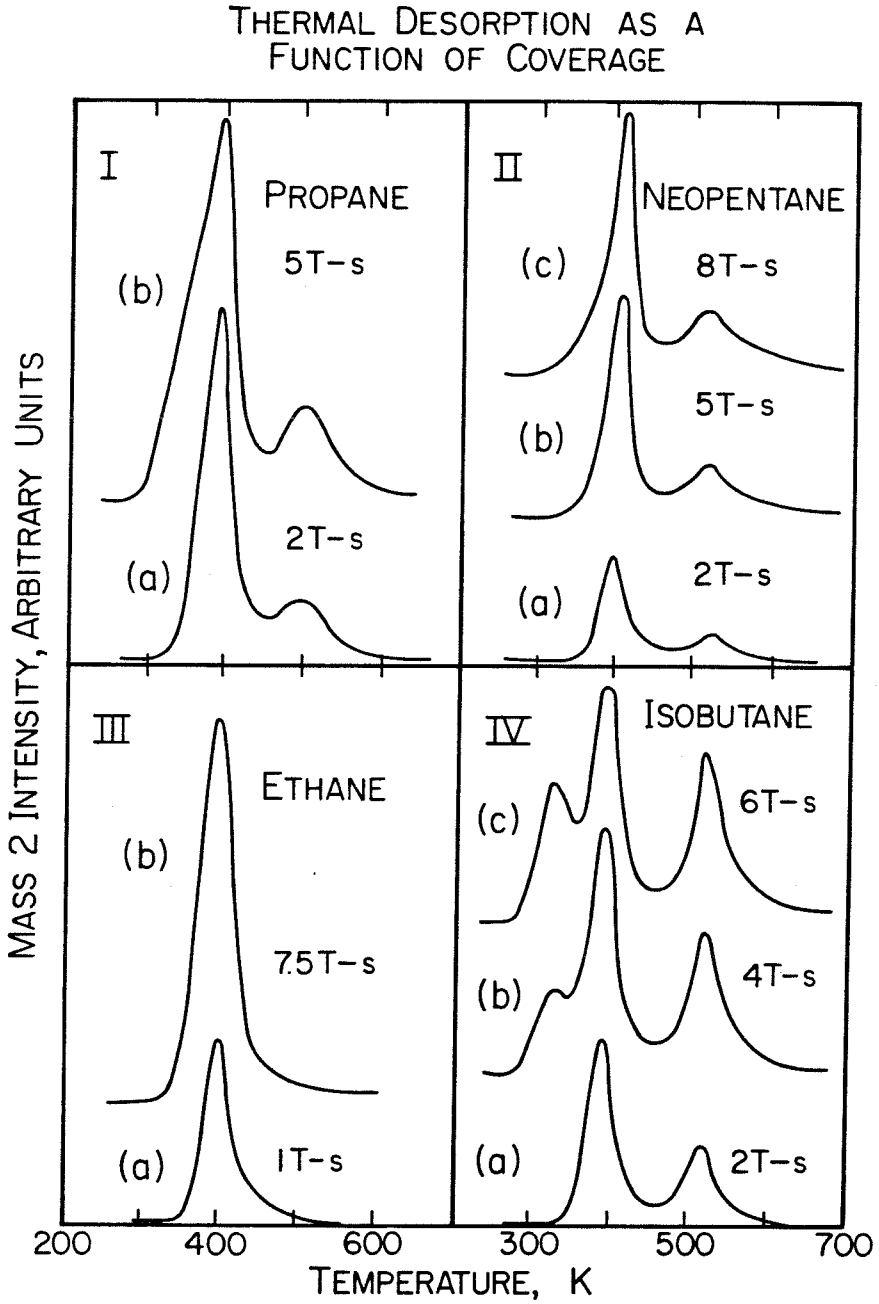
THERMAL DESORPTION AS A
FUNCTION OF COVERAGE
I
PROPANE
(b)
5T-s
(a)
2T-s
II
NEOPENTANE
(c)
8T-s
(b)
5T-s
(a)
2T-s
III
ETHANE
(b)
7.5T-s
(a)
1T-s
IV
ISOBUTANE
(c)
6T-s
(b)
4T-s
(a)
2T-s
MASS 2 INTENSITY, ARBITRARY UNITS
200
400
600
300
500
700
TEMPERATURE, K

Fig. 2

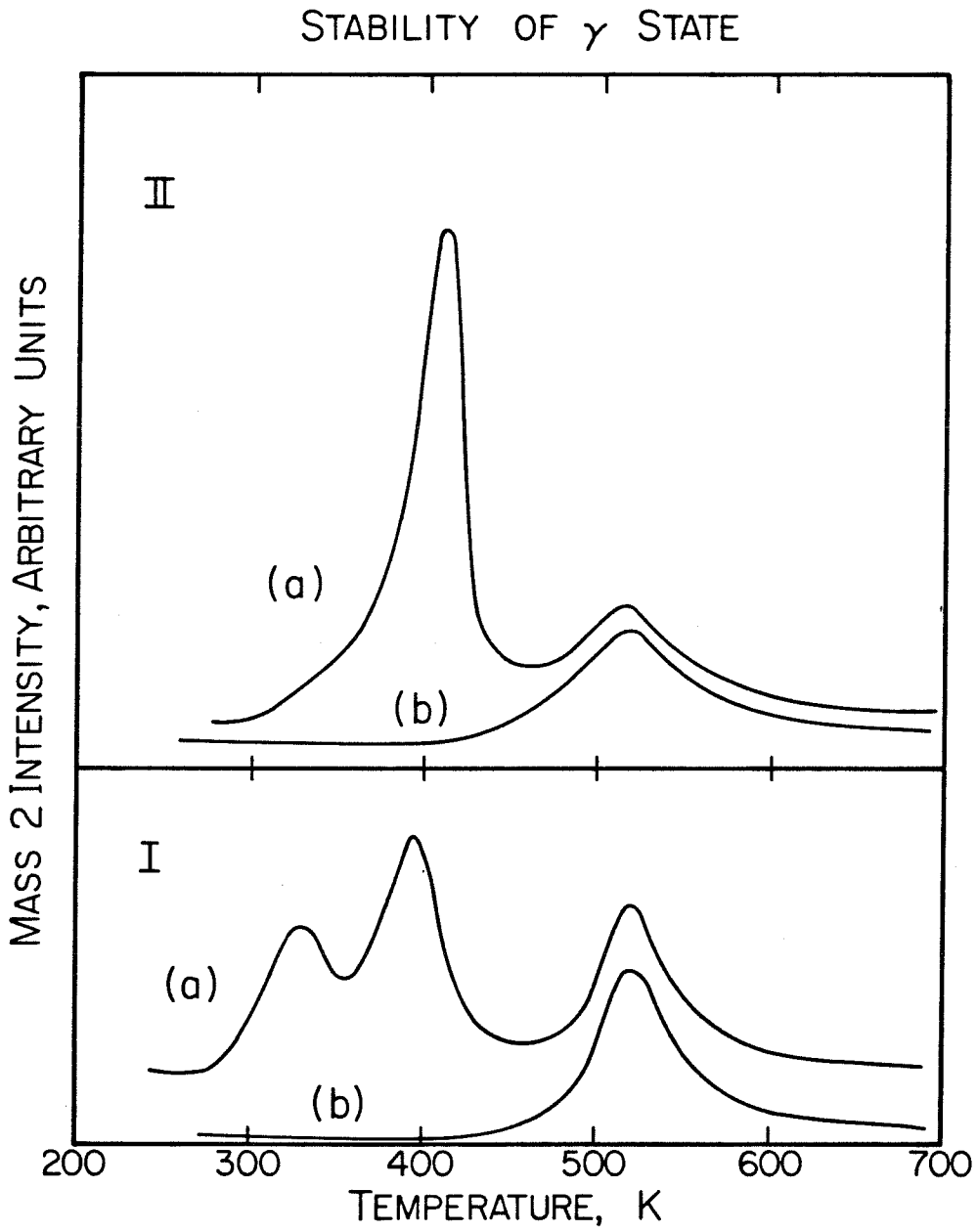
STABILITY OF γ STATE
II
(a)
(b)
I
(a)
(b)
MASS 2 INTENSITY, ARBITRARY UNITS
200
300
400
500
600
700
TEMPERATURE, K

Fig. 3

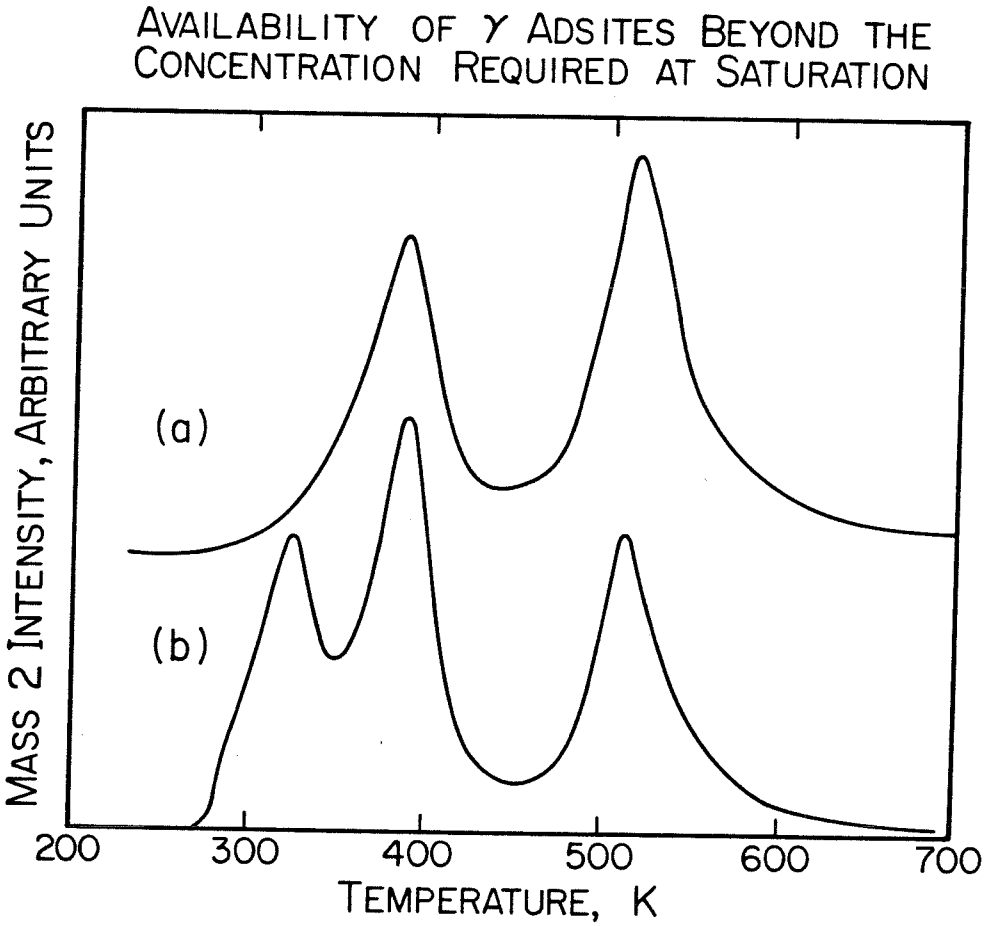
AVAILABILITY OF γ ADSITES BEYOND THE CONCENTRATION REQUIRED AT SATURATION
MASS 2 INTENSITY, ARBITRARY UNITS
(a)
(b)
200
300
400
500
600
700
TEMPERATURE, K

Fig. 4

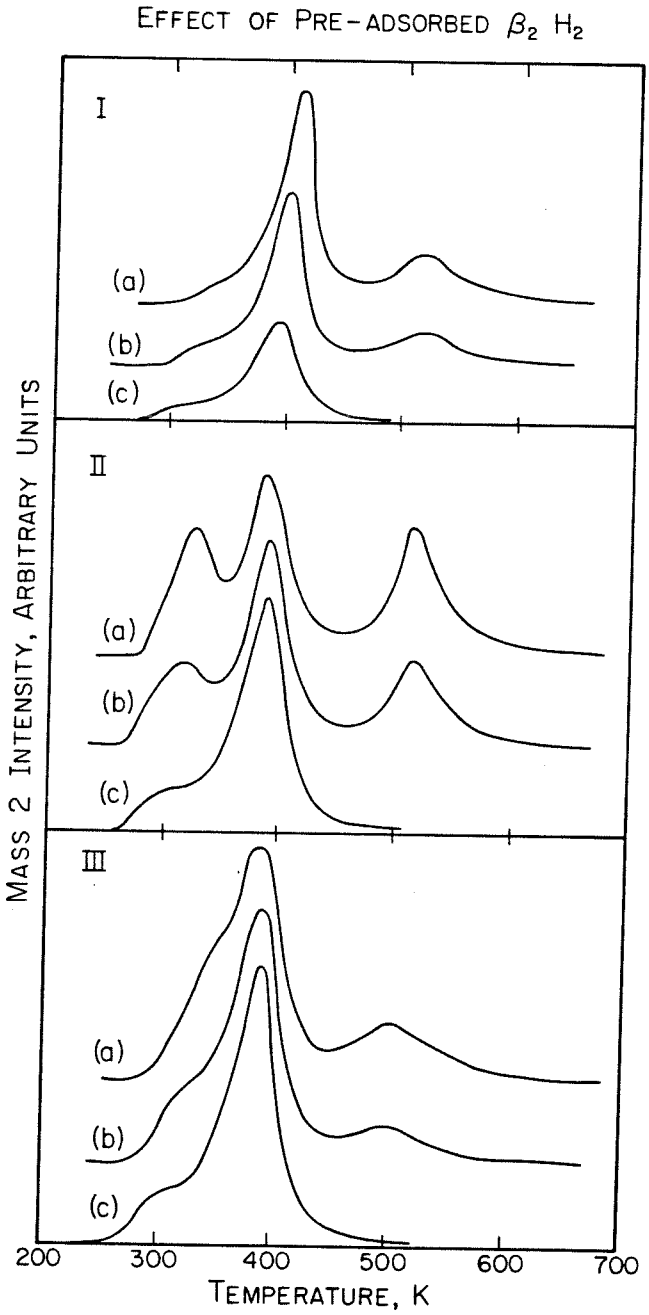
EFFECT OF PRE-ADSORBED β_2 H_2
I
(a)
(b)
(c)
II
(a)
(b)
(c)
III
(a)
(b)
(c)
MASS 2 INTENSITY, ARBITRARY UNITS
200
300
400
500
600
700
TEMPERATURE, K

Fig. 5

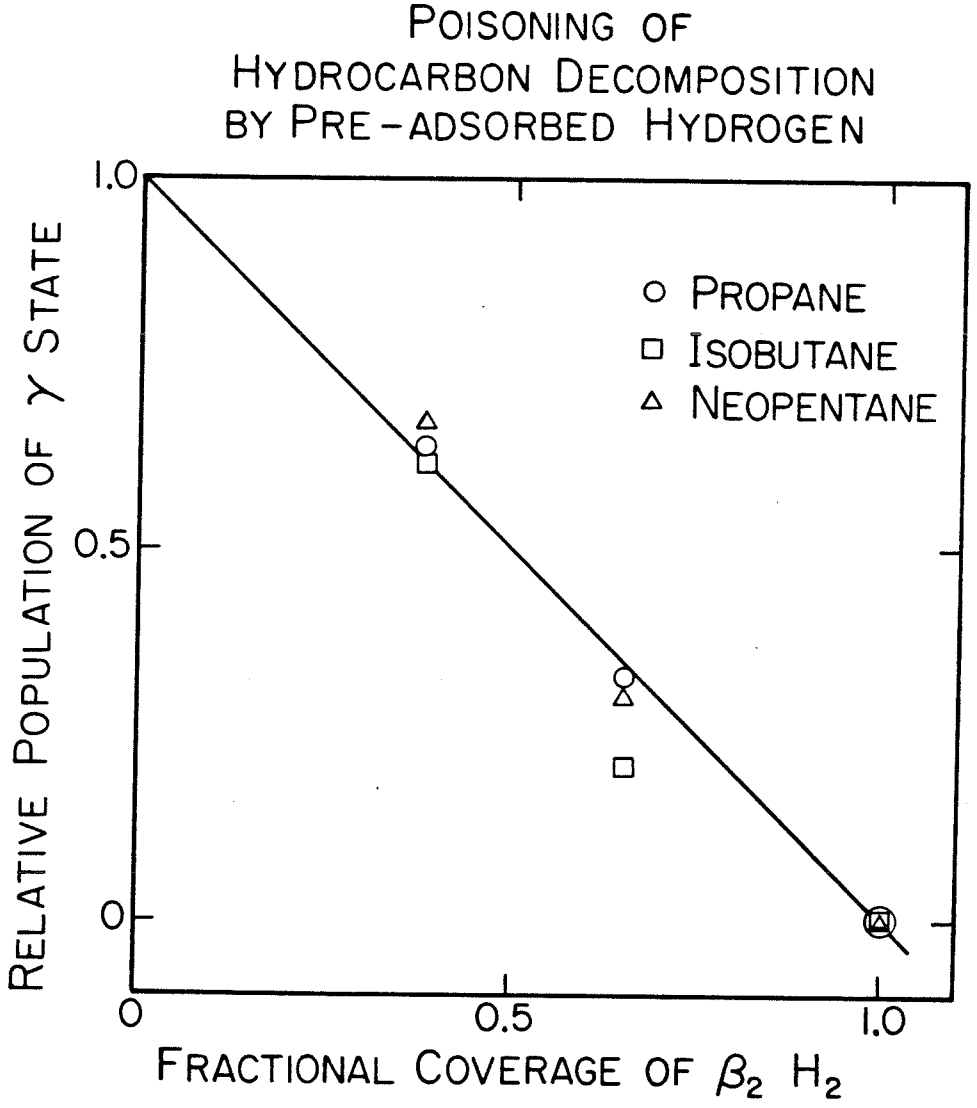
POISONING OF
HYDROCARBON DECOMPOSITION
BY PRE-ADSORBED HYDROGEN
RELATIVE POPULATION OF γ STATE
1.0
0.5
0
0
0.5
1.0
FRACTIONAL COVERAGE OF β_2 H_2
PROPANE
ISOBUTANE
NEOPENTANE

Fig. 6

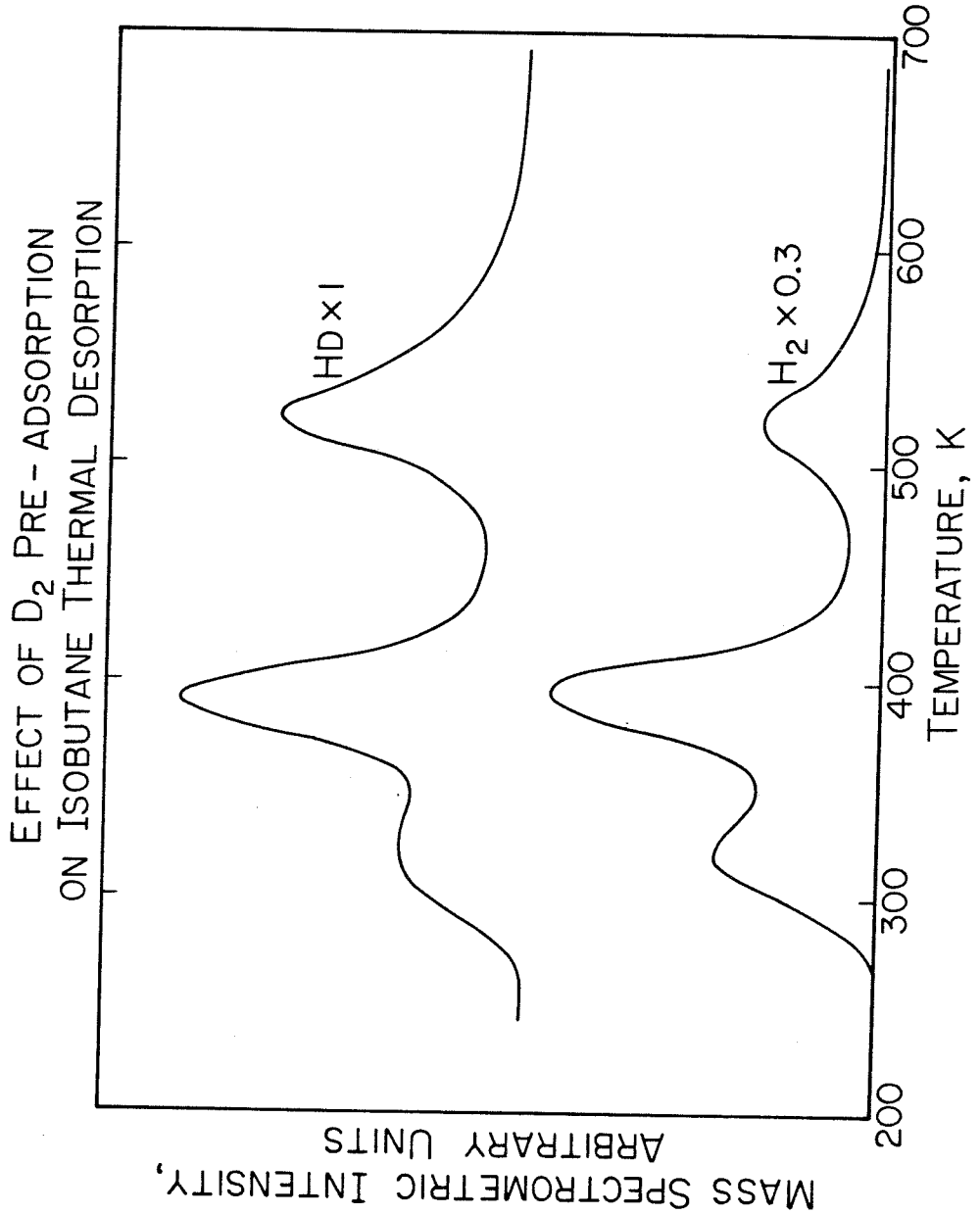
EFFECT OF D_2 PRE-ADSORPTION
ON ISOBUTANE THERMAL DESORPTION
HD x 1
H_2 x 0.3
MASS SPECTROMETRIC INTENSITY,
ARBITRARY UNITS
200
300
400
500
600
700
TEMPERATURE, K

Fig. 7

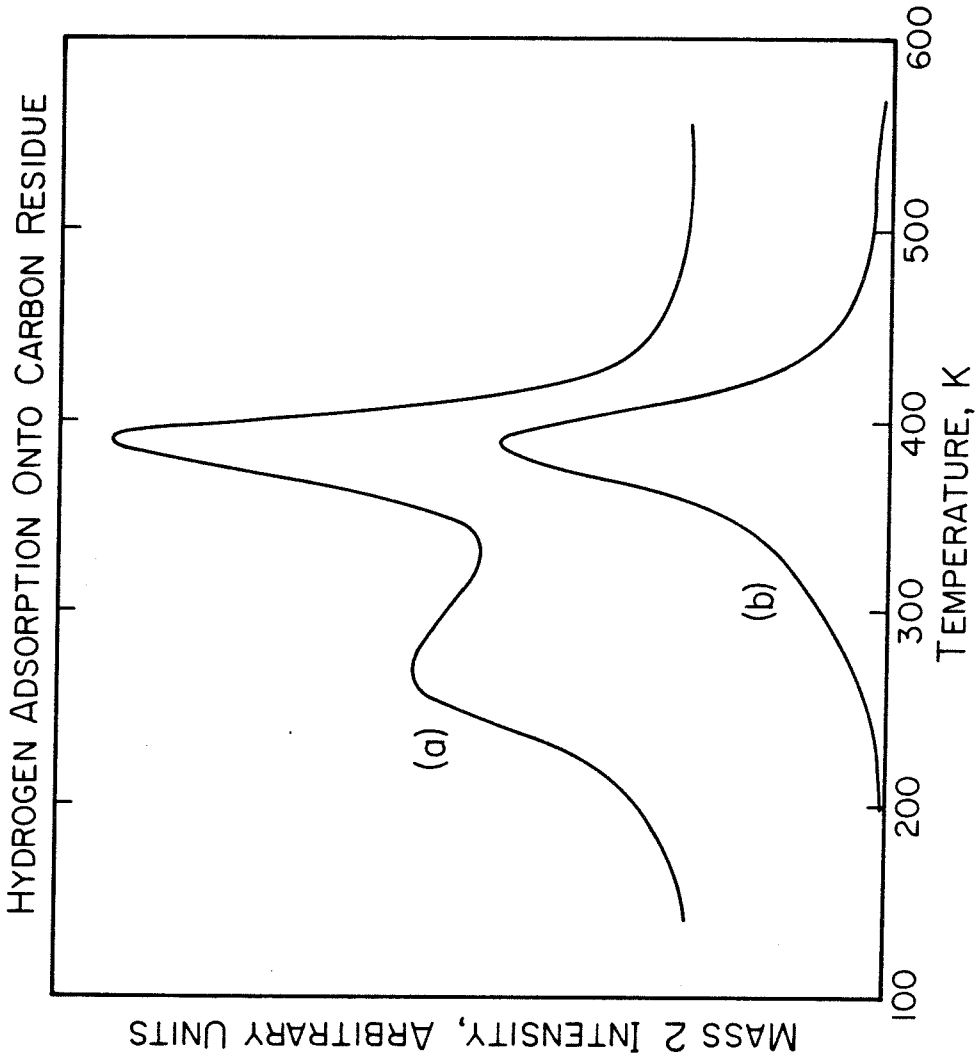
HYDROGEN ADSORPTION ONTO CARBON RESIDUE
MASS 2 INTENSITY, ARBITRARY UNITS
TEMPERATURE, K
100
200
300
400
500
600
(a)
(b)

Fig. 8

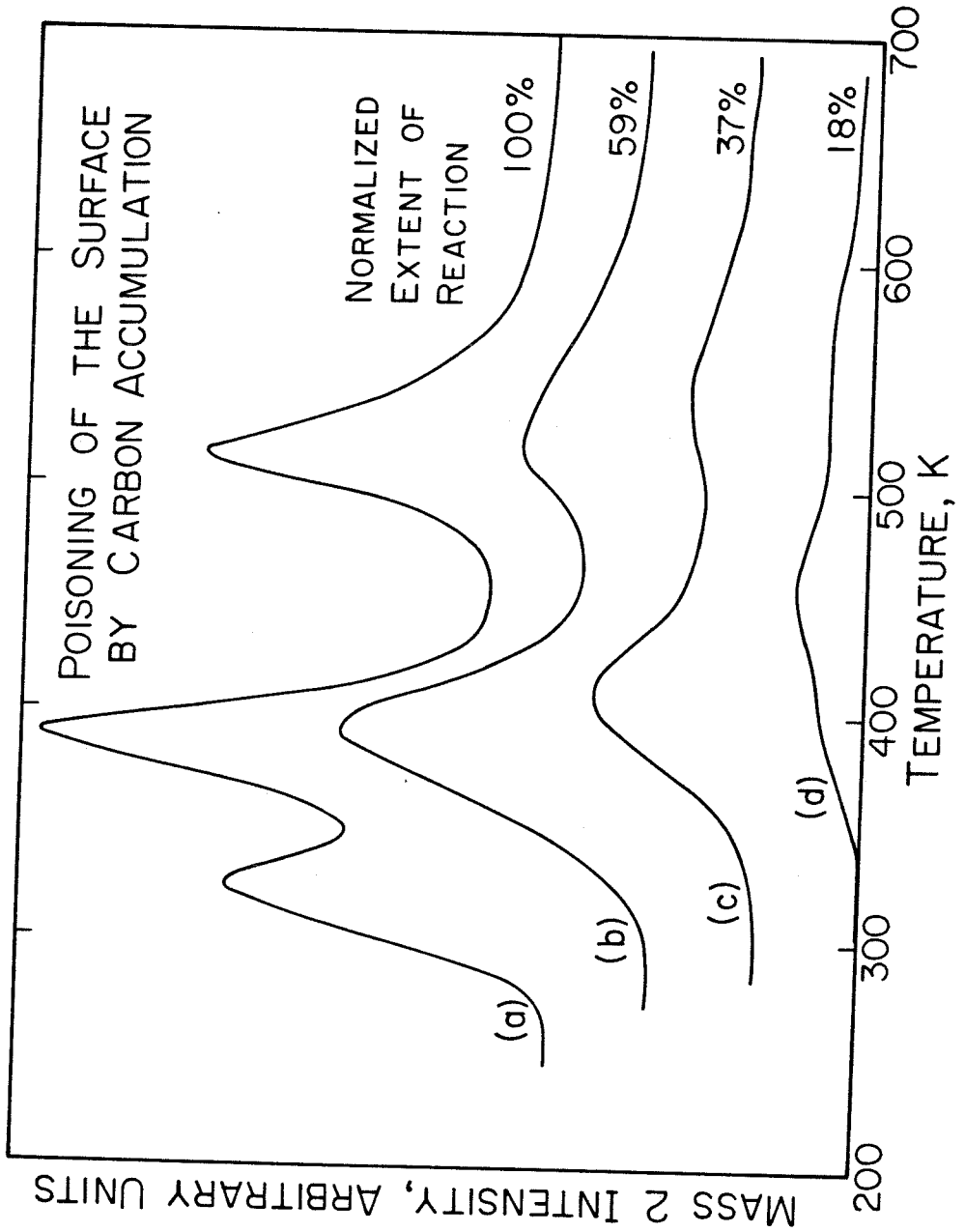
POISONING OF THE SURFACE
BY CARBON ACCUMULATION
NORMALIZED
EXTENT OF
REACTION
100%
59%
37%
18%
(a)
(b)
(c)
(d)
MASS 2 INTENSITY, ARBITRARY UNITS
200
300
400
500
600
700
TEMPERATURE, K

Fig. 9

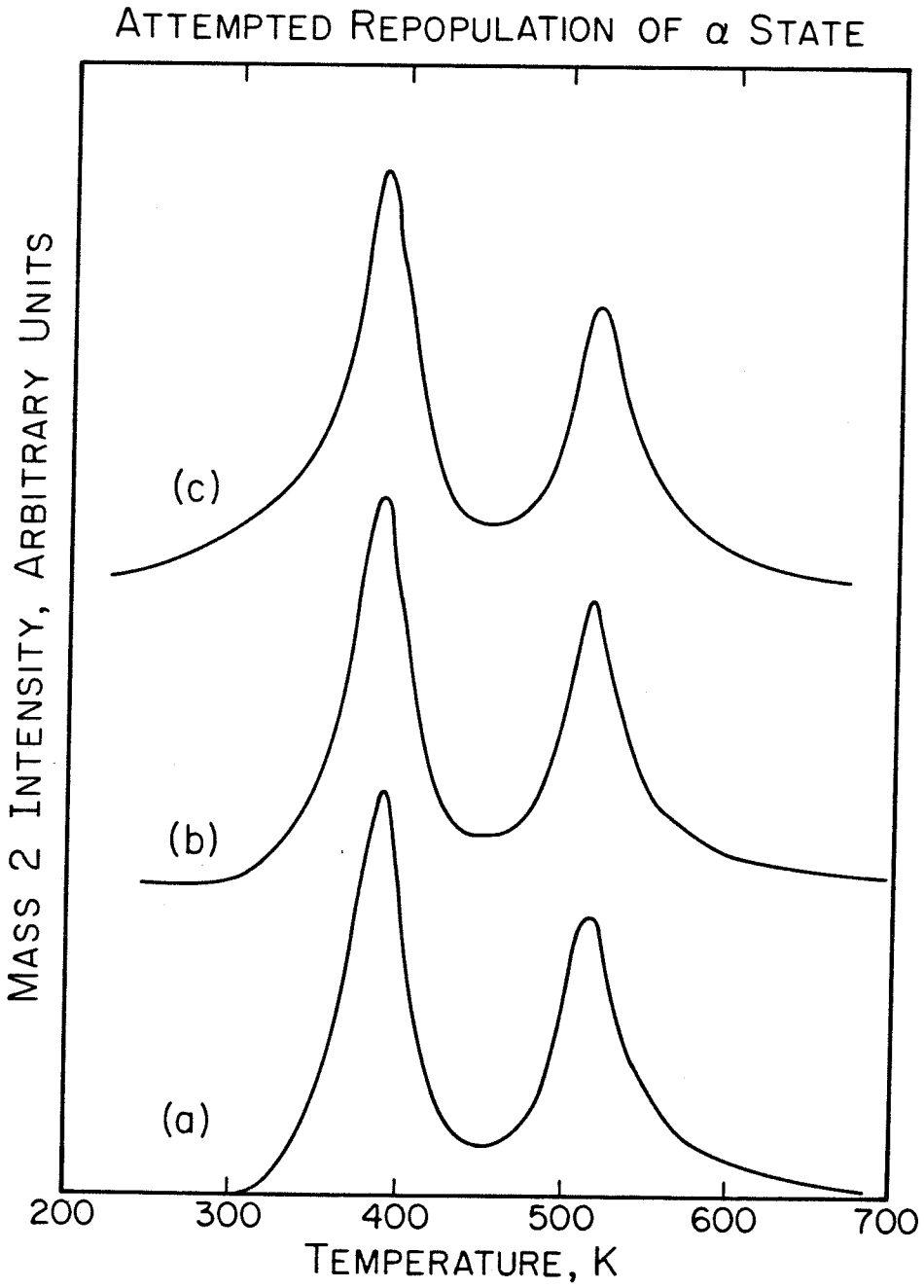
ATTEMPTED REPOPULATION OF α STATE
MASS 2 INTENSITY, ARBITRARY UNITS
(c)
(b)
(a)
200
300
400
500
600
700
TEMPERATURE, K

Fig. 10

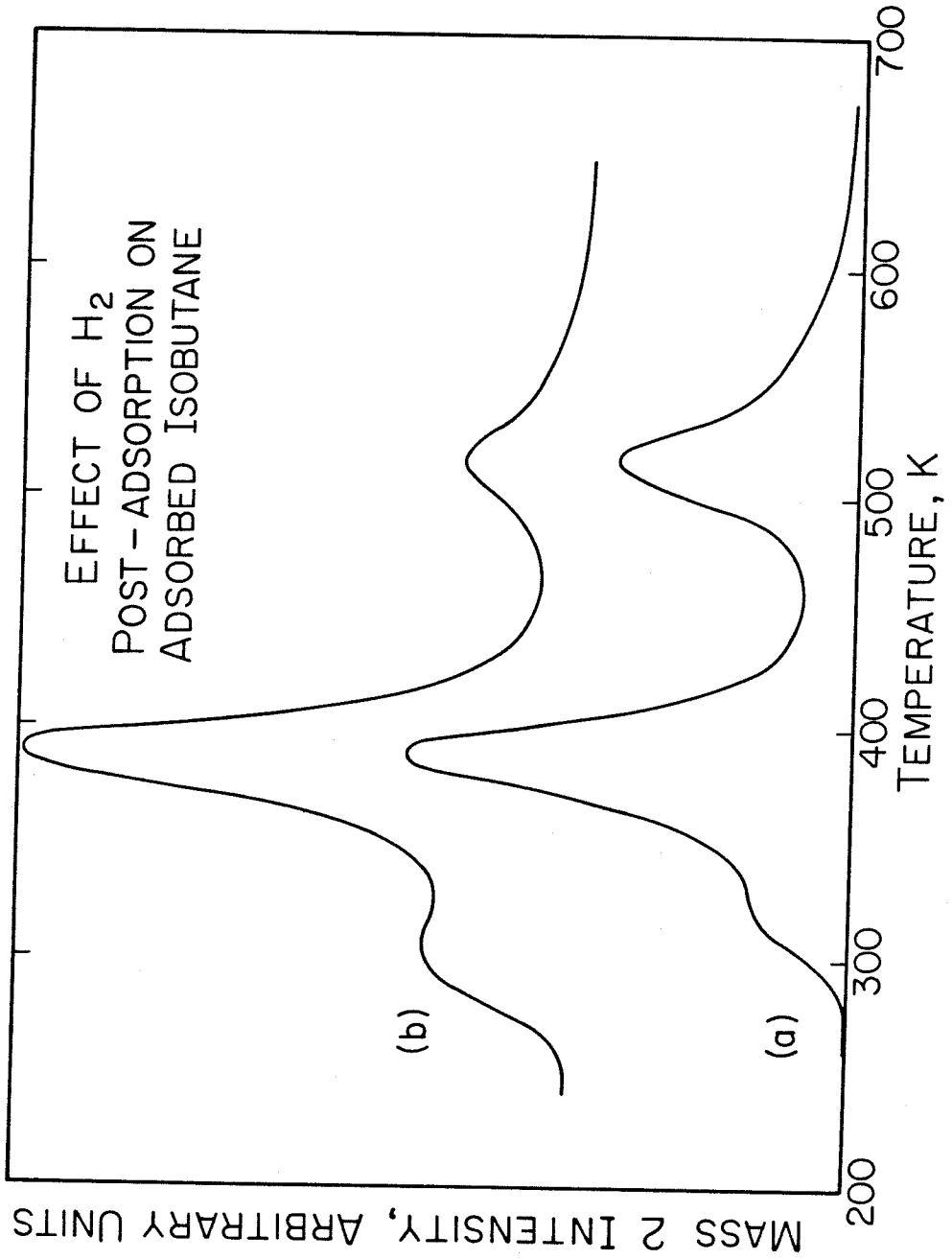
EFFECT OF H_2
POST-ADSORPTION ON
ADSORBED ISOBUTANE
(b)
(a)
MASS 2 INTENSITY, ARBITRARY UNITS
200
300
400
500
600
700
TEMPERATURE, K

Fig. 11

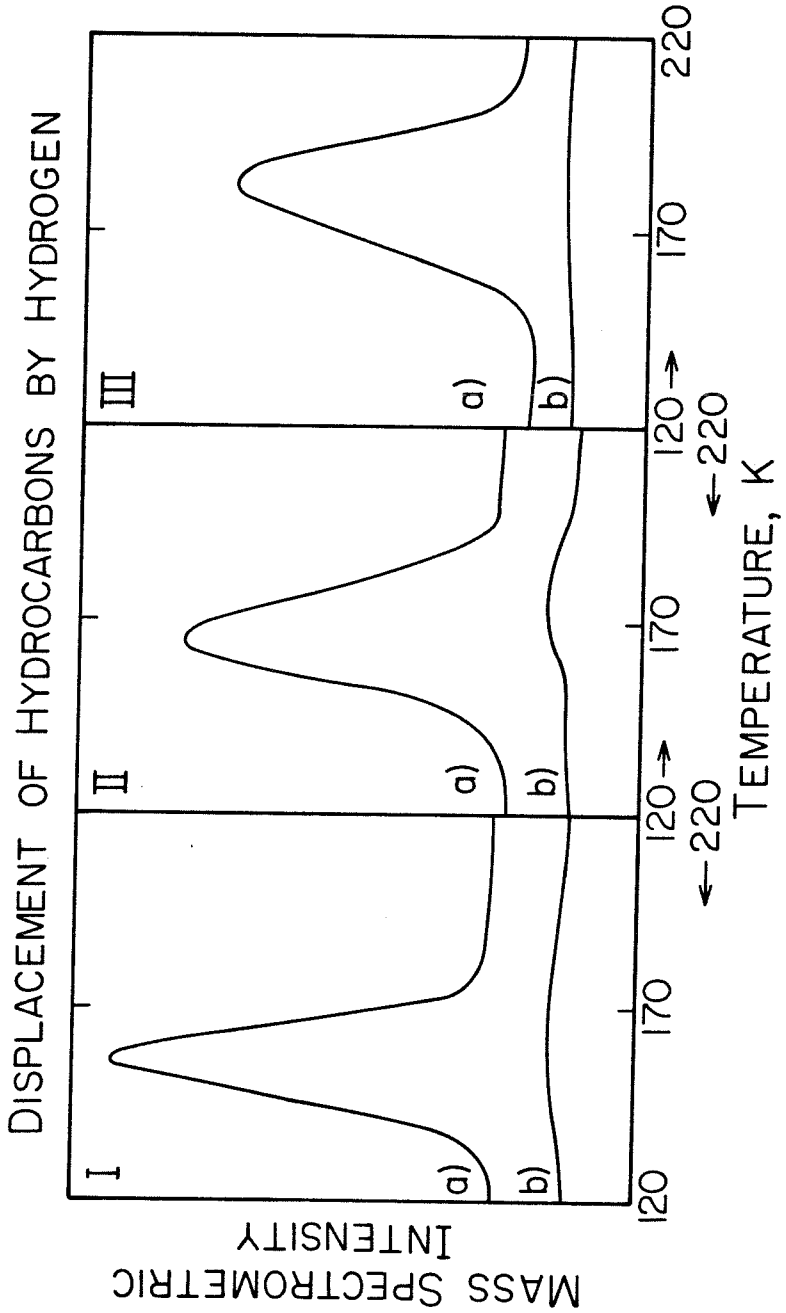
DISPLACEMENT OF HYDROCARBONS BY HYDROGEN
MASS SPECTROMETRIC INTENSITY
I
II
III
a)
b)
120
170
220
120→
←220
TEMPERATURE, K

Fig. 12

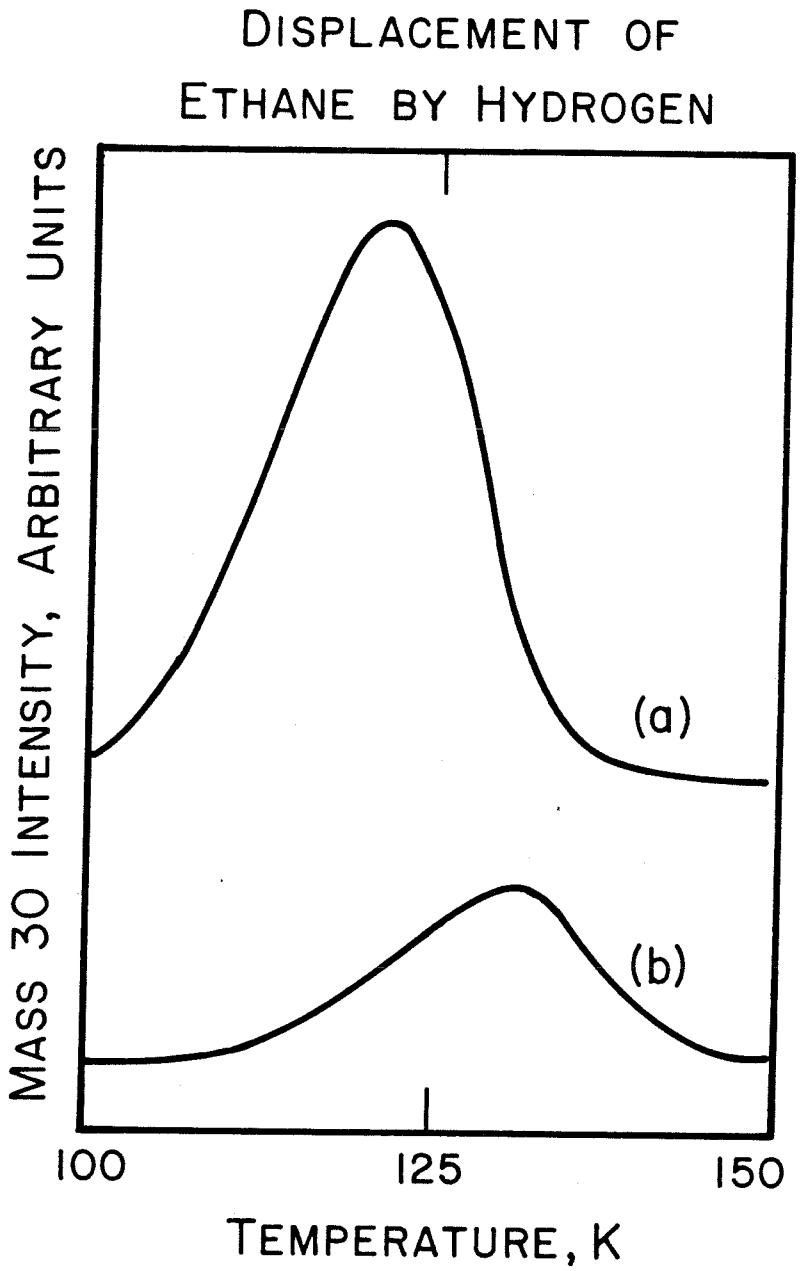
DISPLACEMENT OF
ETHANE BY HYDROGEN
MASS 30 INTENSITY, ARBITRARY UNITS
(a)
(b)
100
125
150
TEMPERATURE, K

Fig. 13

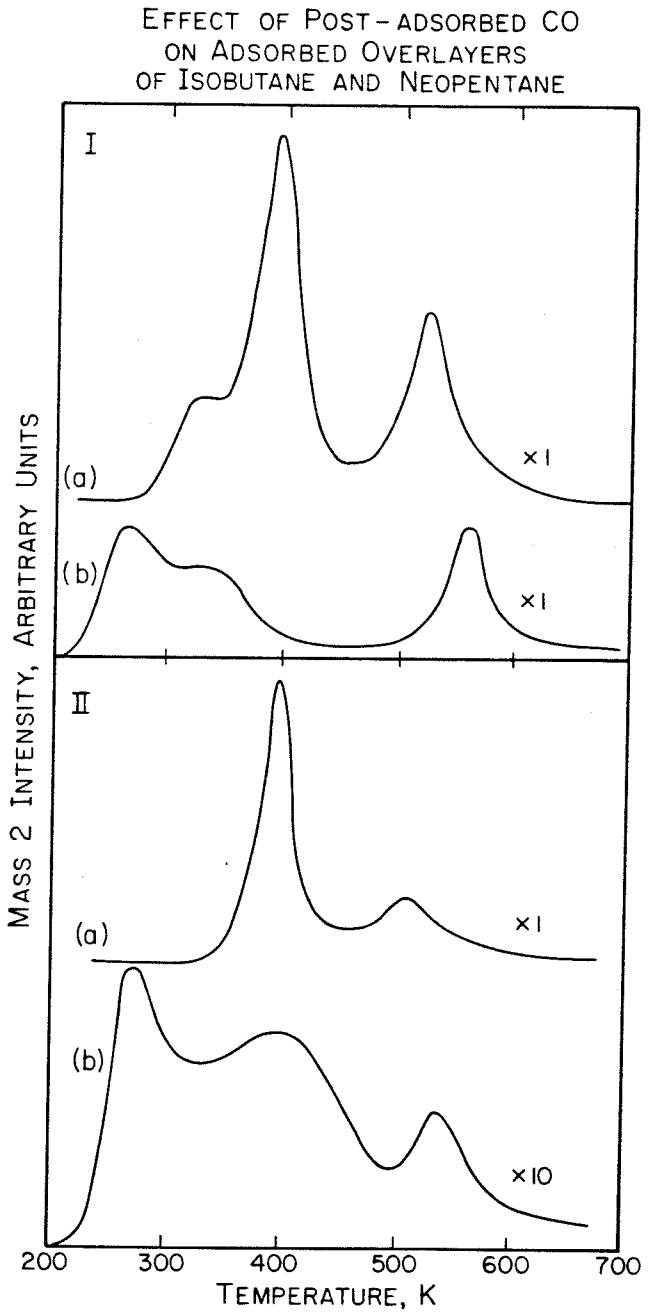
EFFECT OF POST-ADSORBED CO
ON ADSORBED OVERLAYERS
OF ISOBUTANE AND NEOPENTANE
I
(a)
×1
(b)
×1
II
(a)
×1
(b)
×10
MASS 2 INTENSITY, ARBITRARY UNITS
200
300
400
500
600
700
TEMPERATURE, K

Fig. 14

CHAPTER 7

SUMMARY

The conclusions obtained from this thesis may be summarized as shown below.

Chapter 2

(1) Traditional order plots may lead to errors in the true order of the desorption reaction if the rate parameters for desorption vary with coverage.

(2) A procedure for correcting the traditional order plots was developed. A specific example of hydrogen desorption from Ir(110) was discussed for purposes of illustrating this procedure.

Chapter 3

(1) The amount of water that dissociates upon the adsorption of a monolayer of water on Ir(110)-(1x2) at a temperature of 130 K is at most 6% of a monolayer.

(2) When water is adsorbed on an oxygen-covered surface, OH groups are formed on the surface.

(3) Water adsorbs on an Ir(110)-(1x2) surface at a temperature of 130 K with a constant probability of adsorption of unity throughout the submonolayer regime.

(4) Water exhibits four distinct thermal desorption states from the Ir(110)-(1x2) surface. The low coverage γ states develop simultaneously up to 0.5 L exposure. The β state evolves for exposures between 0.5 L and 1.0 L. The α state is the multilayer

ice state and grows without bound for exposures greater than 1.0 L.

Chapters 4-6

(1) The saturated hydrocarbons ethane, propane, cyclopropane, isobutane and neopentane dissociate on the Ir(110)-(1x2) surface at surface temperatures below 130 K.

(2) The dissociation of saturated hydrocarbons on the surface is prevented from occurring by the presence of adsorbed hydrogen or carbon monoxide. This observation leads to the identification of an active site for hydrocarbon dissociation on the surface.

(3) As the surface is heated, the carbon remains adsorbed on the surface and the hydrogen desorbs as H_2.

(4) For ethane, one thermal desorption peak of H_2 is observed that corresponds to hydrogen adsorbed in β_2 hydrogen adsites on the metal surface. This thermal desorption peak was observed for the remaining hydrocarbons, as well as two other thermal desorption states associated with hydrogen that exists in partially dehydrogenated hydrocarbon fragments present on the surface.

(5) No other hydrocarbon species than the hydrocarbon initially adsorbed were observed to desorb from the surface under any of the conditions reported in this work.

APPENDIX A

THE CHEMISORPTION OF HYDROGEN ON THE (110) SURFACE OF IRIDIUM

(The text of Appendix A consists of an article coauthored with D.E. Ibbotson and W.H. Weinberg that has appeared in The Journal of Chemical Physics 72, 4885 (1980).)

Abstract

The chemisorption of hydrogen on Ir(110) was studied under ultra-high vacuum conditions with thermal desorption mass spectrometry, LEED, contact potential difference measurements and ultraviolet photoelectron spectroscopy. The Ir(110)-(1x2) reconstructed surface is stable in hydrogen at pressures from 10^{-9} to 10^{-5} torr and surface temperatures from 130 to 1000 K, the conditions investigated. No streaks or spots were observed in the LEED pattern due to the presence of hydrogen. Absolute coverage measurements indicate the saturation density at 130 K on Ir(110) is $2.2 \pm 0.2 \times 10^{15}$ atoms - cm^{-2}. Thermal desorption measurements indicate that hydrogen obeys second order desorption kinetics and exhibits two features, β_1 and β_2 states, with intensities 2:1, respectively, which exchange isotopically with one another. However, β_2 hydrogen obeys first order adsorption kinetics with an initial sticking probability S_o equal to unity, while β_1 hydrogen has an S_o equal to 7×10^{-3} and obeys second order kinetics. Rate parameters for hydrogen desorption from Ir(110) were calculated as a function of fractional surface coverage. A sympathetic increase in the rate parameters up to at least half of saturation is observed for the β_2 state of hydrogen, where E_d and ν_d assume the values 23 kcal/mole and 1.5×10^{-2} cm^2 - s^{-1}, respectively. The increase is attributed to adatom-adatom attractive interactions of hydrogen in the β_2 state. For the β_1 state, the energy of desorption, in kcal-$mole^{-1}$, is given by $E_d = 17 - 10\theta$ from θ equal to 0.4 - 0.7, and the preexponential factor, ν_d, varies weakly as a function of coverage with an average value of $2 \div 2 \times 10^{-7}$ - s^{-1}. The contact potential difference (CPD) increases

linearly with coverage up to 0.20 eV and reaches a maximum at 0.30 eV for the β_2 state of hydrogen for $T \leq 300$ K. A continuous decrease in the CPD occurs over the β_1 state up to saturation at 140 K and becomes lower than the clean surface contact potential for total fractional coverages above 0.9. Probable binding sites for the β_1 and β_2 states are inferred from the absolute coverage measurements and the CPD measurements. Ultraviolet (HeI, $h\nu$ = 21.2 eV) photoelectron spectra of hydrogen show a broad H(1s) level centered approximately at 6.1 eV below the Fermi level. A strong decrease in the d-band emission occurs near the Fermi level after adsorption of the β_2 state, which suggests preferred binding locations for this state of hydrogen on the Ir(110)-(1x2) surface.

1. Introduction

The study of hydrogen chemisorption on Ir(110) was undertaken to give insight into several of the elementary reactions which are important in reduction catalysis. Thermal desorption mass spectrometry (TDS), LEED, contact potential difference (CPD) measurements and ultraviolet photoelectron spectroscopy (UPS) were used to investigate the properties of hydrogen chemisorption, e.g., desorption kinetics, adsorption kinetics, the structure of the overlayer-substrate system, charge transfer in the overlayer, and the electronic nature of the H-Ir bond.

Although hydrogen chemisorption has been investigated extensively on various surfaces of the platinum metals, including Ni (1,2), Rh (3,4), Pd (5,6), Pt (7 - 12) and Ir (3,13,14), little work has been performed on single crystals of Ir. The present comparative study on Ir(110) will complement the work done on other single crystal surfaces of the platinum metals. In general, many aspects of hydrogen chemisorption have common features among this class of metals. Nonactivated dissociative adsorption is observed with initial sticking probabilities ranging from 0.1 to 0.4 with the exception of Pt(100)-(5x20) which seems not to adsorb hydrogen (10). Generally, adsorption is described either by a dissociative Langmuir model or by a second order precursor model. However, first order adsorption kinetics are observed for hydrogen adsorption on Ni(111) and Ni(100) (2). Two to three features appear in the thermal desorption spectra depending upon the metal and surface orientation. Most of these features are described by second order desorption kinetics, but the low coverage feature for hydrogen desorption from Ni(110) (2) and oxidized Pt(110) (9) displays first order desorption characteristics. Reported values for the activation energy of desorption at low coverage range from 17 to 25 kcal/mole for the

platinum metals. Hydrogen forms few ordered overlayer structures on the platinum metals. A (2x2) structure is observed on Ni(111) (15 - 17), whereas a (1x1) overlayer structure forms on Pd(111) (5,6). Also, a (1x2) structure is formed on (110) surfaces of Pd (4) and Ni (1,2,18). Faint streaks appear in the LEED pattern for a saturated hydrogen overlayer on a stepped Pt(111) surface (12) which are attributed to ordering along the steps. Finally, the CPD increases for hydrogen on most platinum metal surfaces, typically between 0.1 and 0.6 eV depending on the metal and surface orientation, i.e., a net transfer of electrons to H atoms occurs from the metal if hydrogen lies above the surface plane. On Pt(111) (8) and stepped Pt(111) (12), a decrease in CPD occurs with increasing hydrogen coverage in addition to a small initial increase in the CPD which is more pronounced on the stepped surface. Further, an initial increase in the CPD of 0.1 eV and then a decrease to a final value of 0.03 eV is observed at 120 K on Ni(100) (19) and Ni(111) at low temperatures (17). Ultraviolet photoelectron spectra of hydrogen chemisorbed on (111) surfaces of Ni (20,21), Pd (20,21) and Pt (21) show H(1s) induced levels at 5.8, 6.4 and 7.3 eV below the Fermi level, respectively. For Pd (19,20) and Pt (20), a strong redistribution of d-band emission occurs near the Fermi edge, in contrast to Ni. The present work is in general agreement with these previous studies; however, new results are presented for hydrogen on Ir(110).

2. Experimental Procedures

The experiments were performed in an ion-pumped stainless steel bell jar with a base pressure below 2×10^{-10} torr. Several surface sensitive probes — a quadrupole mass spectrometer, LEED optics, a CPD apparatus, an

Auger electron, and X-ray and UV-photoelectron spectrometers — are contained in the experimental chamber. A double pass cylindrical mirror analyzer was used to perform the electron kinetic energy analysis. All probes were interfaced to a PDP 11/10 computer (22). Although all data reported here, except the LEED data, were obtained in digital form, the data are shown in analog form to facilitate the presentation. A detailed description of the experimental system is reported elsewhere (23), with the exception of the ultraviolet lamp. The HeI radiation was produced by a microwave discharge cavity at the end of a two-stage, differentially pumped stainless steel capillary array. When a HeI discharge at a pressure of 1 torr was used, the base pressure in the belljar rose by 1×10^{-9} torr. For HeI radiation, typical count rates near the Fermi edge were from 90,000 to 110,000 count-s^{-1} for a constant pass energy of 25 eV.

The substrate was cut from a single crystal of Ir and was polished to within 1^{o} of the (110) orientation using standard polishing techniques. Carbon was cleaned from the substrate through a series of oxidation and reduction cycles. Annealing above 1600 K removed O, Ca and K impurities. Details of the cleaning procedure are described elsewhere (23). The substrate was heated resistively by two 10 mil Ta support wires or cooled conductively by liquid nitrogen. Temperatures were measured with a W/5%Re-W/26%Re thermocouple spotwelded to a 1 mm^2 Ta foil sandwich on the back of the Ir crystal and were referenced to an icepoint junction. Temperatures are accurate within ± 5 K for all values reported here.

3. LEED Observations

If a simple termination of the bulk is considered, the Ir(110) surface is a series of rows and troughs. However, a clean surface is reconstructed to form a (1x2) LEED pattern (24), a situation which occurs also on Pt (110) (25). Very recently, the structure of reconstructed Ir(110) has been determined to be a surface with every other row of surface atoms missing in the [001] direction (26). Thus, not only are second layer Ir atoms exposed, but third layer atoms under the locations of the missing rows are exposed also. The surface may be thought of as (111) planes inclined to one another containing an equal number of two inequivalent types of three-fold sites and two inequivalent types of two-fold sites between the first and second layers. There are a total of four three-fold sites and four two-fold sites present in each reconstructed unit cell. Also, one additional high symmetry site is contained in each unit cell either on top of the rows of Ir atoms or directly above the third layer of Ir atoms. This knowledge, coupled with other data presented below, may be used to infer preferred binding sites for hydrogen on Ir(110).

Under all conditions examined, i.e., for surface temperatures from 130 to 1300 K and pressures from 10^{-9} to 10^{-5} torr hydrogen, the structure of the surface was stable and showed the (1x2) reconstruction. No additional spots or streaks occurred in the LEED pattern for any coverage of hydrogen on the surface, even at 130 K. As the hydrogen coverage increased, the substrate pattern remained a sharp (1x2) with the background increasing only slightly at high coverage. Annealing a hydrogen-covered substrate to the onset of hydrogen desorption and recooling to 130 K caused no observable changes at any hydrogen coverage.

4. Absolute Coverage Determination

Absolute coverage calibrations were performed for hydrogen on Ir(110) by two methods, both using TDS. The two methods, outlined below, employ known absolute coverages for CO and oxygen on Ir(110) from previous studies in the same experimental system (23,27). The basis for both techniques is to compare relative experimental parameters between hydrogen and another gas which has an accurate coverage calibration in atoms or molecules per unit area to determine the number of hydrogen atoms per unit surface area.

The first technique is a comparison of the integrated intensities of mass 2 and mass 28 in thermal desorption spectra of hydrogen and CO for saturation coverages. The relative mass spectrometric sensitivities for H_2 and CO were determined by calibration with respect to an ion gauge where the ionization efficiencies were known. A poppet valve contained in the system was closed sufficiently so that the ratio of the pumping speeds was equal to the ratio of the square root of the molecular weights of the desorbing molecules. The absolute sensitivity of the mass spectrometer to CO was determined from the CO spectrum for saturation coverage at 300 K, which is equal to 9.6×10^{14} molecules - cm^{-2} (23). The thermal desorption spectrum for a saturation coverage of hydrogen at 130 K, the lowest temperature accessible during these experiments, was obtained by exposing the surface to 300 Langmuirs (L) of H_2 (1 L $\equiv 10^{-6}$ torr-s). At greater exposure to H_2, adsorption becomes reversible at 130 K, although the spectrum is quite reproducible up to 300 L. Then, absolute coverages of hydrogen (atoms - cm^{-2}) were determined from twice the product of the

absolute sensitivity of the mass spectrometer to CO, the ratio of the relative sensitivities for CO and H_2, the ratio of the pumping speeds for H_2 and CO, and the ratio of the pressure-time integrals for the saturation spectra of H_2 and CO.

The second technique used to determine absolute coverages of hydrogen employs oxygen and deuterium. As described below, deuterium and hydrogen have identical adsorption properties on Ir(110). Deuterium was used to minimize baseline drift in the mass spectrometer from adsorption of background H_2O on the sample manipulator. For certain coverage ranges of co-adsorbed deuterium and oxygen, all the oxygen reacts during thermal desorption to form D_2O (28). If one knows the absolute initial coverage of oxygen, then an absolute calibration for D_2O is known. Moreover, if a known relative coverage of deuterium is co-adsorbed with any coverage of oxygen below the temperature where any species desorb, and the surface is heated, the difference between the amount of deuterium that desorbs with no oxygen present and the amount that desorbs with oxygen present is equal to the coverage of deuterium that reacts to form D_2O. This difference can then be used to calculate absolute coverages of deuterium (or, equivalently, hydrogen) from the coverage calibration for D_2O. The experimental conditions that meet the above requirements are described briefly. A more detailed account will appear in a later publication (28).

When more than 100 L D_2 is exposed at 130 K to a surface oxide on Ir(110), and the surface is heated, all the oxide desorbs as D_2O (28). The surface oxide is formed by exposing an Ir(110) surface to more than 0.8 L O_2 followed by annealing to 1200 K. The coverage of the oxide is 2.4×10^{14} atoms - cm^{-2} and has associated with it a (1x4) LEED pattern

(27). Any excess oxygen desorbs as O_2. Since the oxygen coverage on the oxide surface is known, a calibration for D_2O may be obtained from the integrated intensities of the mass 20 signal in the thermal desorption spectrum. To obtain a known relative coverage of deuterium, the Ir(110) surface is exposed to D_2 at 130 K. In order to co-adsorb oxygen and not lose any deuterium during oxygen adsorption due to reaction or desorption, small exposures of O_2 (< 0.5 L) are applied to the deuterium overlayer (28). Any of the D_2 signal lost during a flash will be due to reaction to form D_2O, which is measured simultaneously. The method discussed above allows several measurements to be made quickly in order to minimize inaccuracies due to drift in system constants. This method presents a more accurate technique to determine absolute coverages for hydrogen (deuterium) than the first method described where relative pumping speeds must be known, and large exposures of both gases (H_2 and CO) must be used.

The results of the two independent methods to determine absolute coverages of hydrogen on Ir(110) are in excellent agreement. For saturation (300 L) exposure of H_2 at 130 K, the first method yields $N_{sat} = 2.3 \times 10^{15}$ atoms - cm^{-2}; whereas the second, more accurate, method yields $N_{sat} = 2.2 \pm 0.2 \times 10^{15}$ atoms - cm^2. This value for the saturation coverage of hydrogen on Ir(110) is very reasonable when compared to other platinum metal surfaces. Saturation coverages of hydrogen on the platinum metals are difficult to determine due to the general lack of order in overlayers. However, between 1 and 2 x 10^{15} atoms - cm^{-2} of hydrogen adsorb on Pd(110) (29) and Ni(110) (1,2), in good agreement with the value determined here. As shown below, two distinct states are observed for hydrogen in thermal desorption spectra which have relative populations of

2:1 for low and high binding energy states, respectively. This corresponds to approximately 3 atoms and 1.5 atoms for each state of hydrogen in each unit cell for the reconstructed surface. Since more hydrogen could be adsorbed if surface temperatures below 130 K could be reached, the low binding energy state may reach a saturation of 4 hydrogen atoms in each unit cell — the number of three-fold sites or the number of two-fold sites available on the (1x2) surface. Although the saturation coverage determined at 130 K is only accurate to ± 10%, the agreement between the number of three-fold sites, or the number of two-fold sites, and the number of atoms in the low binding energy state is excellent. Three-fold sites are preferred as probable binding sites since hydrogen binds to both types of inequivalent three-fold sites on Ni(111) (17). Figure 1 presents a summary of the probable binding sites of hydrogen on Ir(110).

5. Desorption Kinetics

Several thermal desorption spectra of H_2 from Ir(110) were measured as a function of H_2 exposure at 130 K. These data are used for investigating both the desorption and the adsorption kinetics of hydrogen on Ir(110).

Figure 2 shows representative curves of 30 desorption spectra for hydrogen on Ir(110). The average heating rate (β) for each spectrum was 21 K/s. Two features appear with relative integrated intensities of 2:1 and are defined as β_1 and β_2 states, respectively. Although both features exhibit a decrease in peak temperature with increasing surface coverage, characteristic of second order desorption kinetics, their rate parameters

display markedly different behavior, as will be shown. The β_2 state fills to completion after 0.35 L and shows only a 15 K decrease in peak temperature. After the β_2 state is occupied fully, the β_1 state fills at a much slower rate and decreases in peak temperature by more than 100 K over the accessible coverage range. The β_2 state of hydrogen shown in Fig. 2 desorbs in the same temperature range as previously seen for hydrogen adsorption on Ir(110) (30) and Ir(111) (31) near 300 K.

Dissociative adsorption of hydrogen on the platinum metals is reported for all surface orientations investigated (1 - 15). However, first order desorption kinetics have been observed on Ni(110) (2) and oxidized Pt(110) (9) for the most tightly bound states. For the β_2 state of hydrogen on Ir(110), the slight decrease in peak temperature may imply first order desorption with a small decrease in the activation energy of desorption. Hydrogen and deuterium were adsorbed sequentially at 130 K to determine if both species (β_1 and β_2) are indeed adsorbed dissociatively and if isotopic exchange occurs between the states. As shown in Fig. 3, H_2, HD and D_2 are desorbed during a thermal desorption experiment in which 0.45 L D_2 was adsorbed to fill the β_2 state, followed by 5.0 L H_2. From the thermal desorption spectra, it is clear that dissociative adsorption and mixing between the β_1 and β_2 states do occur. Many other experiments were performed with various sequential exposures of H_2 and D_2 that are not shown. Regardless of the exposure sequence or the amount of each component adsorbed, the product distribution was similar to those in Fig. 3. Overall, statistical mixing of H and D is confirmed at each point in the desorption spectra: values of the isotope distribution coefficient

$K_{id}\left[\frac{[I_{HD}]^2}{I_{D_2} I_{H_2}}\right]$ range from 3 to 4.5. The terms I_{HD}, I_{D_2} and I_{H_2} are the gas phase intensities of the products of the desorption reaction, corrected for differences among their respective experimental system constants. Within the errors of the experiment, the values of K_{id} agree very well with the calculated value of approximately four for complete mixing (3). Isotopic exchange experiments on polycrystalline Ir resulted in $K_{id} \sim 3$ for adsorption at 100 K (3).

The order plots in Fig. 4 were constructed from the thermal desorption data in Fig. 2 to determine whether the kinetics of desorption of hydrogen in the β_2 state are first order or second order. For low coverages, it is usually assumed that the slope of a plot of $\ln R_d$ as a function of $\ln\theta$ at constant temperature is equal to the desorption order, where R_d and θ are the rate of desorption and the fractional surface coverage of hydrogen, respectively. As calculated from Fig. 4, the slope for $T \geq 380$ K is equal to two, indicating second order desorption for the β_2 state. At lower temperatures, where the β_1 state desorbs, the slopes are much greater than two, indicating a change in the rate parameters with coverage. This is evidenced also by the broad, asymmetric desorption behavior seen in Fig. 2, although the desorption is expected to obey second order kinetics since it adsorbs dissociatively, and the adsorption kinetics (see sect. 6) show no evidence for the participation of a precursor (32).

However, the slope calculated from the order plots, even at low coverages, may not represent the true order of the desorption reaction.

For the β_2 state described here, the calculated order is, in fact, two; but this was shown to be the result of the cancellation of other terms that contribute to the slope of an order plot (33). Briefly, the derivation involves the following expression for the desorption rate,

$$R_d = \nu_d(\theta)\theta^n \exp[-E_d(\theta)/kT] \quad . \tag{1}$$

The order n is assumed to be a constant integer representing the elementary desorption reaction. Logarithmic differentiation of Eq. (1) with respect to the fractional surface coverage at constant T yields

$$\left(\frac{\partial \ln R_d}{\partial \ln \theta}\right)_T = n + \left(\frac{\partial \ln \nu_d(\theta)}{\partial \ln \theta}\right)_T - \frac{1}{kT}\left(\frac{\partial E_d(\theta)}{\partial \ln \theta}\right)_T \quad . \tag{2}$$

Usually, it is assumed that the last two terms of the right-hand side of Eq. (2) are zero, and n is the slope of an order plot. However, recent experimental evidence has shown that both rate parameters, E_d and ν_d can vary strongly with coverage (23,34). This is also the case for hydrogen on Ir(110) as will be shown below. If the terms $\left(\frac{\partial \ln \nu_d}{\partial \ln \theta}\right)_T$ and $\left(\frac{\partial E_d}{\partial \ln \theta}\right)_T$ are large, the slope of an order plot may not be equal to n. As an example, the slope of the experimental order plot in Fig. 4 for T = 390 K is equal to 2.0 ± 0.1. The calculated slope [Eq. (2)], using the rate parameters presented below, is equal to 2.2 ± 1.5. The large error limits are due to the uncertainty in measuring the derivatives $\left(\frac{\partial \ln \nu_d}{\partial \ln \theta}\right)_T$ and $\left(\frac{\partial E_d}{\partial \ln \theta}\right)_T$. Although the experimental and calculated values of the slope of an order

plot are in excellent agreement, the terms $-\frac{1}{kT}\left(\frac{\partial E_d}{\partial \ln\theta}\right)_T$ and $\left(\frac{\partial \ln\nu_d}{\partial \ln\theta}\right)_T$ are equal to -4.6 and 4.8, respectively. It is evidently fortuitous that they cancel one another.

Since the system is pumped rapidly, the desorption rate is proportional to the intensity of the mass spectrometer (I). Thus,

$$\frac{-d\theta}{dt} = \eta I \ , \tag{3}$$

where η is a proportionality constant. The coverage at any point in a desorption spectrum is determined by integrating Eq. (3):

$$\theta^o - \theta(t) = \eta \int_o^t I dt \ . \tag{4}$$

The heating schedule may be of any form so long as the intensity and temperature are monitored independently with time. If the initial coverage (θ^o) is known, the constant η may be calculated from an integration of Eq. (4) over the whole desorption spectrum. The desorption rate and temperature may be varied for any particular coverage either by changing the initial coverage or by changing the heating rate, while keeping the initial coverage constant. Then, Arrhenius plots may be constructed of $\ln R_d$ as a function of T^{-1} at constant coverage with slope $[-E_d(\theta)/k]_\theta$ and intercept $\ln[\nu_d(\theta)\theta^n/\eta]_\theta$. If the coverage is known in absolute units, $\nu_d(\theta)$ may be calculated in units of surface diffusivity, $cm^2 - s^{-1}$.

The rate parameters E_d and ν_d were determined from an integral method using variable heating rates (35). Eleven desorption spectra of hydrogen from Ir(110) were measured by varying the nominal heating rate from 5 to 110 K/s. The initial fractional coverage was fixed at 0.82 ± 0.01 for

each measurement by exposing the surface to 100 L H_2 at 130 K. The high degree of accuracy for the relative initial coverage was obtained since background contaminants of CO and H_2O were low ($\lesssim 10^{-10}$ torr), and the poppet valve in the chamber was partially closed to reduce loading of the pumps during exposures. Arrhenius plots constructed from the data are shown in Fig. 5. Although the change in heating rate was smaller for the plots at higher coverages due to nonlinear heating at the beginning of each measurement, sufficient accuracy was available since the preexponential factor was small, as evidenced by the broad shape of the β_1 state in Fig. 2. This construction may not be valid if simultaneous desorption from multiple, distinct sites occurs at any particular coverage. The β_1 and β_2 states are separated in energy sufficiently that desorption from multiple sites at any instant will not be important except possibly near the depletion of β_1 and the beginning of desorption from β_2. It is, however, probable that if two types of three-fold sites are participating in bonding for the β_1 state (based on the clean surface structure and the coverage determination for hydrogen), the broad desorption spectrum of the β_1 state may be a composite of these sites which cannot be resolved by thermal desorption spectra. However, they may be resolved by CPD measurements (see Sect. 7).

In Fig. 6, the desorption energy and preexponential factor from the Arrhenius plots are shown as a function of surface coverage. An increase in E_d and ν_d is observed up to a fractional coverage of 0.20. It is well known that defects on the surface and edges of the crystal tend to broaden thermal desorption spectra, particularly at low coverage, and this would depress the calculated rate parameters. However, the magnitude of the

increase in E_d (5 kcal/mole) and ν_d (factor of 500) for the β_2 state is too large to be explained in this way. The rapid variation in the rate parameters between fractional coverages of 0.25 and 0.35 is associated with the completion of the β_2 state of hydrogen. At higher coverages, E_d decreases approximately linearly with coverage (10 kcal-mole^{-1}- monolayer^{-1}), and ν_d varies only weakly with coverage. A similar decrease in E_d is observed for CO on Ir(110) (23). A continuous decrease in E_d for hydrogen adsorbed on Ni (2) and Pd (5) has been reported for their respective high coverage states. The dramatic change in the behavior of the rate parameters when the β_2 state is complete and the β_1 state begins to populate is further evidence for different binding sites between β_1 and β_2 states. Furthermore, the adsorption kinetics reflect a marked change in binding sites, as seen in the next section. The maximum value for the energy of desorption, 23 kcal/mole, is close to the isosteric heats of 22 and 24 kcal/mole measured on the (110) surfaces of Ni (2) and Pd (5). These values are comparable since hydrogen adsorption is believed to be unactivated. From the peak temperature for hydrogen desorption from oxidized Pt(110), an energy of desorption of 22 kcal/mole is estimated and 24 kcal/mole is calculated from TDS for polycrystalline Ir (3). Moreover, the maximum ν_d calculated is 1.5×10^{-2} cm^2 - s^{-1} for Ir(110) compared to 2.2×10^{-2} cm^2 - s^{-1} for polycrystalline Ir (3).

The compensation effect (36) occurs for hydrogen desorption from the β_2 state on Ir(110). In other words, the desorption energy and preexponential factor vary in sympathy. This effect was reported for CO on Ir(110) (23) and CO on Ru(001) (34). In the case of Ru(001), the rate parameters pass through a maximum associated with the completion of a

$(\sqrt{3} \times \sqrt{3})R30^{o}$ structure, after which a rapid decrease in the rate parameters was observed. Although the preexponential factor was not measured for hydrogen on Ni(110), an increase in the isosteric heat was seen due to two-dimensional condensation, as evidenced by isotherm data (2). Two-dimensional condensation may occur also for hydrogen on Ir(110). Another possibility is that one-dimensional condensation occurs if hydrogen atoms form chains in the direction of the Ir atoms rows, due to the attractive interactions inferred from the rate parameters. The absence of order in the hydrogen overlayer as observed by LEED (see Sect. 3) in this coverage range may indicate that a substrate temperature of 130 K is too high to observe ordering over the coherence width of the electron beam. This is not surprising since exchange is rapid between β_1 and β_2 states at 130 K as evidenced by hydrogen and deuterium co-adsorption. Moreover, hydrogen is well known to be a weak scatterer in LEED.

6. Adsorption Kinetics

The adsorption kinetics of hydrogen on Ir(110) at 130 K have been calculated from the thermal desorption spectra in Fig. 2 making use of Eq. (4). Identical kinetics are observed for deuterium adsorption. An absolute coverage may be associated with each exposure since the saturation coverage is known, 2.2×10^{15} atoms - cm^{-2}. The surface coverage-gas exposure relations for the β_1 and β_2 states are shown in Fig. 7 where the completion of the β_2 state is indicated at a fractional coverage of 0.33. A smooth curve has been drawn through the data to aid in the presentation.

Since a sharp change in the adsorption characteristics is evident, the kinetics of hydrogen adsorption in the β_1 and β_2 states will be modeled separately.

Figure 8(a) presents the adsorption kinetics of the β_2 state of hydrogen. The fractional coverage has been normalized to the saturation value of the β_2 state. Although adsorption is dissociative, the kinetics fit a first order Langmuir model extremely well with a calculated initial sticking probability S_o equal to 1.1 ± 0.05 from a least squares fit of the data. The 10% error from unity in S_o in absolute terms is quite reasonable, considering errors in the measurement of the integrated intensities and absolute coverage. Deuterium follows the same kinetics with a calculated S_o of 1.06 ± 0.05. Since S_o is equal to one and first order Langmuir kinetics are obeyed, the adsorption of hydrogen into the β_2 state on Ir(110) is limited only by the flux of molecules to the surface that impinge on an empty site. Simple first order adsorption kinetics have been observed also on the (111) and (100) surfaces of Ni (2).

In contrast, the adsorption kinetics of the β_1 state of hydrogen, or deuterium, on Ir(110) are quite different, as shown in Fig. 8(b). Again, the fractional coverage has been normalized to the saturation value (300 L H_2) of the β_1 state. Two models for describing dissociative adsorption were used to fit the kinetic data. The Langmuir model describes the data well with $S_o = (7 \pm 0.3) \times 10^{-3}$. The model developed by Kisliuk is used for describing precursor kinetics (37). A parameter K is contained in the expression for the sticking probability as a function of coverage and is inversely proportional to the lifetime of a precursor species on the surface. The curve in Fig. 8(b) corresponds to K = 1.0 and

$S_o = 7 \times 10^{-3}$. Notice that only at high coverage are the models shown in Fig. 8(b) not identical. The value of K calculated for the β_1 state indicates that if a precursor does exist, it has a very short lifetime. Since both models fit equally well, the contribution of a precursor is not important in this case. Moreover, the preexponential factor calculated for the β_1 state as a function of coverage is nearly constant by assuming a θ^2 dependence in the rate of desorption. These data and the idea of microscopic reversibility tend to rule out precursor kinetics since the calculated preexponential factor would not be constant if a precursor is involved in desorption (32).

7. Contact Potential Difference Measurements

If a clean, well ordered Ir(110) surface is exposed to hydrogen, the CPD ($\Delta\phi$) increases initially to a maximum value of 0.30 eV near the completion of the β_2 desorption state, as shown in Fig. 9(a). Upon further exposure to hydrogen the CPD decreases over the β_1 desorption state and nearly reaches the clean surface value of the contact potential at 250 L, as shown in Fig. 9(b). For hydrogen exposures greater than 250 L, at 140 K, the contact potential continuously drops below the clean surface value until the adsorption of hydrogen becomes reversible. A similar shape of the CPD as a function of hydrogen exposure was observed on Ni(100) (19) and Ni(111) (17) at low temperature and to a lesser extent on Pt(111) (8) and stepped Pt(111) (12), although the magnitude of the decrease on the two platinum surfaces is comparable to the observed decrease in Fig. 9(b) for Ir(110). An increase in the CPD was also observed on Ir

field emission tips (13,14), but no subsequent decrease was seen.

The maximum CPD obtained in Fig. 9(a) depended sensitively on both the cleanliness and the order on the surface. The presence of small amounts of CO markedly depressed the maximum CPD observed for hydrogen due to preferential blocking of β_2 sites (38). Further, for substrate temperatures above 300 K, the CPD decreases in Fig. 9(a) due to slow desorption of hydrogen from β_2 sites. However, if a background pressure of hydrogen is maintained to ensure sufficient hydrogen is present to fill β_2 sites, the CPD still reaches a maximum somewhat less than 0.30 eV. The maximum CPD decreases to 0.26 eV near 380 K, even at pressures of 10^{-5} torr of hydrogen. It is likely that this is due to a change in the equilibrium distribution of adsorbed hydrogen between β_1 and β_2 sites as the substrate temperature increases.

In order to examine more closely the adsorption properties of hydrogen on Ir(110), the CPD measurements were related to the fractional coverage (via the adsorption kinetics) at points of constant exposure, as shown in Fig. 10. A linear relation is observed between $\Delta\phi$ and θ for three coverage ranges: (1) 0 - 0.20, (2) 0.35 - 0.60 and (3) $\geq$ 0.85. Region (1) corresponds to adsorption of hydrogen on β_2 sites, and regions (2) and (3) correspond to adsorption on β_1 sites. Between fractional coverages of 0.20 and 0.35, the CPD becomes nonlinear in its increase in coverage, reaches a maximum near θ = 0.33, and begins to decrease at higher coverages. From both the adsorption kinetics and the desorption kinetics, it is apparent that this is due to the completion of the β_2 state and the simultaneous population of the β_1 state. However, it should be noted that the nonlinear behavior cannot be attributed solely to the superposition of sites being occupied that increase (β_2) and decrease (β_1)

the contact potential since this disagrees with other data presented earlier. The CPD and coverage are related simply in the three linear regions by

$$\Delta\phi = 4\pi C_s \mu_o \theta \ , \qquad (5)$$

where μ_o is the surface dipole for the Ir-H system. The calculated values of μ_o are +0.14, -0.016 and -0.22 Debye (1 Debye $\equiv 10^{-18}$ esu-cm) for coverage regions (1), (2) and (3), respectively, where a positive dipole points away from the surface. On Ni(100) $\mu_o \sim +0.05$ Debye for low hydrogen coverage (19), and this appears to be the general order of magnitude for hydrogen on the platinum metals.

Since the CPD increases when β_2 adsorption sites are populated, either metal atoms donate electrons to H atoms if adsorption is above the surface plane (A in Fig. 1), or H atoms donate electrons to metal atoms if adsorption occurs below the surface plane (B in Fig. 1). The open surface structure of reconstructed Ir(110) and the covalent nature of the H-Ir bond makes either situation plausible à priori. However, the UPS results presented in the next section imply that the location associated with hydrogen in the β_2 state is, in fact, the site B in Fig. 1. For β_1 sites, the CPD decreases continuously, indicating that these are truly different from β_1 sites, as suggested by the absolute coverage measurements, the desorption kinetics and the adsorption kinetics.

The fact that two different slopes ($\frac{d\Delta\phi}{d\theta}$) exist in the coverage range where β_1 sites are filled, as well as the broad desorption behavior, may support further the postulate of two inequivalent sites participating in adsorption for β_1 (C and D in Fig. 1). Assuming that two sites are occupied and that the change in slope of Fig. 10 represents the completion of one site and the population of the second site allows the calculation of the difference in the energy of adsorption between the two sites, the energy difference calculated is between 0.5 and 1.0 kcal/mole, which is quite reasonable for slightly different adsorption sites. For an equal population of these two sites, approximately 20% more hydrogen must be adsorbed at saturation, as evidenced by Fig. 10 and Sect. 4. If Fig. 10 is extrapolated to θ = 1.20, a saturation CPD of -0.50 eV would result, with respect to the clean surface. For a background pressure of hydrogen of 2×10^{-6} torr and a substrate temperature of 140 K, the equilibrium CPD is -0.20 eV. Therefore, to saturate the surface completely, lower substrate temperatures are needed since the saturation coverage used here has a CPD of -0.14 eV.

To summarize the CPD results for hydrogen on Ir(110), at least two types of sites may participate in hydrogen adsorption in the low temperature β_1 desorption feature which are different from the preferred sites that are occupied by the hydrogen that desorbs from the high temperature β_2 sites. The two different β_1 sites are energetically different by approximately 0.5 to 1.0 kcal/mole for adsorption of hydrogen. These data correlate well with the data presented in previous sections, demonstrating the difference in the properties of these sites for hydrogen on Ir(110).

8. Ultraviolet Photoelectron Spectra

If hydrogen is exposed to the Ir(110) surface in order to fill the β_2 state, the HeI UP spectrum shows a strong change in the d-band near the Fermi level (E_F) as seen in curve (b) compared to curve (a) (clean surface) in Fig. 11. The difference spectrum (c) in Fig. 11 exhibits a large attenuation (19%) in the d-band peak centered at 1.6 eV below E_F on the clean surface, a small enhancement at 3.6 eV and the growth of a feature near 6.1 eV. This attenuation is continuous, but nonlinear, with coverage as shown for two smaller coverages of hydrogen in the β_2 state, curves (d) and (e) in Fig. 11. Somewhat similar changes in the d-band emission have been observed on Pt(111) (21) and Pd(111) (20,21), in contrast, however, to results for hydrogen on Ni(111) (20,21).

However, the attenuation observed here for hydrogen in the β_2 state on Ir(110) is quite large compared to Pt and Pd. This attenuation is probably not due to the destruction of a surface state of the reconstructed clean surface since CO adsorption on Ir(110) only causes a weaker, uniform decrease in the same region of the d-band (38). Further, the change in shape is not likely to be the formation of a surface state when hydrogen is adsorbed in the β_2 state since small amounts of CO co-adsorbed with hydrogen displace H atoms from β_2 sites to β_1 sites (via TDS), and the HeI UPS reflect only a continuous decrease in β_2 population (38). This marked attenuation may be a result of interference between the wave-functions of the metal d-electrons and the hydrogen electron as suggested in a theoretical prediction of photoemission spectra of hydrogen on transition metals (39). It was predicted also in the theory (39) that,

for a strong attenuation, the H atom may be below the surface plane of the metal. Therefore, the UPS data for hydrogen on Ir(110) in the β_2 state imply that site B in Fig. 1, in the missing row trough, would be more likely than site A, on top of the existing rows. From the CPD measurements presented in the last section, site B would represent a net electron transfer from H atoms to the metal since the CPD increases over the β_2 state. Also, the data presented in previous sections suggest that the β_1 state corresponds to a net electron transfer to the metal if three-fold sites are populated, C and D in Fig. 1.

For an equal coverage of hydrogen in the β_1 state, the additional change in the region near E_F is much less as seen by comparing HeI difference spectra for saturated β_2 and equal coverages of β_1 and β_2 in curves (a) and (b) in Fig. 12, respectively. A comparison of curves (a) and (b) further shows the increase in the intensity of the H(1s) induced level at 6.1 eV below E_F. To accentuate this broad feature, (a) and (b) were subtracted from one another, and this is shown in curve (c) of Fig. 12. The full-width at half-maximum of the H(1s) level in (c) is approximately 2.3 eV, larger than observed for Pt(111) (21) and Pd(111) (20,21).

9. Summary

The chemisorption of hydrogen on Ir(110) has been studied under ultra-high vacuum conditions with thermal desorption mass spectrometry, LEED, contact potential difference measurements and ultraviolet photoelectron spectroscopy. The results of the present study were compared with other work performed previously on the platinum metals.

Although no ordered structures were observed with LEED to correlate exposures with absolute coverages for hydrogen, absolute coverages were determined by two methods using thermal desorption mass spectrometry. The maximum coverage of hydrogen on Ir(110) at 130 K is $2.2 \pm 0.2 \times 10^{15}$ atoms - cm^{-2}. Two states, β_1 and β_2, of hydrogen desorb with relative intensities of 2:1 and exhibit marked differences in their adsorption and desorption kinetics. The rate parameters for hydrogen desorption were measured as a function of surface coverage of hydrogen. Hydrogen in the β_2 state shows a sympathetic <u>increase</u> in the rate parameters up to at least half of its saturation coverage where E_d and ν_d assume values of 23 kcal/mole and 1.5×10^{-2} cm^2 - s^{-1}, respectively. This increase may be due to a strong H-H interaction. The energy for hydrogen desorption from the β_1 state decreases linearly with increasing surface coverage and obeys the relation $E_d = 17 - 10\theta$ for total fractional coverages between 0.4 and 0.7. The preexponential factor for desorption varies only weakly with coverage for β_1 and is approximately equal to $2 \div 2 \times 10^{-7}$ cm^2 - s^{-1}.

Both states are adsorbed dissociatively, and isotopic exchange occurs between them. Desorption for all surface coverages was modeled best as second order.

The adsorption kinetics of the β_2 state of hydrogen follows a first order Langmuir model with an initial sticking probability of <u>unity</u>. The initial sticking probability of the β_1 state of hydrogen is 7×10^{-3} and obeys second order Langmuir kinetics. The adsorption kinetics of both states are independent of substrate temperature up to desorption. Contact potential differences were measured as a function of hydrogen ex-

posure at 140 K and were related to the fractional coverage by the adsorption kinetics. For the β_2 state, the CPD increases to a maximum of 0.30 eV for $T \leq 300$ K and is linear with respect to coverage up to 0.20 eV. The CPD decreases continuously over the β_1 state and reaches values that are below the clean surface contact potential near the saturation coverage that is attainable at 140 K. Two linear regions were observed with very different slopes $(\frac{d\Delta\phi}{d\theta})$ for the β_1 state of hydrogen. This implies that more than one type of site is participating in this coverage region.

Probable sites for hydrogen adsorption on Ir(110) were postulated from the absolute coverage determination and the CPD measurements. Bonding either above the top rows of Ir atoms or between the rows of Ir atoms in the locations of the missing Ir rows are preferred for the β_2 state of hydrogen with trough sites between the rows more likely from the UPS results. The β_1 state of hydrogen may bind to two types of three-fold sites or to two types of two-fold sites exposed on the reconstructed surface [(111) microfacets on the terraces], with the former being preferred in analogy to results obtained on Ni.

The HeI UPS data show a marked change in the d-band emission near E_F for the β_2 state of hydrogen. A large attenuation and change in shape occurs which is continuous, but nonlinear, with fractional coverage. These phenomena may be due to destructive interference between metal d-electrons and the hydrogen electron. Furthermore, they suggest that β_2 hydrogen adsorbs below the surface plane of the metal. As the surface is increasingly covered with hydrogen, the H(1s) induced level grows in, centered at 6.1 eV below E_F, with a concomitant decrease in the emission near E_F. In the case of β_1 hydrogen, this effect is much less pronounced than in the case of β_2 hydrogen.

Acknowledgment

The authors are grateful for the financial support of the National Science Foundation under Grant Number DMR77-14976.

References

1. T. N. Taylor and P. J. Estrup, J. Vacuum Sci. Technol. 11, 244 (1974).
2. K. Christmann, O. Schober, G. Ertl and M. Neumann, J. Chem. Phys. 60, 4528 (1974).
3. V. J. Mimeault and R. S. Hansen, J. Chem. Phys. 45, 2240 (1966).
4. J. T. Yates, Jr., P. A. Thiel and W. H. Weinberg, Surface Sci. 84, 427 (1979).
5. H. Conrad, G. Ertl and E. E. Latta, Surface Sci. 41 235 (1974).
6. T. Engel and H. Küppers, Surface Sci. (to be published).
7. K. E. Lu and R. R. Rye, Surface Sci. 45, 677 (1974).
8. K. Christmann, G. Ertl and T. Pignet, Surface Sci. 54, 365 (1976).
9. R. W. McCabe and L. D. Schmidt, Surface Sci. 60, 85 (1976).
10. C. R. Helms, H. P. Bonzel and S. Kelemen, J. Chem. Phys. 65, 1773 (1976).
11. R. W. McCabe and L. D. Schmidt, Surface Sci, 65, 189 (1977).
12. K. Christmann and G. Ertl, Surface Sci. 60, 365 (1976).
13. J. R. Arthur and R. S. Hansen, J. Chem. Phys. 36, 2062 (1962).
14. H. F. Kempin, K. Klapper and G. Ertl, Nouveau J. Chim (Paris) 1, 295 (1977).
15. J. C. Bertolini and G. Dalmai-Imelik, Colloqu. Intern. CNRS, Paris 1969, p. 135.
16. J. Behm, K. Christmann and G. Ertl, Solid State Commun. 25, 763 (1978).
17. M. A. Van Hove, G. Ertl, K. Christmann, J. Behm and W. H. Weinberg, Solid State Commun. 28, 373 (1978); K. Christmann, J. Behm, G. Ertl, M.A. Van Hove and W. H. Weinberg, J. Chem. Phys. 70, 4168 (1979).

References (continued)

18. K. H. Reider and T. Engel, Phys. Rev. Letters 43, 373 (1979).

19. K. Christmann, Z. Naturforsch. 34a, 22 (1979).

20. H. Conrad, G. Ertl, J. Küppers and E. E. Latta, Surface Sci. 58, 578 (1976).

21. J. E. Demuth, Surface Sci. 65, 369 (1977).

22. J. L. Taylor, Ph.D. Thesis, California Institute of Technology, 1978.

23. J. L. Taylor, D. E. Ibbotson and W. H. Weinberg, J. Chem. Phys. 69, 4298 (1978).

24. K. Christmann and G. Ertl, Z. Naturforsch. 28a, 1144 (1973).

25. C. M. Comrie and R. M. Lambert, J. Chem. Soc. Faraday Trans. I. 72, 1659 (1976).

26. C. M. Chan, M. A. Van Hove, W. H. Weinberg and E. D. Williams, Solid State Commun. 30, 47 (1979); Surface Sci. 90, 000 (1979).

27. J. L. Taylor, D. E. Ibbotson and W. H. Weinberg, Surface Sci. 79, 349 (1979).

28. D. E. Ibbotson, Ph. D. Thesis, California Institute of Technology, 1981.

29. H. Conrad, G. Ertl and E. E. Latta, J. Catal. 35, 363 (1974).

30. B. E. Nieuwenhuys and G. A. Somorjai, Surface Sci. 72, 8 (1978).

31. B. E. Nieuwenhuys, D. I. Hagen, G. Rovida and G. A. Somorjai, Surface Sci. 59, 155 (1976).

32. R. Gorte and L. D. Schmidt, Surface Sci. 76, 559 (1978).

33. T. S. Wittrig, D. E. Ibbotson and W. H. Weinberg, Appl. Surface Sci. 4, 234 (1980).

34. H. Pfnür, P. Feulner, H. A. Engelhardt and D. Menzel, Chem. Phys. Letters 59, 481 (1978).

35. J. L. Taylor and W. H. Weinberg, Surface Sci. 78, 259 (1978).

36. G. C. Bond, Catalysis by Metals, Academic Press, New York, 1962.

References (continued)

37. P. Kisliuk, J. Phys. Chem. Solids 5, 78 (1958).

38. D. E. Ibbotson, T. S. Wittrig and W. H. Weinberg, Surface Sci. 97, 297(1980).

39. G. Doyen and G. Ertl, J. Chem. Phys. 68, 5417(1978).

Figure Captions

Fig. 1: Probable locations of hydrogen on Ir(110)-(1 x 2). A and B represent two possible locations for the β_2 state of hydrogen. C and D denote the preferred binding sites for the β_1 state of hydrogen, which are inequivalent three-fold sites.

Fig. 2: Thermal desorption spectra of hydrogen from Ir(110) as a function of gas exposure. The adsorption temperature is 130 K, and the heating rate is 21 K/s. The ratio of the β_1 and β_2 states is 2:1 at saturation coverage.

Fig. 3: Representative thermal desorption spectra of H_2, HD and D_2 from a co-adsorbed layer of hydrogen and deuterium. In this experiment, 0.45 L D_2 was exposed first, which approximately fills the β_2 state, and then, subsequently, 5.0 L H_2 was exposed.

Fig. 4: Order plots for hydrogen desorption from Ir(110) using the data in Fig. 2.

Fig. 5: Arrhenius plots obtained for hydrogen desorption by keeping the initial coverage constant and varying the heating rate (see text).

Fig. 6: Activation energy (E_d) and preexponential factor (ν_d) for hydrogen desorption from Ir(110) as a function of fractional surface coverage.

Fig. 7: The coverage-exposure relation for hydrogen on Ir(110). The β_2 state saturates after a 0.35 L exposure as noted in the figure. A smooth curve has been drawn through the data to facilitate the presentation.

Fig. 8: Analytic fits to the adsorption kinetics derived from the data in Fig. 2. (a) First order Langmuir fit to the β_2 state with S_o calculated to be 1.1. The coverage is normalized to saturation of the β_2 state. (b) Second order fits to the β_1 state: —— Langmuir with $S_o = 7 \times 10^{-3}$; --- Kisliuk with K = 1.0 and $S_o = 7 \times 10^{-3}$. The coverage is normalized to saturation of the β_1 state.

Fig. 9: The CPD of hydrogen on Ir(110) as a function of exposure at 140K. (a) Hydrogen adsorption on β_2 sites. (b) Hydrogen adsorption on β_1 sites.

Fig. 10: The CPD of hydrogen on Ir(110) as a function of fractional coverage at 140K. The data were calculated from Figs. 7 and 9.

Fig. 11: Hydrogen adsorbed into the β_2 state on Ir(110). HeI UP spectra are shown for the clean surface in (a) and for $\theta_H = 0.33$ in (b). Included are difference spectra for various fractional coverages of β_2 hydrogen: (c) 1.0, (d) 0.6 and (e) 0.4.

Fig. 12: HeI UP difference spectra for (a) β_2 hydrogen, (b) equal coverages of β_1 and β_2 hydrogen, and (c) β_1 hydrogen only.

PROBABLE LOCATIONS OF HYDROGEN ON IR (110)-(1×2)

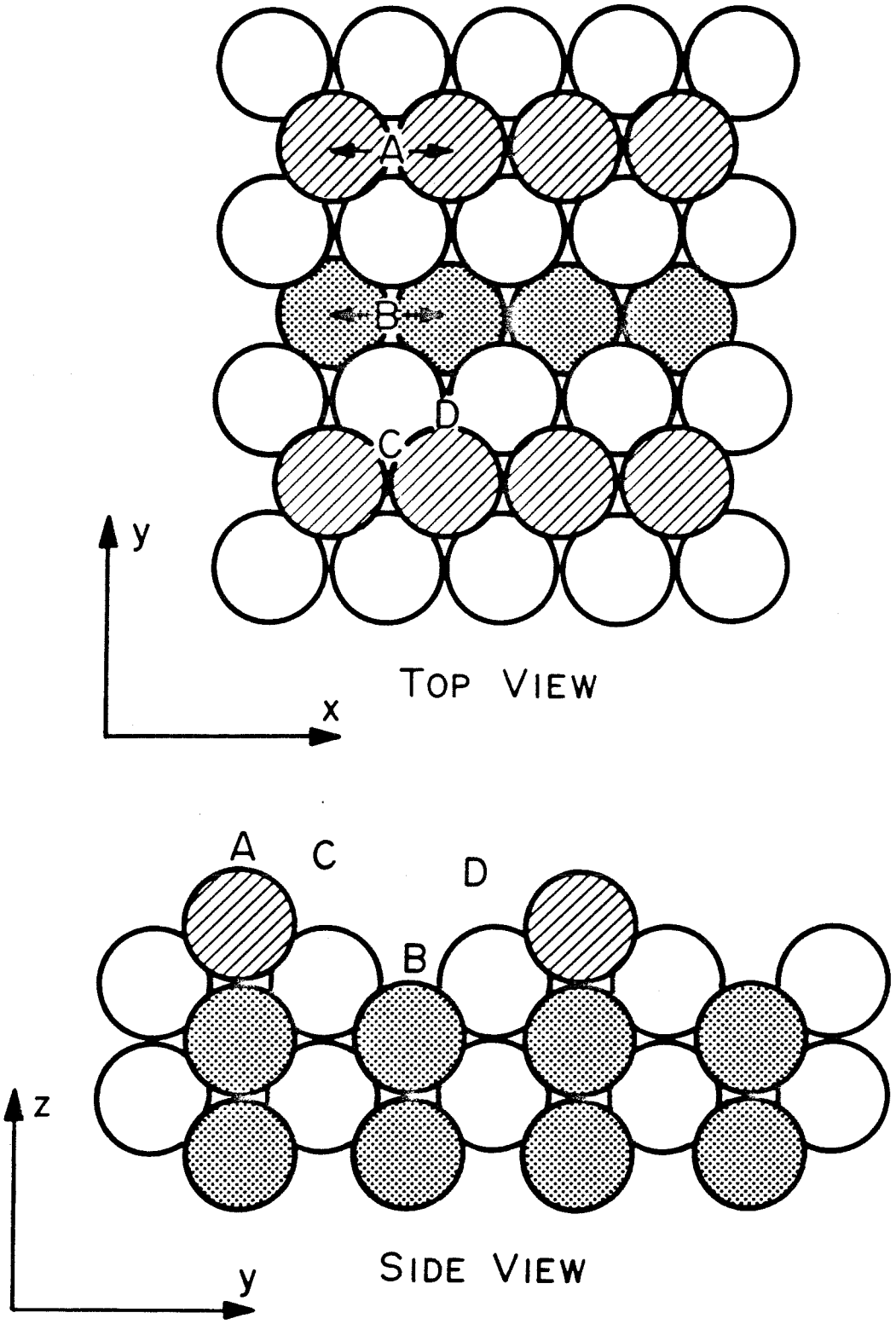

Fig. 1

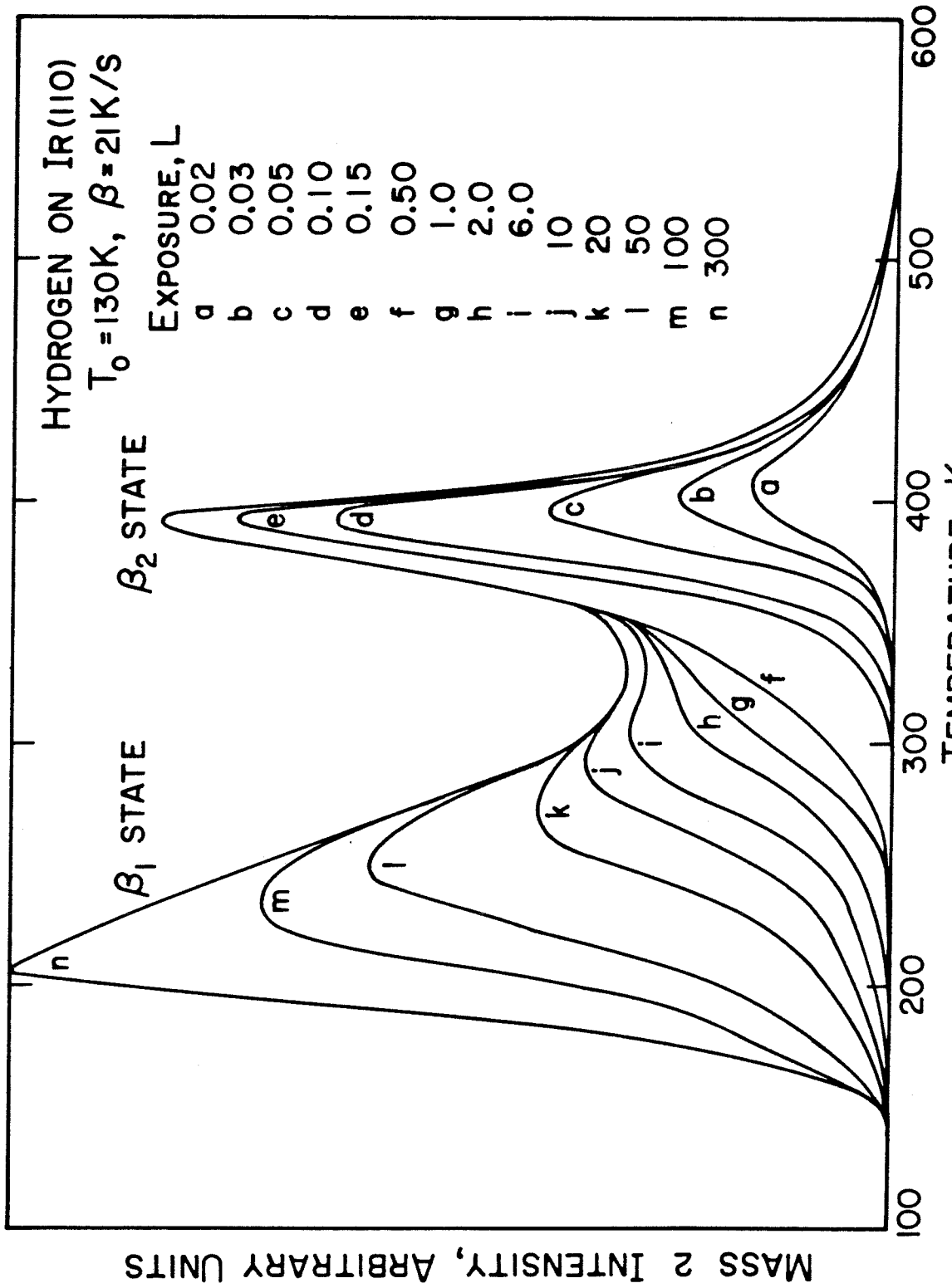
HYDROGEN ON IR(110)
T_0=130K, β=21K/S
EXPOSURE, L
a 0.02
b 0.03
c 0.05
d 0.10
e 0.15
f 0.50
g 1.0
h 2.0
i 6.0
j 10
k 20
l 50
m 100
n 300
β_1 STATE
β_2 STATE
MASS 2 INTENSITY, ARBITRARY UNITS
TEMPERATURE, K
100
200
300
400
500
600

Fig. 2

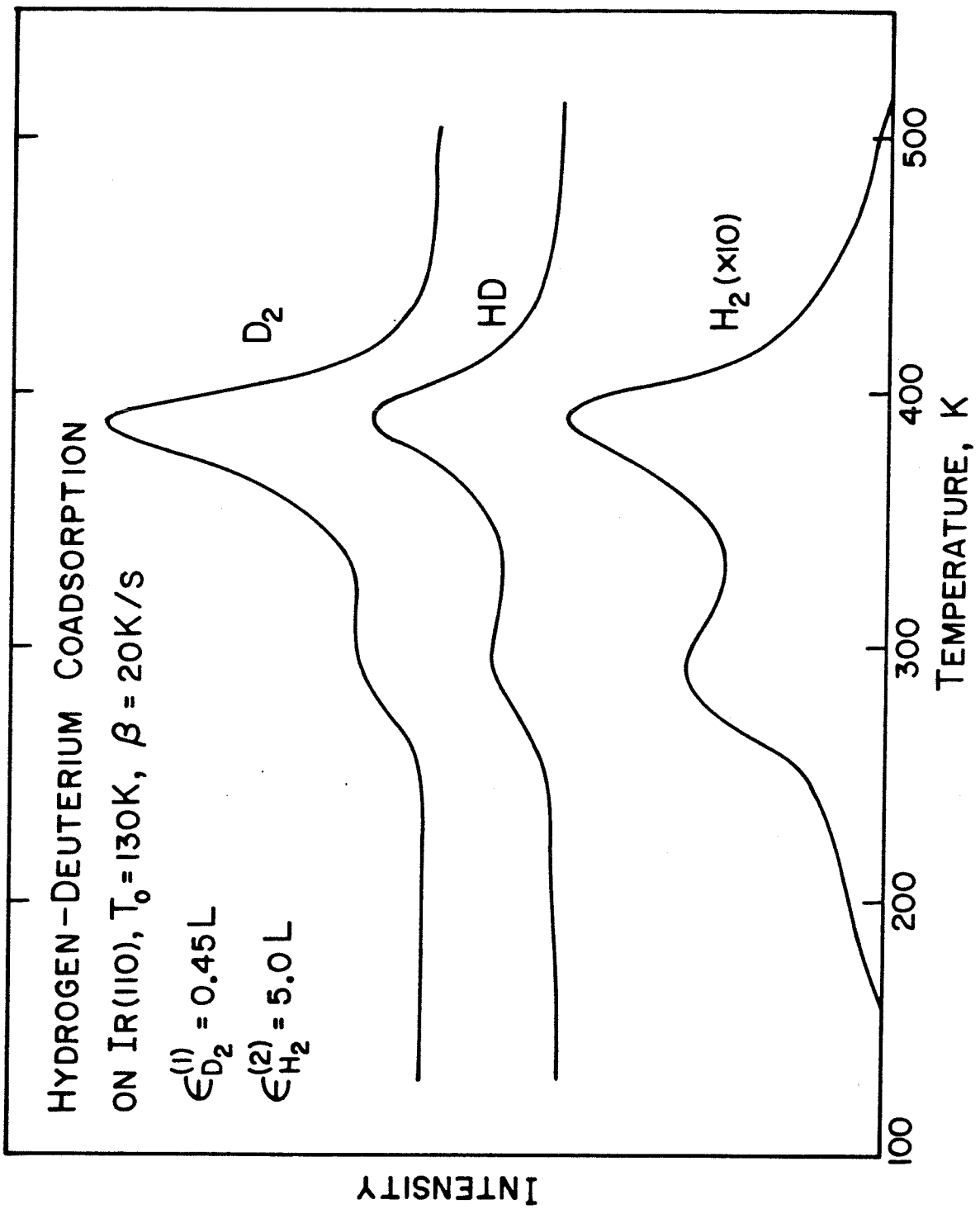
HYDROGEN-DEUTERIUM COADSORPTION
ON IR(110), T_o = 130K, β = 20K/S
$\epsilon^{(1)}_{D_2}$ = 0.45 L
$\epsilon^{(2)}_{H_2}$ = 5.0 L
D_2
HD
H_2 (x10)
INTENSITY
100
200
300
400
500
TEMPERATURE, K

Fig. 3

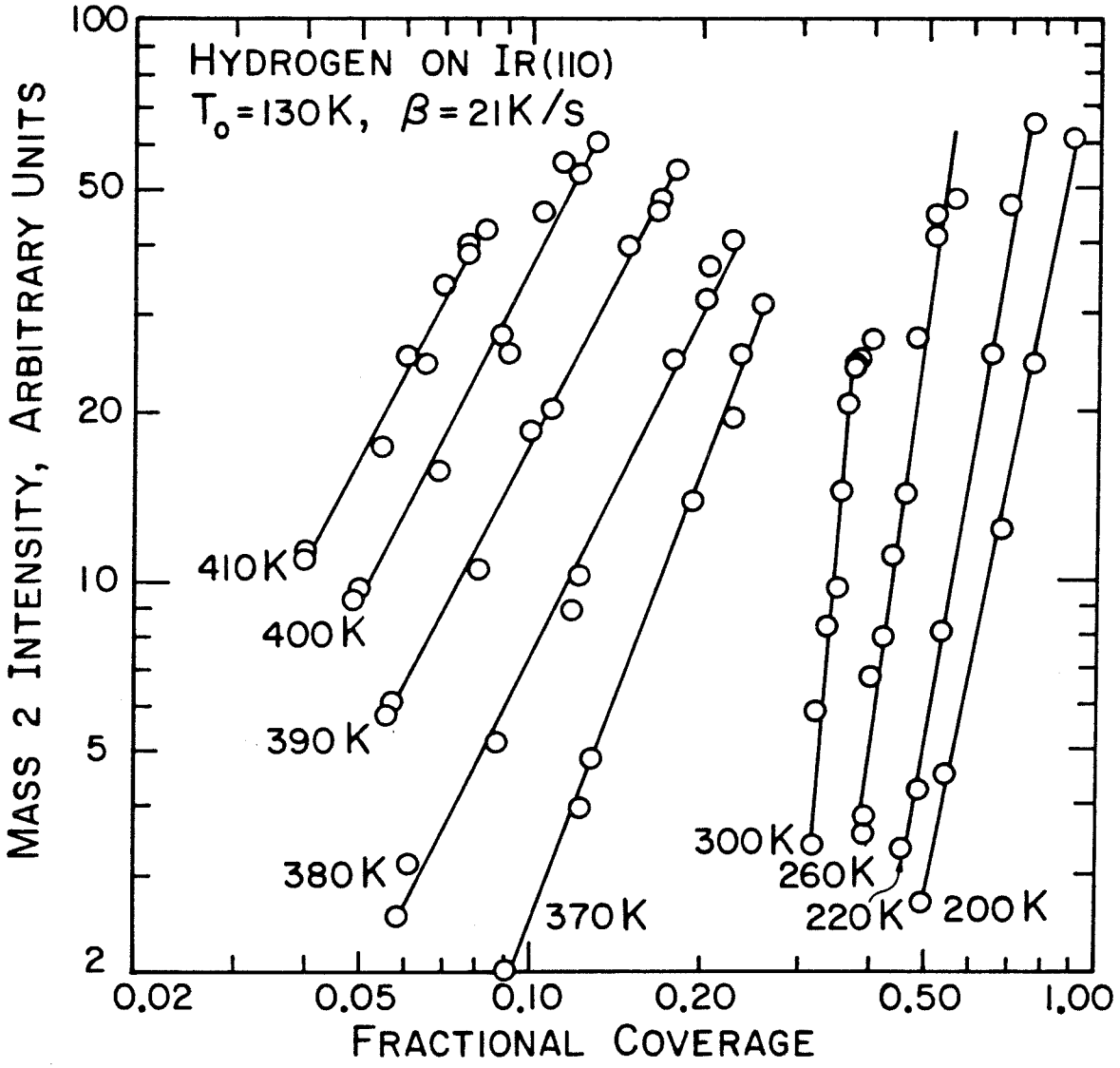
HYDROGEN ON IR(110)
T_o=130K, β=21K/S
MASS 2 INTENSITY, ARBITRARY UNITS
FRACTIONAL COVERAGE
100
50
20
10
5
2
0.02
0.05
0.10
0.20
0.50
1.00
410K
400K
390K
380K
370K
300K
260K
220K
200K

Fig. 4

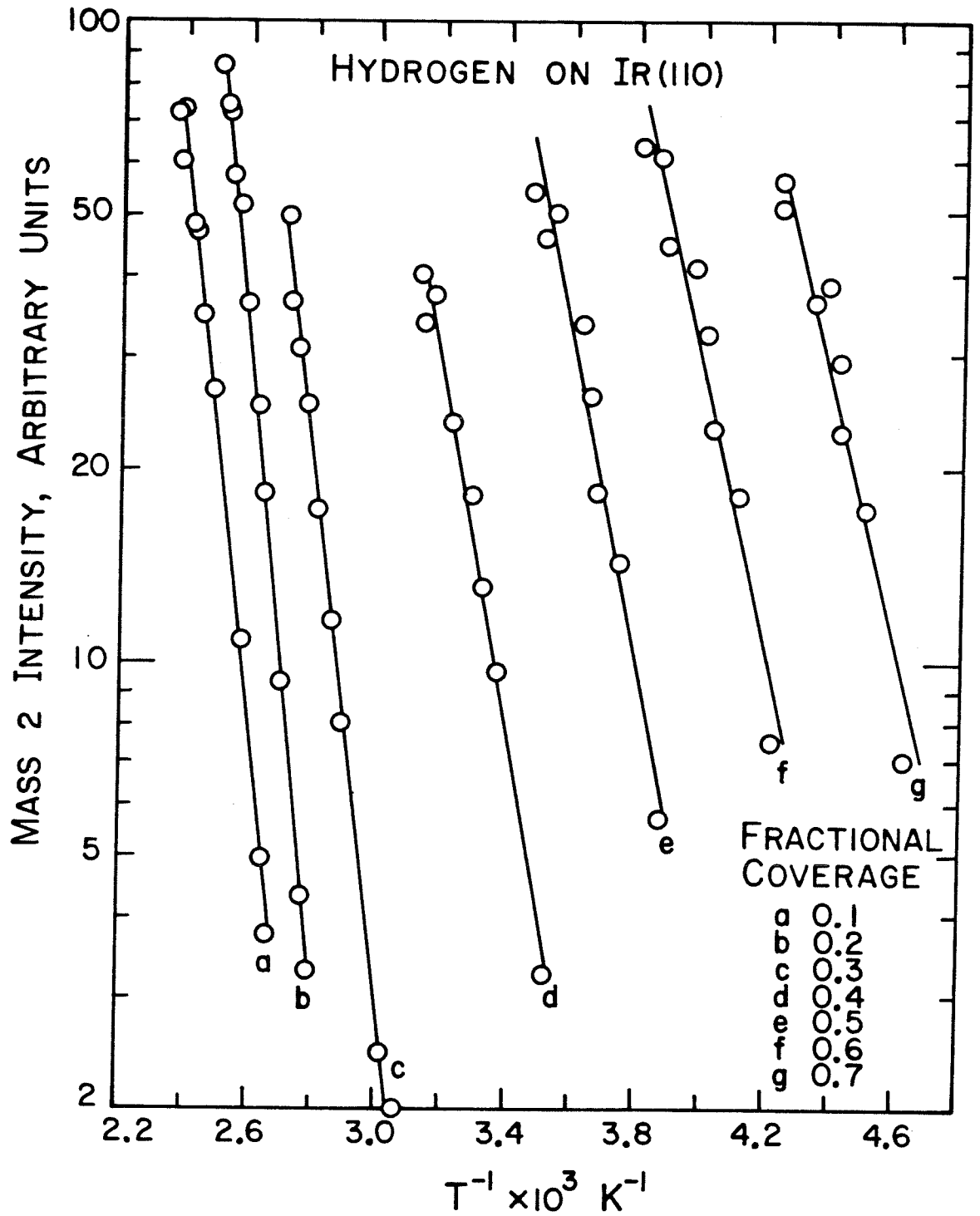
HYDROGEN ON IR(110)
MASS 2 INTENSITY, ARBITRARY UNITS
100
50
20
10
5
2
2.2
2.6
3.0
3.4
3.8
4.2
4.6
T⁻¹ ×10³ K⁻¹
a
b
c
d
e
f
g
FRACTIONAL COVERAGE
a 0.1
b 0.2
c 0.3
d 0.4
e 0.5
f 0.6
g 0.7

Fig. 5

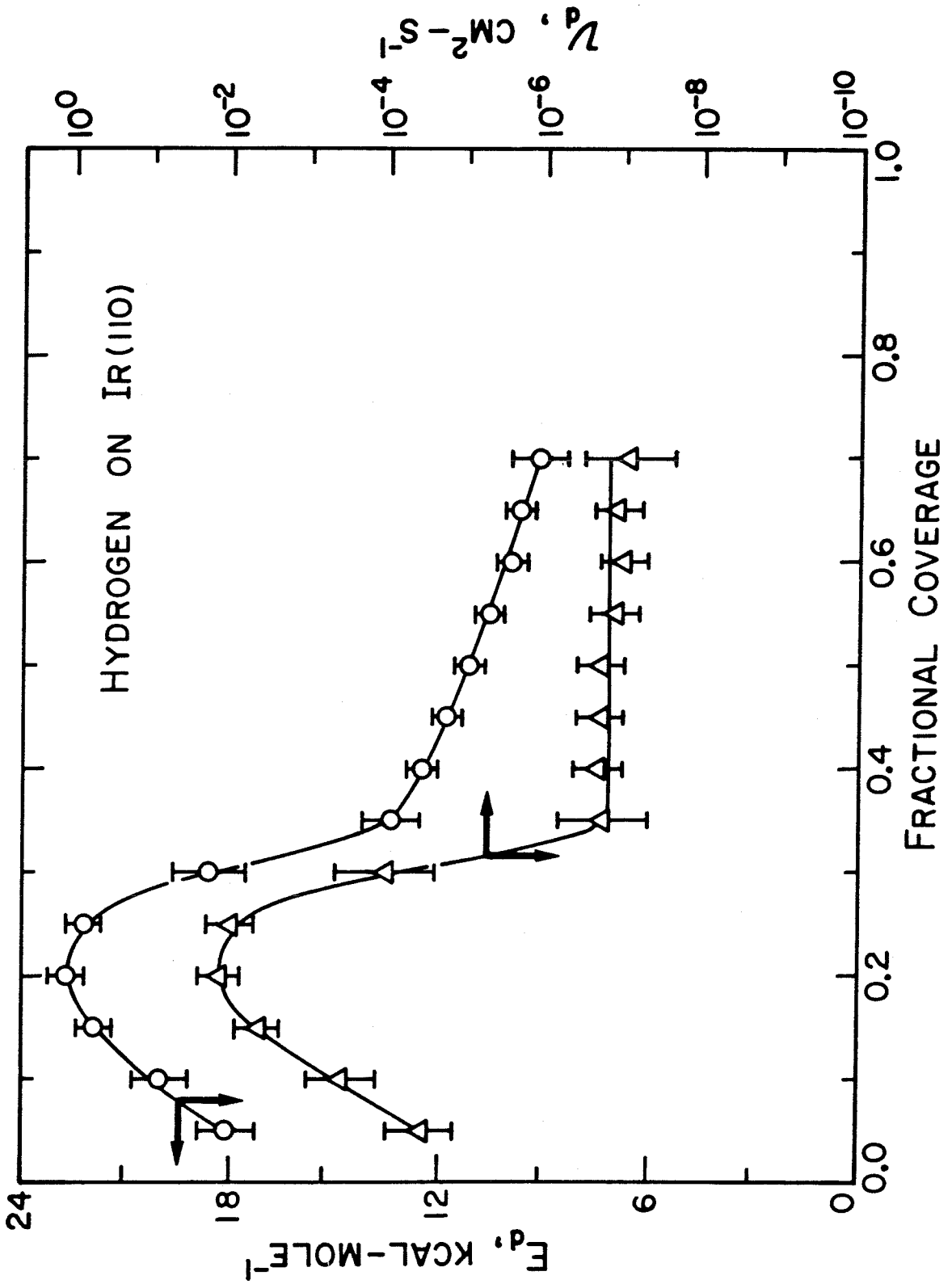
HYDROGEN ON IR(110)
E_d, KCAL-MOLE^{-1}
ν_d, CM^2-S^{-1}
FRACTIONAL COVERAGE
0
6
12
18
24
10^0
10^{-2}
10^{-4}
10^{-6}
10^{-8}
10^{-10}
0.0
0.2
0.4
0.6
0.8
1.0

Fig. 6

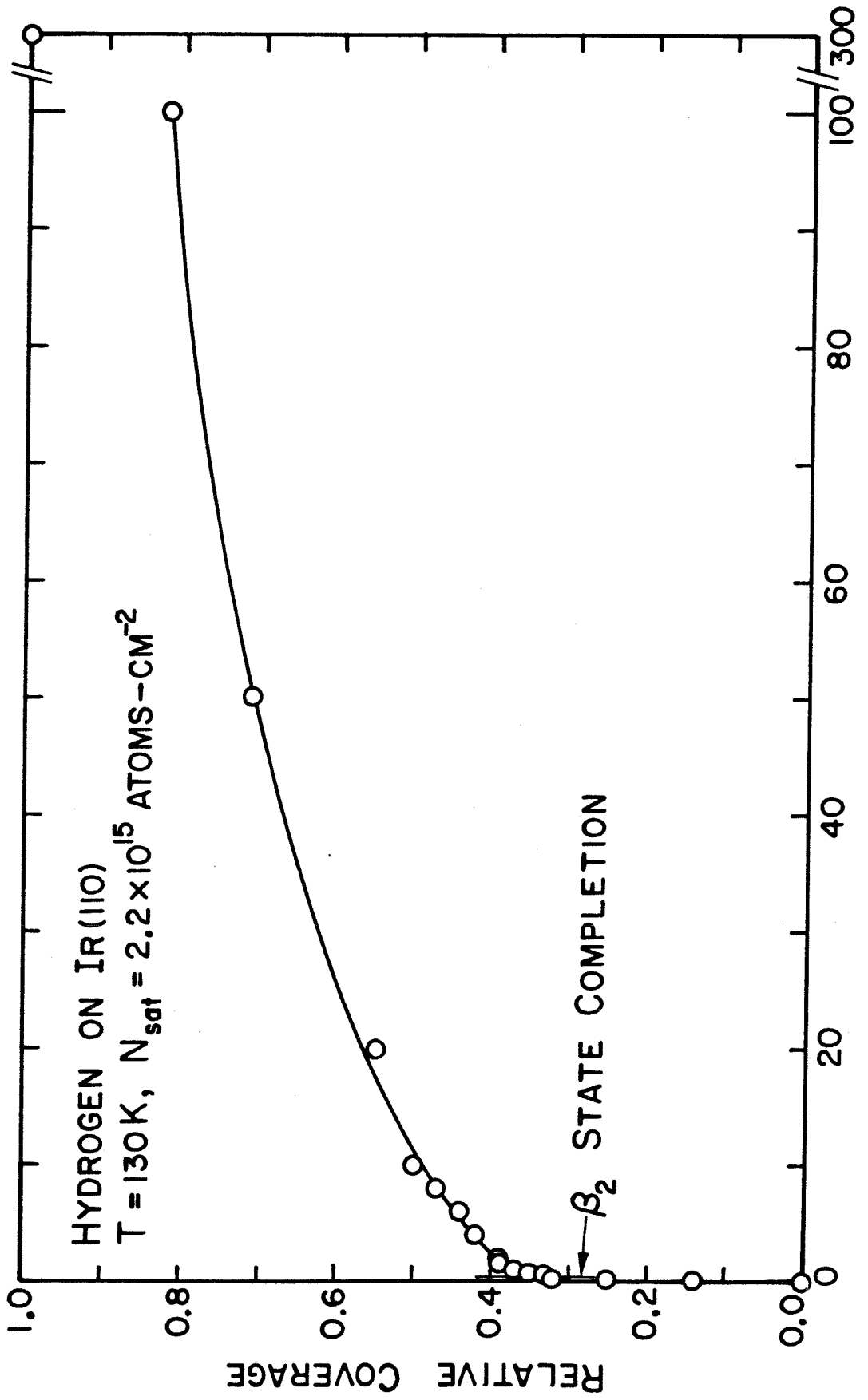
HYDROGEN ON IR(110)
T = 130K, $N_{sat} = 2.2 \times 10^{15}$ ATOMS-CM^{-2}
β_2 STATE COMPLETION
RELATIVE COVERAGE
EXPOSURE, L
0.0
0.2
0.4
0.6
0.8
1.0
0
20
40
60
80
100
300

Fig. 7

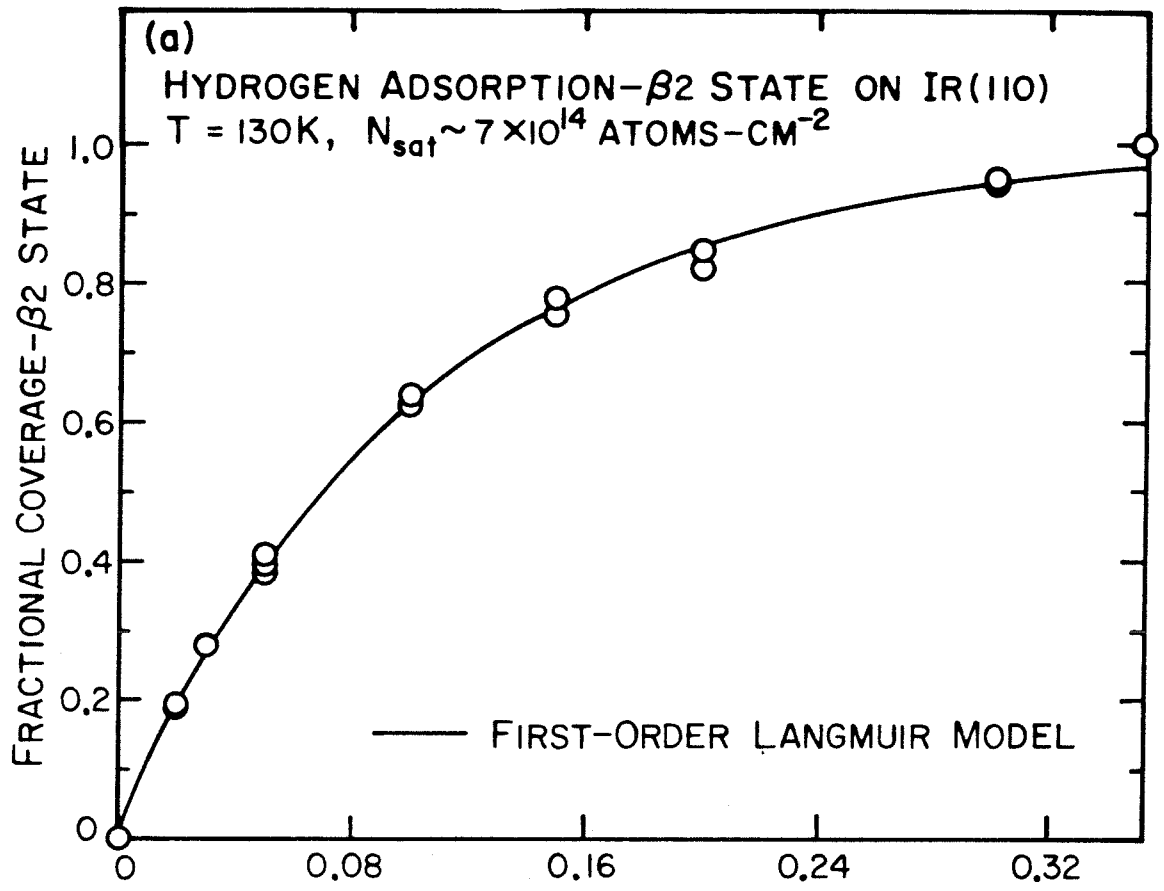
(a)
HYDROGEN ADSORPTION-β2 STATE ON IR(110)
T = 130K, N_sat ~ 7×10^14 ATOMS-CM^-2
FRACTIONAL COVERAGE-β2 STATE
1.0
0.8
0.6
0.4
0.2
0
0
0.08
0.16
0.24
0.32
FIRST-ORDER LANGMUIR MODEL

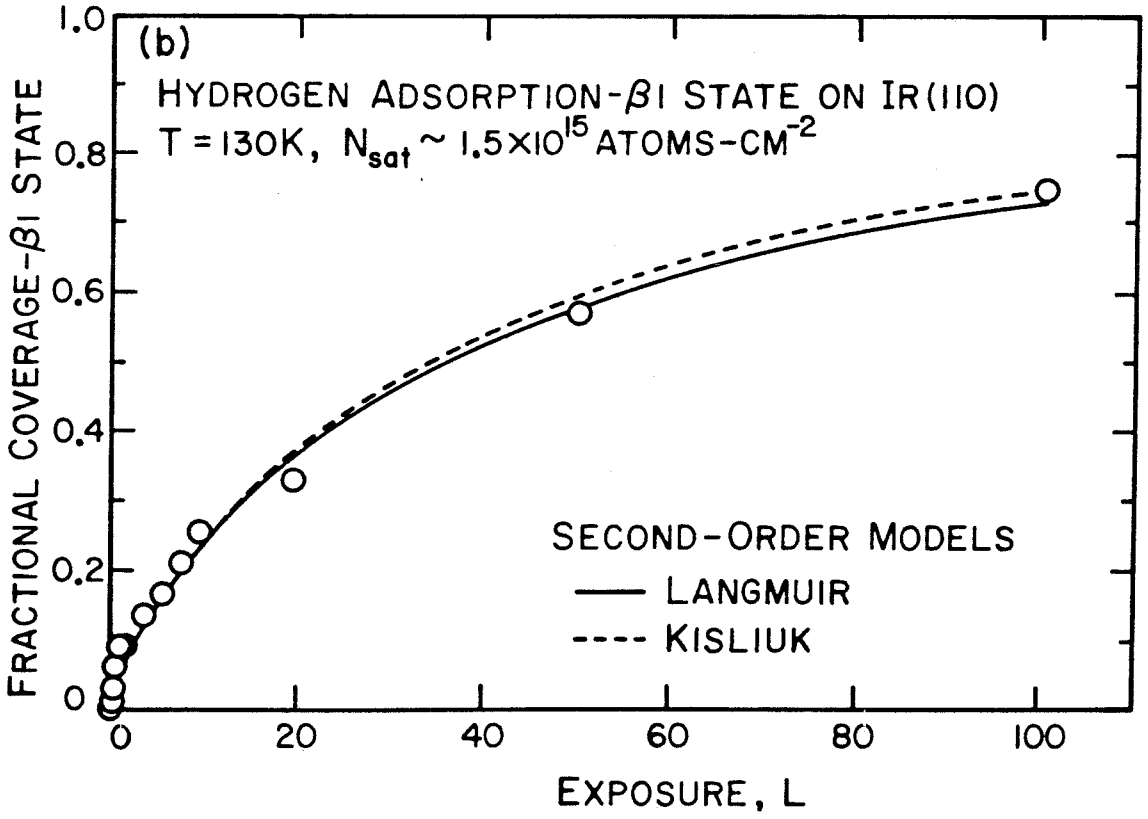
(b)
HYDROGEN ADSORPTION-β1 STATE ON IR(110)
T = 130K, N_sat ~ 1.5×10^15 ATOMS-CM^-2
FRACTIONAL COVERAGE-β1 STATE
1.0
0.8
0.6
0.4
0.2
0
0
20
40
60
80
100
EXPOSURE, L
SECOND-ORDER MODELS
LANGMUIR
KISLIUK

Fig. 8

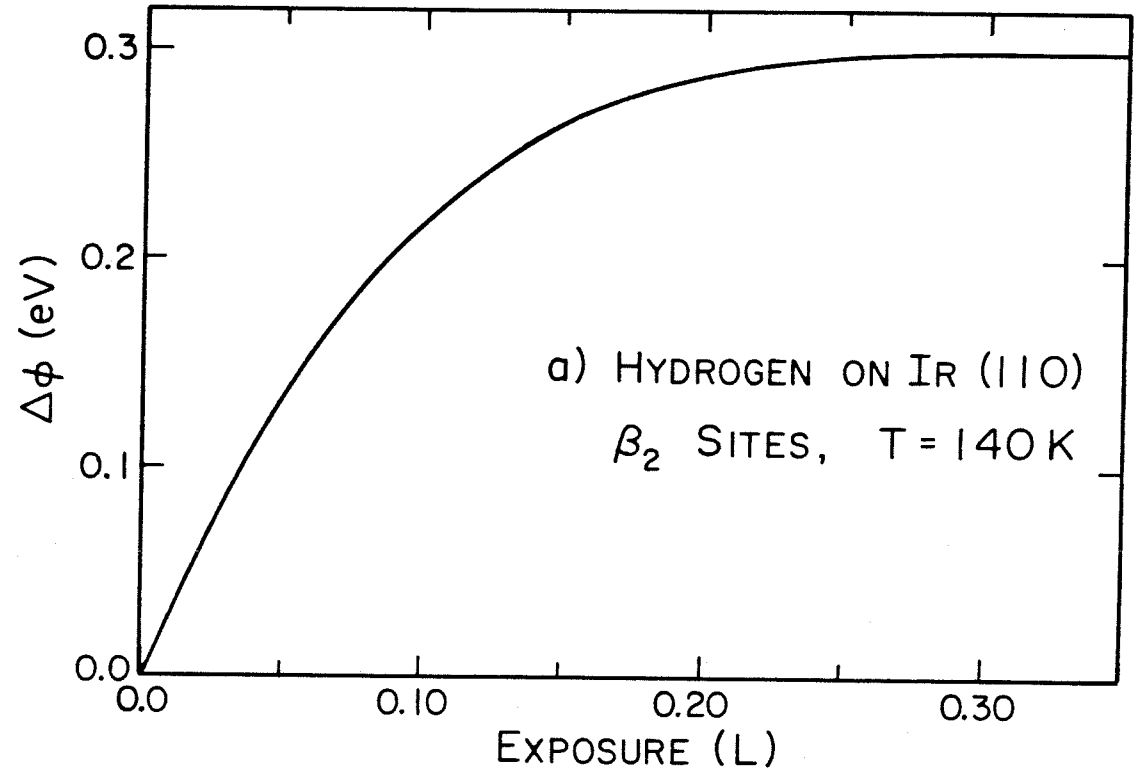
0.3
0.2
0.1
0.0
Δφ (eV)
a) HYDROGEN ON IR (110)
β_2 SITES, T = 140 K
0.0
0.10
0.20
0.30
EXPOSURE (L)

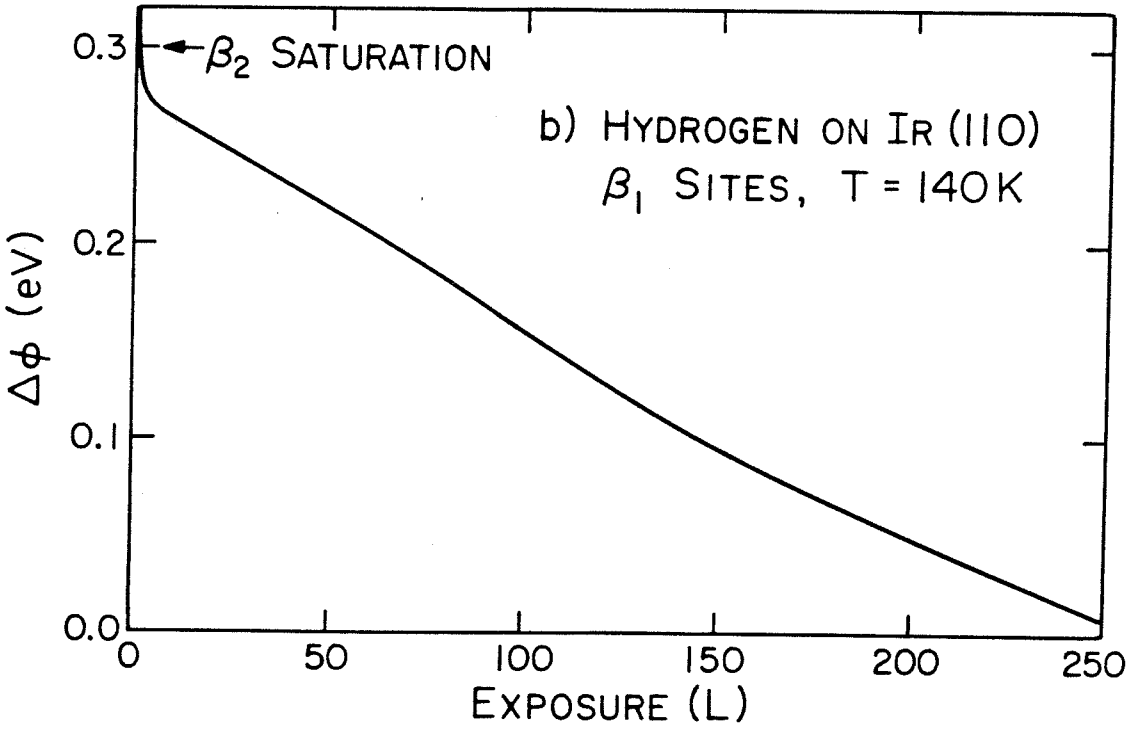
0.3
β_2 SATURATION
b) HYDROGEN ON IR (110)
β_1 SITES, T = 140K
0.2
0.1
0.0
Δφ (eV)
0
50
100
150
200
250
EXPOSURE (L)

Fig. 9

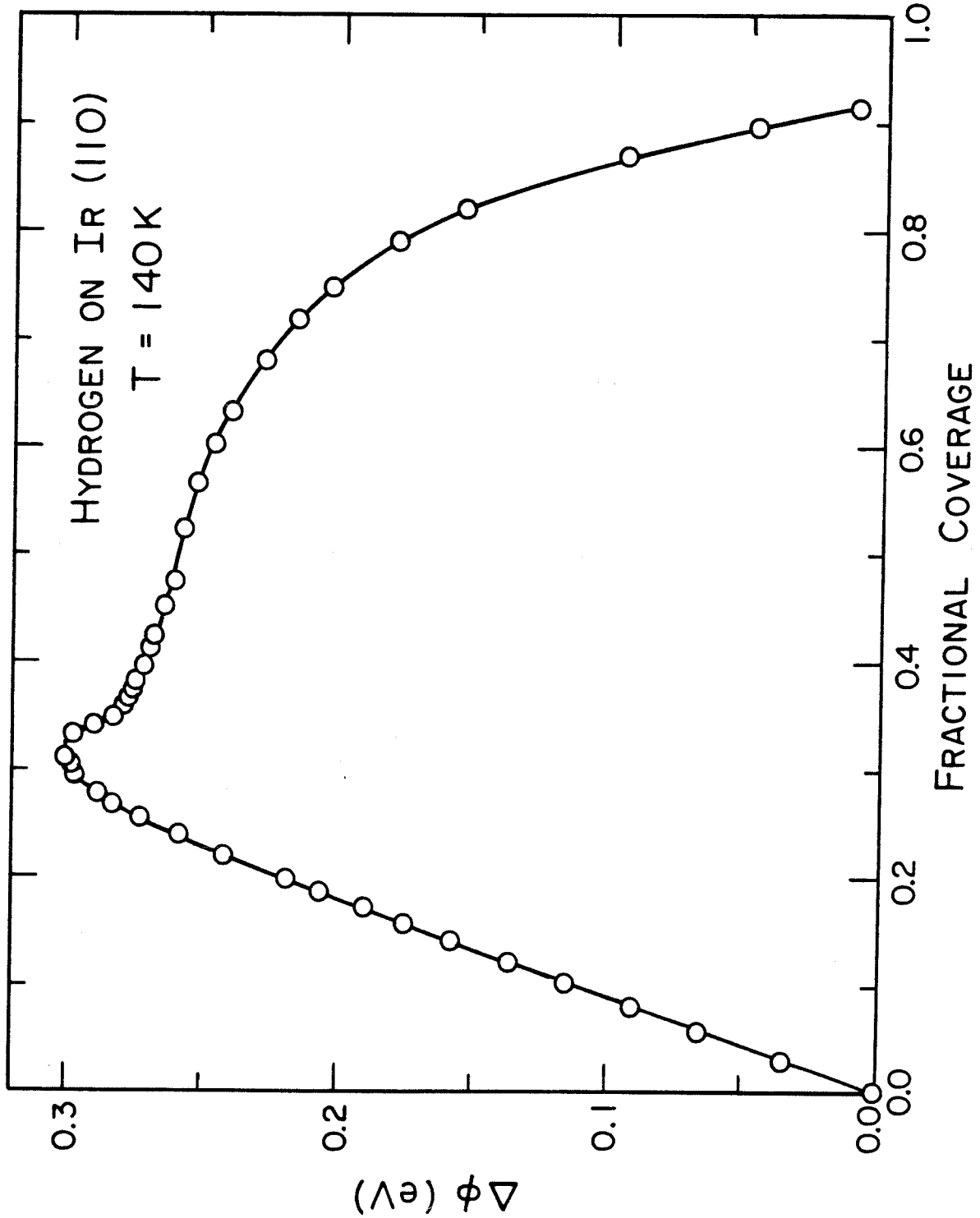
HYDROGEN ON IR (110)
T = 140 K
Δφ (eV)
0.00
0.1
0.2
0.3
0.0
0.2
0.4
0.6
0.8
1.0
FRACTIONAL COVERAGE

Fig. 10

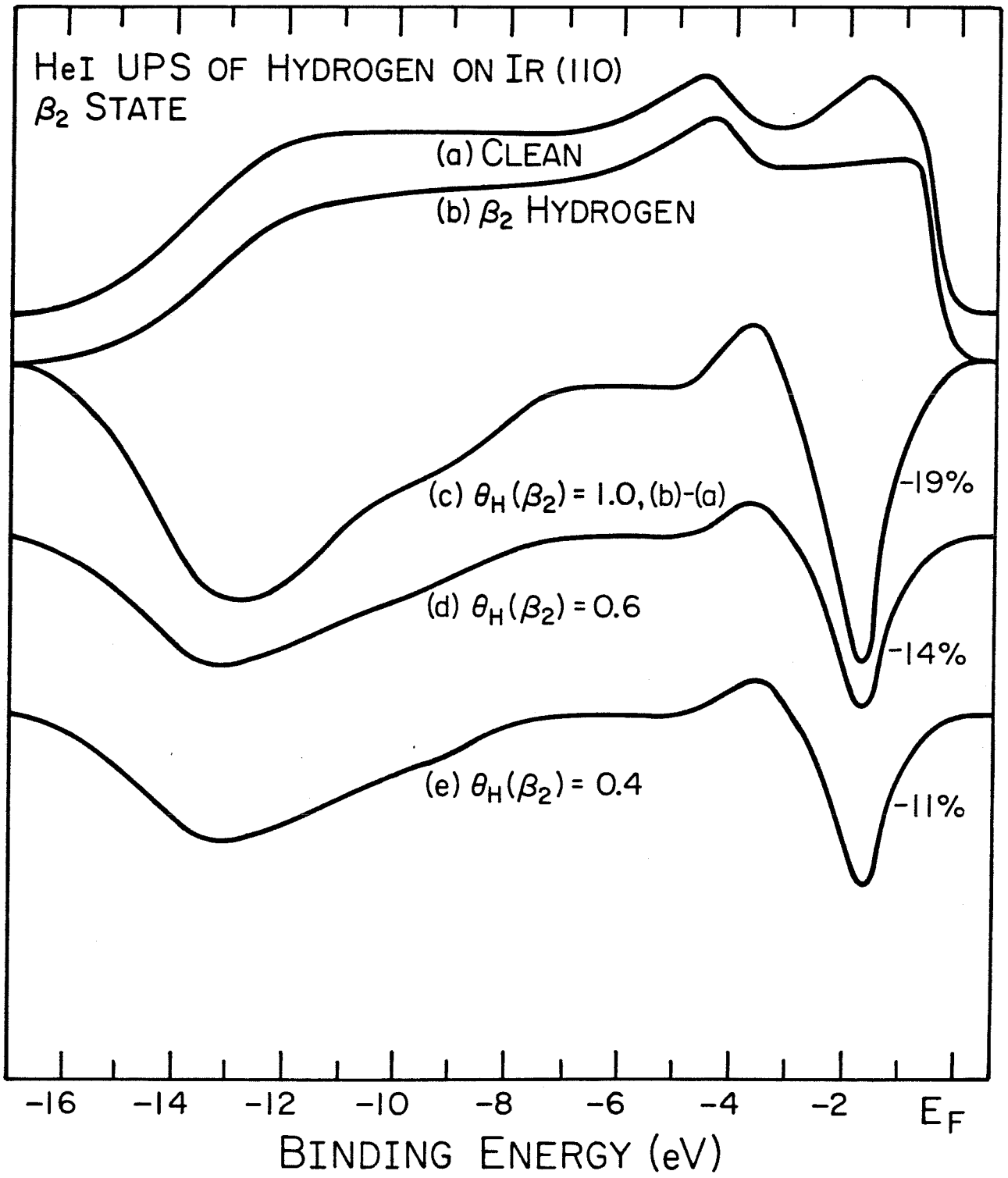
HeI UPS OF HYDROGEN ON IR (110)
β_2 STATE
(a) CLEAN
(b) β_2 HYDROGEN
(c) $\theta_H(\beta_2)$ = 1.0, (b)-(a)
-19%
(d) $\theta_H(\beta_2)$ = 0.6
-14%
(e) $\theta_H(\beta_2)$ = 0.4
-11%
-16
-14
-12
-10
-8
-6
-4
-2
E_F
BINDING ENERGY (eV)

Fig. 11

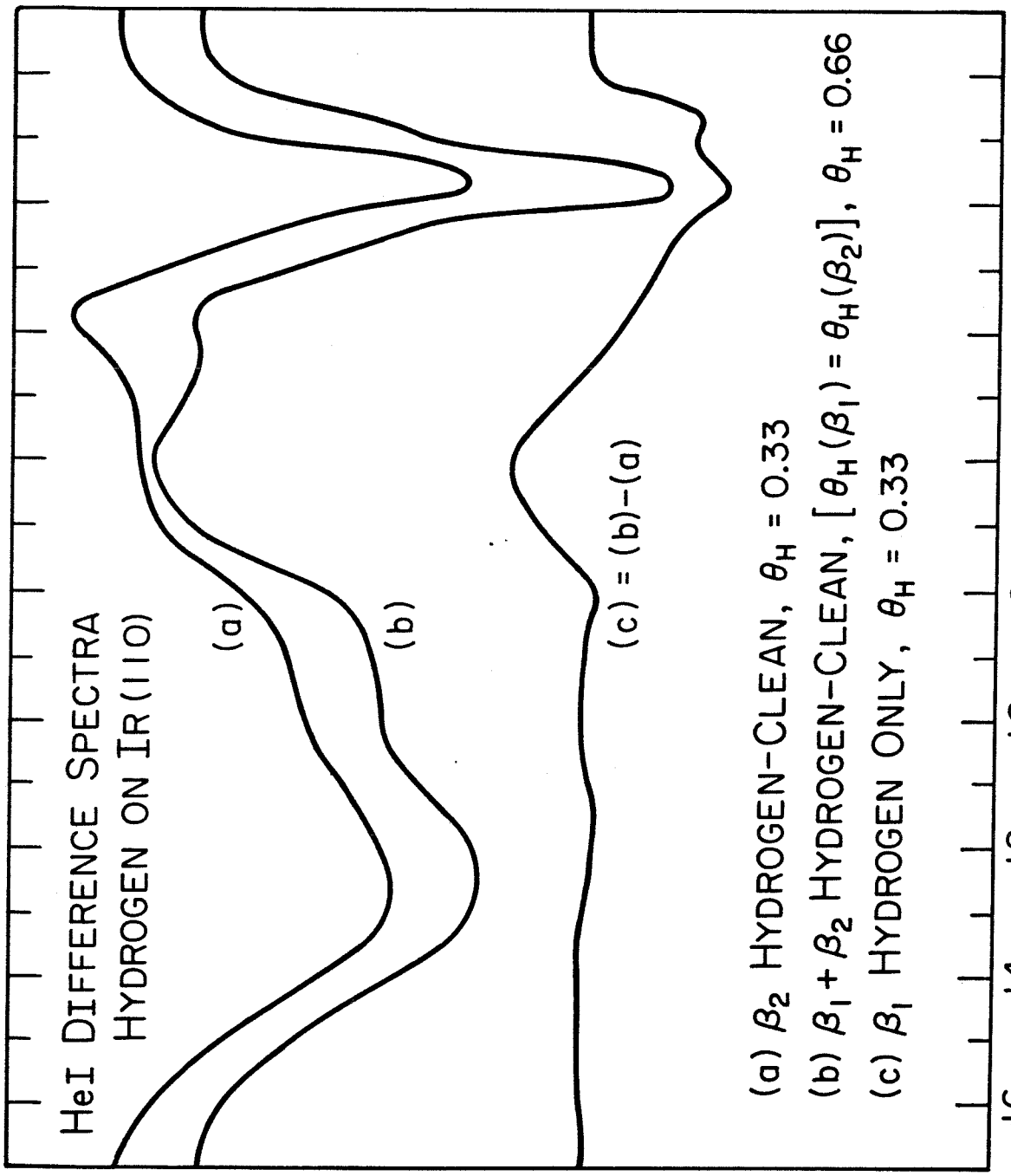
HeI Difference Spectra
Hydrogen on Ir(110)
(a)
(b)
(c) = (b)-(a)
(a) β_2 Hydrogen-Clean, θ_H = 0.33
(b) $\beta_1 + \beta_2$ Hydrogen-Clean, $[\theta_H(\beta_1) = \theta_H(\beta_2)]$, θ_H = 0.66
(c) β_1 Hydrogen Only, θ_H = 0.33
-16
-14
-12
-10
-8
-6
-4
-2
E_F
Binding Energy (eV)

Fig. 12

APPENDIX B

THE COADSORPTION OF HYDROGEN AND CARBON MONOXIDE ON THE (110) SURFACE OF IRIDIUM

(The text of Appendix B consists of an article coauthored with D.E. Ibbotson and W.H. Weinberg that has appeared in Surface Science 97, 297 (1980).)

Surface Science 97 (1980) 297–308

THE CO-ADSORPTION OF HYDROGEN AND CARBON MONOXIDE ON THE (110) SURFACE OF IRIDIUM †

D.E. IBBOTSON, T.S. WITTRIG * and W.H. WEINBERG **

Division of Chemistry and Chemical Engineering, California Institute of Technology, Pasadena, California 91125, USA

Received 21 January 1980; accepted for publication 23 April 1980

The nonreactive co-adsorption of hydrogen and carbon monoxide on Ir(110) was studied under ultra-high vacuum conditions with thermal desorption mass spectrometry, LEED, contact potential difference measurements and UPS. No changes in the Ir(110)-(1 × 2) reconstructed surface structure or ordering of the adsorbed layers were observed with LEED due to the presence of hydrogen and CO co-adsorbed. The adsorption of hydrogen on pre-adsorbed CO, or vice versa, causes less hydrogen to occupy the high temperature β_2 state and shifts the occupancy to the low temperature β_1 state preferentially. An apparent increase in the sticking probability of hydrogen for adsorption in the β_1 state for small CO coverage is discussed. At high CO coverage, the Ir(110) surface is poisoned to hydrogen adsorption. Exposing CO to pre-adsorbed hydrogen causes the binding energy of hydrogen to decrease with increasing CO exposure. Eventual displacement of hydrogen from the surface occurs for large CO exposures. The contact potential difference (CPD) as a function of hydrogen exposure on pre-adsorbed CO complements the desorption data for both the β_1 and β_2 states of hydrogen. For low coverages of CO, relating the CPD to hydrogen coverage shows the induced dipole of hydrogen is unchanged from the clean surface. Furthermore, the HeI UP spectra of small coverages of hydrogen and CO indicate the valence orbitals of CO are not affected detectibly by the presence of hydrogen. The results indicate CO poisons β_2 sites for hydrogen by a simple site blocking mechanism and may exclude β_1 sites at high CO coverages by a hydrogen–CO repulsive action.

1. Introduction

The co-adsorption of hydrogen and carbon monoxide on Ir(110) was undertaken to understand the effects of a model poison, CO, for hydrogen chemisorption. Thermal desorption mass spectrometry (TDS), LEED, contact potential difference (CPD) measurements and ultraviolet photoelectron spectroscopy (UPS) were used

† Supported by the National Science Foundation under Grand No. CHE 77-14976.
* Fannie and John Hertz Foundation Predoctoral Fellow.
** Camille and Henry Dreyfus Foundation Teacher–Scholar.

to investigate the influence of CO on the chemisorption properties of hydrogen on Ir(110).

Previous work concerned with the co-adsorption of hydrogen and carbon monoxide on the Group VIII transition metals included studies on Pt(111) [1], polycrystalline Pt [2] and Rh [3,4], Rh(111) [5], Pd(110) [6] and an Ir field emission tip [7]. Generally, it has been observed that CO displaces hydrogen from the surface when hydrogen is pre-adsorbed, and CO blocks sites for subsequent hydrogen adsorption, i.e., acts as a poison for hydrogen adsorption. Only one ordered LEED superstructure has been observed for hydrogen and CO co-adsorbed which is a (1×3) overlayer pattern on Pd(110) [6] when both adsorbates are in intimate contact with one another at a third their individual saturation concentrations. Weak mutual interactions are inferred since no variation in the desorption energy of H_2 was measured. However, anomalously high temperatures for hydrogen desorption have been reported for large exposures of a H_2/CO gas mixture to polycrystalline Pt [2] and Rh [3] surfaces. Moreover, H_2 desorption spectra from Pt(111) [1] and Rh films [4] change due to the presence of CO. Also, segregation of hydrogen and CO may occur on Rh(111) [5]. The results described here for the co-adsorption of hydrogen and CO on Ir(110) complement this previous work on the other Group VIII metals.

2. Experimental procedures

The experiments were performed in an ion-pumped stainless steel bell jar with a base pressure below 2×10^{-10} Torr. A detailed description of the experimental system is reported elsewhere [8], with the exception of the ultraviolet lamp. The HeI radiation was produced by a microwave discharge cavity at the end of a two stage, differentially pumped stainless steel capillary array. Operation of the HeI discharge at one torr caused the pressure in the bell jar to rise by 1×10^{-9} Torr. For HeI radiation, typical count rates near the Fermi edge were from 90,000 to 110,000 counts s^{-1} using a double pass CMA at a constant pass energy of 25 eV. Details of the preparation of the Ir(110) crystal and the cleaning procedure are described elsewhere [8,9].

3. Hydrogen TDS from hydrogen/CO overlayers and LEED results

Three sets of thermal desorption spectra were collected as a function of exposure for hydrogen on Ir(110) with various precoverages of CO at 130 K. The spectra are shown in fig. 1 for CO fractional coverages of 0.10, 0.25 and 0.50, where $\theta_{CO} = 1.0$ corresponds to 9.6×10^{14} molecules cm^{-2} [8]. In addition, the spectra for hydrogen chemisorbed on a surface with no CO present are reproduced [9] for comparison. The thermal desorption spectra of CO are not presented since CO

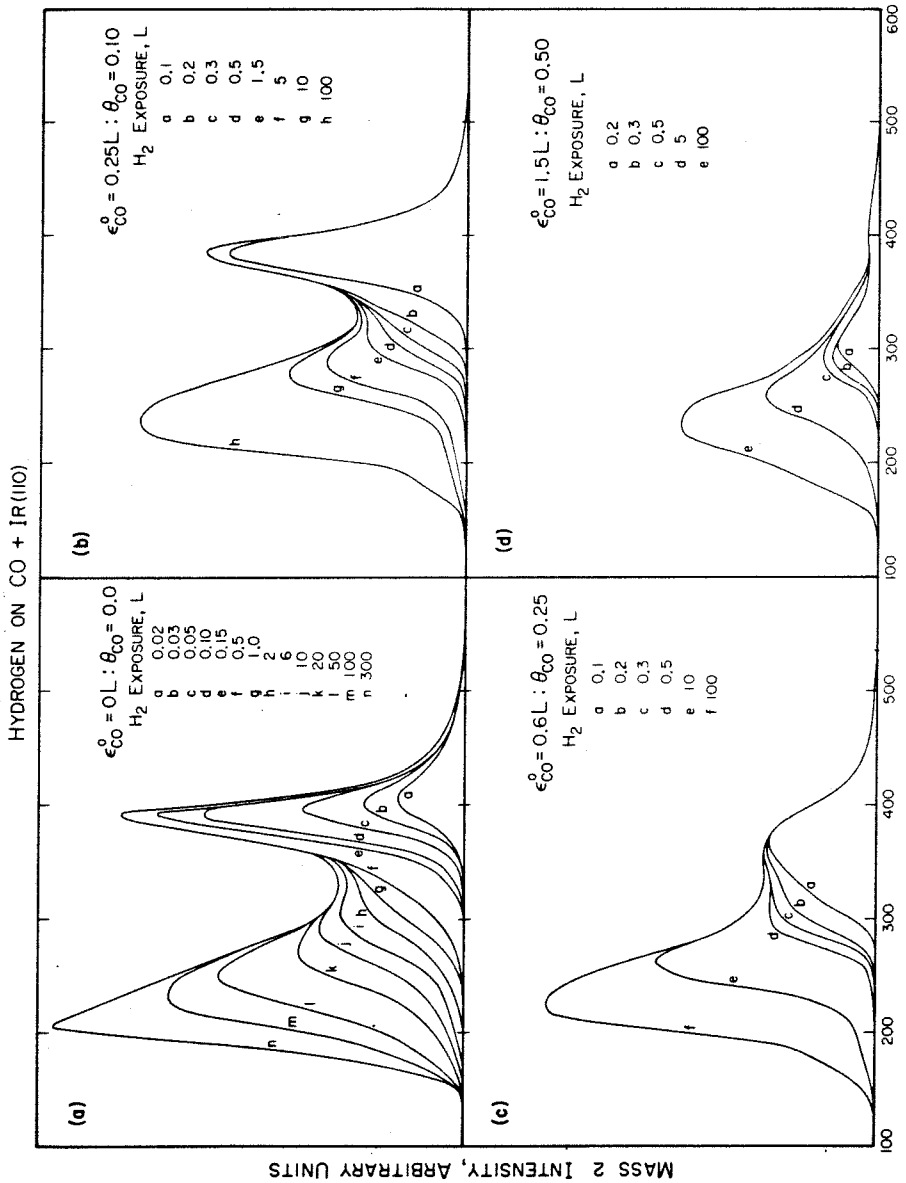

Fig. 1. Thermal desorption spectra from Ir(110) of hydrogen which was adsorbed at 130 K on various fractional coverages of CO. The initial coverage of CO was accomplished by exposing the surface to CO at 300 K and cooling to 130 K: (a) θ_{CO} = 0, (b) θ_{CO} = 0.10 (c) θ_{CO} = 0.25, and (d) θ_{CO} = 0.50.

desorbs at temperatures where hydrogen desorption is complete [8]. For each curve shown in figs. 1b–1d, the surface was exposed to a known flux of CO at 300 K as noted in the figures. Then the surface was cooled to 130 K and exposed to H_2 with a subsequent heating rate for desorption of 20 K s^{-1}. Small errors in the CO exposure or variation of the CO background pressure cause noticeable fluctuation in the shape of the high temperature desorption state, which will be referred to as the β_2 state of hydrogen. A 10 L exposure of CO on Ir(110), followed by a saturation exposure of H_2, caused no hydrogen to adsorb.

The most striking observation about the influence of CO on hydrogen adsorption is that the β_2 state is affected more strongly than the β_1 state (low temperature state), particularly at low CO coverages. This is not due to a change in the surface structure since the reconstructed Ir(110)-(1 × 2) is stable upon CO adsorption [8] and hydrogen adsorption [9], but rather it is due to a direct hydrogen–CO interaction. Although an extensive search for an ordered overlayer superstructure was performed, no ordering over the coherence width of the LEED beam occurred for any coverage of hydrogen and CO co-adsorbed. Therefore, no long range order is established between hydrogen and CO, but a short range interaction must take place.

As the coverage of CO increases, the amount of hydrogen that desorbs in the β_2 state decreases, as seen in fig. 1. Since the integrated intensities can be related to an absolute coverage of H atoms [9] that desorb from the β_2 state and the coverage of CO is known, the number of sites blocked by CO can be calculated. For clean Ir(110), the saturation coverage of the β_2 state is 7×10^{14} atoms cm^{-2}, and it obeys first order adsorption kinetics with an initial sticking probability of unity [9]. For every CO molecule adsorbed, approximately 1.5 sites for H atoms are blocked for the CO coverages presented in fig. 1. At a coverage of 0.50, CO effectively blocks hydrogen from the β_2 sites. Interestingly, the number of sites of hydrogen in the β_2 state blocked by each CO is nearly equal to the ratio of the saturation coverage of CO in molecules cm^{-2} and the saturation coverage of β_2 hydrogen in atoms cm^{-2}. Moreover, if the number of blocked sites are accounted for when $\theta^0_{CO} = 0.25$, the initial sticking probability for hydrogen is still equal to one. For $\theta^0_{CO} = 0.10$ the calculated initial sticking probability is 0.8, a 20% decrease over simple site blocking. Still, the interaction of hydrogen with the β_2 sites is strong when low coverages of CO are present, and the rate of adsorption depends essentially on an impinging H_2 molecule finding an empty site as the controlling step. At least for the spectra shown in fig. 1b, where the β_2 feature is still resolved well, only a small decrease occurs in peak temperature at its saturation coverage compared to the results for the clean surface shown in fig. 1a. The presence of CO evidently does not affect strongly the desorption of the β_2 state of hydrogen other than blocking sites. The sites associated with the β_2 state have been deduced from the absolute coverage of hydrogen and UPS results to be above the third layer of Ir atoms exposed in the missing row locations on the reconstructed Ir(110) surface [9]. Inferences drawn from contact potential difference measurements for CO on Ir(110) also place the binding sites of CO between the topmost row of Ir atoms [8], which would be

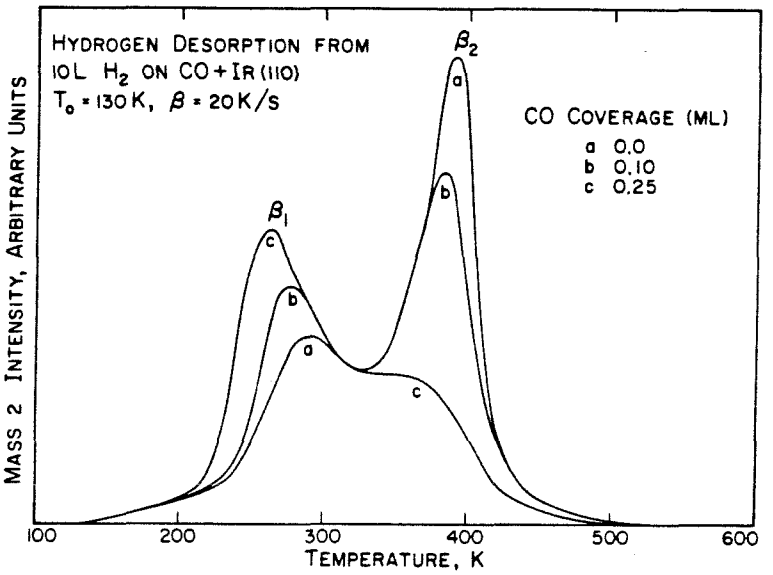

Fig. 2. Thermal desorption of 10 L H_2 exposed at 130 K to 0, 0.10 and 0.25 fractional coverages of CO. Note the decrease in the area of the β_2 state and the increase in the area of the β_1 state as the precoverage of CO increases.

reasonable if CO directly blocks β_2 sites for hydrogen as this data and data presented later suggests.

Whereas the β_2 state is attenuated even for low coverages of CO, the β_1 state of hydrogen is enhanced in coverage for equal exposures compared to the clean surface. Fig. 2 reproduces the thermal desorption spectra of 10 L H_2 exposed to a surface containing fractional coverages of CO of 0, 0.10 and 0.25. An increase in the coverage of the β_1 state up to a CO coverage of 0.25 occurs, where for this CO coverage the β_1 state contains as much hydrogen as would be present for 50 L H_2 on the clean surface, although the desorption occurs at lower temperature when CO is present for equal $\theta_H(\beta_1)$. At least up to $\theta_{CO} = 0.25$, the saturation coverage of the β_1 state is not affected. However, increasing the coverage of CO always decreases the total coverage of hydrogen for a constant exposure, particularly above $\theta_{CO} = 0.25$.

The enhancement of adsorption of hydrogen into the β_1 state in the presence of small amounts of CO may be explained in two ways. First, adsorbed CO molecules may tend to orient H_2 molecules as they impinge on the surface to favor β_1 sites, which are the two types of three-fold sites on the clean surface [9]. At higher CO coverages, this effect becomes unimportant since CO is compressed on the surface blocking β_1 sites as well. Second, a channeling effect may occur from hydrogen originally adsorbed in β_2 sites to hydrogen adsorbed in β_1 sites leaving a β_2 site

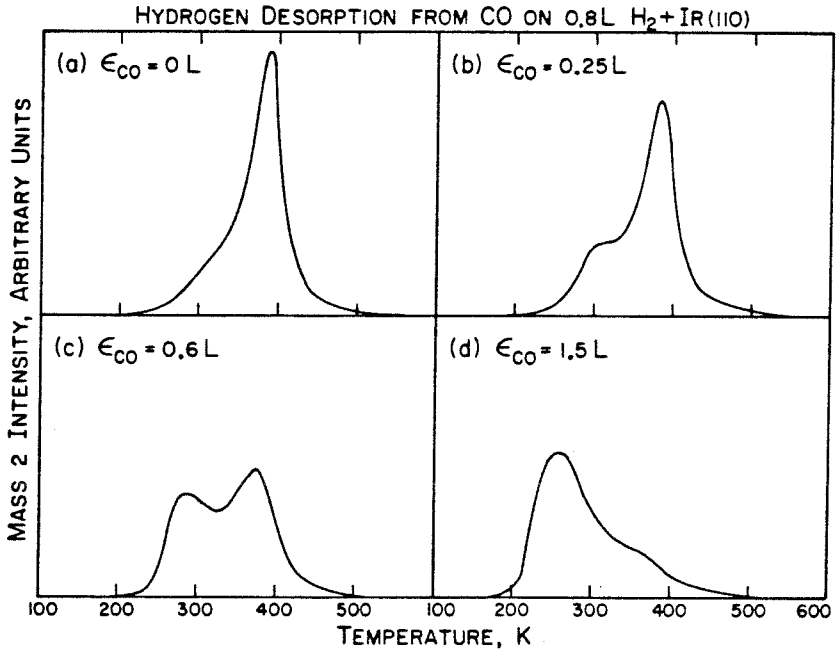

Fig. 3. Thermal desorption of H_2 from pre-adsorbed hydrogen (0.8 L) exposed to varying amounts of CO: (a) 0 L, (b) 0.25 L, (c) 0.6 L, and (d) 1.5 L. All exposures were carried out at 130 K. The coverage of hydrogen is constant over these CO exposures.

vacant for additional hydrogen adsorption during the exposure. This possibility cannot be ruled out since CO is still somewhat mobile even at 130 K [8], and exchange does occur between the β_1 and β_2 sites [9]. As adsorbed CO migrates, β_2 hydrogen may be pushed to β_1 sites. The reverse conversion from β_1 to β_2 may in turn be inhibited by CO, but more hyrogen may adsorb into β_2 from the gas phase. This would describe a channeling of hydrogen to enhance artifically the apparent sticking probability of hydrogen adsorption into the β_1 state on Ir(110). Either of the two mechanisms presented is equally plausible. A small effect that enhances β_1 adsorption will be reflected as a large effect in the amount of β_1 hydrogen adsorbed compared to the clean surface, since for this case second order Langmuir kinetics are obeyed with a small initial sticking probability of 7×10^{-3}.

The effect of CO adsorption on a constant amount of pre-adsorbed hydrogen is shown in fig. 3. In this experiment, 0.8 L H_2 was exposed to the surface at 130 K and subsequently to different amounts of CO, as noted in the figure, at the same temperature. The desorption spectra were then recorded at a heating rate of 20 K s^{-1}. The integrated intensity of hydrogen for each spectrum is the same for these CO exposures; in other words no displacement of hydrogen from the surface by CO occurs. A continuous displacement is observed from the β_2 to the β_1 sites, how-

ever, with increasing CO exposures. For exposures greater than 10 L some hydrogen is desorbed from the surface. Comparisons of figs. 1 and 3 show that for equivalent coverages of hydrogen and CO, the desorption spectra for hydrogen are the same. Regardless of the exposure sequence, CO tends to occupy its preferred sites rather than hydrogen. It should be noted that the sticking probability of CO is decreased somewhat from the clean surface when hydrogen is present, although this effect was not investigated in detail.

These results indicate that segregation of H atoms and CO molecules on the surface into separate islands does not occur since β_2 hydrogen should be observed to desorb from hydrogen islands. However, partial segregation of H atoms and CO molecules does occur on Rh(111) [5]. Coadsorption studies of hydrogen and CO on Pd(110) show no change in the desorption energy for hydrogen compared to the clean surface [6], different from the observations on Ir(110). Finally, no high temperature desorption states of hydrogen were observed under the conditions examined, although such states have been reported for large exposures of an H_2/CO gas mixture both on polycrystalline Pt [2] and Rh [3].

4. CPD and UPS measurements

Contact potential differences measurements were performed to complement the TDS data presented in the previous section and to observe how the charge transfer of hydrogen is affected by the presence of CO. Also, UPS measurements were performed for low coverages of hydrogen and CO to determine if a strong mutual interaction is reflected in the valence orbitals of CO.

For various precoverages of CO, the CPD of hydrogen in the β_2 state on Ir(110) changes strongly with exposure, compared to the clean surface, as shown in fig. 4. The CPD of hydrogen in the β_2 state was not plotted as a function of fraction coverage because the coverage–exposure relation of hydrogen in this state, for a given precoverage of CO, is quite sensitive to small errors in CO precoverage, particularly with such small exposures of hydrogen (fig. 4). However, for the β_1 state of hydrogen, the coverage–exposure relation could be determined, since small errors in CO precoverage affected the β_1 coverage to a small extent only. The same precoverages of CO were used as for the TDS results presented in the previous section: 0, 0.10, 0.25 and 0.50 ML. It is apparent that small amounts of CO depress markedly the maximum CPD observed for hydrogen in β_2 sites. From the TDS results, it was seen that CO blocks β_2 sites for hydrogen; and for $\theta_{CO} = 0.50$ ML, β_2 desorption is almost totally suppressed. For this coverage of CO in fig. 4, the CPD monotonically decreases in contrast to the other three curves shown in this figure. This indicates that β_2 sites are blocked effectively and β_1 sites are populated since the CPD of the latter decreases with the coverage of hydrogen, as will be shown. At least for a precoverage of CO of 0.10 ML, the calculated dipole for the hydrogen–metal complex over the first half of β_2 adsorption is equal to the dipole

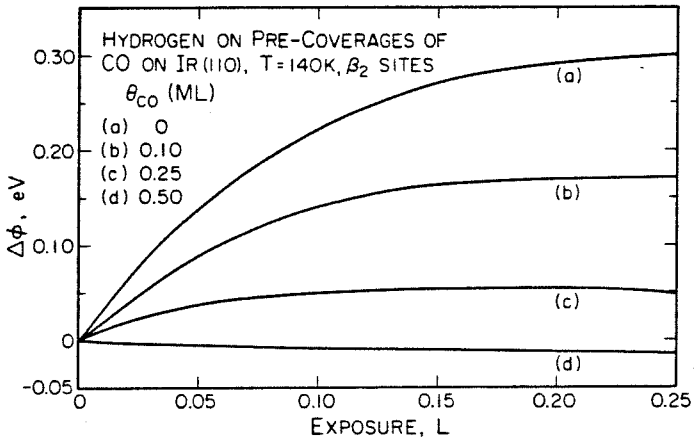

Fig. 4. The CPD of hydrogen as a function of exposure for the β_2 sites (low coverage) on Ir(110) for various precoverages of CO: (a) 0, (b) 0.10, and (c) 0.25, and (d) 0.50 ML.

calculated for the clean surface, 0.14 Debye [9], where the CPD is linear with the fractional coverage of hydrogen. Therefore, the charge transfer for hydrogen in β_2 sites in the presence of small amounts of CO is not affected to a measurable extent. Site blocking by CO is the dominant effect in this coverage regime.

Since the observed dipole of β_2 hydrogen does not change with small amounts of CO present, the HeI UP spectra of hydrogen and CO coadsorbed in this coverage regime were measured to determine whether the valence levels of these two species shift, indicative of a strong mutual interaction. Sufficient hydrogen was exposed to the surface to fill the β_2 state on surfaces with 0, 0.10 and 0.25 ML CO present. The corresponding HeI UP difference spectra are shown in fig. 5. For the spectrum with no CO present, fig. 5a, the H(1s) level can be seen as a broad transtion centered at 6.1 eV below the Fermi level, E_F. Also in fig. 5a, the large attenuation in the d-band centered at 1.6 eV below E_F and a small enhancement at 3.6 eV below E_F are observed due to hydrogen in β_2 sites [9]. As the precoverage of CO increases, the valence levels of CO grow in as evidenced in figs. 5b and 5c by peaks at 11.3, 8.7 and 7.6 eV below E_F which are not changed either in shape or energy from that measured for CO with no hydrogen present. Therefore, CO does not appear to be affected markedly by hydrogen in β_2 sites although they compete directly for these sites as shown previously. Also, as the coverage of CO increases, both the attenuation of the d-band of the metal as well as the enhancement at 3.6 eV decrease. Furthermore, the H(1s) level becomes indiscernible in figs. 5b and 5c. These changes with the coverage of CO indicate the coverage of β_2 hydrogen is decreased since any hydrogen adsorbed in β_1 sites has a small effect on the d-band, and CO at, for example, 0.25 ML attenuates the d-band uniformly by less than 5%. It is concluded from these UPS data that the valence levels of CO are not strongly

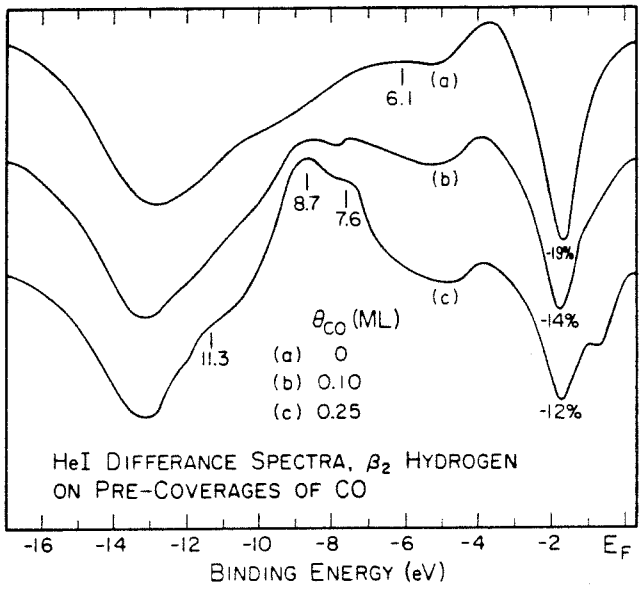

Fig. 5. HeI UP difference spectra for β_2 hydrogen on Ir(110) on precoverages of CO: (a) 0, (b) 0.10, and (c) 0.25 ML. For each spectrum, the surface was exposed to sufficient hydrogen to fill the β_2 sites as evidenced by TDS and CPD measurements.

perturbed by hydrogen on Ir(110), and CO blocks β_2 sites for hydrogen, in agreement with the TDS and CPD results.

In contrast to the β_2 sites of hydrogen in the presence of CO on Ir(110), TDS data show an enhancement of the sticking probability of hydrogen into β_1 sites when small coverages of CO are present. This enhancement is reflected in the CPD

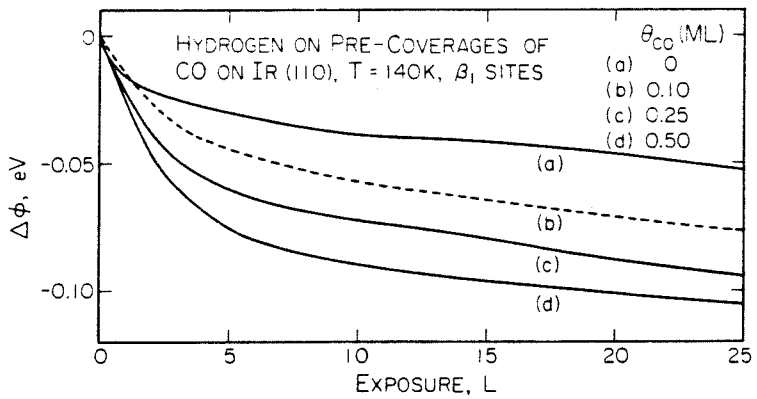

Fig. 6. The CPD of hydrogen as a function of exposure for the β_1 sites (high coverage) on Ir(110) for precoverages of CO: (a) 0, (b) 0.10, (c) 0.25, and (d) 0.50 ML.

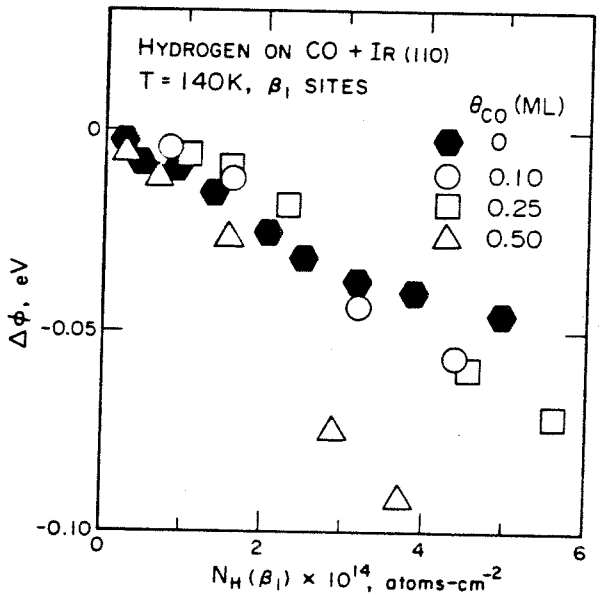

Fig. 7. The CPD of hydrogen as a function of the concentration in the β_1 sites for 0, 0.10, 0.25, and 0.50 ML of CO pre-adsorbed. The data were calculated from the integrated intensities in fig. 1, the coverage calibration from ref. [9], and fig. 6.

measurements in fig. 6 as well. Increasing the precoverage of CO causes the CPD of hydrogen adsorbing into β_1 sites to decrease more rapidly with exposure as compared to the clean surface. The data were obtained by exposing the surface to the various amounts of CO, exposing the surface to sufficient hydrogen to fill first β_2 sites, and then recording the CPD as a function of hydrogen exposure.

In order to examine more carefully how the adsorption of hydrogen into β_1 sites on Ir(110) is affected by CO, the coverage determination of hydrogen [9] was used to relate the CPD and the concentration of hydrogen in the β_1 sites as shown in fig. 7. It is seen that for precoverages of CO of 0, 0.10 and 0.25 ML, the slopes of the CPD ($\Delta\phi$) as a function of coverage of β_1 hydrogen [$N_H(\beta_1)$] are very nearly the same for the range of $N_H(\beta_1)$ shown here which accounts for approximately one-third of the total β_1 concentration on the clean surface. For these coverages of CO and hydrogen, it may be concluded that the dipole of the hydrogen–metal complex is relatively unaffected. However, a cursory examination of the trend for β_1 hydrogen adsorbing on 0.50 ML CO seen in fig. 7 would point to a definite change in the induced dipole for hydrogen due to the presence of CO. But some of the initial β_1 sites are actually excluded by this coverage of CO as seen in fig. 1d. The higher coverage β_1 sites of hydrogen that must then be occupied exhibit a larger decrease in the CPD as a function of coverage [9]. Therefore, the change in behavior of hydrogen for 0.50 ML of CO pre-adsorbed in fig. 7 may be reflecting essentially this

partial blockage of the first β_1 sites occupied by hydrogen and that even for this range of hydrogen and CO coverages the induced dipole of hydrogen is not affected greatly on a microscopic scale. The partial blockage of β_1 sites at higher CO coverage may be more due to an H–CO repulsive interaction than a direct competition for binding sites.

5. Summary

The co-adsorption of hydrogen and CO on Ir(110) has been studied under ultra-high vacuum conditions with thermal desorption mass spectrometry, LEED, contact potential difference measurements and UPS. The present results complement other work performed previously on the platinum metals.

Although no ordered structures were observed with LEED when hydrogen and CO were co-adsorbed under any of the conditions examined, the adsorption and desorption properties of hydrogen are affected strongly by the presence of small amounts of CO. For small coverages of pre-adsorbed CO, a continuous decrease in desorption from the low coverage β_2 state of hydrogen is observed with increasing CO coverages. A concomitant increase occurs for the high coverage β_1 state of hydrogen which is interpreted as either an orienting effect by CO for an impinging H_2 molecule or a continuous conversion of hydrogen from the β_2 to the β_1 state during the hydrogen exposure due to the partial mobility of CO which converts H atoms from the β_2 to the β_1 state. At high CO coverages, the surface is poisoned to hydrogen adsorption. The adsorption of CO on pre-adsorbed hydrogen shows the same desorption trends for H_2 as for the reverse exposure sequence at equivalent coverages. The binding energy of hydrogen decrease as the CO coverage increases, and H_2 desorption occurs at the adsorption temperature (130 K) for large CO exposures.

The CPD of hydrogen on pre-adsorbed CO also is affected strongly. However, the induced dipole of hydrogen in the β_2 state is the same as for the clean surface if the number of sites blocked by each CO molecule (1.5) is taken into account. Moreover, the HeI UP spectra of low coverages of CO and of hydrogen in the β_2 sites show no changes in the valence orbitals of CO and only reflect the blocking of β_2 sites by CO for hydrogen adsorption. For the β_1 state, the induced dipole of hydrogen in the presence of less than 0.25 ML of CO is the same as for clean Ir(110) as well. For 0.50 ML of CO pre-adsorbed, some of the first β_1 sites are excluded for hydrogen adsorption due to either a direct blocking or a hydrogen–CO repulsive interaction. The CPD in this case reflects a shift in the hydrogen to the second β_1 site that exhibits a larger decrease with coverage.

References

[1] V.H. Baldwin, Jr. and J.B. Hudson, J. Vacuum Sci. Technol. 8 (1971) 49.
[2] K. Kawasaki, T. Kodama, H. Miki and T. Kioka, Surface Sci. 64 (1977) 349.

[3] K. Kawasaki, M. Shibata, H. Miki and T. Kioka, Surface Sci. 81 (1979) 370.
[4] M.G. Wells, N.W. Cant and R.G. Greenler, Surface Sci. 67 (1977) 541.
[5] E.D. Williams, P.A. Thiel, W.H. Weinberg and J.T. Yates, Jr., J. Chem. Phys. 72 (1980) 3496.
[6] H. Conrad, G. Ertl and E.E. Latta, J. Catalysis 35 (1974) 363.
[7] H.F. Kempin, K. Klapper and G. Ertl, Nouveau J. Chim. (Paris) 1 (1977) 295.
[8] J.L. Taylor, D.E. Ibbotson and W.H. Weinberg, J. Chem. Phys. 69 (1978) 4298.
[9] D.E. Ibbotson, T.S. Wittrig and W.H. Weinberg, J. Chem. Phys. 72 (1980) 4885.

APPENDIX C

THE CHEMISORPTION OF N_2 ON THE (110) SURFACE OF IRIDIUM

(The text of Appendix C consists of an article coauthored with D.E. Ibbotson and W.H. Weinberg that will appear in Surface Science 111, 000 (1981).

Abstract

The molecular chemisorption of N_2 on the reconstructed Ir(110)-(1x2) surface has been studied with thermal desorption mass spectrometry, XPS, UPS, AES, LEED and the co-adsorption of N_2 with hydrogen. Photoelectron spectroscopy shows molecular levels of N_2 at 8.0 ($5\sigma + 1\pi$) and 11.8 (4σ) eV in the valence band and at 399.2 eV with a satellite at 404.2 eV in the N(1s) region, where the binding energies are referenced to the Ir Fermi level. The kinetics of adsorption and desorption show that both precursor kinetics and interadsorbate interactions are important for this chemisorption system. Adsorption occurs with a constant probability of adsorption of unity up to saturation coverage (4.8×10^{14} cm^{-2}), and the thermal desorption spectra give rise to two peaks. The activation energy for desorption varies between 8.5 and 6.0 kcal-$mole^{-1}$ at low and high coverages, respectively. Results of the co-adsorption of N_2 and hydrogen indicate that adsorbed N_2 resides in the missing-row troughs on the reconstructed surface. Nitrogen is displaced by hydrogen, and the most tightly bound state of hydrogen blocks virtually all N_2 adsorption. A p1g1(2x2) LEED pattern is associated with a saturated overlayer of adsorbed N_2 on Ir(110)-(1x2).

1. Introduction

The chemisorption of molecular nitrogen [N_2(ad)] has been studied on Ir(110)-(1x2) at low temperatures with thermal desorption mass spectrometry (TDS), LEED, AES, XPS and UPS measurements. Also, the co-adsorption of hydrogen and molecular N_2 was investigated to clarify the type of sites occupied by N_2 and to observe the influence of hydrogen on the chemisorption properties of the molecularly adsorbed N_2 overlayer.

For all transition metals that have been studied previously, molecular adsorption of N_2 has been observed only at temperatures below 200 K. Molecular adsorption of N_2 occurs on Ni *(1 - 4)*, Pd *(3)*, Ru *(5)*, Pt *(6,7)*, Ir *(8,9)*, Fe *(10 - 12)*, and W *(13,14)*, usually with a high probability of adsorption. Desorption of N_2 occurs between 130 and 200 K, exhibiting either one or two features in the thermal desorption spectrum, with activation energies ranging between 4 and 11 kcal-mole^{-1}. However, Fe *(11,12)* does not chemisorb molecular N_2 at surface temperatures above 140 K, but does below this temperature *(10)*.

The X-ray photoelectron spectra reported for N_2(ad) show two to three features in the N(1s) region. On Ni films *(1,2)*, Fe films *(10,11)* and W(110) *(13)*, the binding energies reported are (400.6, 405.7), (400.3, 405.3) and (399.1, 400.4, 405.5) eV, respectively. The transitions near 400 eV are normal values for a nitrogen containing molecular species, in this case N_2 . However, the transitions between 405 and 406 eV are too far removed (5 eV) to be attributed to another molecular species. Therefore, this transition is most likely a satellite due to an incomplete screening of the core hole, which is a consequence of

the relatively weak N_2-metal bond *(13)*. An earlier explanation of results obtained for N_2(ad) on Fe *(11)* at 80 K was that the two widely separated features represented N_2 bonding perpendicular and parallel to the surface. Recent electron energy loss (EELS) experiments of N_2(ad) on W(100) *(14)* showed that N_2 bonds through one nitrogen atom in analogy to CO. Hence, this is probably the case also on Fe.

Although the chemisorption bond of N_2(ad) is much weaker than CO on the transition metals, they are isoelectronic and should give somewhat similar UP sectra. On polycrystalline Ni *(1)*, N_2(ad) yields levels at 8.0 and 11.8 eV below the Fermi level, E_F, by HeI UPS. Similarly, on W(110) *(13)* levels are observed at 7.0 and 11.7 eV below E_F. The 5σ and 1π orbitals are assigned to the higher lying level and the 4σ orbital is assigned to the lower lying level on the respective surfaces, as for adsorbed CO. However, recent calculations, comparing CO and N_2 bonding to a Ni atom and UP spectra of CO and N_2 on Ni(100), have concluded that the 4σ and 5σ orbitals of CO and N_2 behave differently *(15,16)*, due to the greater degree of bonding interaction of the 4σ orbital in N_2 compared to CO. It was shown that the absolute separation between the 4σ and 5σ orbitals *increases* when N_2 is chemisorbed compared to free N_2 due to final state effects, opposite to the change in separation for CO *(16)*. Alignment of ionization potentials for free N_2 and valence band emissions for adsorbed N_2 therefore should be with the nonbonding 1π orbital *(15)*.

Finally, only two investigations have examined the influence of hydrogen adsorption on an N_2(ad) overlayer under UHV conditions. Hydrogen displaces N_2(ad) from a polycrystalline Fe surface *(10)*. Also, adsorbed hydrogen on

W(100) tends to displace N_2(ad) from a bridging site to an on-top site as shown by EELS results *(14)*.

These previous results will provide a comparison for the present study of N_2 adsorbed molecularly on the reconstructed Ir(110) surface. In addition, LEED will be used to investigate the stability of the clean surface reconstruction to N_2 adsorption and to observe whether N_2(ad) forms an ordered superstructure. No ordered superstructures due to N_2(ad) have been reported previously on the transition metals.

2. Experimental Methods

The experiments were conducted in an ion pumped stainless steel belljar that has been described previously *(17,18)*. The base pressure for these experiments was below 2×10^{-10} torr of reactive contaminants. The Ir(110) crystal is the same as that used for the study of hydrogen chemisorption in this apparatus *(17)*, and it shows the (1x2) reconstruction when clean, which is a surface with every other row of Ir atoms missing in the [001] direction. Since this previous work *(17)*, the conduction path between the liquid nitrogen cooling reservoir and the crystal has been improved so that the lowest temperature routinely achieved is now 95 K compared to 130 K. The lower base temperature proved to be important for the study of nitrogen adsorbed molecularly on Ir(110)-(1x2).

3. XPS, UPS and AES of Adsorbed Nitrogen

This section presents results from electron spectroscopy measurements performed for low temperature adsorption of N_2 on Ir(110). The XPS, UPS and AES transitions observed when N_2 is exposed to the Ir(110) surface at 95 K are consistent with molecular adsorption, as seen by previous studies on other transition metals at low temperature.

Figure 1 shows XPS results for N_2 adsorbed on Ir(110) as a function of fractional coverage of N_2. The coverages were measured from the relative areas under the N(1s) features in Fig. 1 and from thermal desorption spectra presented in the next section. Two transitions appear in the N(1s) region at binding energies of 399.2 and 404.2 eV. The ratio of the intensities of the two binding energies is equal to 1.37 at all coverages. The spectra shown here are similar to those measured for N_2 adsorption on polycrystalline Ni *(1,2)* and Fe *(10,11)* and W(110) *(13)* which has been attributed to molecular N_2. The transition at 399.2 eV is reasonable for N_2(ad), and the transition at 404.2 eV represents a satellite. The relatively high intensity of this satellite is due to the weak chemisorption bond, NN-Ir, which can cause incomplete screening of the core-hole as described previously for the case of N_2 on W(110) *(13)*.

The HeI UPS presented in Fig. 2 verifies the molecular nature of N_2 adsorption on Ir(110) at low temperature. Spectra are shown in Fig. 2 for a surface saturated with N_2 (1.25 L) and a clean surface, and the corresponding difference spectrum. Two levels and a slight decrease in the d-band intensity near E_F are apparent in the difference spectrum. The level at 8.0 eV below E_F

may be assigned to a combination of the 5σ and 1π orbitals of N_2(ad) where the 5σ orbital has shifted toward the 1π level due to its (bonding) interaction with the surface. The 4σ orbital of N_2(ad) is less certain in its energy due to interference from secondary electrons at low kinetic energy, but it may be assigned at approximately 11.8 ± .3 eV below E_F . These levels are similar to those reported for molecular N_2 on polycrystalline Ni *(1)*, Ni(100) *(15)* and W(110) *(13)*, and orbital assignments are analogous to CO.

The final electron spectrum of N_2(ad) on Ir(110) is the AE spectrum shown in Fig. 3. The Ir transitions at 355 and 380 eV in the clean surface spectrum have been subtracted. The features observed due to N_2(ad) are peaks at 362.0, 381.7 and 389.3 eV as well as a shoulder at 375.5 eV. The XAES result for N_2 on W(110) *(13)* is quite similar to Fig. 3, but both are different from the gas phase *(19)*.

In Fig. 3, the labels A-J show calculated Auger transitions from a correlation of core and valence levels that have been presented above. The correlation *(20)* can be summarized by the following equation

$$E(kjl) = E(k) - E(j) - E(l) - (F_{jl} - R_{jl}), \tag{1}$$

where E(kjl) is the normal Auger transition, E(k) is the binding energy of state k, F_{jl} is the hole-hole repulsion energy in the final state,and R_{jl} is the excess relaxation energy in the final state. Here, $(F_{jl} - R_{jl})$ will be assumed to be zero when involving the N(1s) level at 399.2 eV. As indicated shortly, this term will be taken as -1.1 eV for transitions involving the N(1s) satellite at 404.2 eV. The binding energies used here are the N(1s), 5σ and 1π, 4σ, and 3σ levels for

N_2(ad) on Ir(110). With the exception of the 3σ orbital, the other binding energies are measured directly as presented above. The binding energy of the 3σ orbital was estimated from gas phase data *(19)* as 30.5 eV with respect to E_F. Table 1 summarizes the calculated transitions that are shown as letters in Fig. 3. Good agreement between observed and calculated Auger transitions is achieved only if participation of the N(1s) satellite is included. Moreover, a value of -1.1 eV for the (F-R) contribution involving the N(1s) satellite aligns the calculated transitions D and F with the observed transitions at 389.3 and 381.7 eV in Fig. 3.

To summarize, XPS and UPS measurements indicate that adsorbed N_2 is molecular, and the spectra are similar to those reported for adsorption on other transition metals. Also, AES measurements of N_2(ad) and calculated Auger transitions, derived from the difference in core level and valence level binding energies, agree quite well so long as the satellite level found in XPS is included.

4. Desorption and Adsorption Kinetics

When N_2 is exposed to Ir(110)-(1x2) at 95 K and then the surface is heated, N_2 is observed to desorb above 120 K, as shown in Fig. 4. Mass 14 was monitored to eliminate any interference due to CO in the measurement. No N_2 desorption occurs above 250 K where dissociatively chemisorbed nitrogen atoms would combine and desorb *(21)*. The temperature range in which N_2 desorbs is further evidence of molecular adsorption. As the coverage of N_2 increases, the first peak that appears broadens and shifts to lower

temperatures. Near 0.8 L of N_2, a second feature appears at lower temperature. It too shifts and broadens up to the saturation exposure, which is between 1.25 and 1.50 L. The fact that two peaks appear in the TD spectra may indicate two different sites are occupied on the Ir(110) surface. However, as will be seen later, the saturation coverage, adsorption kinetics, substrate structure and an overlayer LEED superstructure point to one site at saturation and to a compression of the adsorbed layer occurring as the coverage nears saturation. Therefore, the desorption characteristics seen in Fig. 4 indicate that precursor kinetics (see below) as well as intermolecular repulsive interactions influence desorption strongly for N_2(ad) on Ir(110).

The adsorption kinetics of N_2 on Ir(110) were calculated from the areas under the TD spectra in Fig. 4, and the results are presented in Fig. 5. As seen in Fig. 5, the coverage of N_2 as a function of exposure is fit very well by a zero-order dependence of the probability of adsorption on coverage up to saturation, which corresponds to an exposure between 1.25 and 1.50 L N_2. If one assumes an initial probability of adsorption, S_0, of unity, the saturation coverage is equal to 4.8×10^{14} molecules-cm^{-2}. Moreover, a p1g1(2x2) LEED structure of adsorbed N_2 is observed at saturation (see Section 6), and this is consistent with the above coverage calculation.

Zero-order adsorption kinetics for N_2 on Ir(110) indicate the participation of a precursor state in the adsorption reaction. From microscopic reversibility, the same type of precursor should be involved also in desorption. Broadening and shifts of a thermal desorption peak with increasing coverage are predicted if a precursor is involved in desorption *(22,23)*, which would explain

partially the desorption behavior of N_2 seen in Fig. 4. However, precursor kinetics alone cannot explain multiple peaks in the thermal desorption spectra. An additional complication (with the assumption of one type of site for adsorption) is embodied in the spectra if interadsorbate interactions become important at high coverage. An adsorbate-adsorbate interaction model, including repulsive interactions, predicts a shift in temperature with increasing coverage and multiple peaks *(24)*. Since the adsorption kinetics strongly suggest that a precursor is involved and two peaks appear in the thermal desorption spectra, neither type of desorption model *alone* can explain the experimental data in a qualitative way. Multiple-site participation is not a valid argument from the LEED results presented in Section 6. Therefore, a combination of the precursor model and the interaction model for the N_2-Ir(110) system is necessary to explain the adsorption and desorption kinetics.

To examine the desorption kinetics more closely, the rate parameters for desorption are needed: the activation energy, E_d, and the preexponential, ν_d, of the desorption rate coefficient. Since N_2 adsorption is molecular, the starting point for a desorption model is a first-order expression,

$$R_d = \nu(\Theta)\,\Theta\,\exp[-E_d(\Theta)/kT], \tag{2}$$

where the terms in Eq. (2) have their usual significance. An analysis of precursor kinetics *(22)* indicates that a coverage dependence embodied in the preexponential factor would result from the presence of the precursor, even in the absence of additional interactions. If the activation energy for desorption can be measured as a function of coverage, independent of ν_d, then any variation of

E_d with coverage would be due to interactions between adsorbates.

An integral method of analysis by varying the heating rate *(25)* was used to measure E_d and ν_d at points of constant coverage. The method involves changing the heating rate over a wide range for each coverage. The slope of an Arrhenius plot, for a given coverage, is then proportional to E_d, and the intercept is proportional to ln ν_d. In these experiments, heating rates were varied from 5 to 120 K-s^{-1}, and the initial coverage was kept constant at 0.80 ML. Complicating factors of importance were desorption from the sample holder and changes in the pumping speed of the system with time. Consequently, the usable coverage range that could be analyzed in this way was between 0.05 and 0.60 ML. It was found that ν_d varied randomly in the Arrhenius plots, from 10^8 to 10^{11} s^{-1} for coverages below 0.30 ML. Also, at low coverages, the calculated E_d was uncertain due to varying amounts of desorption from the sample holder. Therefore, it was deemed necessary to average the values of ν_d and then calculate the corresponding E_d from the desorption curves. Above 0.60 ML, ν_d was assumed to be constant near the average value $\overline{\nu_d} = 2 \times 10^9$ s^{-1}. With these uncertainties, the results for $E_d(\theta)$ shown in Fig. 6 are only semi-quantitative. At low coverage, E_d is 8.5 kcal-mole^{-1}, nearly that which is observed on Ni(110) *(4)* and Ru(10$\bar{1}$0) *(5)*, but lower than the estimated activation energy of desorption from the (110) orientation of an Ir FEM tip *(8)*. However, N_2 was found to desorb in the same temperature range for the FEM tip *(8)* and in the present case, and thus the differences in the values of E_d are due solely to different choices of ν_d. In Fig. 6, a small linear decrease in E_d is observed below 0.75 ML and a larger linear decrease in E_d is observed for

$\Theta > 0.75$ ML of N_2. The uncertainties in the values of $E_d(\Theta)$ and ν_d preclude a further analysis of the desorption kinetics beyond the qualitative arguments concerning the inclusion of both precursor and interadsorbate interaction contributions.

5. Co-adsorption of Nitrogen and Hydrogen

The co-adsorption of hydrogen and N_2 was examined in order to gain more insight concerning the type of site on the surface into which N_2 chemisorbs and what influence chemisorbed hydrogen has on pre- and post-adsorbed N_2. Much is known concerning the interaction of hydrogen with Ir(110) *(17)*, and this lends another approach to understanding the chemisorption of N_2.

HeI difference spectra for three surface conditions of co-adsorbed hydrogen and N_2 are presented in Fig. 7 where the clean surface spectrum in Fig. 2 has been subtracted from each of the original spectra. For spectra (a) and (b) in Fig. 7, the initial fractional coverages of N_2 were 0.8 and 0.4, respectively. Both surfaces were exposed to sufficient hydrogen to obtain a coverage of hydrogen $\Theta_H = 0.25$, where $\Theta_H = 1$ corresponds to a saturation of the surface by hydrogen. It is apparent from (a) and (b) in Fig. 7 that N_2(ad) maintains its molecular character, which was seen in Fig. 2. The difference between the spectra in Fig. 7 and Fig. 2 lies in the shape of the curves near the Fermi level. Spectra (a) and (b) in Fig. 7 show evidence of adsorbed hydrogen *(17)*, although the H(1s) level cannot be detected at 6.1 eV below E_F.

Spectrum (c) in Fig. 7 shows the result of a 5 L N_2 exposure to a surface

with an initial precoverage of hydrogen of 0.33 ML. No observable evidence for N_2 adsorption is seen, but now the H(1s) level at -6.1 eV is clear. For $\Theta_H = 0.33$ on the clean Ir(110)-(1x2) surface, the high temperature β_2-state is filled completely *(17)*. The sites associated with β_2-hydrogen are in the locations of the missing rows of Ir atoms for this reconstructed surface *(17)*. This implies that N_2 prefers these sites as well, as discussed in Section 6.

A series of thermal desorption spectra measured for co-adsorbed overlayers of hydrogen and N_2 is shown in Figs. 8(A) H_2 and 8(B) (N_2). The labels in Fig. 8(B) correspond to those in Fig. 8(A), and in the latter figure ( ) denotes the first exposure in the sequence for each overlayer. Considering the desorption of N_2 shown in Fig. 8(B), spectra (a) and (b) show the effect of two different exposures of H_2 to a saturated overlayer of N_2. As the H_2 exposure increases from 5 to 10 L, the high temperature peak of N_2 decreases in intensity, and the low temperature peak increases in intensity. Moreover, the coverage of N_2 decreases to 0.77 ML in spectrum (a) and to 0.71 ML in spectrum (b). Hydrogen, on the other hand, increases in coverage in the same experiment as may be seen in spectra (a) and (b) in Fig. 8(A). As a comparison, spectrum (g) in Fig. 8(B) was reproduced from Fig. 4 for a 1.0 L N_2 exposure to the clean surface. Also, compare in Fig. 8(B) desorption spectra (c) and (g). In spectrum (c), 5 L H_2 was exposed to a surface preexposed to 1.0 L N_2 with the resulting loss of approximately 0.1 ML N_2 and the shift of some of the remaining N_2 to the low temperature peak. Although none of the N_2(ad) was lost in spectrum (d) of Fig. 8(B) compared to spectrum (e) of Fig. 4, the same shift in desorption temperature is seen. For spectrum (e), the β_2-state of hydrogen was filled *(17)*,

and this caused almost no N_2 to adsorb, even after an exposure of 5 L N_2. The small amount of N_2 desorption in (e) reflects mainly contributions from the sample holder.

With regard to the H_2 desorption shown in Fig. 8(A), the amount of H_2 increases as the precoverage of N_2(ad) decreases for a given H_2 exposure, but appears to be always less than the coverage of β_2-hydrogen at saturation on the clean surface. The rate of adsorption of hydrogen is lowered if N_2 is present on the surface, indicating at least a partial blockage by N_2 of adsites of hydrogen occurs. Another interesting aspect of the H_2 desorption spectra is that a small amount of H_2 desorbs at the same temperature of that of N_2 and has the same relative shape as that of N_2. However, this was not investigated further considering the low intensities (coverages) involved.

The findings of the co-adsorption of N_2 and hydrogen may now be summarized. The β_2-state of hydrogen, which bonds in the missing row troughs on the reconstructed Ir(110)-(1x2) surface, competes directly with N_2(ad) for chemisorption sites. Moreover, hydrogen, in part, occupies these preferred sites when chemisorbed on a surface preexposed to N_2 and displaces a part of the N_2 from the surface. When the β_2-state of hydrogen is filled on Ir(110), N_2 does not chemisorb appreciably. From HeI UPS, the N_2(ad) molecular orbitals are not perturbed detectibly when N_2 is co-adsorbed with hydrogen. Therefore, the interaction of hydrogen and N_2, when present together on the surface at low temperature, is largely a site competition and a compression of N_2(ad) away from its preferred sites by hydrogen.

6. LEED Observations

The chemisorption of N_2 on Ir(110)-(1x2) was investigated at low temperature with LEED. As background information, an fcc (110)-(1x1) is a surface consisting of a series of rows and troughs. However, Ir(110) reconstructs from the bulk structure to form a surface with every other row of Ir atoms missing in the [001] direction *(26)*. Moreover, the reconstruction is stable to the adsorption of hydrogen *(17)*, CO *(18)*, NO *(21)*, with oxygen *(27)* (< 700 K), water *(28)* and sulfur *(29)*.

For exposures of N_2 below 0.6 L, the LEED pattern maintains a bright (1x2) structure of the reconstructed surface with little increase in the background intensity. Between 0.6 and 1.0 L N_2, streaks appear between the rows of half-order substrate spots. For exposures of N_2 greater than 1.0 L up to saturation ($\approx$ 1.5 L), the streaks begin to coalesce into spots and the background intensity increases uniformly. However, the pattern did not yield sharp spots, even at a temperature of 95 K or by maintaining a background pressure of N_2. Careful annealing and cooling cycles failed to improve the order as well. The pattern observed is brightest at saturation coverage and is shown in Fig. 9(A). The photograph was taken at a beam energy of 137 eV and represents a "streaky" (2x2) pattern with extinguished beams at (n+½,0) on the (1x2) substrate.

The fact that the (1x2) substrate beams remain sharp and bright throughout the exposure sequence indicates the Ir(110) surface does not relax from its reconstructed state. The (2x2) pattern with missing beams then implies that a glide plane of symmetry is present on the surface. Consistent

with the saturation coverage of 4.8×10^{14} cm^{-2} (one N_2 molecule per reconstructed unit cell) and the fact that β_2-hydrogen directly blocks N_2 adsorption, the overlayer structure is a p1g1(2x2) where the real space representation is shown in Fig. 9(B). The glide plane is parallel to the missing-row troughs, and the (2x2) unit cell is drawn in the figure. This superstructure for N_2(ad) at saturation coverage is identical to a possible structure found for sulfur adsorbed on the Ir(110)-(1x2) surface *(29)*. Mobility of N_2(ad) might be expected even at 95 K due to the weak chemisorption bond, and this would cause disorder along the rows in the x-direction drawn in Fig. 9(B).

7. Summary

The results for the adsorption of N_2 on the Ir(110)-(1x2) surface may be summarized as follows:

1. XPS and UPS results show N_2 chemisorbs molecularly at low temperature. Two features appear for the N(1s) binding energy at 399.2 and 404.2 eV, the former indicating a molecular species and the latter indicating a satellite. The degenerate 5σ and 1π, and the 4σ orbitals are seen at binding energies of 8.0 and (11.8 ± 0.3) eV.
2. The Auger electron spectrum of N_2(ad) on Ir(110) shows transitions similar to that seen on W(110) *(13)*. The peaks can be assigned to normal Auger transitions by a simple calculation *(20)*. However, the N(1s) satellite must be included in the calculation to account for all the Auger

features that are observed.

3. Thermal desorption of N_2(ad) and the corresponding adsorption kinetics imply that precursor kinetics and repulsive adsorbate-adsorbate interactions are important in this chemisorption system. Adsorption occurs with an initial probability of adsorption of unity independent of coverage, and the surface coverage saturates at one molecule per reconstructed unit cell. However, thermal desorption measurements indicate that repulsive interactions become important at high coverages, as seen by the appearance of a second thermal desorption peak. At low coverage, the activation energy for desorption is approximately 8.5 kcal-mole^{-1} and decreases to 6.0 kcal-mole^{-1} at saturation.
4. The co-adsorption of hydrogen and N_2 was studied by UPS and TDS. The presence of hydrogen does not perturb the valence orbitals of N_2 detectibly. However, hydrogen does displace N_2(ad) from the surface and, at least in part, takes up its preferred sites in the missing row troughs.
5. A p1g1(2x2) pattern forms for N_2(ad) at saturation on Ir(110)-(1x2). The proposed structure is consistent both with the probable locations of N_2 in the missing-row troughs and the saturation coverage. This appears to be the first LEED superstructure reported for molecularly adsorbed nitrogen on a transition metal surface.

Acknowledgment

The authors are grateful to the National Science Foundation for support of this reseach (Grant No. CHE77-14976). The assistance of P. Szuromi in some of the experiments is appreciated.

References

1. C. R. Brundle and A. F. Carley, Discussions Faraday Soc.60, 51 (1975).
2. C. R. Brundle, J. Vacuum Sci. Technol. 13, 301 (1976).
3. D. A. King, Surface Sci. 9, 375 (1968).
4. M. Grunze, R. K. Driscoll, G. N. Burland, J. C. L. Cornish and J. Pritchard, Surface Sci. 89, 381 (1979).
5. R. Klein and A. Shih, Surface Sci. 69, 403 (1977).
6. R. A. Shigeishi and D. A. King, Surface Sci. 62, 379 (1977).
7. M. Wilf and P. T. Dawson, Surface Sci. 60, 561 (1976).
8. B. E. Nieuwenhuys, D. Th. Meijer and W. M. H. Sachtler, Surface Sci. 40, 125 (1973).
9. J.-M. Derochette, Phys. Stat. Sol. (a) 45, 163 (1978).
10. D. W. Johnson and M. W. Roberts, Surface Sci.87, L255 (1979).
11. K. Kishi and M. W. Roberts, Surface Sci.62, 252 (1977).
12. F. Bozso, G. Ertl, M. Grunze and M. Weiss, J. Catalysis 49, 18 (1977).
13. J. C. Fuggle and D. Menzel, Surface Sci. 79, 1 (1979).
14. W. Ho, R. F. Willis and E. W. Plummer, Surface Sci. 95, 171 (1980).
15. P. S. Bagus, C. R. Brundle, K. Hermann and D. Menzel, J. Electron Spectrosc. Relat. Phenom. 20, 253 (1980).
16. K. Hermann, P. S. Bagus, C. R. Brundle and D. Menzel, to be published.

17. D. E. Ibbotson, T. S. Wittrig and W. H. Weinberg, J. Chem. Phys. 72, 4885 (1980).

18. J. L. Taylor, D. E. Ibbotson and W. H. Weinberg, J. Chem. Phys. 69, 4298 (1978).

19. W. E. Moddeman, T. A. Carlson, M. O. Krausse, B. P. Pullen, W. E. Bull and G. K. Schweitzer, J. Chem. Phys. 55, 2317 (1971).

20. G. G. Tibbetts and J. M. Burkstrand, J. Vacuum Sci. Technol. 15, 497 (1978).

21. D. E. Ibbotson, T. S. Wittrig and W. H. Weinberg, in preparation.

22. R. Gorte and L. D. Schmidt, Surface Sci 76, 559 (1978).

23. D. A. King, Surface Sci. 64, 43 (1977).

24. D. L. Adams, Surface Sci. 42, 12 (1974).

25. J. L. Taylor and W. H. Weinberg, Surface Sci. 78, 259 (1978).

26. C. M. Chan, M. A. Van Hove, W. H. Weinberg and E. D. Williams, Solid State Commun. 30, 47 (1979); Surface Sci. 91, 400 (1980).

27. J. L. Taylor, D. E. Ibbotson and W. H. Weinberg, Surface Sci. 79, 349 (1979).

28. T. S. Wittrig, D. E. Ibbotson and W. H. Weinberg, Surface Sci., in press.

29. E. D. Williams, C. M. Chan and W. H. Weinberg, Surface Sci. 81, L309 (1979).

Table 1

Calculated Auger Transitions from Eq. (1).

Orbital (B.E., eV)

K = N(1s) = 399.2

K' = N'(1s) = 404.2 (satellite)

I = $1\pi, 5\sigma$ = 8.0

II = 4σ = 11.8

III = 3σ ~ 30.5 [estimated from Ref. *(17)*]

Figure 3	*Designation*	*E (kjl), eV*
A	KI I	383.2
B	KI II	379.4
C	KII II	375.6
D	K'I I	389.3*
E	K'I II	385.5*
F	K'II II	381.7*
G	KII III	356.9
H	KI III	360.7
I	K'II III	363.0*
J	K'I III	366.8*

* All K' transitions have been shifted by +1.1 eV in kinetic energy to align D and F with observed transitions in Fig. 3 at 389.3 and 381.7 eV, respectively.

Figure Captions

Fig. 1. XPS of N_2 molecularly adsorbed on Ir(110) at 95 K as a function of N_2(ad) fractional coverage.

Fig. 2. HeI UPS of N_2(ad) on Ir(110) at 95 K. (a) Saturated layer of N_2, (b) Clean surface, and (c) Difference sectrum.

Fig. 3. Nitrogen-KLL AES for N_2(ad) on Ir(110) at 95 K. The letters A-J denote calculated transitions for normal Auger processes. See Eq.(1) and Table 1 for assignments.

Fig. 4. Thermal desorption spectra of N_2(ad) on Ir(110) at 95 K. Mass 14 was monitored at a heating rate of 22 K-s^{-1}.

Fig. 5. Adsorption kinetics of N_2 on Ir(110) at 95 K. These were derived from the thermal desorption spectra in Fig. 4.

Fig. 6. Activation energy for N_2 desorption from Ir(110). See the text for details.

Fig. 7. HeI UP difference spectra of co-adsorbed N_2(ad) and hydrogen on Ir(110) at 95 K. (a) 5 L H_2 on 0.80 ML N_2(ad), (b) 1 L H_2 on 0.40 ML N_2(ad), and (c) 5 L N_2 on 0.33 ML H_2(ad).

Fig. 8. Thermal desorption spectra of H_2, (A), and N_2, (B), from several overlayers of co-adsorbed hydrogen and N_2 on Ir(110) at 100 K. The heating rate for these spectra is 20 K-s^{-1}.

Fig. 9. (A) LEED pattern at 137 eV of a saturated N_2 overlayer on Ir(110) at 95 K. The substrate maintains its (1x2) reconstruction, and the overlayer forms a p1g1(2x2) superstructure. (B) Real space representation of the p1g1(2x2) pattern. The large circles are N_2 molecules and the small circles are Ir atoms, with diameters of 3.0 (Van der Waals Diameter) and 2.72 $\mathring{A}$, respectively.

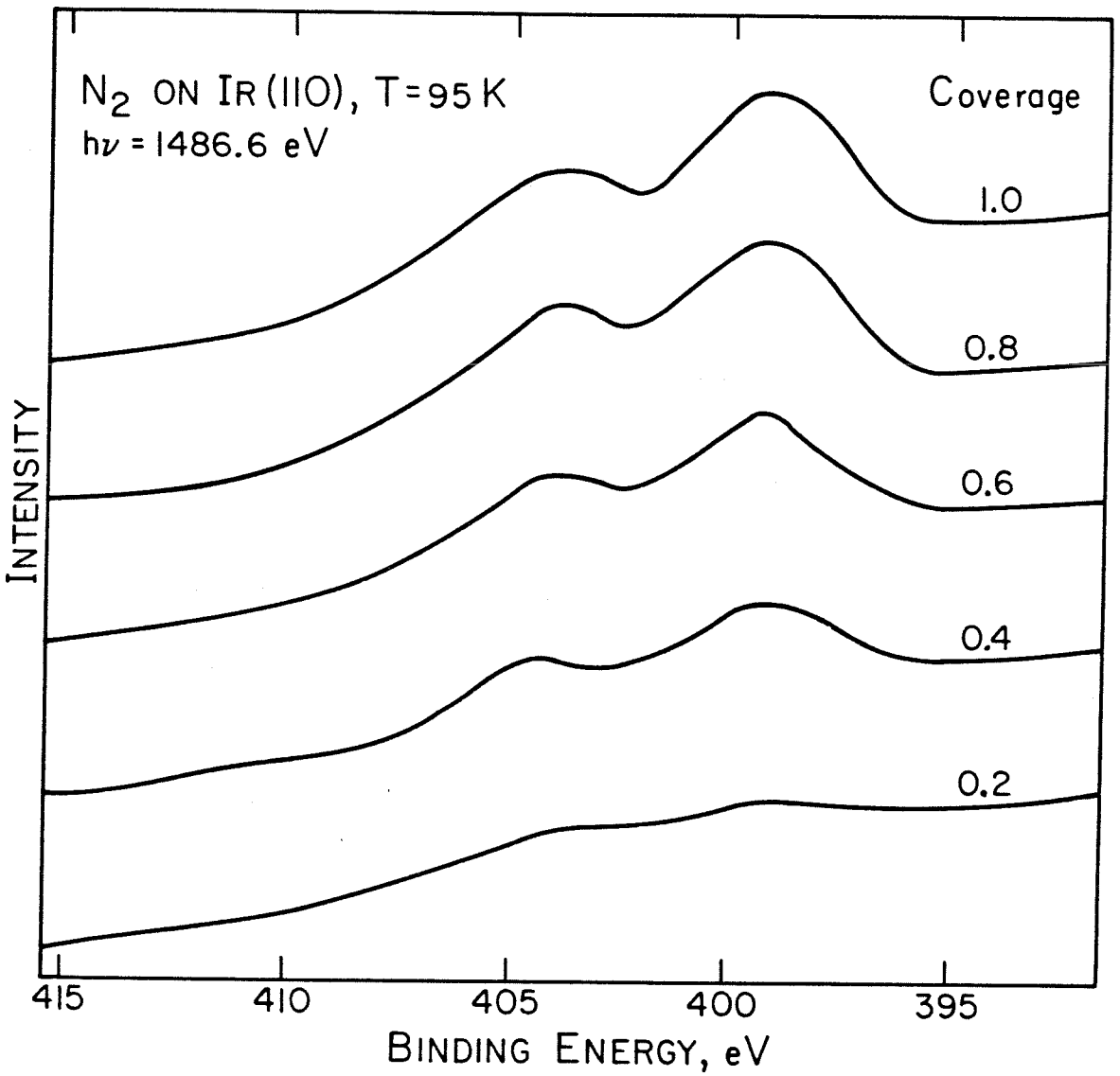
N_2 ON IR(110), T=95 K
hν = 1486.6 eV
Coverage
1.0
0.8
0.6
0.4
0.2
INTENSITY
415
410
405
400
395
BINDING ENERGY, eV

Figure 1

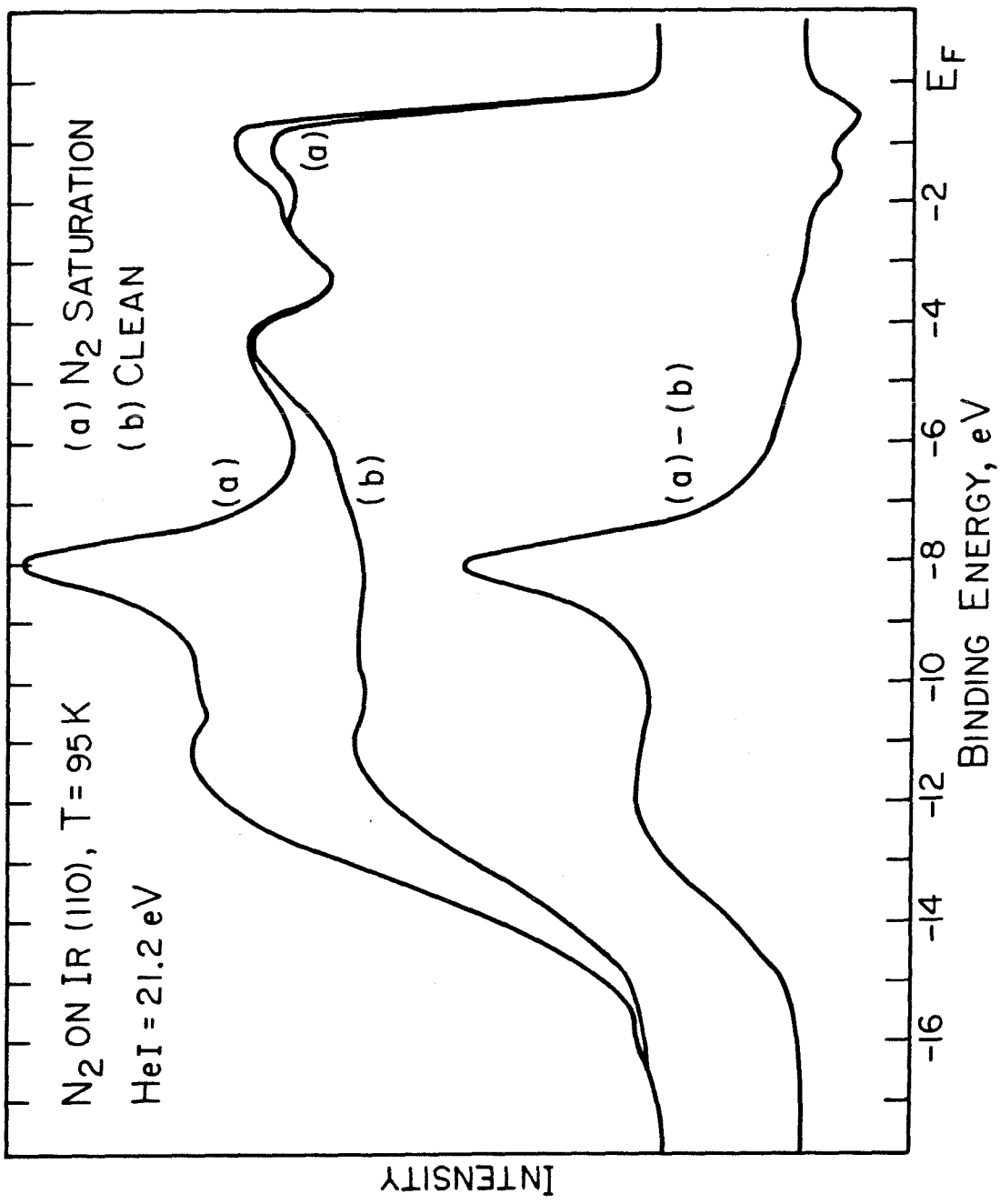
N_2 ON IR (110), T = 95 K
HeI = 21.2 eV
(a) N_2 SATURATION
(b) CLEAN
(a)
(b)
(a)
(a) - (b)
INTENSITY
-16
-14
-12
-10
-8
-6
-4
-2
E_F
BINDING ENERGY, eV

Figure 2

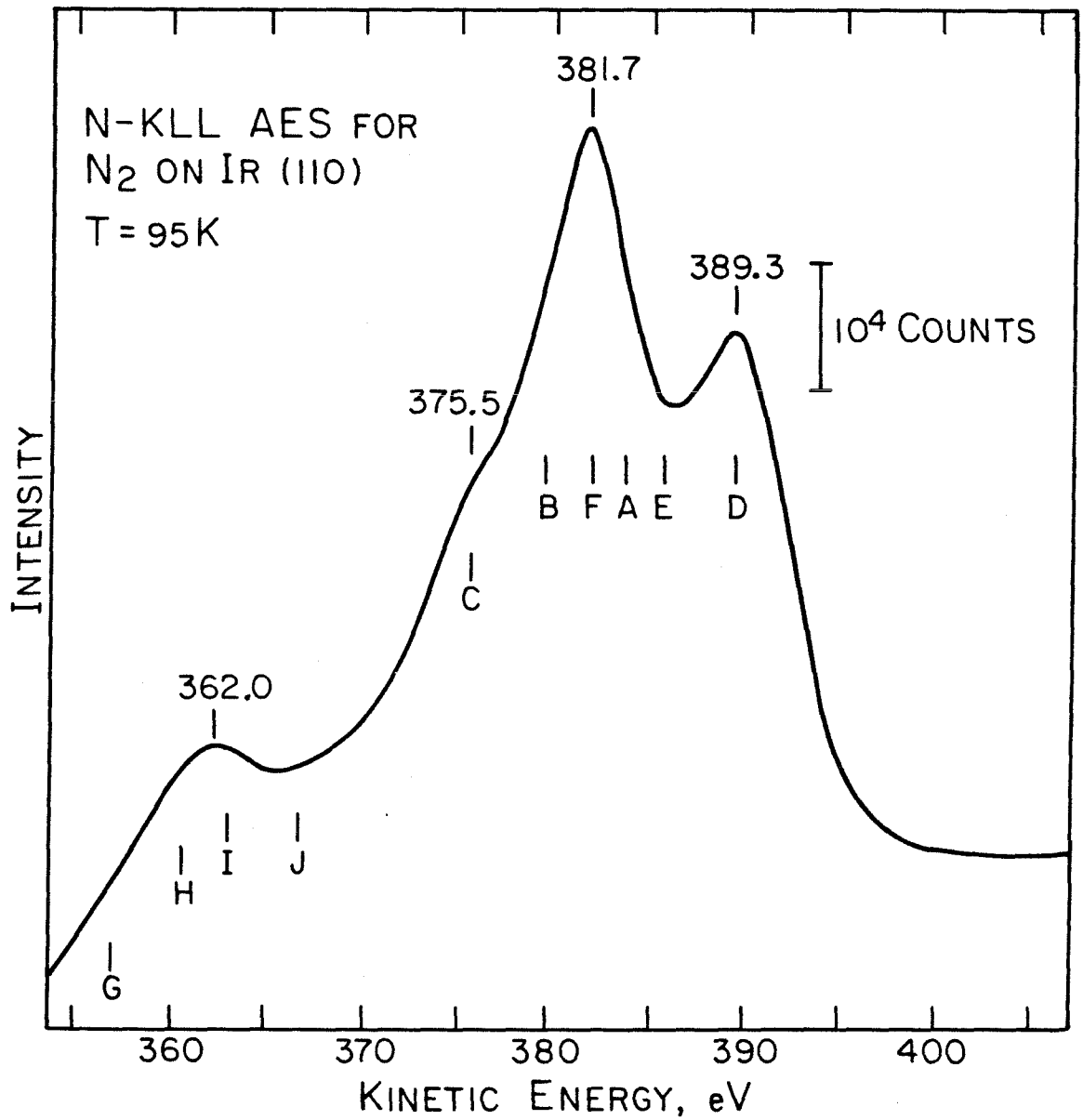
N-KLL AES FOR
N_2 ON IR (110)
T = 95K
381.7
389.3
10^4 COUNTS
375.5
B F A E D
C
362.0
H I J
G
INTENSITY
360 370 380 390 400
KINETIC ENERGY, eV

Figure 3

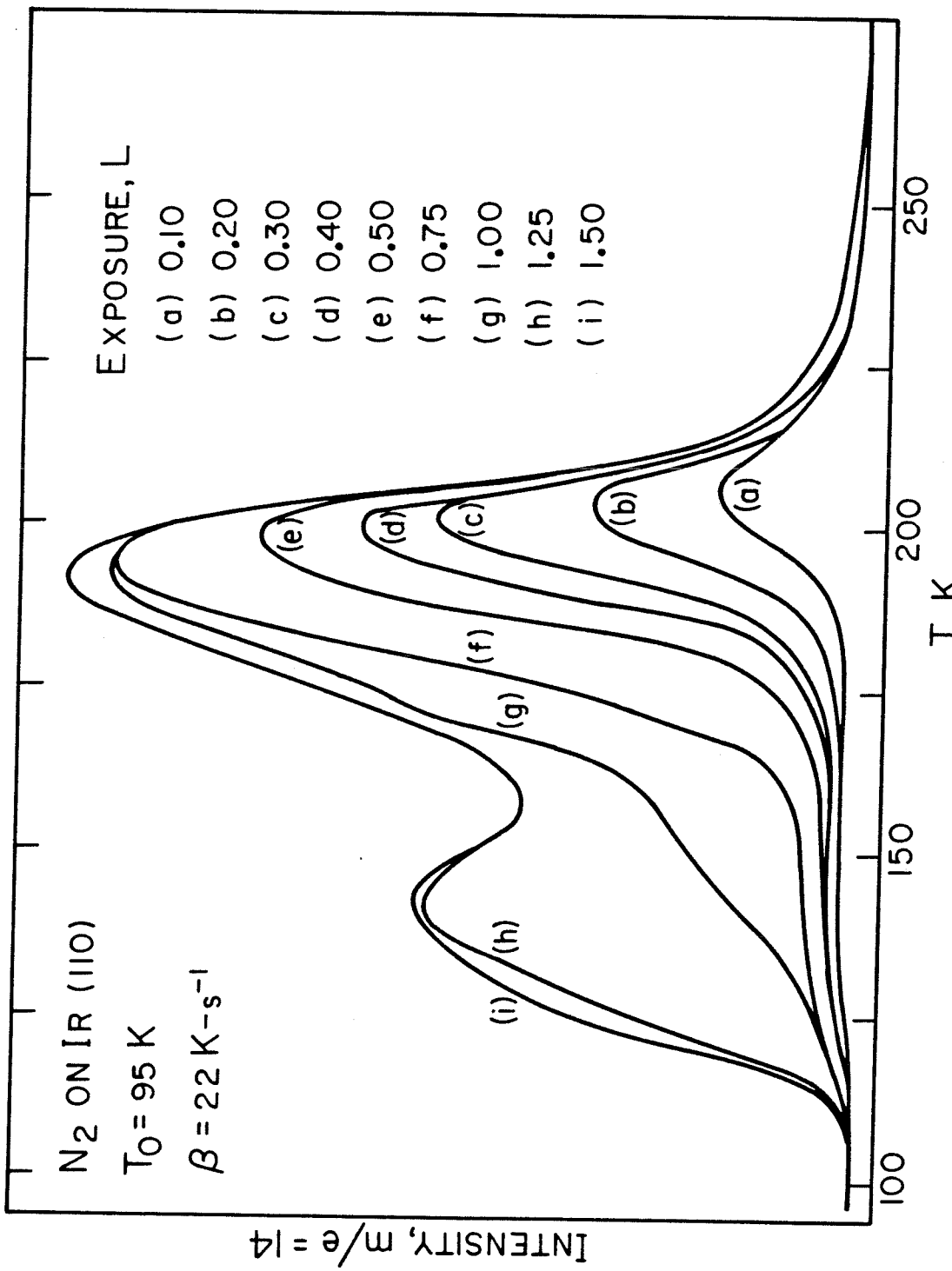
N_2 ON IR (110)
T_0= 95 K
β = 22 K-s^{-1}
EXPOSURE, L
(a) 0.10
(b) 0.20
(c) 0.30
(d) 0.40
(e) 0.50
(f) 0.75
(g) 1.00
(h) 1.25
(i) 1.50
INTENSITY, m/e = 14
T, K
100
150
200
250

Figure 4

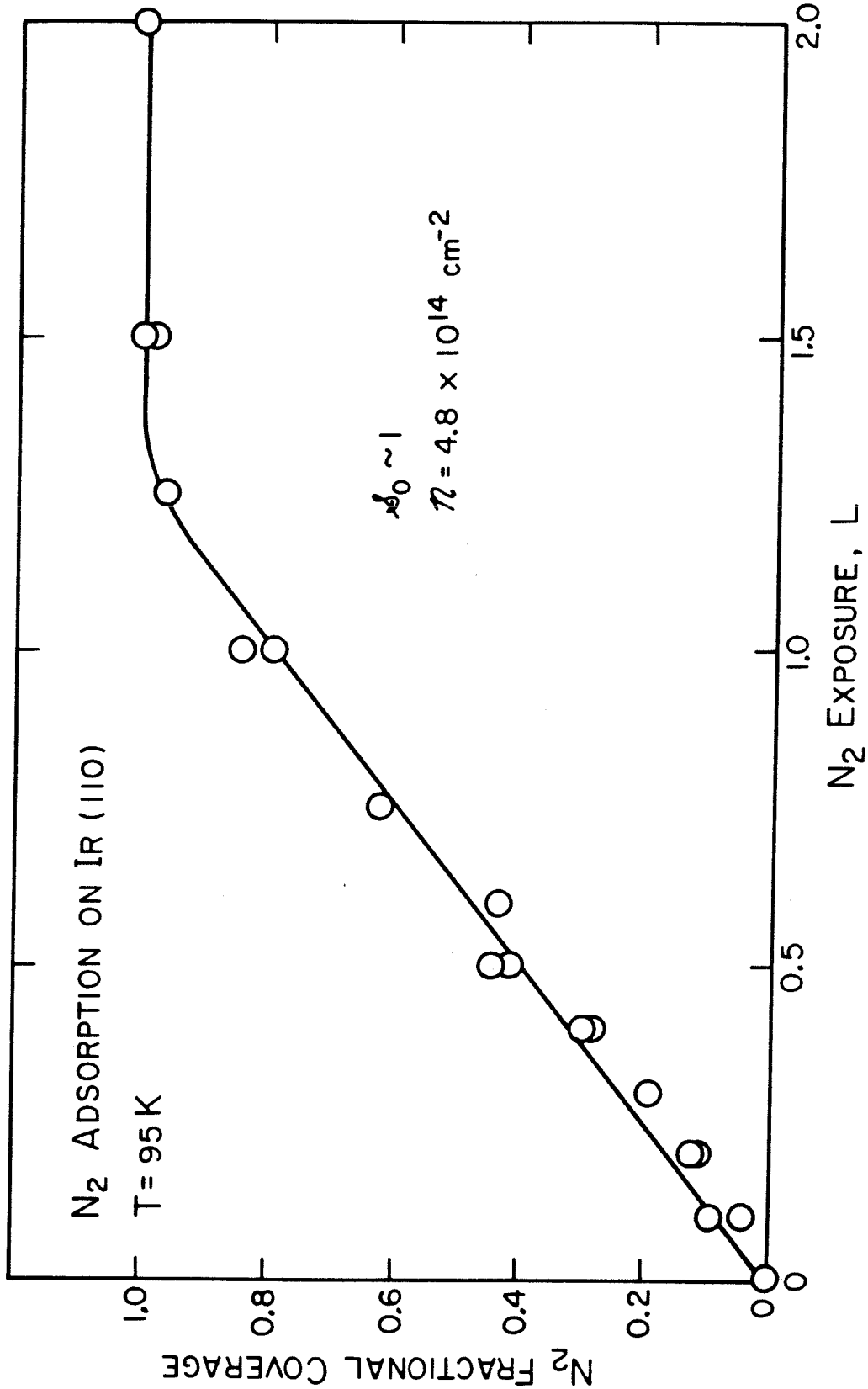
N_2 ADSORPTION ON IR (110)
T = 95 K
$s_0 \sim 1$
$n = 4.8 \times 10^{14}$ cm^{-2}
N_2 FRACTIONAL COVERAGE
N_2 EXPOSURE, L
0
0.2
0.4
0.6
0.8
1.0
0.5
1.0
1.5
2.0

Figure 5

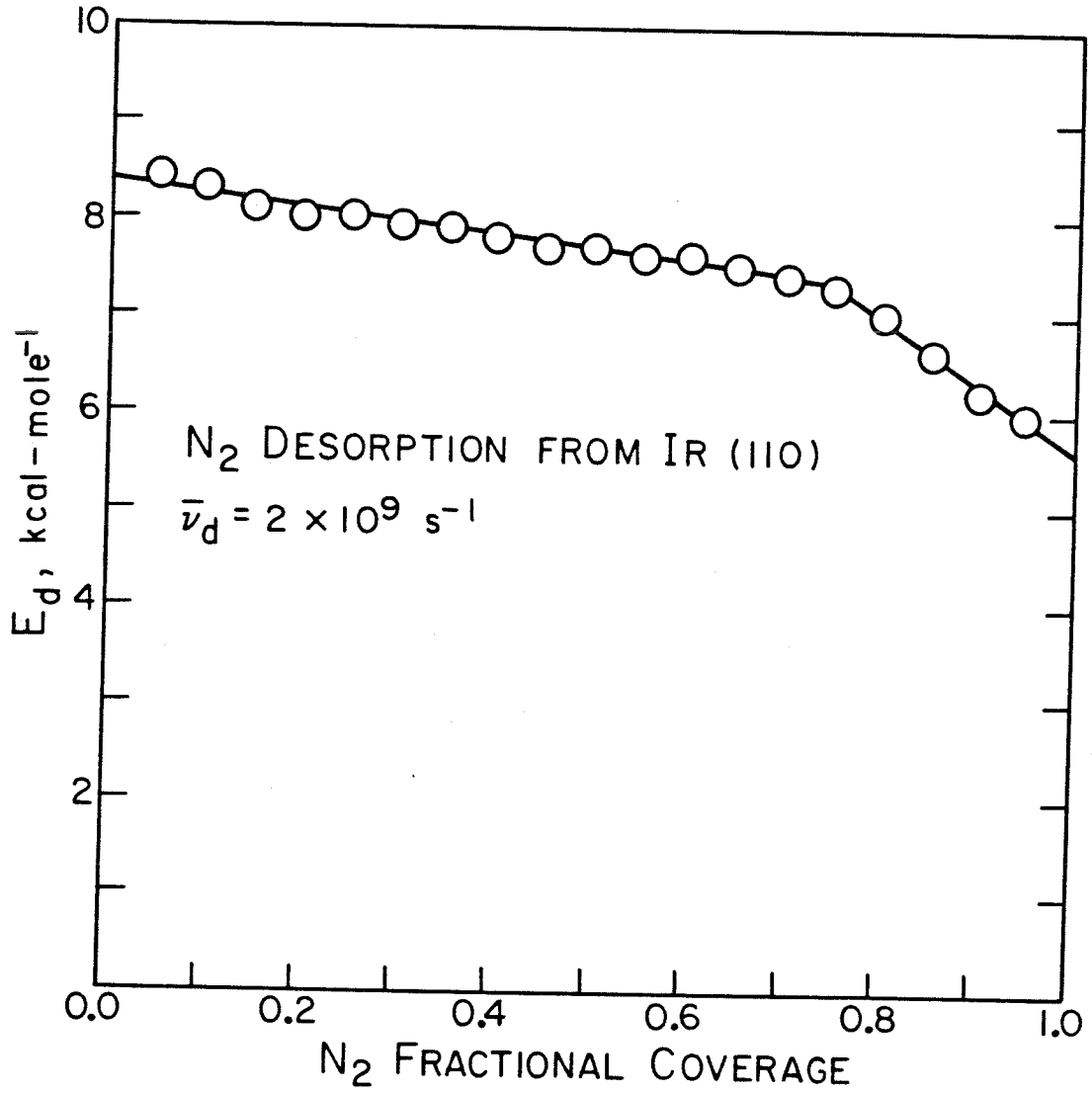
10
8
6
4
2
0.0
0.2
0.4
0.6
0.8
1.0
E_d, kcal-mole^{-1}
N_2 DESORPTION FROM IR (110)
$\bar{\nu}_d = 2 \times 10^9$ s^{-1}
N_2 FRACTIONAL COVERAGE

Figure 6

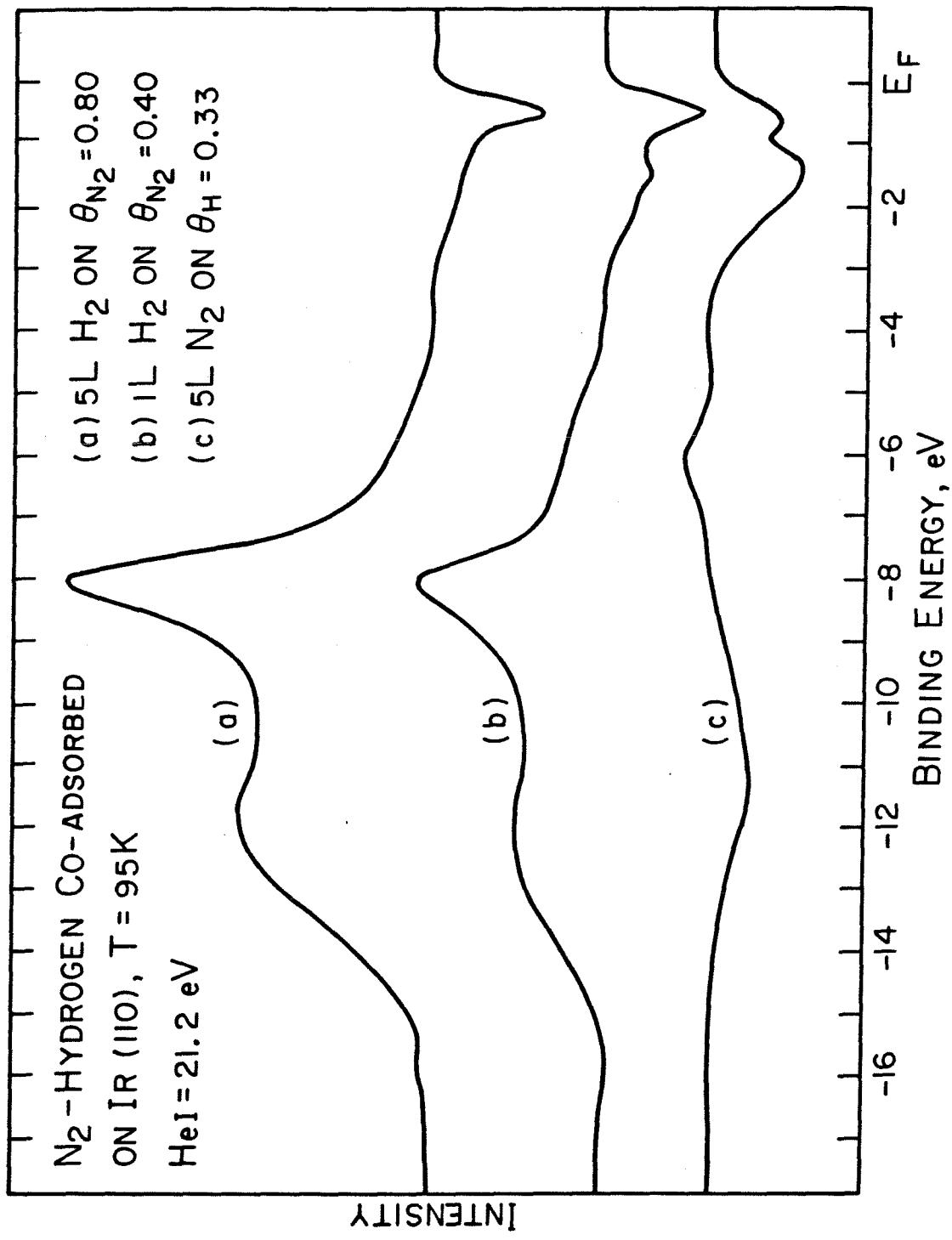
N2-HYDROGEN CO-ADSORBED
ON IR (110), T = 95K
HeI = 21.2 eV
(a) 5L H2 ON θN2 =0.80
(b) 1L H2 ON θN2 =0.40
(c) 5L N2 ON θH = 0.33
(a)
(b)
(c)
INTENSITY
-16
-14
-12
-10
-8
-6
-4
-2
EF
BINDING ENERGY, eV

Figure 7

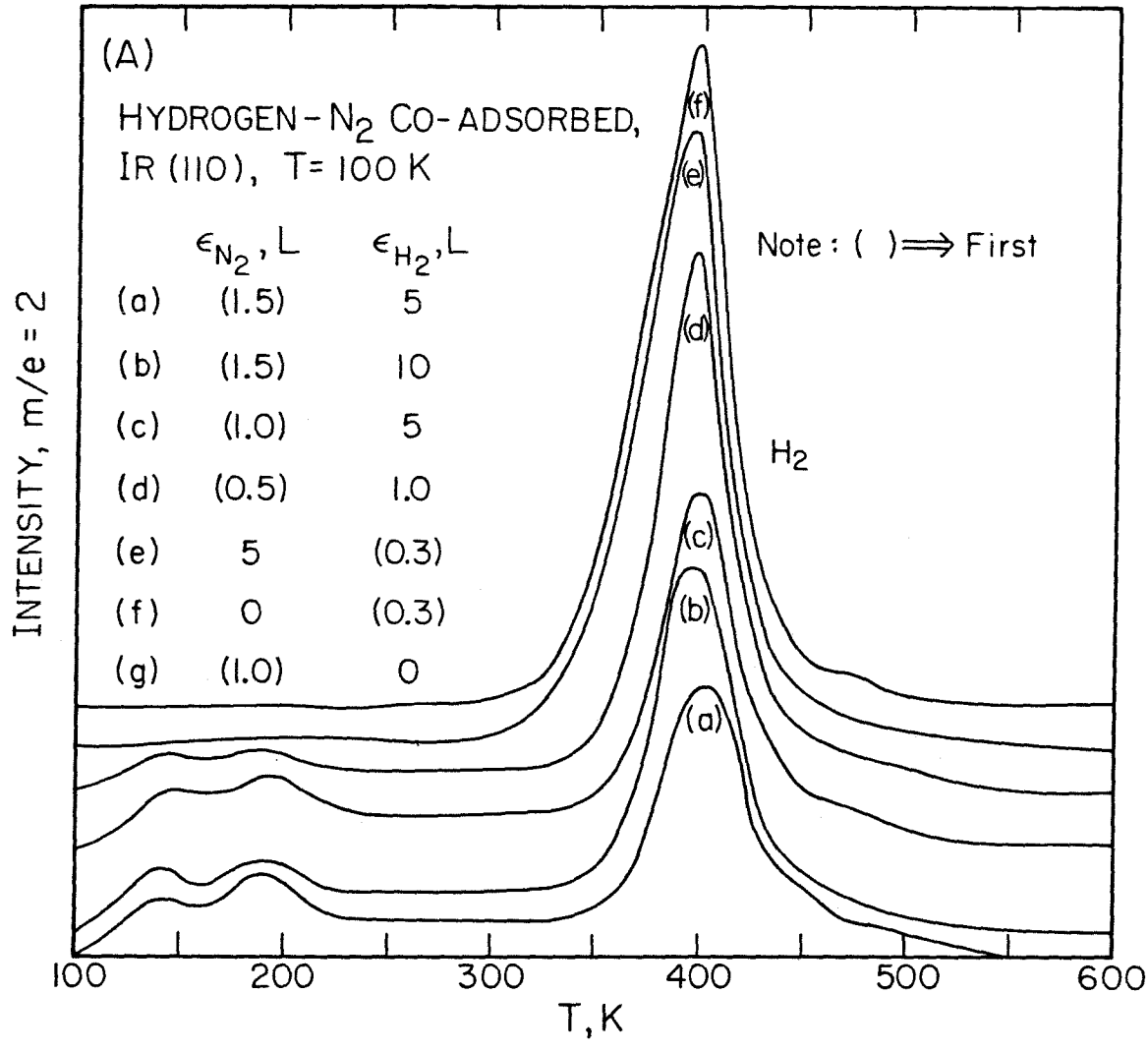
(A)
HYDROGEN - N_2 CO-ADSORBED,
IR (110), T= 100 K
ϵ_{N_2}, L
ϵ_{H_2}, L
(a) (1.5) 5
(b) (1.5) 10
(c) (1.0) 5
(d) (0.5) 1.0
(e) 5 (0.3)
(f) 0 (0.3)
(g) (1.0) 0
Note : ( ) ⟹ First
H_2
INTENSITY, m/e = 2
T, K
100
200
300
400
500
600

Figure 8 (a)

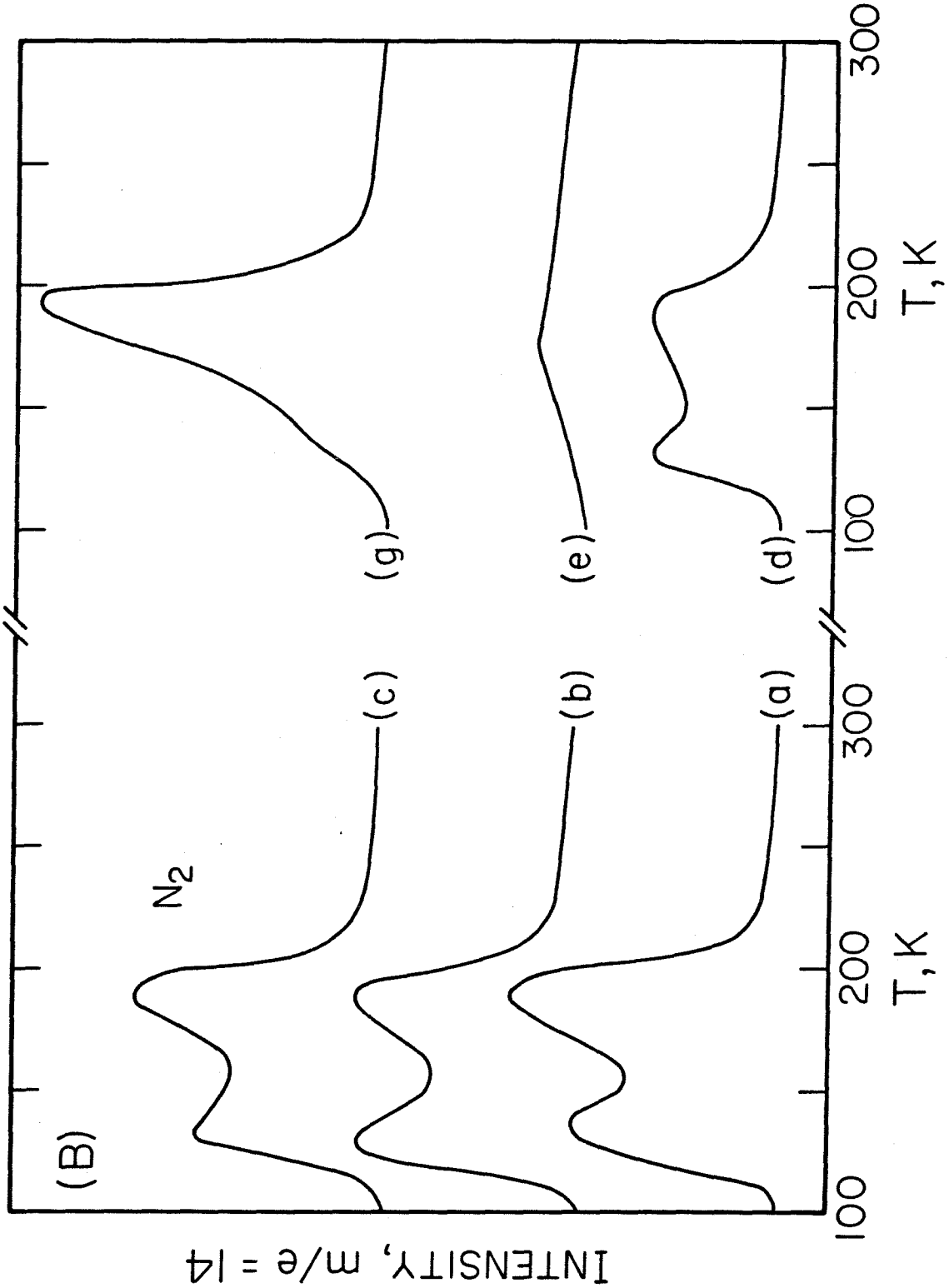

Figure 8(b)

A

N_2 - p(1 g 1)(2×2) ON Ir(110) - (1×2)

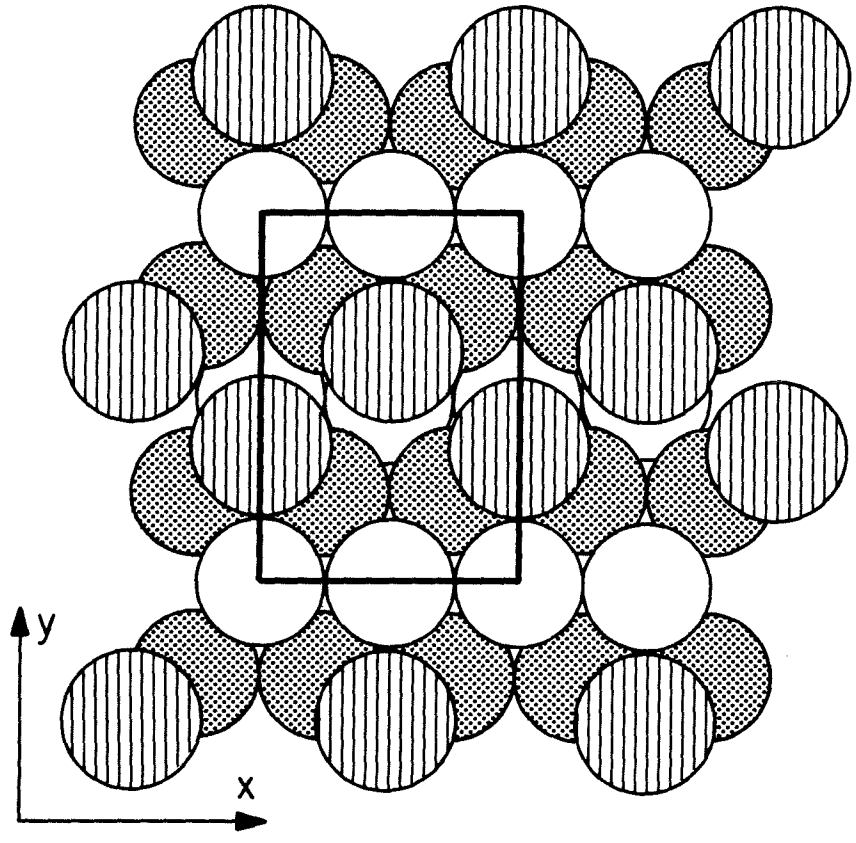

B

Figure 9

APPENDIX D

THE CHEMISORPTION OF NO ON THE (110) SURFACE OF IRIDIUM

(The text of Appendix D consists of an article coauthored with D.E. Ibbotson and W.H. Weinberg that will appear in Surface Science 111, 000 (1981).

Abstract

The chemisorption of NO on Ir(110) has been studied with thermal desorption mass spectrometry (including isotopic exchange experiments), X-ray and UV-photoelectron spectroscopies, Auger electron spectroscopy, LEED and CPD measurements. Chemisorption of NO proceeds by precursor kinetics with the initial probability of adsorption equal to unity independent of surface temperature. Saturation coverage of molecular NO corresponds to 9.6×10^{14} cm^{-2} below 300 K. Approximately 35% of the saturated layer desorbs as NO in two well-separated features of equal integrated intensity in the thermal desorption spectra. The balance of the NO desorbs as N_2 and O_2 with desorption of N_2 beginning after the low-temperature peak of NO has desorbed almost completely. Molecular NO desorbs with activation energies of 23.4-28.9 and 32.5-40.1 kcal-$mole^{-1}$, assuming the preexponential factor for both processes is between 10^{13}–10^{16} s^{-1}. At low coverages of NO, N_2 desorbs with an activation energy of 36-45 kcal-$mole^{-1}$, assuming the preexponential factor is between 10^{-2} and 10 $cm^2 \cdot s^{-1}$. Levels at 13.5, 10.4 and 8.5 eV below the Fermi level are observed with HeI UPS, associated with 4σ, 5σ and 1π orbitals of NO, respectively. Core levels of NO appear at 531.5 eV [O(1s)] and 400.2 eV [N(1s)], and do not shift in the presence of oxygen. Oxygen overlayers tend to stabilize chemisorbed NO as reflected in thermal desorption spectra, a downshift in the 1π level to 9.5 eV and the CPD behavior of NO on the oxygen overlayers.

1. Introduction

The chemisorption of NO on the Ir(110)-(1x2) surface has been studied with thermal desorption mass spectrometry (TDS), X-ray and UV-photoelectron spectroscopies (XPS and UPS), Auger electron spectroscopy (AES), LEED and contact potential difference (CPD) measurements. The motivation for this investigation of NO on iridium is to gain insight into the various elementary chemical reactions that may be important in the dissociation and reduction of NO.

There have been many previous studies of NO on other transition metals, including Pd *(1)*, Ru *(2 - 5)*, Ni *(9 - 11)*, Pt *(8,12 - 17)*, Ir *(18 - 21)* and Rh *(22)*. Adsorption behavior near 300 K ranges from completely dissociative for Ru, Rh and Ni and partially dissociative on Ir to molecular on Pd and Pt. Initial probabilities of adsorption tend to be greater than 0.5 and are usually close to unity. The kinetics of adsorption typically vary weakly with coverage, indicating that often a precursor species is involved.

However, with the exception of Pd *(1)*, heating the surface causes the majority of nitrogen to desorb as N_2 rather than in NO. Near saturation coverage, NO desorbs molecularly on the transition metals. Therefore, the following reactions are generally observed with increasing surface temperature: desorption of NO, dissociation of NO, desorption of N_2 and finally desorption of O_2. The accumulation of oxygen during the first three reactions causes further complications that cannot be separated from the dissociation and desorption reactions. An additional mechanism, not mentioned above, is atom recombina-

tion [$N_{(a)} + O_{(a)} \rightarrow NO_{(g)}$] which is thought to be important on Ir(100)-(1x1) *(21)*. In summary, the successful separation of these competing reactions depends on their relative rates for a particular surface of a particular metal.

During adsorption, a c(4x2) LEED structure due to molecular NO is common to Pd(111) *(1)*, Ru(100) *(2,3)* and Ni(111) *(9)*. Also, a (2x2) structure is observed for NO on Pd(111) *(1)*, Pt(111) *(15,16)* and Ir(111) *(18)*. At saturation, a (2x1) forms on Ru(100) *(2)*, and a (1x1) forms on Ni(100) *(11)*. However, most of these superstructures are formed below room temperature due to the dissociative behavior of NO on the transition metals.

Generally, the valence region of chemisorbed NO exhibits three emission ranges which are near 2 eV, 7.3 - 10.5 eV and 13.9 - 15.2 eV relative to the Fermi level, E_F, of each metal. The first region falls in the metallic d-band, which makes the NO orbital less visible, but this is attributed to the singly-occupied 2π level of NO coupling to the metal. The second region from 7.3 to 10.5 eV contains the 1π and 5σ levels of NO. However, the separation and assignment of these levels are rather ambiguous. Using either HeI or HeII radiation, only one peak is observed on Pd(111) *(1)*, Ru(100) *(8)*, Pt(100) *(8,12)* and Ni(111) *(9)* near 9 eV. On Ru(001) *(6)*, Ir(111) *(18,20)*, Ir(100) *(18)* and Ni(100) *(23)* multiple features appear in the UP spectra. Different assignments have been made for the various metals. Multiple sites occupied by NO may give different emissions which is the case for Ru(001) *(6)* and is suggested by the data of one study on Ir(111) *(20)*. Multiple features have been assigned also to separated 1π and 5σ orbitals on the (111) and (100) surfaces of Ir *(18)* and on Ni(100) *(23)*. In this case, the ordering of the levels is subject to disagreement.

Angular-resolved photoemission results on Ni(100) show that the 1π orbital lies higher in energy than the 5σ orbital of NO *(23)*. However, on Ir(111) and Ir(100), the assignment of these orbitals was reversed by assuming the same relative intensity variation of the two levels for adsorbed NO as for gas phase NO *(18)*. Bent bonding was suggested in both cases *(18,23)* for NO on Ir and Ni, even though the two studies assign the 1π and 5σ orbitals differently. This issue will be discussed further with the present results for NO chemisorbed on Ir(110). Finally, the least ambiguous assignment is for the lowest lying emission which corresponds to the 4σ orbital of NO.

Bent bonding and multiple site adsorption may be inferred through XPS measurements as well. On Ru(001) *(6)* and Ir(111) *(19,20)*, two peaks are observed in the O(1s) region near 531 eV and are attributed to multiple site occupation. For Ru(001), EELS *(5)* and TDS results *(7)* support this conclusion. The difference between O(1s) and N(1s) binding energies for NO chemisorbed on Pt(100) prompted the suggestion that NO bonds in a bent geometry, drawing on analogies to metal nitrosyls *(12)*. Upon dissociation, the N(1s) and O(1s) core levels show peaks near 397 and 529 eV, respectively, on the transition metals.

Evidence that linear and bent bonding as well as multiple site participation occurs for NO indicates the complex adsorption behavior for NO. The desorption behavior is equally complex, considering the competition between desorption of N_2 and NO, dissociation of NO and the accumulation of oxygen. The present investigation of NO on Ir(110) will provide a comparative study to the previously mentioned results. In addition to examining the molecular

phase of NO, coadsorption studies of NO on oxygen overlayers will be presented. Since oxygen remains on the surface in appreciable concentrations as NO decomposes and N_2 desorbs, the adsorption of NO on oxygen overlayers will lend further insight into the reduction of NO by hydrogen performed on the Ir(110) surface *(24)*.

2. Experimental Procedures

The experiments were performed in an ion pumped stainless steel belljar that has been described previously *(25,26)*. The base pressure for these experiments was below 2 x 10^{-10} torr of reactive contaminants. The clean Ir(110) surface shows a (1x2) reconstruction, which is a surface with every other row of Ir atoms missing in the [001] direction *(27)*. The surface may be visualized as alternate rows and troughs exposing (111) planes which are inclined to one another. Isotopic ^{15}NO was used to separate $^{15}N_2$ desorption from any spurious effects due to CO (m/e = 28). Hereafter, ^{15}NO and $^{15}N_2$ will be referred to only as NO and N_2, with the exception of the figure captions.

Exposures of the surface to NO were carried out both with a leak valve and with a directional beam doser that has not been described previously. With the exception of the LEED and contact potential difference (CPD) measurements, all the exposures were performed by the doser, once it was calibrated in Langmuirs. The doser consists of a baffled stainless steel tube capped with a glass capillary array. During dosing, the crystal is positioned approximately 3 mm from the doser face, which places the crystal in line-of-sight of the mass

spectrometer. The beam pressure to background pressure ratio is approximately 100:1. Gas is admitted to the dosing line by a capillary leak, the dosing line being pumped by a baffled, two-inch diffusion pump. Exposures by the beam doser are in torr-s where the pressure refers to the pressure in the storage bulb behind the capillary leak. Calibration of the exposure units (torr-s) of the beam doser to Langmuirs (L) was accomplished by comparison of the exposure needed to cause the appearance of a thermal desortion feature of NO (see Section 3) by the leak value and the doser. The result is that 7.2 ± 0.4 torr-s is equal to 1.0 L.

It is well known that NO interacts strongly with stainless steel. To insure that the stainless steel exposed in the belljar was as passive as possible, 1 x 10^{-7} torr NO was admitted after a bakeout, for one hour. Thereafter, only O_2 and NO were introduced into the system. During any leak valve exposure, less than 2% of the NO was converted to N_2 and the CO partial pressure increased by less than 5% over a period of a half hour. In all cases, doser exposures produced negligible amounts of background contamination.

3. Adsorption and Desorption Kinetics

When NO is exposed to Ir(110) at low temperature and the substrate is heated, both N_2 and NO are observed to desorb between 300 and 800 K, depending on the initial coverage of NO. Oxygen remaining on the surface, after all nitrogen species are removed, desorbs as O_2 above 900 K and shows the same shape as seen for oxygen desorption alone *(28)*. No other desorption products,

such as N_2O or NO_2 were observed. Figures 1(A) and 1(B) present the thermal desorption spectra for N_2 and NO, respectively, at a heating rate of 27 K - s^{-1}. Three exposure ranges of NO may be separated, as seen from the NO and N_2 desorption curves in Fig. 1: (1) $\varepsilon < 0.33$ L, (2) $0.33 < \varepsilon < 1.7$ L and (3) $\varepsilon > 1.7$ L. These regimes will be discussed in turn.

At low exposures of NO only N_2 desorbs, as seen, for example, in Fig. 1(A), curve (a). The desorption maximum is near 650 K and the shape is symmetric, suggesting second-order kinetics for desorption. Furthermore, this shows that the NO has dissociated below 500 K at this exposure of NO (0.26 L) and this heating rate (27 K - s^{-1}). The next exposure, 0.33 L NO, shows a second peak appearing on the low temperature side of the original N_2 feature. By an exposure of 0.83 L, the shape of the N_2 thermal desorption trace has changed considerably. The onset in N_2 production becomes much more abrupt and asymmetric. The third N_2 feature that appears (at 520 K for an exposure of 0.83 L) becomes dominant, shifts to lower temperature and sharpens with increasing exposure. At an exposure of 0.83 L, some NO desorption is observed as shown in Fig. 1(B). Near an exposure of 1.7 L, a second feature appears in the NO thermal desorption spectra that increases in intensity as saturation coverage is approached. Estimates of the activation energies for the desorption of N_2, the dissociation of NO and the desorption of NO may be calculated from the thermal desorption spectra. Due to the observed complexity of the desorption spectra apparent in Fig. 1, only peak temperatures and "normal" preexponential factors (ca. $10^{13} - 10^{16}$ s^{-1})will be assumed in order to estimate bounds on the activation energies of these competing reactions.

For low exposures of NO, only N_2 desorbs. Assuming that spectrum (a) in Fig. 1(A) represents adatom-adatom recombination as the rate limiting step, the activation energy for N_2 desorption may be estimated to lie between 36 and 45 kcal-mole^{-1} (for $10^{-2} \leq \nu \leq 10^{1}$ cm^2 – s^{-1}). The desorption peak temperature, 650 K, is comparable to that observed for N_2 desorbing from dissociated NO on Pd(111) *(1)* and polycrystalline Rh *(22)*. Higher exposures of NO causes the onset of N_2 desorption to become more abrupt and asymmetric, and this may well indicate that the rate of dissociation of NO is now rate limiting. The shift in peak temperature in Fig. 1(A) for the desorption of N_2 [spectra (c) - (h)] does not imply second-order kinetics; rather, it is related to the changing activation energy for the dissociation of NO, E_{dis}(NO)and is first order. Thus, the desorption peak temperature of N_2 is related to an *upper* bound for E_{dis}(NO). Correlating E_{dis}(NO) with the initial coverage of NO (see adsorption kinetics below) gives $E_{dis}(NO) = (33.4 - 10.3\ \Theta_{NO})$ kcal-mole^{-1} for $0.3 \leq \Theta_{NO} \leq 0.8$ if ν_{dis} is equal to 10^{13} s^{-1} and $E_{dis}(NO) = (39.6 - 10.3\ \Theta_{NO})$ kcal-mole^{-1} if ν_{dis} is equal to 10^{16} s^{-1}. Therefore, E_{dis}(NO) decreases with increasing Θ_{NO} until the yield of N_2 saturates. The activation energy for the first order desorption kinetics of NO may be estimated from the thermal desorption spectra of Fig. 1(B). The low temperature peak near 400 K represents the desorption of NO from an oxygen-free surface, whereas the high temperature peak near 550 K represents desorption of NO from a surface containing significant concentrations of oxygen. The desorption energy for the former is between approximately 23.4 - 28.9 kcal-mole^{-1} and for the latter approximately 32.5 - 40.1 kcal-mole^{-1}, for a preexponential factor for desorption between 10^{13} to 10^{16}

s^{-1}. Comparing desorption and dissociation energies of NO estimated from Fig. 1 suggests that three regimes of desorption are important. At saturation coverage, some NO desorbs near 400 K (~17%) before appreciable dissociation occurs followed by N_2 desorption near 430 K. Finally, the desorption rates of N_2 and NO become comparable above 450 K.

Recently, it was concluded that recombination of nitrogen and oxygen adatoms becomes important for the high temperature desorption feature of NO on Ir(100) *(21)*. Precoverages of ^{18}O exchanged with the high temperature feature of NO, whereas the lower temperature desorption was unperturbed. This is the case also on Ir(110). Enriched (23 at. %) ^{18}O was exposed to various precoverages of NO at 100 K. For low exposures of oxygen (< 5 L), the high temperature feature in Fig. 1(B) exchanges statistically. Therefore, the exchange experiment on Ir(110) is conclusive that the first peak is molecular in nature only and the second peak is at least partially due to the recombination process. In the N(1s) region of binding energy, no nitrogen atoms were detectable by XPS at a sensitivity level of approximately 0.1 ML if the desorption was terminated between 380 K and 500 K and the crystal cooled (see Section 4). Thus, although the high temperature peak of NO is at least partially due to nitrogen and oxygen adatom recombination, the concentration of nitrogen adatoms is always small. During desorption, preadsorbed oxygen inhibits the formation of N_2 and shifts the desorption population of NO to the higher temperature peak.

To obtain the adsorption kinetics of NO on Ir(110), integration of the thermal desorption spectra for NO and N_2 with respect to time is necessary. Also, a

calibration between the integrated intensities of NO and N_2 and the saturation coverage of NO is needed. Since at low exposures only N_2 and O_2 desorb, a convenient calibration for N_2 exists via a mass balance with oxygen, the coverage of which is known *(28)*. This gives the initial coverage of NO and the initial probability of adsorption of NO, S_0. The relative mass spectrometer intensity to N_2 and NO is found by monitoring the saturation coverage of NO, which was measured by comparing O(1s) intensities of NO and oxygen by XPS. The saturation coverage measured for NO at 100 K is 9.6×10^{14} cm^{-2} ($\pm$ 5%). The adsorption kinetics of NO on Ir(110) at 100 K may be deduced from Fig. 2 where S_0 is unity. The kinetics are fit well by a first-order Kisliuk precursor model wth the parameter K = 0.3, where K = 0 corresponds to Langmuir kinetics (zero lifetime of the precursor), and K = 1 corresponds to a constant probability of adsorption (infinite lifetime of the precursor) *(29)*. A high value of S_0 and precursor kinetics for the adsorption of NO on the transition metals are common *(1,3,4,9,10,13)*. The relative yields of N_2 and NO from thermal desorption are shown in Fig. 3. At saturation coverage of NO, 35% of the nitrogen on the surface desorbs as NO with approximately equal amounts in each feature [Fig. 1(B)], and 65% desorbs as N_2.

In summary, the desorption kinetics of N_2 and NO from an adlayer of NO depend strongly upon one another. The desorption kinetics of N_2 at medium to high coverages of NO reflect the rate of dissociation of NO. For the desorption of NO, two features develop fully at saturation coverage, one of which represents desorption from an oxygen-free surface and the other of which, a higher temperature feature, represents desorption from a surface partially

covered with oxygen. The adsorption kinetics follow a first-order precursor model at 100 K with an initial probability of adsorption of unity. At saturation coverage of NO, 65% desorbs as N_2 and 35% desorbs as NO. The adsorption kinetics of NO at higher temperatures will be discussed in Section 5.

4. UPS, XPS and AES Measurements of NO

Presented in Fig. 4 are HeI difference spectra of NO adsorbed at various coverages on Ir(110) at 100 K. Three levels are observed at 8.5, 10.4 and approximately 13.5 eV below the Fermi level, E_F. The lowest lying level at 13.5 eV may be assigned immediatelly as the 4σ orbital of molecularly chemisorbed NO. However, the levels at 8.5 and 10.4 eV are less straightforward in assignment. Gas phase ionization potentials for the 4σ, 5σ, 1π and 2π orbitals of NO are 21.7, 19.5, 15.7 and 9.3 eV, respectively. Assuming that the 4σ orbital for NO adsorbed on Ir(110) and gaseous NO are related by a static shift (8.2 eV), the orbitals of adsorbed NO would require the 5σ to destabilize by 0.9 eV and the 1π to stabilize by 1.0 eV with the premise that the 5σ and 1π levels maintain the same order in energy when NO is chemisorbed. If these levels cross, the 5σ level would destabilize to an even greater extent, and the 1π would stabilize correspondingly further upon chemisorption. It is thought that bonding of NO with the surface is through the 5σ orbital which is weighted toward the nitrogen end of the molecule. Furthermore, a backbonding interaction is assumed to occur through the singly-occupied 2π level, although this orbital is not observed in the spectra of Fig. 4. If NO bonds in a linear fashion to the

metal, the 5σ should stabilize. However, bent bonding has been suggested for NO on Pt(100) *(12)*, Ir(111) *(18)*, Ir(100) *(18)* and Ni(100) *(23)*. Hence, rehybridization of valence orbitals may make a direct comparison between gaseous NO and adsorbed NO inappropriate.

Although bent bonding has been inferred for NO on Ir *(18)* and Ni *(23)*, the 5σ and 1π orbital assignments disagree. For Ir(111) and Ir(100), the relative intensity variation with photon energy of 5σ and 1π orbitals in the gas phase was assumed to maintain for adsorbed NO, and it was concluded that the 5σ and 1π orbitals cross in energy when the NO is chemisorbed *(18)*. For Ni(100), angular-resolved UPS and photon energy variation were employed to show that the 5σ and 1π levels do not cross, and the 1π orbital still lies higher in energy *(23)*. The 1π orbital showed an increase in intensity as the photon energy decreased *(23)*. Our present HeI results on Ir(110) compared to HeII results on the same surface *(20)* show the same trend. Moreover, an extensive investigation of $Cr(NO)_4$ placed the 1π level higher than the 5σ one for this metal nitrosyl *(30)*. Therefore, the most probable assignment of NO on Ir(110) is that the 5σ and 1π orbitals are at 10.4 and 8.5 eV, respectively. Data presented in Sections 3, 6 and below indicate that NO is stabilized by the presence of adsorbed oxygen. Results presented below show that the 1π level shifts from 8.5 to 9.5 eV when NO is coadsorbed with oxygen, an observation which is not understood at this time.

Annealing experiments were performed for low coverages of chemisorbed NO to determine above what temperature dissociation takes place. In Fig. 5 are shown UP difference spectra for two coverages of NO comparing annealed

and unannealed surfaces. Adsorption of 0.19 ML and 0.43 ML of NO on the clean surface at 100 K yields the spectra shown in Figs. 5(a) and 5(c), respectively. Annealing these two coverages of NO to 400 K yields the spectra shown in Figs. 5(b) and 5(d), respectively. It is apparent that for 0.19 ML coverage, dissociation has taken place by 400 K as judged by the disappearance of the molecular levels of NO and the appearance of a broad level near 5.7 eV which is due to emission from O(2p) and N(2p) orbitals. However, annealing 0.43 ML of NO does not cause complete dissociation since emission from the NO molecular orbitals is still observed. In fact, the peak intensities at 8.5 eV and 10.5 eV in Fig. 5(d) are equal to those in Fig. 5(c), although in Fig. 5(d) the 4σ orbital at 13.5 eV is not observed, and the intensity decrease near E_F is larger which is due to NO and oxygen coadsorbed. No desorption of either NO or N_2 occurs below 400 K for either initial coverage, so the changes in the UP spectra reflect a chemical reaction occurring *on the surface*. Therefore, depending on the initial coverage of NO, annealing to 400 K causes all or part of the overlayer of NO to dissociate.

UP difference spectra of coadsorbed NO and oxygen are shown in Fig. 6. The UP spectrum for the saturation coverage of NO on the initially clean surface is reproduced in Fig. 6(a) for comparison. Whether chemisorbed oxygen is converted to an oxide [curve (b)], or not [curve (c)], a shift in the highest lying (1π) level of NO is observed, from 8.5 eV on the clean surface to 9.1 eV in curve (b), and to 9.5 eV in curve (c). The other two levels at 10.5 eV and 13.5 eV do not shift, however. The substrate structure has a small effect since in curve (b) the substrate is (1x1) and in curve (c) it is (1x2). The presence of oxygen

on the surface is more important, in agreement with the CPD results in Section 6. In addition to the shift of the 1π level, its relative intensity with respect to the 5σ peak at 10.5 eV increases as the coverage of oxygen increases.

A downshift in at least one of the levels in the valence region and the desorption of NO at higher temperatures when NO is chemisorbed on oxygen overlayers are consistent with the conclusion that NO is stabilized by the presence of oxygen on Ir(110). Site blocking by oxygen may also inhibit dissociation of NO as found for NO on Ru(001) *(5,6)*. However, since the CPD of NO reflects the amount of oxygen present regardless of the substrate structure [(1x1) or (1x2)], the interaction to stabilize NO may be a charge transfer effect through the metal about each oxygen atom (see Section 6).

Spectra of the N(1s) and O(1s) regions of binding energy are shown in Fig. 7. Peaks due to NO are clear in spectra (a) at 531.5 eV for the O(1s) level and 400.2 eV for the N(1s) level. Saturating the surface with NO at 400 K, cooling to 95 K and exposing the surface further to NO to insure saturation results in two features in the O(1s) level at 531.5 and 528.8 eV due to NO and oxygen adatoms, respectively, as seen in Fig. 7(b). The N(1s) level remains unchanged at 400.2 eV, and no intensity is observed at 397 eV, where the N(1s) level of nitrogen adatoms occurs *(24)*. Annealing a saturated overlayer of NO to 430 K [Fig. 7(c)] gives the same O(1s) peaks as in spectrum (b), but the intensity due to molecular NO has decreased as a consequence of desorption. Again, no nitrogen adatoms are observed in the N(1s) spectrum. Although no nitrogen adatoms are detected by XPS in Figs. 7(b) and 7(c), they may be present in concentrations of less than 0.1 ML which is the detection limit found here.

Furthermore, in spectrum (b) the surface was saturated with NO after partial dissociation had occurred, which tends to displace nitrogen adatoms from the surface by the desorption of N_2. Thus, the XPS results verify the TDS results presented in Fig. 1 that oxygen accumulates on the surface when the overlayer of NO is heated slightly above 400 K.

Finally, O-KLL and N-KLL Auger transitions are presented in Fig. 8 for a saturated overlayer of NO at 95 K. The electron beam current density used was 10^{-8} amp - mm^{-2} at an energy of 2 keV. Electron beam exposures to the surface were limited to 10 min. before a fresh surface was prepared in order to minimize beam induced dissociation. In Fig. 8 the peak positions are nearly identical to those found for X-ray induced Auger transitions observed of NO on Ru(001) *(6)*, but they are somewhat different from gas phase spectra *(31)*. The spectra of Fig. 8 point up very nicely the similarity of AES transitions for the same molecule adsorbed on different metals. An additional feature in the N-KLL region at 371 eV, not seen on Ru(001) *(6)*, is attributed to nitrogen atoms formed by electron induced dissociation of NO. Nitrogen atoms formed during the steady state reaction between NO and H_2 *(24)* show an Auger transition here.

5. Isothermal Decomposition of NO

A series of mass spectrometric experiments at various constant surface temperatures was performed in order to measure the rate of NO adsorption and the rate of N_2 desorption on Ir(110). The calibration of the mass spec-

trometer intensity for NO (in absolute coverage units) and of the relative intensity of NO and N_2 allows the adsorption kinetics of NO to be measured at a given surface temperature (see Section 3).

The Ir crystal was exposed to NO by the beam doser at a constant beam pressure (approximately 9×10^{-8} torr). Since the doser and the crystal were positioned so that part of the molecules scattered from the crystal was in line-of-sight of the mass spectrometer, the intensities of NO and N_2 could be measured directly. Therefore, the decrease in the NO intensity is due to adsorption, and the increase in the N_2 intensity is due to desorption. Prior to each experiment, the crystal was cleaned by annealing above 1600 K and then was cooled to the appropriate surface temperature. The crystal was moved in front of the doser, and N_2 and NO intensities were monitored as a function of time until no further changes occurred.

Results of an experiment at 400 K, representative of other surface temperatures, are shown in Fig. 9. Shown in Fig. 9 are the adsorption rate of NO, the desorption rate of N_2 and the integrated intensities of NO and N_2 as a function of exposure (or equivalently time). The rate of adsorption of NO is inversely proportional to the measured gas phase partial pressure. It is clear from Fig. 9 that N_2 does not desorb immediately. However, for small exposures of NO, decomposition does occur at 400 K as seen, for example, from the UPS results in Fig. 5. Desorption of N_2 appears only after sufficient NO adsorbs, either associatively or dissociatively. Consequently, the activation energy for the desorption of N_2 decreases with surface coverage. Also, the initial adsorption rate of NO remains the same as that seen at 100 K (Fig. 2), so the initial

adsorption kinetics are independent of temperature and S_0 is unity. Interestingly, near the maximum in the rate of desorption of N_2, a small but reproducible change in the rate of adsorption of NO occurs, presumably due to the desorption of N_2 and the accumulation of oxygen.

The integrated mass spectrometric intensities, calibrated in absolute coverage units, represent the total amounts of NO that is adsorbed and of N_2 that is desorbed during the experiment. Subtraction of these curves gives directly the coverage of nitrogen (as NO or N) present on the surface at any point of exposure (time). The total coverage of N present on the surface as a function of exposure at various surface temperatures is shown in Fig. 10. Results from the TDS measurements for adsorption at 100 K are reproduced in Fig. 10(a) for comparison and are offset for clarity. For temperatures below 350 K, where desorption is negligible (cf. Fig. 1), the adsorption kinetics are identical. Although the initial rate of adsorption remains constant between 400 and 700 K, the shape of the curves in Fig.10 changes due to desorption of N_2 and NO. A relative maximum occurs in the coverage of N as a function of exposure since N_2 desorption and NO adsorption are competitive reactions. As the temperature increases, the relative maximum in the coverage of N appears at lower exposures and decreases in magnitude. Above 600 K, no nitrogen species are present once the oxygen uptake is complete. Only NO is detected by XPS on the surface at the end of each experiment if any nitrogen species are still present, so nitrogen atoms ($\geq$ 0.1 ML) are not favored once the surface is at steady state. Oxygen tends to stabilize the NO that remains on the surface with respect to dissociation.

The total yields of adsorbed NO and desorbed N_2 are shown in Table 1. The coverage of N left on the surface at steady state is the coverage of NO to a good approximation. By mass balance, the coverage of oxygen coadsorbed with the remaining NO is equal to the amount of N_2 desorbed since no other species desorbs. The maximum coverage of oxygen is near 0.5 ML, and this is associated with the formation of a c(2x2)-O superstructure on the (1x1) Ir surface (see Section 7). This oxygen superstructure inhibits further dissociation of NO as it does for oxygen adsorption at these temperatures *(28)*. Since the NO remaining on the surface is at steady state with the pressure of the beam doser, an estimate may be made for the activation energy of desorption of NO, E_d(NO), between 400 and 621 K. The flux of NO onto the surface is equated to the desorption flux of NO, and the preexponential is assumed to be $10^{13} - 10^{16}$ s^{-1} as in Section 3. The results for E_d(NO) are shown in Table 1. As the coverage of NO decreases and the coverage of oxygen increases, E_d(NO) increases. These values are comparable to that calculated for the higher temperature peak in TDS, 32.5 - 40.1 kcal-mole^{-1} (half of the NO that desorbs from a saturated layer of NO) associated with a surface on which oxygen adatoms are present.

To summarize, isothermal decomposition measurements of NO on Ir(110) provide complementary information concerning the adsorption of NO either on the clean surface (low temperature) or on a surface with oxygen adatoms present due to the dissociation of NO (high temperature). The initial probability of adsorption maintains near unity regardless of the surface temperature. Approximately 0.5 ML of NO may be decomposed above 500 K, after which no

further dissociation can occur due to the high concentration of oxygen. Estimates for the activation energy for NO to desorb, E_d(NO), agree with the TDS estimate and show that E_d(NO) increases as NO decreases and oxygen increases in coverage.

6. CPD of NO and Coadsorbed NO and Oxygen

Although NO exhibits identical adsorption kinetics for temperatures below 350 K as seen previously, the contact potential difference of NO is different for adsorption at 100 K compared to near room temperature. The CPD of NO adsorbed at 100 K and 317 K are shown in Fig. 11 as a function of fractional surface coverage. At 100 K [curve (a)], the CPD decreases, attains a minimum at -0.085 eV at half a monolayer and increases to a final value of -0.04 eV at saturation. The increase between 0.75 and 0.85 ML is associated with the appearance of a streaked LEED pattern containing a mirror plane or glide plane of symmetry (see Section 7). This superstructure disorders above 0.85 ML, but the CPD does not change further. At 317 K the CPD decreases more strongly, reaches a minimum at higher coverage (-0.115 eV) and increases slightly, to a final value of -0.100 eV at saturation. The change in shape of the CPD with coverage, comparing the two adsorption temperatures, indicates that some dissociation has taken place at 317 K. Assuming the presence of oxygen causes the CPD of NO to be modified, a small precoverage of oxygen was adsorbed, and the CPD was measured for NO [curve (a) of Fig. 12] where Θ_O = 0.13 ML. It is apparent that oxygen does influence the CPD of NO considerably

since the shape of the curve has changed and the magnitude of the decrease is much larger, -0.36 eV. If the change in the CPD is linear in oxygen coverage at low coverages of oxygen, then the amount of NO dissociated at 317 K is less than 5%. Therefore, the CPD of NO on Ir(110) is a sensitive indicator for the dissociation of NO.

Two different effects may occur to alter the CPD of NO when oxygen is present. First, NO may chemisorb on different sites due to the blockage of its preferred sites by oxygen adatoms. Second, a chemical interaction may occur between oxygen and NO on the surface. These two possibilities were investigated by preparing the surface in several different ways with preadsorbed oxygen and recording the CPD of NO as a function of exposure, as shown in Fig. 12. For curves (a), (b), (d), (e) and (g), the substrate is the reconstructed (110)-(1x2) surface with various initial coverages of chemisorbed oxygen. Curves (c) and (f) represent NO adsorbed on the unreconstructed (110)-(1x1) surface which is stabilized by a surface oxide *(28)* with two different coverages of preadsorbed oxygen present. Although the adsorption kinetics are not known so that the exposures of NO cannot be related to coverages on these oxygen overlayers, the trend in the CPD is quite useful to gain insight into the interaction between coadsorbed NO and oxygen. However, it is known that approximately one-half the amount of NO adsorbs on an oxygen-saturated surface as compared to the clean surface, measured by TDS.

Since the adsorption kinetics are not known for NO in these cases, except for curve (g) of Fig. 12 [clean (1x2) surface], the shapes of the CPD curves as a function of exposure are less instructive than the magnitude of the CPD of NO

when the surface is saturated. Noting that the zero of the CPD has been shifted by pairs for clarity in Fig. 12, the CPD of NO at saturation increases in magnitude, but is always negative, as the precoverage of oxygen increases, regardless of whether the substrate structure is (1x1) or (1x2). Moreover, the saturation CPD of NO relative to the *clean* surface [$\Delta\varphi(O) - \Delta\varphi(NO)$] is always between 0 and +0.25 eV when oxygen is preadsorbed. Therefore, the CPD of NO is approximately proportional to the amount of oxygen present and depends much less upon the structure of the substrate. Moreover, the CPD is rather insensitive to the binding site occupied by oxygen since oxygen changes its preferred sites from low coverage ($\theta < 0.25$) to high coverage, and from chemisorbed oxygen to the surface oxide *(28)*. The interaction between NO and oxygen may be described best by through-metal interactions. Oxygen, which is quite electronegative, draws charge from the metal and causes the CPD to increase strongly. Adsorption of NO may then occur more readily near the electron deficient regions of the metal, which may cause the CPD relative to the *clean* surface to change only slightly, as observed. In effect, NO "titrates" the charge induced by oxygen. A similar CPD dependence for one state of NO coadsorbed with oxygen on Ru(001) has been reported *(7)*. As was shown in Section 4, UPS of coadsorbed NO and oxygen indicates a strong interaction between the adsorbates as well.

7. LEED Observations

A clean, well-ordered Ir(110) surface gives a sharp (1x2) LEED pattern,

which is a surface with every other row of Ir atoms missing *(27)*. At 100 K, fractional coverages of NO below 0.75 (exposures below 2 L) produce only a high background intensity which diminishes the intensity of the substrate beams uniformly. At fractional coverages between 0.75 and 0.85 (exposures between 2 and 2.5 L), very broad streaks appear between the rows containing half-order spots. In addition, little or no intensity is observed above and below the (00) beam. Although the streaks did not coalesce even with annealing cycles from 100 to 250 K, the absence of intensity where (n ± ½ 0) beams would occur indicates that a mirror plane or glide plane of symmetry lies along the [001] direction, along the rows of Ir atoms. At fractional coverages above 0.85 (exposures above 2.5 L), the streaking diminished until only a disordered superstructure was present. Since no ordered superstructures were found with the exception of the one mentioned above, it is not possible to assign any surface structure to NO on the (1x2) substrate.

Annealing a saturated overlayer of NO above 400 K causes streaking reminiscent of chemisorbed oxygen adatoms *(28)*. Furthermore, annealing a saturated overlayer to 750 K and cooling forms a sharp oxygen c(2x2) superstructure which occurs on the oxidized Ir(110)-(1x1) surface *(28)*. A c(2x2) superstructure can be formed easily also by exposing NO to the surface above 700 K until the surface is saturated. Saturating the surface on which the c(2x2)-O superstructure is present at 300 K with NO forms a coadsorbed (1x2) superstructure having sharp integral order spots and large, diffuse half-order spots. It is not likely that this pattern is due to the oxidized (1x1) surface relaxing back to a (1x2) superstructure, since this does not occur for NO

adsorbed on the (1x1) oxide. Since the coverages of the two adsorbates are known, 0.5 ± 0.05 ML, a structure may be postulated. For oxygen, an analysis of the c(2x2)-O superstructure shows that it binds on top of the rows of Ir atoms in short-bridged sites *(32)*. A possible structure for coadsorbed NO and oxygen on Ir(110)-(1x1) is one in which oxygen still occupies its preferred short-bridged sites, but half of the oxygen adatoms have shifted to yield a (1x2) superstructure. The NO molecules may then distribute randomly on the remaining open areas between the rows of oxygen adatoms. No superstructures could be found that contained both ordered NO and oxygen. However, the observed superstructure may certainly be due to other possible arrangements of the adsorbates on the surface.

8. Summary

The chemisorption and decomposition of NO on Ir(110) may be summarized as follows.

(1) Molecular chemisorption of NO occurs below room temperature and saturates near 9.6×10^{14} cm^{-2}. Adsorption occurs via precursor kinetics, and the initial probability of adsorption is equal to unity independent of surface temperature. Adsorption becomes competitive with NO dissociation and N_2 desorption above 400 K.

(2) Above 300 K, desorption of NO and N_2 occurs in three phases. First, approximately 17% of the NO desorbs near 400 K. Second,

N_2 desorbs near 430 K as NO dissociates leaving an oxygen overlayer. Third, both NO and N_2 desorb where the NO desorption (18% of the adsorbed NO) is associated with oxygen present and at least in part is due to adatom-adatom recombination. Estimates of activation energies for the desorption of NO in the first and third steps are 23.4 - 28.9 and 32.5 - 40.1 kcal-mole^{-1}, respectively. The activation energy for the dissociation of NO was estimated from data involving the desorption of N_2, and is equal to 25.2 - 30.7 kcal-mole^{-1} for desorption from a saturated overlayer. The activation energy for N_2 to desorb in the low coverage limit of NO is approximately 36 - 45 kcal-mole^{-1}. The preexponential factor for each process is assumed to lie between $10^{13} - 10^{16}$ s^{-1}.

(3) HeI UPS of NO shows levels at 13.5, 10.4 and 8.5 eV corresponding to the 4σ, 5σ and 1π orbitals, respectively. XPS of NO yields the O(1s) and N(1s) levels of NO at 531.5 and 400.2 eV, respectively, with or without oxygen present. The O(1s) level of chemisorbed oxygen at 528.8 eV is seen for surface temperatures above 400 K.

(4) From TDS, oxygen overlayers tend to stabilize NO with respect to dissociation and to desorption. A strong interaction between NO and oxygen is seen by the shift of the 1π level to 9.5 eV and by the CPD behavior of NO on surfaces precovered with oxygen adatoms. Both phenomena may be due to charge transfer effects between NO and oxygen through the metal.

References

1. H. Conrad, G. Ertl, J. Kuppers and E. E. Latta, Surface Sci. 65, 235 (1977).

2. R. Ku, N.A. Gjostein and H. P. Bonzel, Surface Sci. 64, 65 (1977).

3. T. W. Orent and R. S. Hansen, Surface Sci. 67, 325 (1977).

4. P. D. Reed, C. M. Comrie and R. M. Lambert, Surface Sci. 72, 423 (1978).

5. P. A. Thiel, W. H. Weinberg and J. T. Yates, Jr., Chem. Phys. Letters 67, 403 (1979); G. E. Thomas and W. H. Weinberg, Phys. Rev. Letters 41, 1181 (1978).

6. E. Umbach, S. Kulkarni, P. Feulner and D. Menzel, Surface Sci. 88, 65 (1979).

7. P. Feulner, S. Kulkarni, E. Umbach and D. Menzel, to be published.

8. H. P. Bonzel and T. E. Fischer, Surface Sci. 51, 213 (1975).

9. H. Conrad, G. Ertl, J. Kuppers and E. E. Latta, Surface Sci. 50, 296 (1975).

10. G. L. Price, B. A. Sexton and B. G. Baker, Surface Sci. 60, 506 (1976).

11. G. L. Price and B. G. Baker, Surface Sci. 91, 571 (1980).

12. H. P. Bonzel and G. Pirug, Surface Sci. 62, 45 (1977).

13. H. P. Bonzel, G. Broden and G. Pirug, J. Catalysis 53, 96 (1978).

14. C. M. Comrie, W. H. Weinberg and R. M. Lambert, Surface Sci. 57, 619 (1976).

15. J. L. Gland and B. A. Sexton, Surface Sci. 94, 355 (1980).

16. H. Ibach and S. Lehwald, Surface Sci. 76, 1 (1978).

17. G. Pirug and H. P. Bonzel, J. Catalysis 50, 64 (1977).

18. J. Kanski and T. N. Rhodin, Surface Sci. 65, 63 (1977).

19. P. A. Zhdan, G. K. Boreskov, W. F. Egelhoff, Jr. and W. H. Weinberg, J. Catalysis 45, 281 (1976).

20. P. A. Zhdan, G. K. Boreskov, A. I. Boronin, A. P. Scheplin, W. F. Egelhoff, Jr. and W. H. Weinberg, J. Catalysis 60, 93 (1979).

21. J. Kuppers and H. Michel, Surface Sci. 85, 201 (1979).

22. C. T. Campbell and J. M. White, Appl. Surface Sci. 1, 347 (1978).

23. G. Loubriel, E. W. Plummer, T. Gustafsson and C. L. Allyn, submitted to Surface Science.

24. D. E. Ibbotson, T. S. Wittrig and W. H. Weinberg, in preparation.

25. D. E. Ibbotson, T. S. Wittrig and W. H. Weinberg, J. Chem. Phys. 72, 4885 (1980).

26. J. L. Taylor, D. E. Ibbotson and W. H. Weinberg, J. Chem. Phys. 69, 4298 (1978).

27. C.-M. Chan, M. A. Van Hove, W. H. Weinberg and E. D. Williams, Solid State Commun. 30, 47 (1979); Surface Sci. 91, 400 (1980).

28. J. L. Taylor, D. E. Ibbotson and W. H. Weinberg, Surface Sci. 79, 349 (1979).

29. P. Kisliuk, J. Phys. Chem. Solids 3, 95 (1957).

30. G. Loubriel, E. W. Plummer, D. Rajora, M. Albert, L. Sneddon and

W. R. Salaneck, J. Electron Spectrosc. Relat. Phenom. 19, 35 (1980).

31. W. E. Moddeman, T. A. Carlson, M. O. Krausse, B. P. Pullen, W. E. Bull and G. K. Schweitzer, J. Chem. Phys. 55, 2317 (1971).

32. C.-M. Chan, K. L. Luke, M. A. Van Hove, W. H. Weinberg and S. P. Withrow, Surface Sci. 78, 386 (1978).

Table 1

Yields of adsorbed NO and desorbed N_2 at various adsorption temperatures on Ir(110) from isothermal decomposition measurements. Estimates of the activation energy for desorption of NO at selected temperatures are also given.

T,K	Θ(NO)	$\Theta(N_2)$	Θ(NO)	E_d(NO)*
100	1.00	0	1.00	
312	1.00	0	1.00	
350	0.98	0.01	0.97	
400	0.85	0.23	0.62	
450	0.87	0.45	0.42	29.2-35.4
500	0.85	0.52	0.33	32.1-39.0
550	0.57	0.50	0.07	33.8-41.2
621	0.55	0.55	0	~36.0-44.5
650	0.49	0.49	0	
680	0.47	0.47	0	
700	0.48	0.48	0	
720	0.49	0.49	0	

*Assuming 10^{13} to 10^{16} s^{-1} for the preexponential factor of desorption.

Figure Captions

Fig. 1. Thermal desorption spectra of (A) $^{15}N_2$ and (B) ^{15}NO as a function of exposure for ^{15}NO on Ir(110). Exposures were performed by a beam doser and have been converted to Langmuir units. The initial temperature was 100 K and the (linear) heating was 27 K - s^{-1}.

Fig. 2. The adsorption kinetics of ^{15}NO on Ir(110) as calculated from the TDS results in Fig. 1. The initial probability of adsorption is unity, and the saturation coverage as determined by XPS measurements is 9.6 x 10^{14} cm^{-2}. See the text for details.

Fig. 3. Yields of $^{15}N_2$ and ^{15}NO from the TDS results in Fig. 1. The fractional coverage scale for $^{15}N_2$ has been normalized to provide a nitrogen atom balance. Desorption yields of $^{15}N_2$ and ^{15}NO saturate at 0.65 and 0.35 ML, respectively.

Fig. 4. HeI UP difference spectra of ^{15}NO on Ir(110) as a function of the fractional coverage of ^{15}NO. The binding energy scale is referenced to the Fermi level, E_F.

Fig. 5. HeI difference spectra of NO on Ir(110) showing the effects of annealing two coverages to 400 K and cooling. (a) 0.19. (b) 0.19 annealed to 400 K. (c) 0.43. (d) 0.43 annealed to 400 K.

Fig. 6. HeI difference spectra of a saturated overlayer of ^{15}NO on various coverages of preadsorbed oxygen and substrate structures.

(a) Clean (1x2) substrate. (b) Surface oxide (0.25 ML) with (1x1) substrate. (c) 0.25 ML oxygen with (1x2) substrate, (d) 0.98 ML oxgen on (1x2) substrate.

Fig. 7. XPS of ^{15}NO adsorbed on Ir(110). Top: N(1s), Bottom: O(1s). (a) 14.0 L ^{15}NO adsorbed and recorded at 95 K (saturation). (b) 7.0 L exposed at 400 K and an additional 7.0 L exposed at 95 K. (c) Saturated ^{15}NO layer (95 K) annealed to 430 K and recorded at 95 K.

Fig. 8. Electron excited AES. (A) O-KLL and (B) N-KLL of NO on Ir(110) at 95 K for a saturated overlayer.

Fig. 9. Isothermal decomposition of ^{15}NO on Ir(100) at 400 K. The adsorption rate of ^{15}NO, the desorption rate of ^{15}NO, the desorption rate of $^{15}N_2$ and their respective coverages as a function of NO exposure are shown. These data were used to calculate curve (c) in Fig. 8.

Fig. 10. The total coverge of $N(^{15}N_{(a)} + {}^{15}NO_{(a)})$ as a function of exposure to ^{15}NO on Ir(110). Several different surface temperatures are shown. Curve (a) is reproduced from Fig. 2. (b) ← 350 K, (c) 400 K, (d) 450 K, (e) 500 K, (f) 550 K, (g) 621 K, (h) 650 K and (i) 700 K. Curves (b) - (i) were calculated from beam doser experiments. See the text for details.

Fig. 11. CPD, $\Delta\varphi$, of ^{15}NO as a function of fractional coverage at (a) 100 K and (b) 317 K. The change in $\Delta\varphi$

between the two temperatures is evidence for partial dissociation near room temperature.

Fig. 12. CPD of ^{15}NO exposed to various precoverages of oxygen on Ir(110). With the exceptions of (c) and (f) [(1x1)], the substrate maintains a (1x2) structure. The fractional coverages of oxygen are as follows: (a) 0.13, (b) 0.25, (c) 0.25 (oxide), (d) 0.41, (e) 0.46, (f) ~1.2 and (g) 0

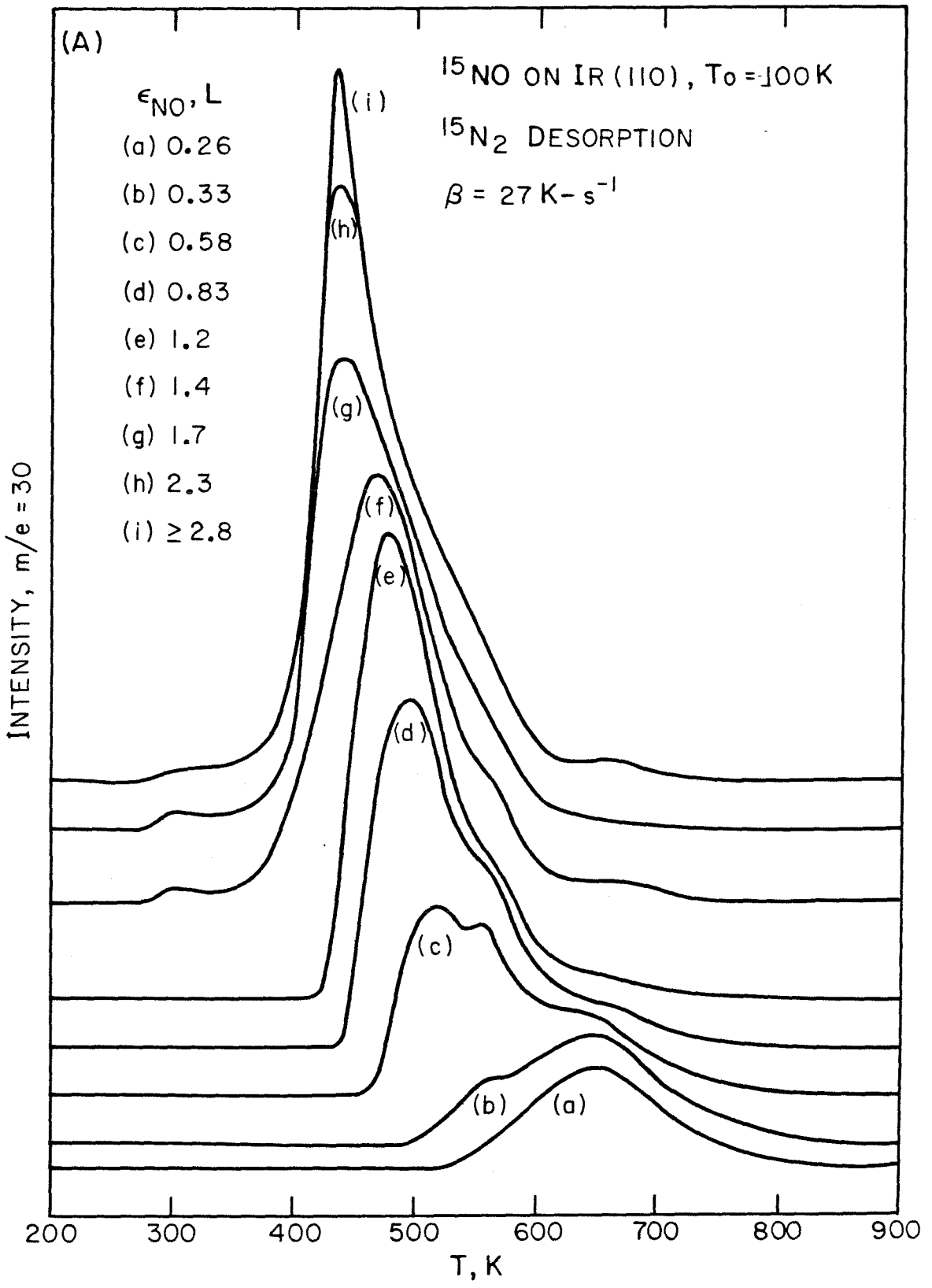
(A)
^{15}NO ON IR (110), To = 100 K
$^{15}N_2$ DESORPTION
β = 27 K-s^{-1}
ϵ_{NO}, L
(a) 0.26
(b) 0.33
(c) 0.58
(d) 0.83
(e) 1.2
(f) 1.4
(g) 1.7
(h) 2.3
(i) ≥ 2.8
INTENSITY, m/e = 30
T, K
200
300
400
500
600
700
800
900

Figure 1 (a)

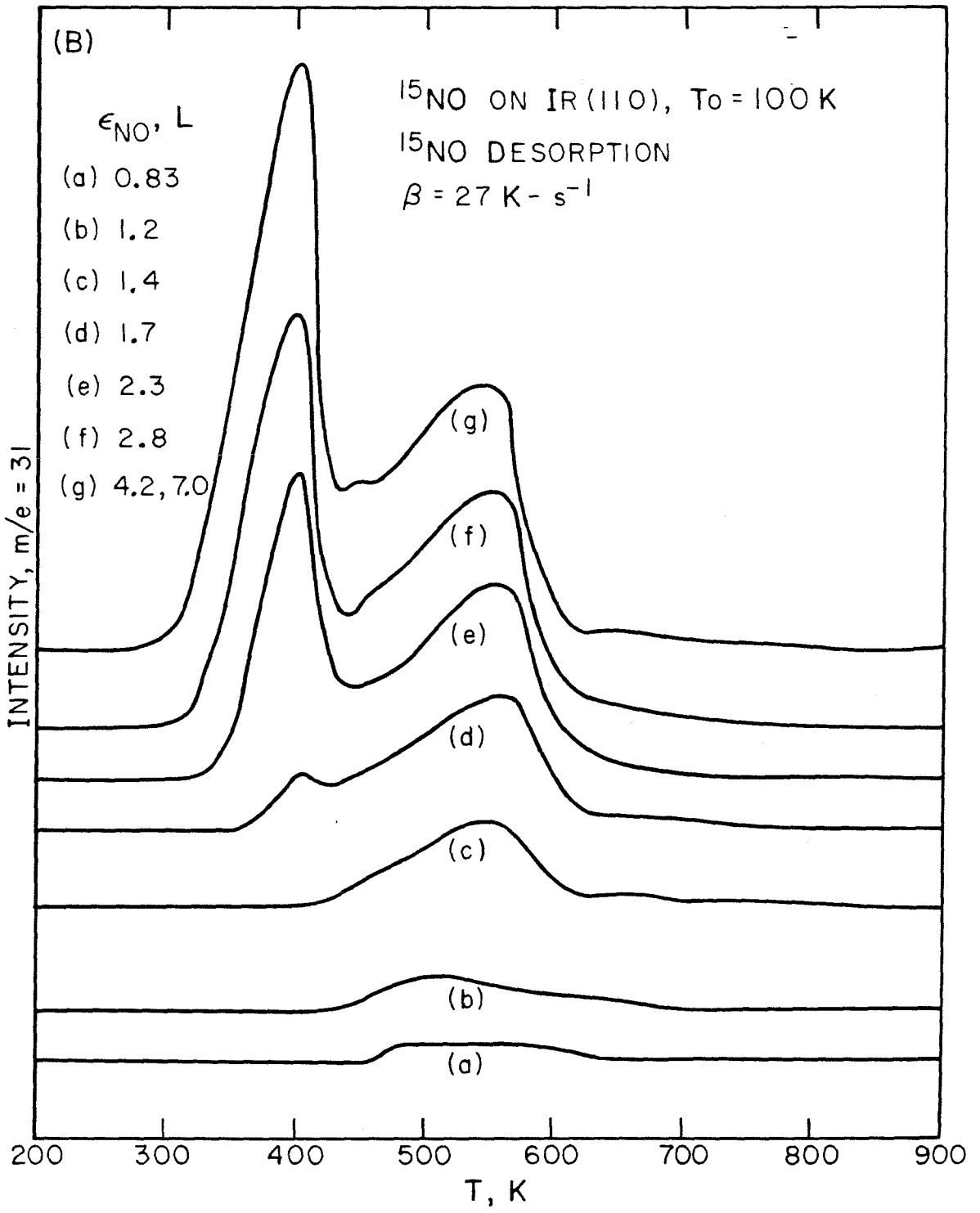
(B)
ϵ_{NO}, L
(a) 0.83
(b) 1.2
(c) 1.4
(d) 1.7
(e) 2.3
(f) 2.8
(g) 4.2, 7.0
^{15}NO ON IR(110), To = 100 K
^{15}NO DESORPTION
β = 27 K - s^{-1}
INTENSITY, m/e = 31
200
300
400
500
600
700
800
900
T, K

Figure 1(b)

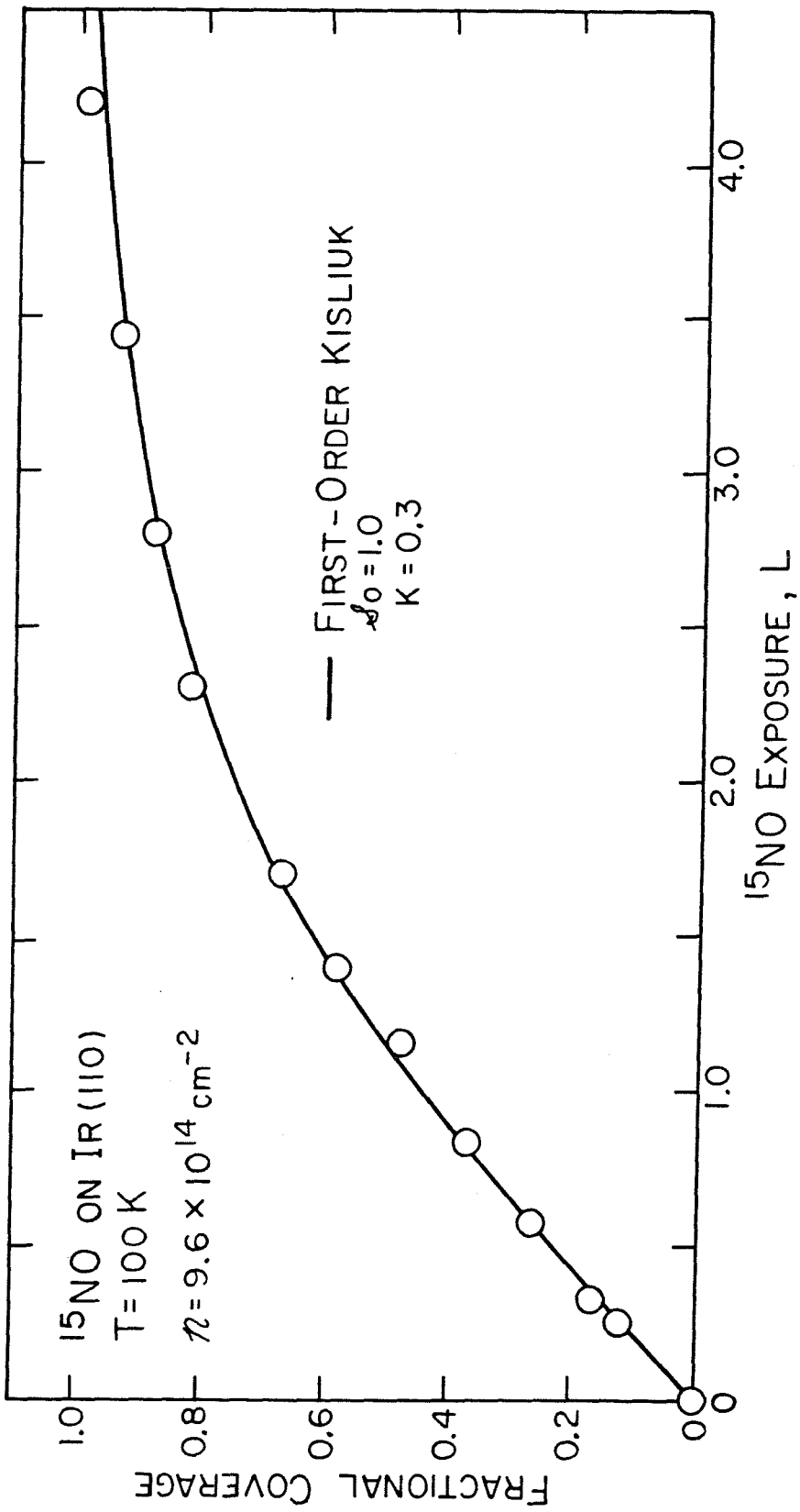
FRACTIONAL COVERAGE
0
0.2
0.4
0.6
0.8
1.0
0
1.0
2.0
3.0
4.0
^{15}NO EXPOSURE, L
^{15}NO ON Ir(110)
T = 100 K
$\eta = 9.6 \times 10^{14}$ cm^{-2}
FIRST-ORDER KISLIUK
$s_0 = 1.0$
K = 0.3

Figure 2

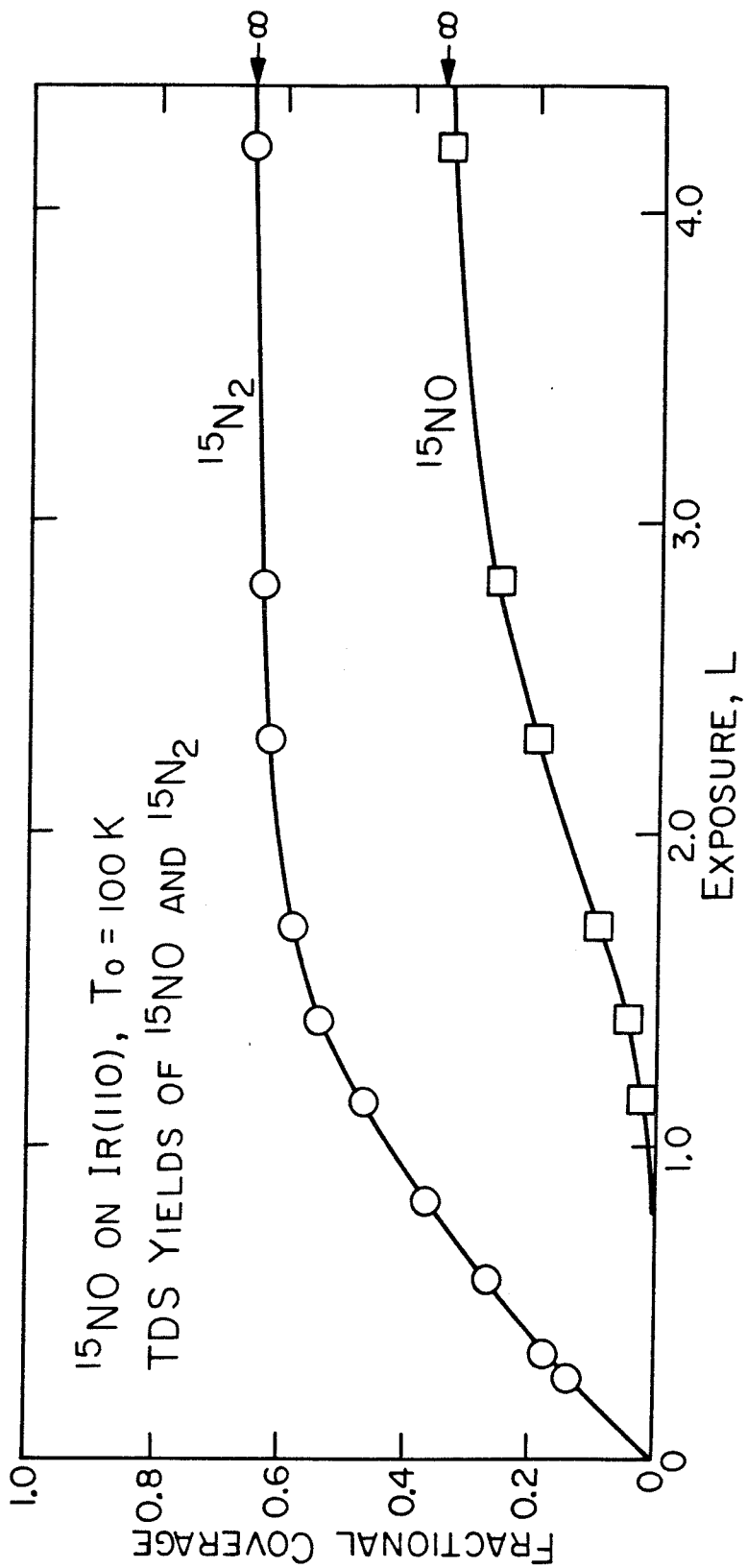
^{15}NO ON IR(110), T_o = 100 K
TDS YIELDS OF ^{15}NO AND $^{15}N_2$
$^{15}N_2$
^{15}NO
∞
∞
FRACTIONAL COVERAGE
0
0.2
0.4
0.6
0.8
1.0
1.0
2.0
3.0
4.0
EXPOSURE, L

Figure 3

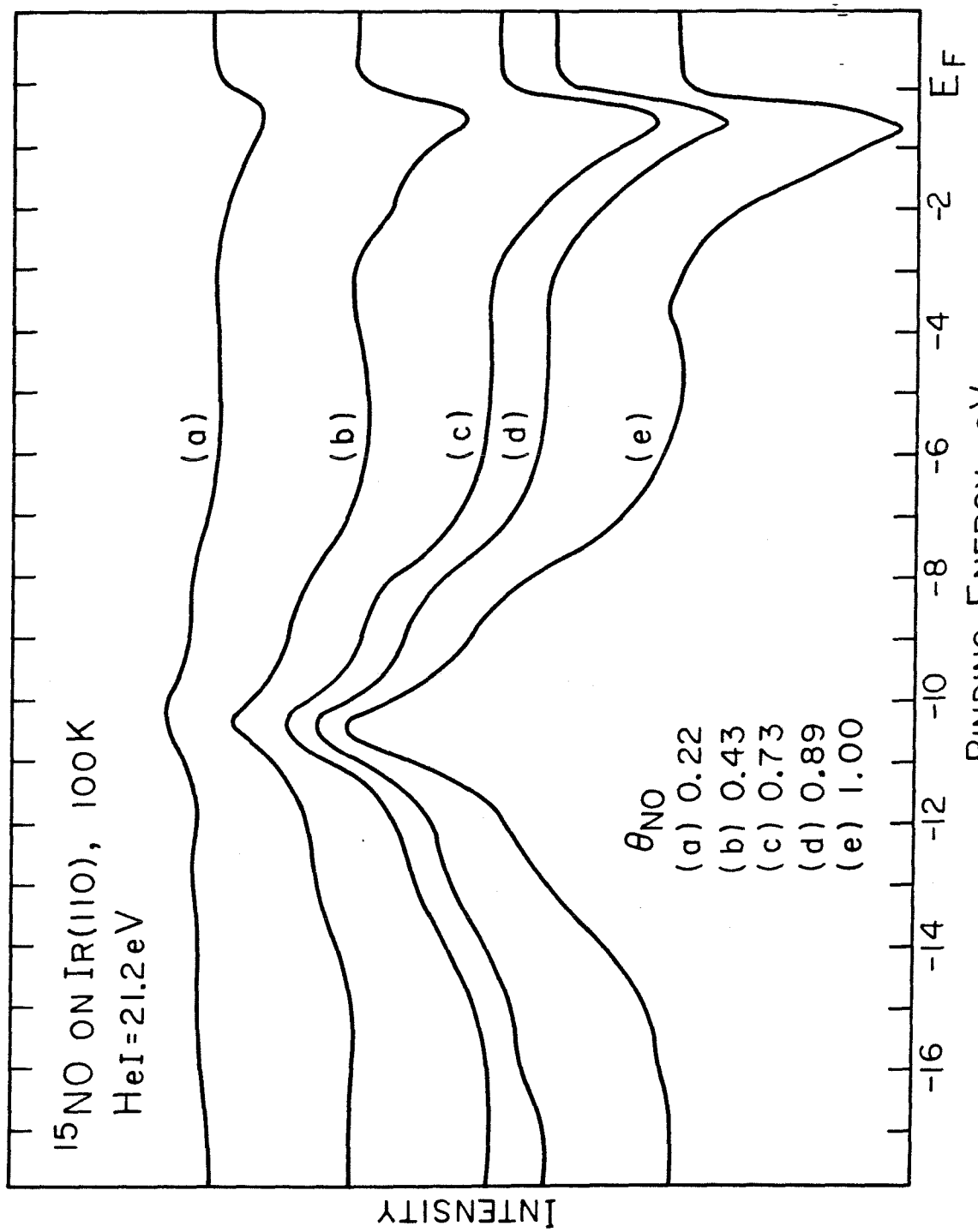
^{15}NO ON IR(110), 100K
HeI=21.2eV
(a)
(b)
(c)
(d)
(e)
θ_{NO}
(a) 0.22
(b) 0.43
(c) 0.73
(d) 0.89
(e) 1.00
-16
-14
-12
-10
-8
-6
-4
-2
E_F
BINDING ENERGY, eV
INTENSITY

Figure 4

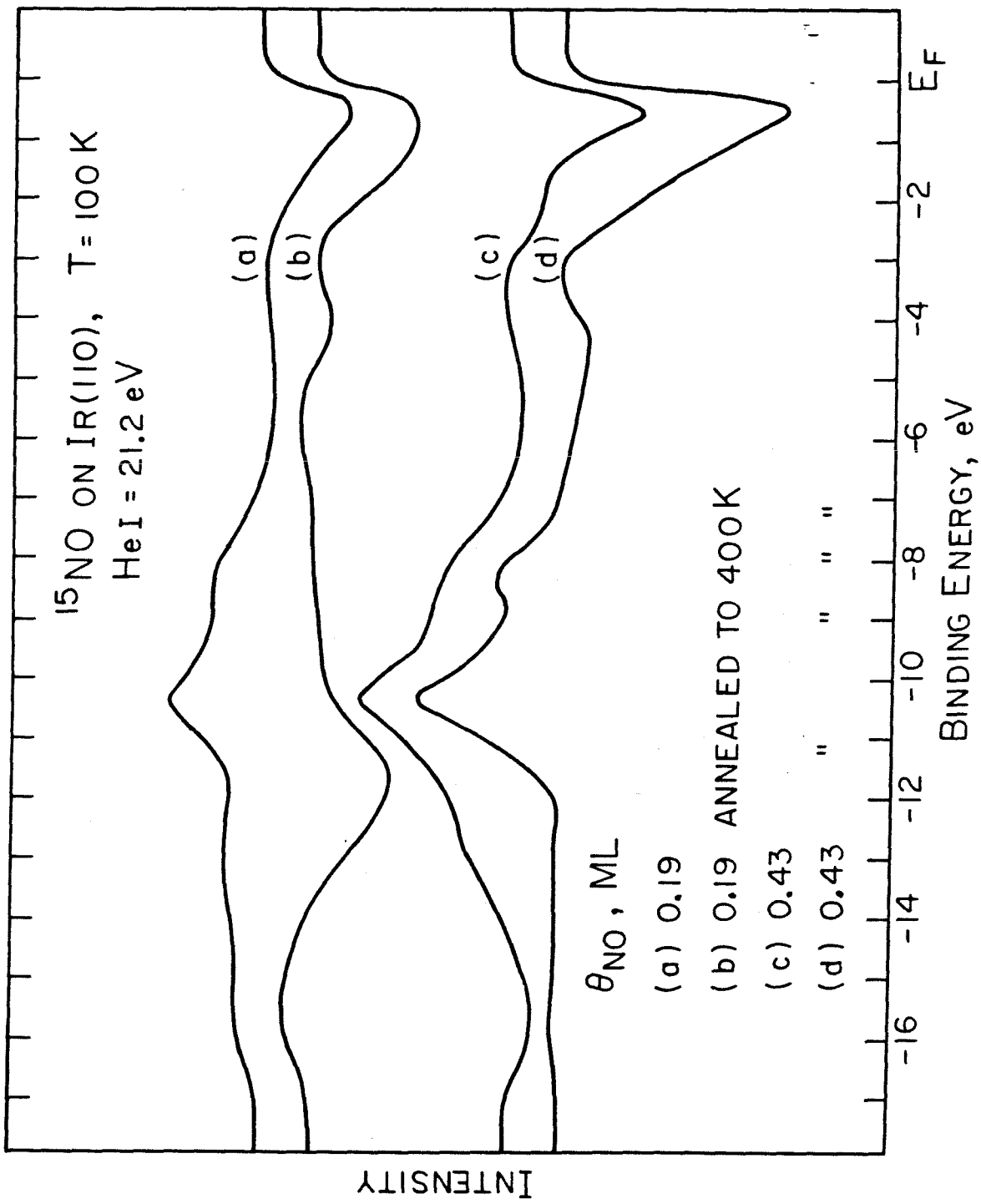
^{15}NO ON IR(110), T= 100 K
HeI = 21.2 eV
(a)
(b)
(c)
(d)
θ_{NO}, ML
(a) 0.19
(b) 0.19 ANNEALED TO 400K
(c) 0.43 " " "
(d) 0.43 " "
INTENSITY
BINDING ENERGY, eV
-16
-14
-12
-10
-8
-6
-4
-2
E_F

Figure 5

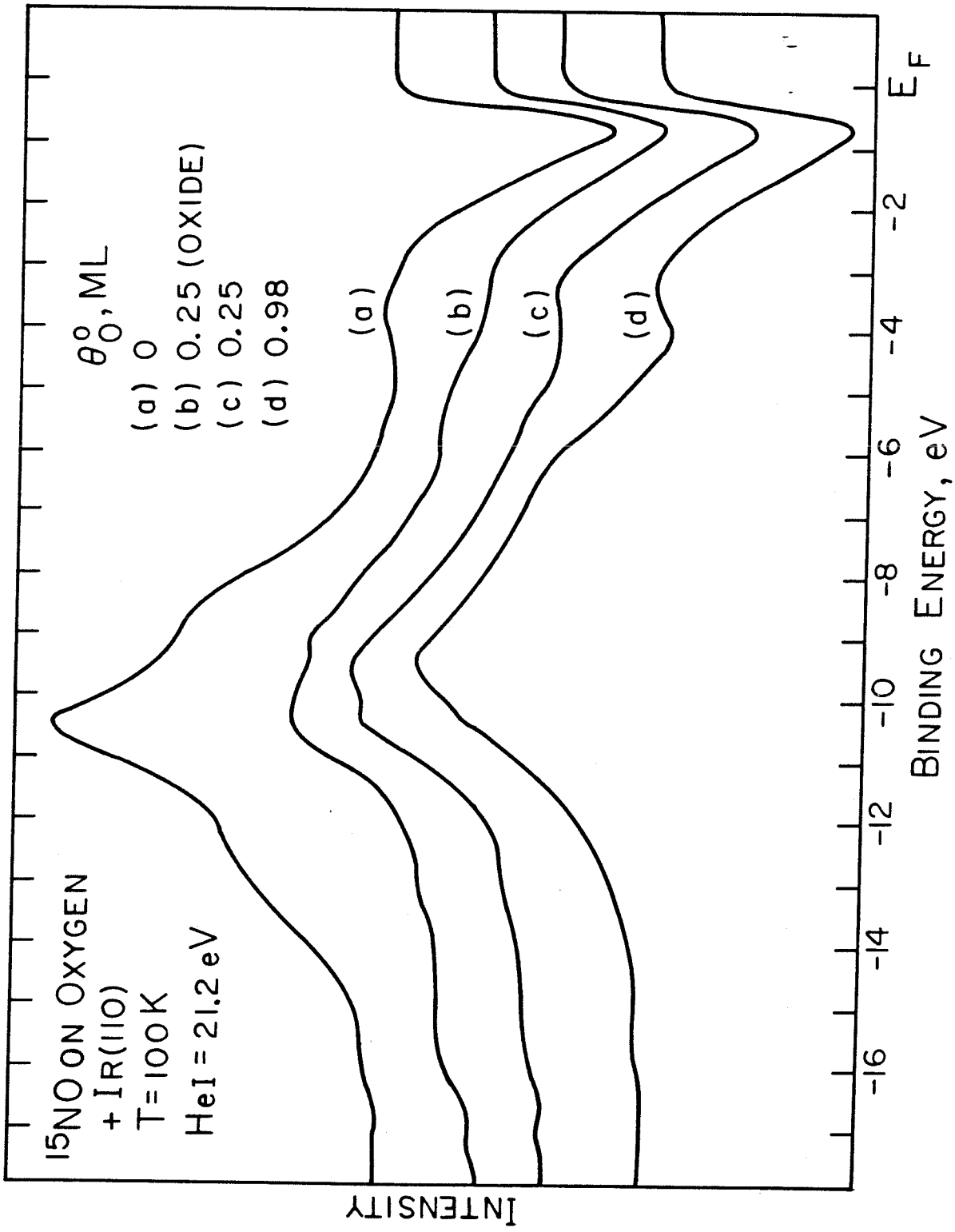
^{15}NO ON OXYGEN
+ IR(110)
T = 100 K
HeI = 21.2 eV
θ_O^o, ML
(a) 0
(b) 0.25 (OXIDE)
(c) 0.25
(d) 0.98
(a)
(b)
(c)
(d)
INTENSITY
-16
-14
-12
-10
-8
-6
-4
-2
E_F
BINDING ENERGY, eV

Figure 6

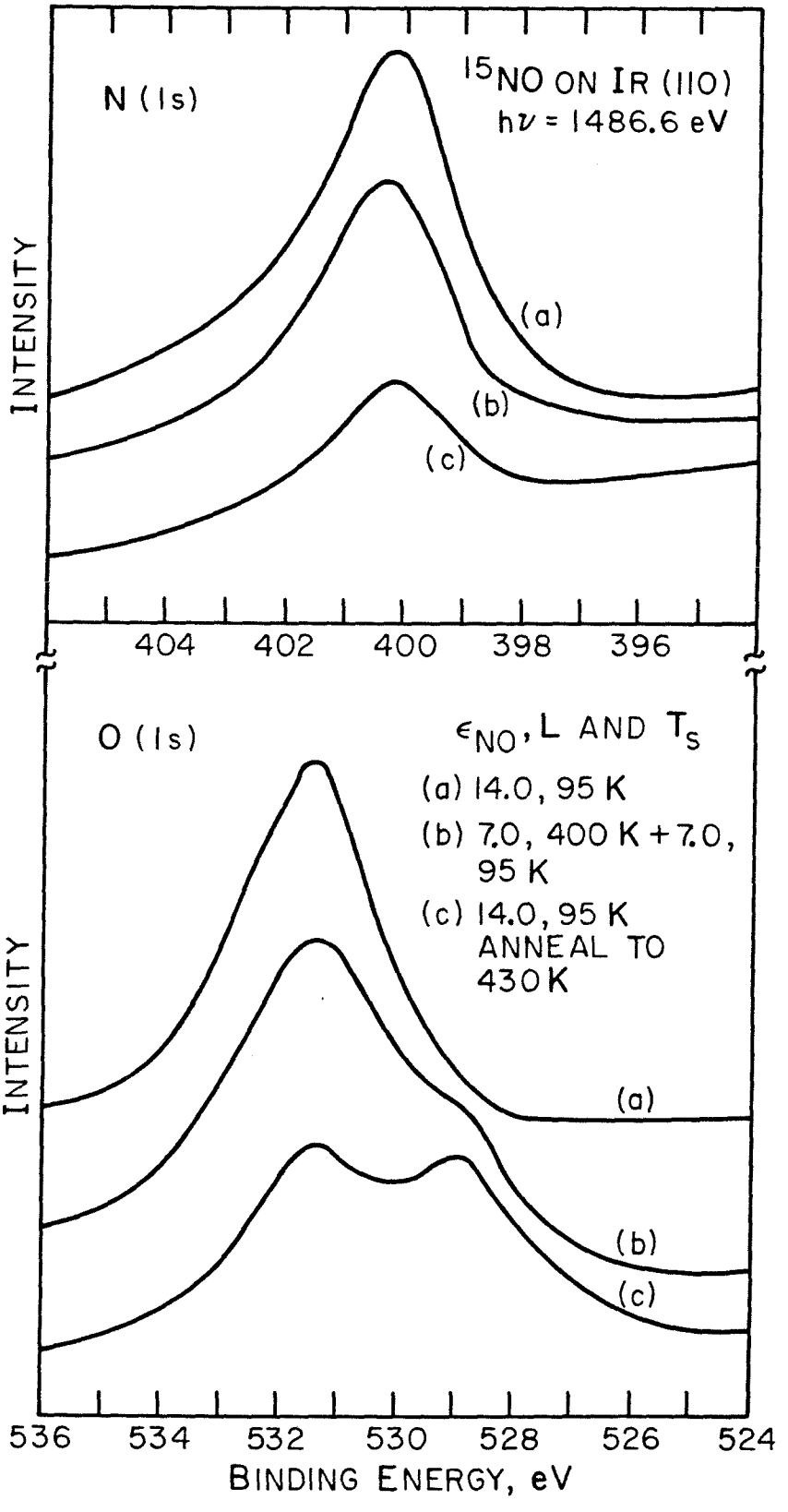
N (1s)
^{15}NO ON IR (110)
hν = 1486.6 eV
INTENSITY
(a)
(b)
(c)
404
402
400
398
396
O (1s)
ϵ_{NO}, L AND T_S
(a) 14.0, 95 K
(b) 7.0, 400 K + 7.0, 95 K
(c) 14.0, 95 K ANNEAL TO 430 K
INTENSITY
(a)
(b)
(c)
536
534
532
530
528
526
524
BINDING ENERGY, eV

Figure 7

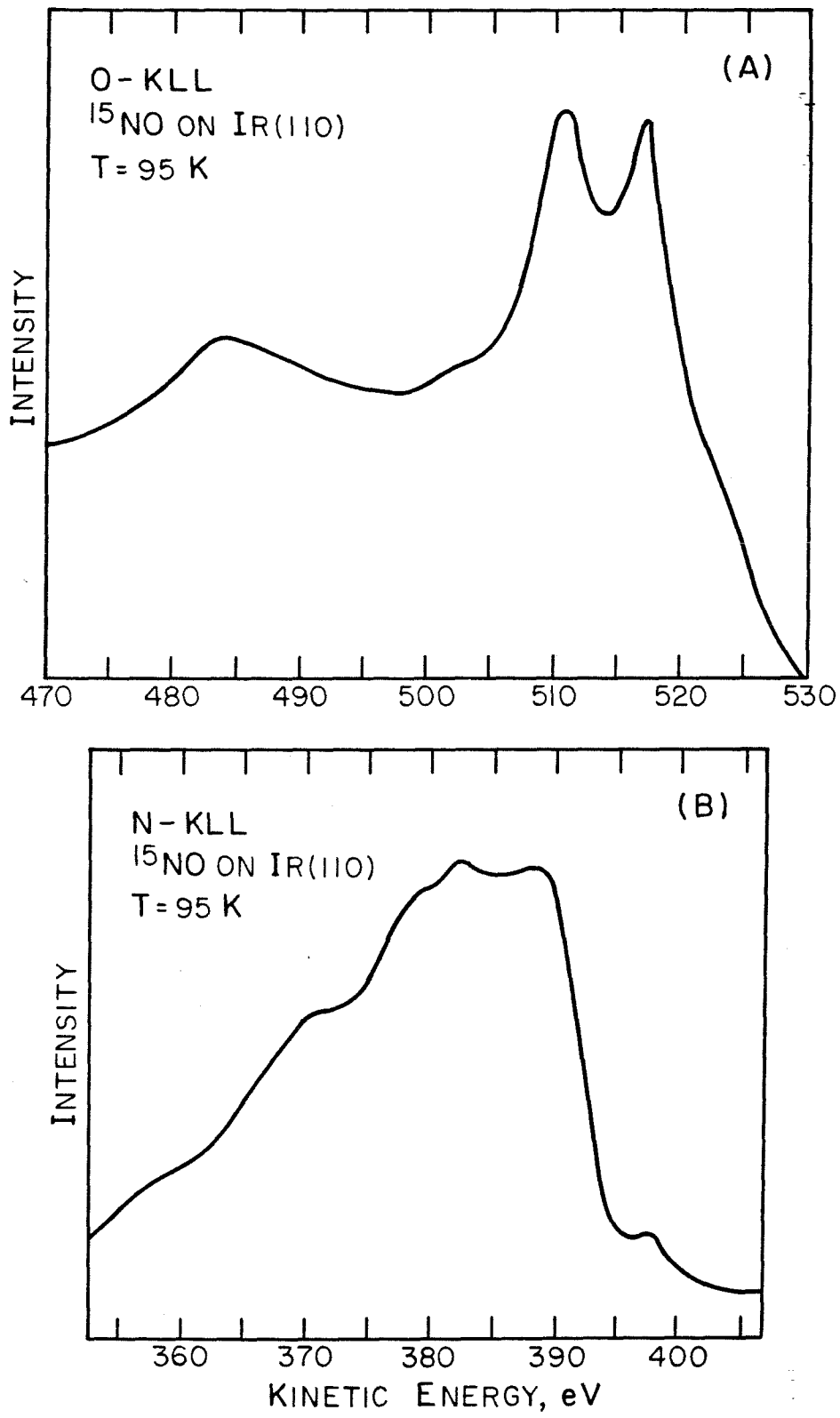
O-KLL
^{15}NO ON IR(110)
T = 95 K
(A)
INTENSITY
470
480
490
500
510
520
530
N-KLL
^{15}NO ON IR(110)
T = 95 K
(B)
INTENSITY
360
370
380
390
400
KINETIC ENERGY, eV

Figure 8

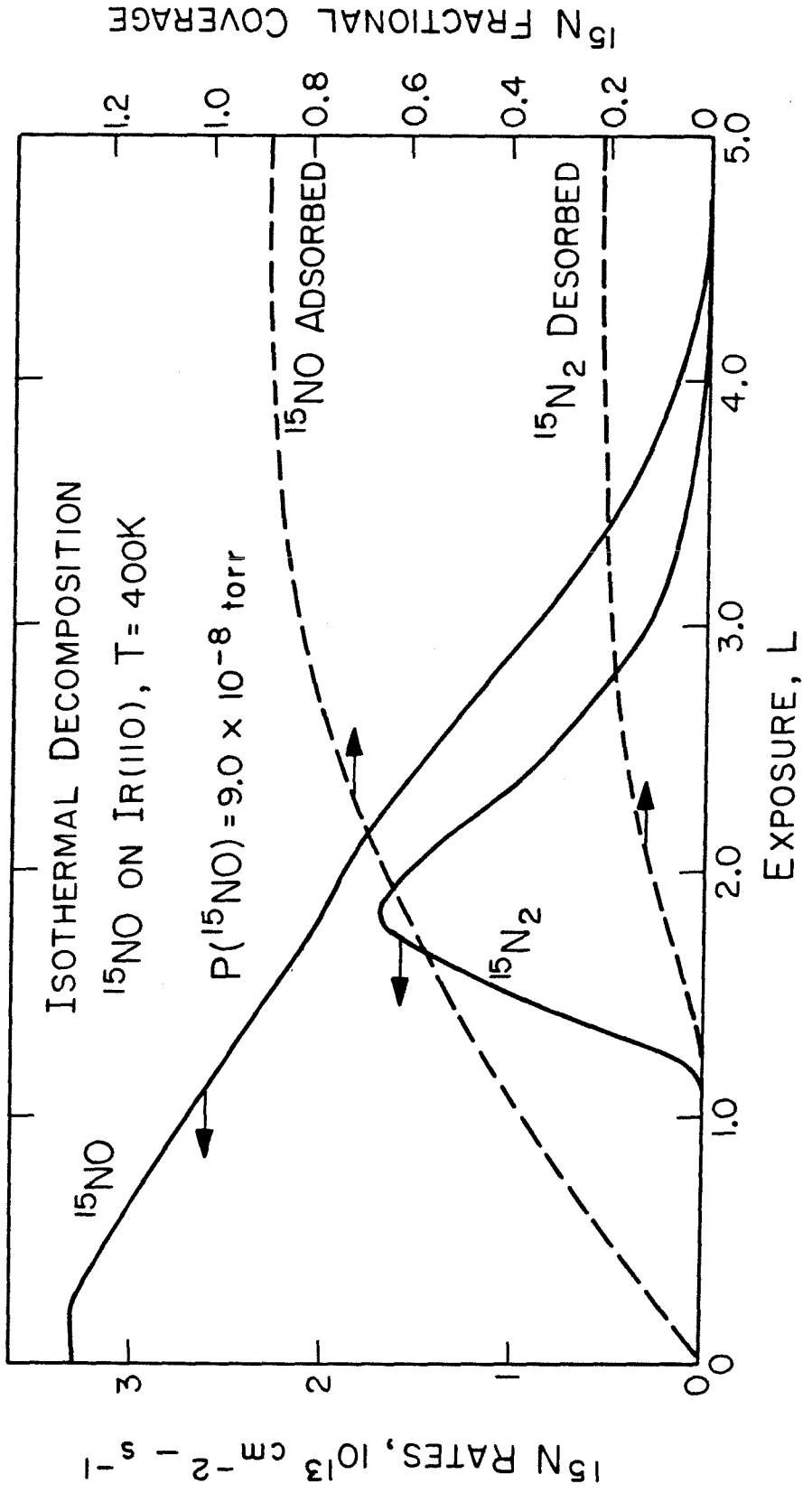
ISOTHERMAL DECOMPOSITION
^{15}NO ON IR(110), T = 400K
$P(^{15}NO) = 9.0 \times 10^{-8}$ torr
^{15}NO
^{15}NO ADSORBED
$^{15}N_2$
$^{15}N_2$ DESORBED
^{15}N RATES, 10^{13} $cm^{-2} - s^{-1}$
^{15}N FRACTIONAL COVERAGE
EXPOSURE, L
0
1
2
3
1.0
2.0
3.0
4.0
5.0
0.2
0.4
0.6
0.8
1.0
1.2

Figure 9

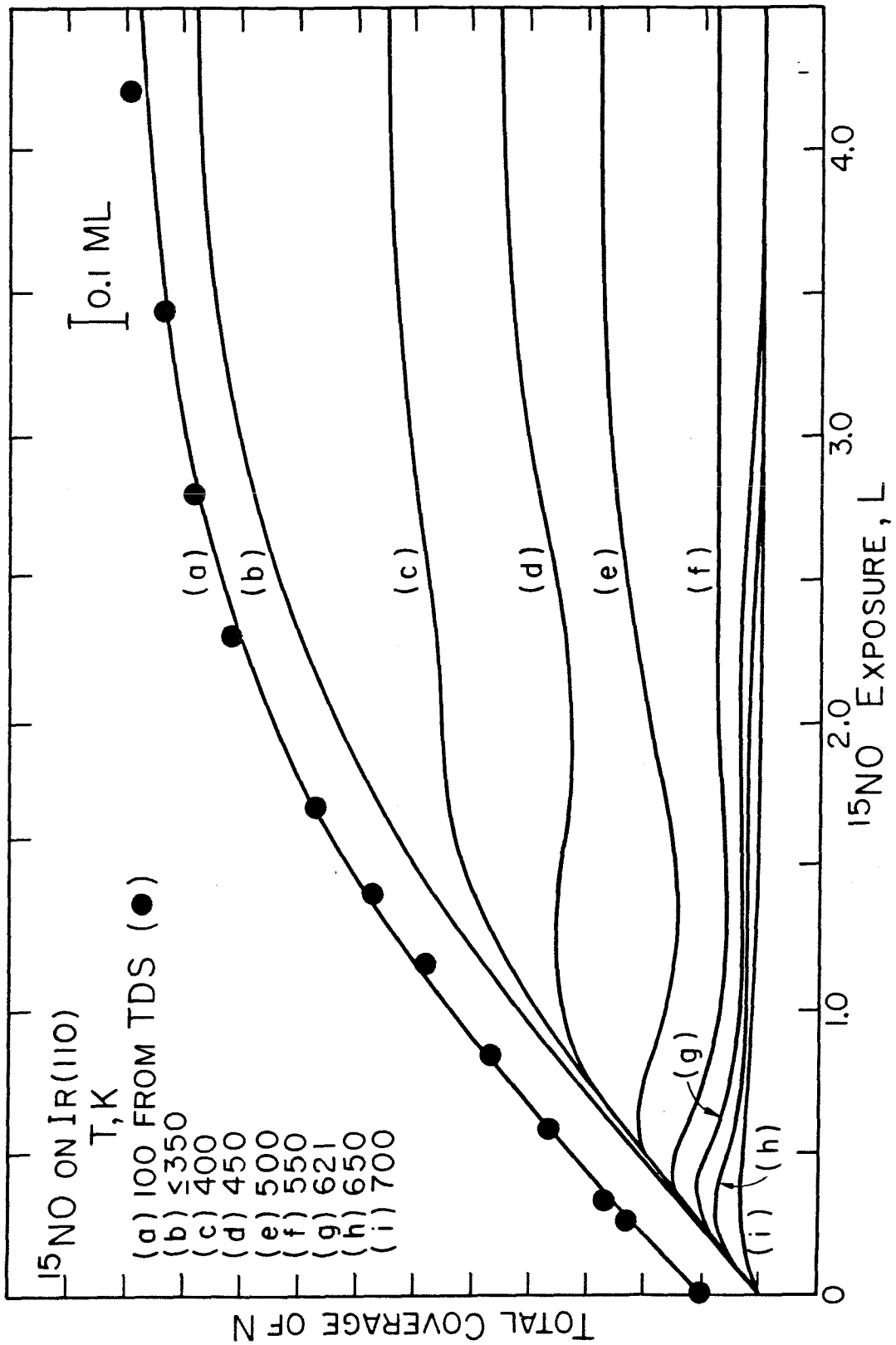
^{15}NO ON IR(110)
T, K
(a) 100 FROM TDS (●)
(b) ≤350
(c) 400
(d) 450
(e) 500
(f) 550
(g) 621
(h) 650
(i) 700
0.1 ML
(a)
(b)
(c)
(d)
(e)
(f)
(g)
(h)
(i)
TOTAL COVERAGE OF N
0
1.0
2.0
3.0
4.0
^{15}NO EXPOSURE, L

Figure 10

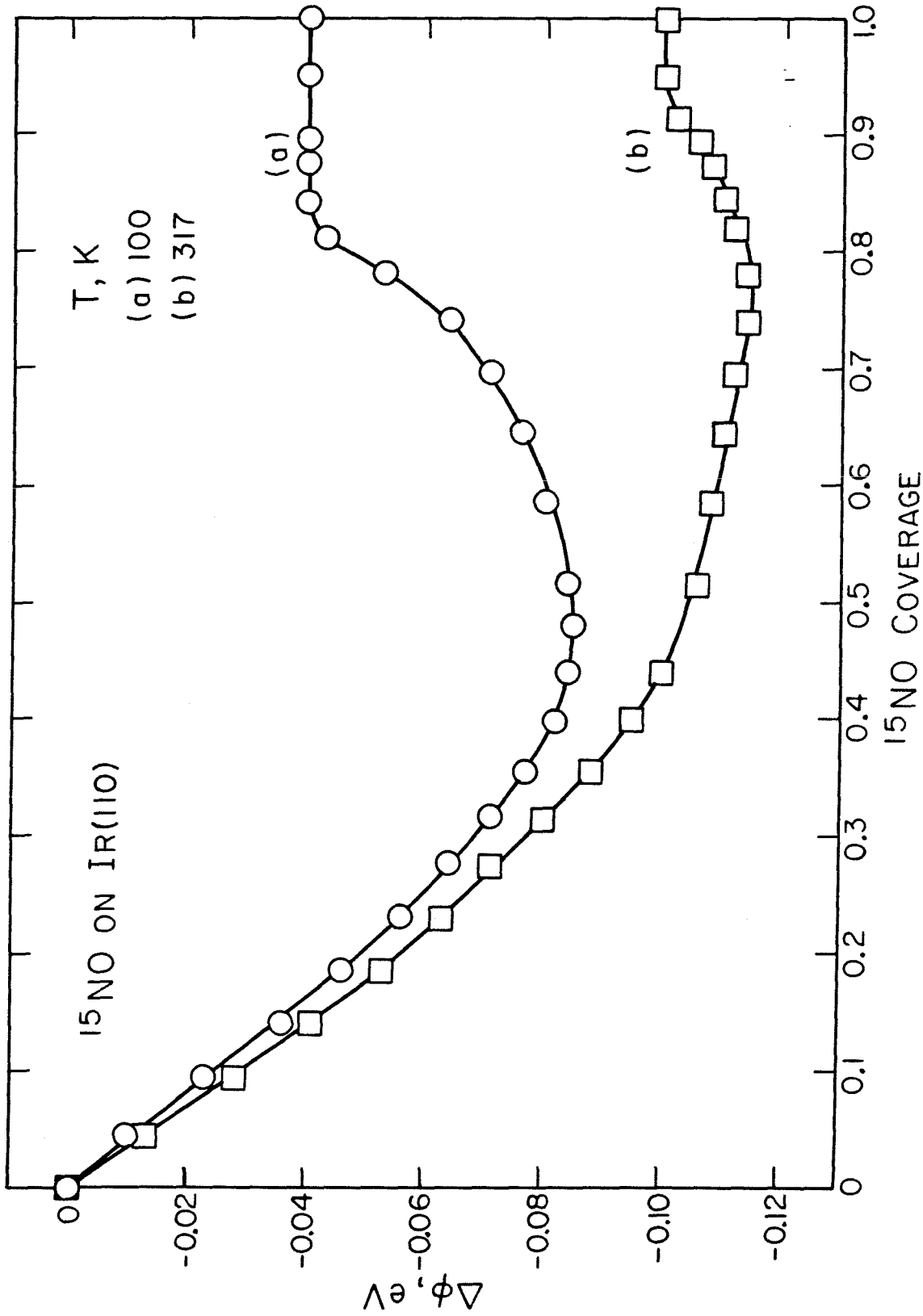
15NO ON IR(110)
T, K
(a) 100
(b) 317
(a)
(b)
Δφ, eV
0
-0.02
-0.04
-0.06
-0.08
-0.10
-0.12
0
0.1
0.2
0.3
0.4
0.5
0.6
0.7
0.8
0.9
1.0
15NO COVERAGE

Figure 11

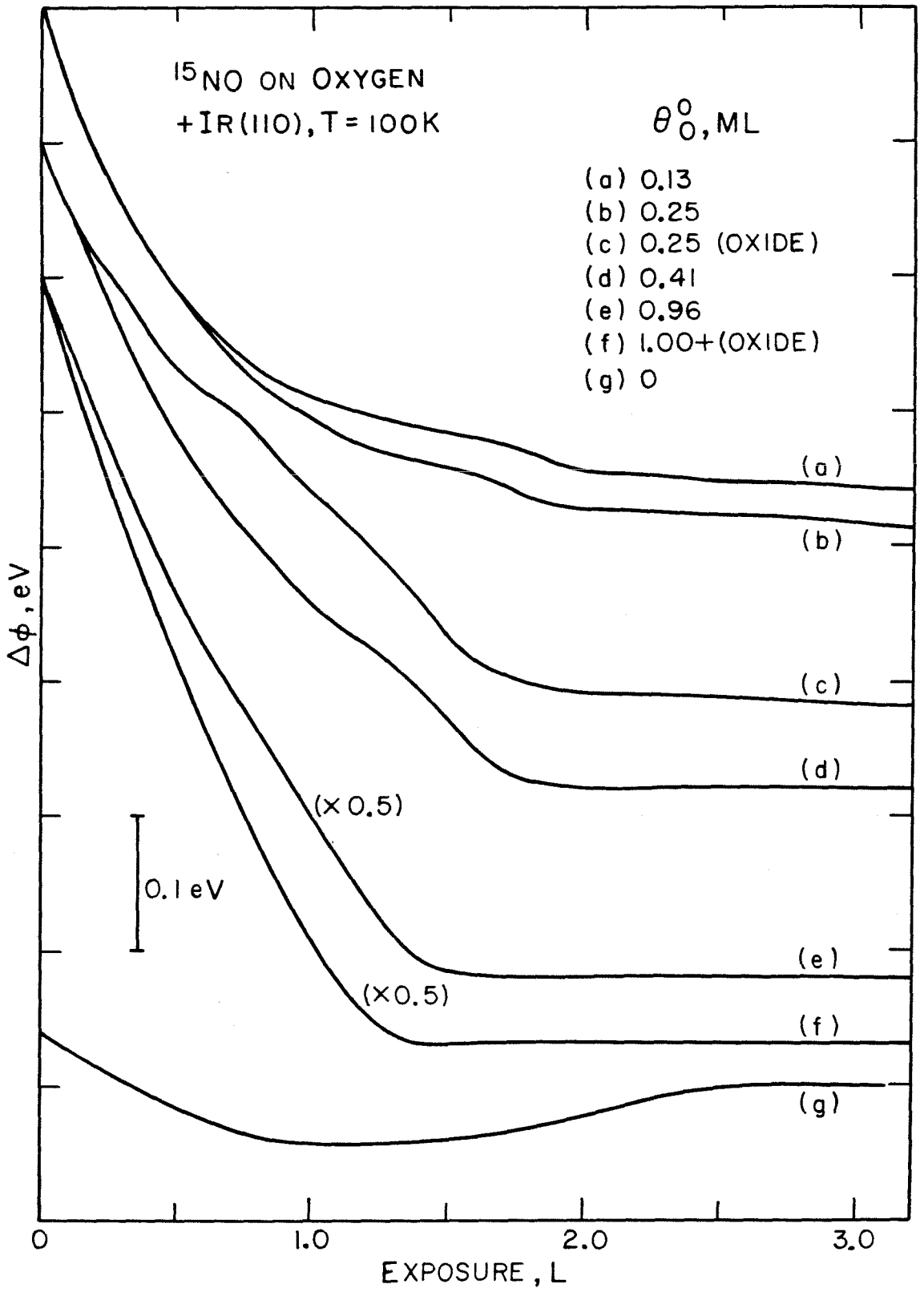
^{15}NO ON OXYGEN
+IR(110), T = 100K
θ_O^O, ML
(a) 0.13
(b) 0.25
(c) 0.25 (OXIDE)
(d) 0.41
(e) 0.96
(f) 1.00+(OXIDE)
(g) 0
(a)
(b)
(c)
(d)
(×0.5)
0.1 eV
(e)
(×0.5)
(f)
(g)
Δφ, eV
0
1.0
2.0
3.0
EXPOSURE, L

Figure 12

APPENDIX E

THE REDUCTION OF NO WITH D_2 OVER IR(110)

(The text of Appendix E consists of an article coauthored with D.E. Ibbotson and W.H. Weinberg that has been accepted for publication in Surface Science.)

Abstract

The heterogeneously catalyzed reaction between NO and D_2 to produce N_2, ND_2 and D_2O over Ir(110) was investigated under ultra high vacuum conditions for partial pressures of the reactants between 5 x 10^{-8} and 1 x 10^{-6} torr, total pressures between 10^{-7} and 10^{-6} torr, and surface temperatures between 300 and 1000 K. Mass spectrometry, LEED, UPS, XPS and AES measurements were used to study this reaction system. In addition, the competitive coadsorption of NO and deuterium was investigated via thermal desorption mass spectrometry and contact potential difference measurements to gain further insight into the observed steady state rates of reaction. Depending on the ratio of partial pressures ($R \equiv P_{D_2}/P_{NO}$), the rate of NO reduction to N_2 shows a pronounced enhancement when the surface is heated above a critical temperature. As the surface is cooled, the rate maintains a high value independent of temperature until a lower critical temperature is reached, where the rate drops uncontrollably. This hysteresis is due to a change in the structure and composition of the surface. For sufficiently large values of R and for an "activated" surface, N_2 and ND_3 are produced competitively between 470 and 630 K. Empirical models of the different regions of the steady state reaction are presented with interpretations of these models. Finally, the selectivity of Ir to form N_2 or ND_3 is discussed as compared to the other transition metals.

1. Introduction

The reduction of NO by deuterium has been studied on the Ir(110)-(1x2) surface under ultra-high vacuum conditions with thermal desorption mass spectrometry, LEED, X-ray and UV-photoelectron spectroscopies, Auger electron spectroscopy and contact potential difference measurements. Both transient and steady state conditions were investigated. The motivation for this study is to elucidate the mechanism of a heterogeneously catalyzed reduction reaction, using the NO/D_2 system as a model.

Although much has been reported concerning NO, hydrogen and CO chemisorbed on the transtion metals, few studies are available for the heterogeneously catalyzed reduction of NO with either CO or hydrogen as the reducing agent. In ultra-high vacuum, the NO/H_2 system has been studied on polycrystalline Pt under steady state conditions *(1)*, and the NO/CO system has been studied on the (111) and (110) surfaces of Pt *(2)* and polycrystalline Rh *(3)* under transient conditions via thermal desorption mass spectrometry. At atmospheric pressure the reduction of NO with CO or hydrogen under steady state conditions was conducted over supported Pt, Pd, Rh and Ru *(4,5)*. It is more pertinent to discuss the results cited for the reduction of NO with hydrogen than with CO in the present context of the reaction between NO and D_2 on Ir(110).

Depending on the ratio of partial pressures of H_2 and NO ($R \equiv P_{H_2}/P_{NO}$) under steady state reaction conditions, the products were H_2O, N_2, NH_3 and N_2O on polycrystalline Pt for surface temperatures between 300 and 900 K and a total pressure of approximately 10^{-7} torr *(1)*. It was suggested that the

limitation of the reduction reaction is related to the dissociation of NO *(1)*. For R = 1/2, the major products are N_2 and H_2O with N_2O formed as a minor product. However, for R = 5 (excess hydrogen), NH_3, N_2 and H_2O are observed. In this case, NH_3 competes strongly for nitrogen adatoms that are formed from the dissociation of NO. The reaction maximum at 495 K for the formation of NH_3 (R = 5) on polycrystalline Pt *(1)* agrees well with the reaction maximum at 500 K observed on supported Pt at atmospheric pressure *(4)*. Good agreement is observed for the temperature at which 50% reduction of NO occurs for similar R values *(1,4)*. Thus, a connection has been established in this case between these widely different pressures ranges.

The investigations of the NO/H_2 system over the supported metals *(4,5)* reveal the selectivity of each catalyst with regard to the products formed. The overall reduction activity observed for NO/H_2 (R = 4) is Pd > Pt > Rh > Ru using the temperature at which 50% of the NO is reduced as the criterion. However, the major products formed are different among the metals. For Pd and Pt, NH_3 is formed preferentially; whereas for Rh and Ru, N_2 is the major product formed *(4)*, more so for Ru. The relationship between the product distribution in the reduction reaction and the facility of the metal to dissociate NO may well be the factor that determines the behavior of each metal. The ease of dissociation of NO occurs in the following order: Pd *(6,7)* < Pt *(1,2,8,9)* < Rh *(3)* < Ru *(9 - 11)*. The activity for NO dissociation on Ir *(12 - 16)* places this metal between Pt and Rh. Therefore, it would be expected that the product distribution for the NO/H_2 system over Ir would be intermediate between Pt and Rh when the reduction reaction is performed under steady state condi-

tions. This postulate will be tested for the present case of NO/H_2 over Ir(110).

The steady state reaction of NO and deuterium over Ir(110) has been examined for the partial pressure of the reactants varying from 5×10^{-8} to 1×10^{-6} torr, the total pressures varying from 1×10^{-7} to 1×10^{-6} torr, the surface temperature varying from 300 to 1000 K, and ratios of the partial pressures of the reactants, $R(P_{D_2}/P_{NO})$, varying from 1/2 to 20. Both reactants and products were monitored with mass spectrometry during the steady state reaction. In order to assess the chemical composition of the overlayer under various conditions, XPS and UPS measurements were performed. The degree of order in the overlayer-substrate system was monitored using LEED.

In addition, the nonreactive coadsorption of NO and deuterium at low temperature has been investigated on Ir(110) as well as the rate of the transient reaction upon heating the surface on which these overlayers are present. Contact potential difference measurements of deuterium (NO) exposed to a surface partially covered with preadsorbed NO (deuterium) provide further insight into the competitive chemisorption of the two reactants. These data will supplement the previous studies of the chemisorption of NO *(16)* and deuterium *(17)* on Ir(110) and will aid in the interpretation of the steady state reduction reaction between NO and deuterium.

2. Experimental Details

The experiments were performed in an ion pumped stainless steel belljar that has been described previously *(17,18)*. The base pressure was less than 2×10^{-10} torr of reactive contaminants. A clean Ir(110) surface shows a (1x2)

reconstruction, which is a surface with every other row of Ir atoms missing in the [001] direction *(19)*. The surface may be visualized as alternate rows and troughs exposing (111) planes inclined to one another. Isotopic ^{15}NO and D_2 [which has identical adsorption properties as H_2 on Ir(110)] were used in both the transient and steady state experiments to separate the mass spectrometric intensities for each of the products and reactants. Monitored species are D_2 (4), D_2O (20), $^{15}ND_3$ (21), $^{15}N_2$ (30), ^{15}NO (31), $^{15}N_2O$ (46), and $^{15}NO_2$ (47). With the exception of the figure captions, the ^{15}N species will be referred to without the superscript hereafter.

For both the transient and the steady state experiments, NO was exposed to the surface using a directional beam doser, where the pressure of the beam has been calibrated with the pressure of the storage bulb that supplies the dosing gas *(16)*. During the transient experiments involving coadsorbed overlayers of deuterium and NO, exposures of D_2 were performed via a leak valve. However, for the steady state reaction of D_2 and NO, both partial pressures of the reactants were exposed to the surface via the directional beam doser. A known partial pressure of each gas was admitted to the storage bulb of the doser. The partial pressures of the gases are calculated from the calibration for each gas, which is measured separately. For example, one torr of NO or D_2 in the storage bulb is approximately equal to 1.1×10^{-7} or 1.3×10^{-7} torr in the dosing beam, respectively. The calibration appropriate for the separate gases was the same as that when NO and D_2 were mixed in the bulb. The total pressure in the storage bulb was limited to 10 torr which is upper bound to the pressure that could be measured by the capacitance monometer (MKS Instru-

ments). Since the doser and the crystal were positioned so that part of the gases desorbing from the crystal are in line-of-sight of the mass spectrometer, the intensities of the reactants and products could be measured directly (although this is not crucial to the results). Also, the gas flux from the doser does not load the ion pumps, causing pumping speed variations since the beam-to-background pressure ratio for NO is approximately 100:1. Another advantage of the beam method is that wall effects caused by backfilling the reactor are minimized.

The steady state reaction sequence is as follows. For a given pressure ratio R and a total pressure P_T, the surface was annealed in vacuum above 1600 K to remove any contaminants. The surface was allowed to cool to near room temperature before it was exposed to the beam of reactants for 10 minutes to saturate the adsorbed overlayer fully. Then, the surface was heated (< 0.5 K - s^{-1}), and the reactant and product intensities were measured with each sample every three seconds. Upon reaching the maximum temperature desired, the surface was cooled at approximately the same rate to near room temperature. In many temperature cycles, the temperature was held at various points for several minutes to ensure a steady state rate had been established. Under the chosen reaction conditions ($R \geq 1/2$), the intensity of D_2 did not vary measurably, and neither N_2O nor NO_2 were observed.

3. Coadsorption of NO and Deuterium

When NO is exposed to low precoverages of deuterium on Ir(110) at 100 K, the adsorption kinetics of NO are unchanged from NO adsorbed on a clean sur-

face *(16)*, as evidenced by the combined thermal desorption yields of NO and N_2. Figure 1 presents thermal desorption spectra of NO, N_2, D_2O and D_2 from Ir(110). The surface was precovered first with 0.33 ML deuterium at 100 K, which saturates the most tightly bound state of deuterium *(17)*, and subsequently various exposures of NO were applied. Heating the surface (20 K - s^{-1}) produces various amounts of the desorption products, depending on the initial exposure of NO. Although the saturation coverage of NO (9.6×10^{14} cm^{-2}) is not affected by preadsorbed deuterium, the yields of NO and N_2 are different than that from the clean surface. Approximately 23% of the NO present initially desorbs as NO at saturation in Fig. 1, whereas 35% desorbs as NO from the clean surface *(16)*. However, the fraction of NO desorbing from the high temperature feature is unchanged from the clean surface (18%) and represents desorption from a surface with oxygen present *(16)*. The fraction of NO desorbing from the low temperature featured is decreased (at saturation) from 17% to 5% when deuterium is preadsorbed. This feature represents desorption of NO from a surface free of oxygen. The temperature and shape of the desorption features of NO and N_2 are unchanged in Fig. 1 from the clean surface. Therefore, low coverages of deuterium affect only the distribution of NO and N_2, i.e. the selectivity of the reaction for nitrogen desorption.

The desorption of D_2 in Fig. 1 is affected strongly by the presence of increasing coverges of NO as compared to the clean surface. The fractional coverages of D_2 calculated from the thermal desorption spectra among the five desorption curves of D_2 and D_2O was in the range 0.33 to 0.43 ML and varies by the coverage range since some background D_2 adsorbs on the surface during

the exposure to NO. Two peaks appear near 240 K and 490 K for the desorption of D_2 when the surface is saturated with NO compared to a single peak at 390 K when the surface is clean. The peak at 240 K is in the temperature region where D_2 desorbs from the low temperature state of deuterium (hydrogen) when present at higher coverages on the clean surface *(17)*. Moreover, contact potential difference (CPD) measurements indicate that NO shifts deuterium from the high temperature state to the low temperature state as NO chemisorbs at 100 K, as presented later. After the desorption maximum of D_2 at 240 K is passed, a desorption peak for D_2O occurs when the deuterium layer is saturated with NO as seen in Fig. 1. Some dissociation of NO takes place below 300 K to cause D_2O to be formed, although the yield of D_2O is small since the curves are expanded by a factor of 25. Approximately 5% of the NO dissociates during adsorption near 300 K when deuterium is absent from the surface *(16)*, and it may be approximately the same fraction that dissociates as the surface is heated in this case. The higher temperature peaks of D_2 (490 K) and D_2O (440 K) are of low intensity but are quite broad. These occur in the same temperature range where N_2 and NO desorb. In this region, the surface has large coverages of oxygen and NO and has low coverages of deuterium and nitrogen adatoms. As the temperature increases, the concentration of deuterium adatoms decreases causing the formation of D_2 to dominate over D_2O due to the larger mobility of deuterium compared to oxygen and due to diatomic recombination (D_2) being more likely than triatomic recombination (D_2O).

Thermal desorption spectra of reaction products from a surface prepared with a saturated layer of NO under three different conditions and then exposed

to 2 L D_2 are presented in Fig. 2. As in Fig. 1, the yield of D_2O is low compared to D_2, but in Fig. 2 the yield of D_2 is lower than in Fig. 1. The desorption of D_2 at high temperature occurs as NO and N_2 desorb in Fig. 2, as in Fig. 1. Again, the temperature at which N_2 and NO desorb is not affected by exposures of D_2 if the overlayer of NO is saturated at 100 K. Also, the distribution of N_2 and NO is not affected and is the same as if no deuterium were adsorbed. However, the desorption results for the other two surface preparations are not so obvious. The concentration of deuterium that chemisorbs does not depend in a simple way upon the coverage of NO and the coverage of oxygen. Adsorbing NO at 450 K, cooling and exposing to 2 L D_2 at 100 K causes the surface composition to be 0.51, 0.31 and 0.20 fractional coverages of oxygen, NO and deuterium, respectively. Saturating the surface at 100 K with NO and then exposing to 2 L D_2 allows 0.33 fractional coverage of deuterium to chemisorb. Annealing the saturated overlayer of NO at 100 K to 400 K, cooling to 100 K and exposing to 2 L D_2 causes the surface composition to be 0.32, 0.51 and 0.23 fractional coverages of oxygen, NO and deuterium. Also, 2 L D_2 exposed to a saturated oxygen overlayer results in the adsorption of approximately 0.3 ML of deuterium. Thus, saturated overlayers of NO or oxygen (individually) do not block the adsorption of deuterium as does co-adsorbed NO and oxygen. Saturating the surface with oxygen and then saturating further with NO (< 0.5 ML) blocks deuterium adsorption completely. This observation will be pertinent to the steady state reaction of NO and D_2 presented in the following section. Finally in Fig. 2, the desorption temperature for D_2O and the yields of N_2 and NO depend on the relative initial surface coverages of NO and oxygen. Adsorbing NO at 450 K and adsorbing deuterium at low temperature allows deuterium to

react with oxygen to form D_2O more readily than the other two surface preparations in Fig. 2. Comparing the NO/N_2 desorption yields in this case and for the surface prepared by annealing a saturated overlayer of NO to 400 K shows that the presence of oxygen tends to cause increasing amounts of NO to desorb rather than N_2 , as observed when no deuterium is present *(16)*.

As an additional technique to gain insight into the competitive adsorption of NO and deuterium (hydrogen), CPD measurements of NO (D_2) on deuterium (NO) overlayers were performed on Ir(110) at 100 K. The CPD of NO is presented in Fig. 3 as a function of fractional coverage for NO adsorbed on (a) a clean surface, and (b) a surface with 0.33 ML deuterium adsorbed initially [β_2-state *(17)*]. The CPD of NO in Fig. 3(a) has been reported previously *(16)* but is reproduced here for comparison. Note that the CPD of NO decreases weakly with coverage, attains a minimum near 0.5 ML and increases slightly near 0.8 ML as the completion of a disordered overlayer superstructure is reached *(16)*. However, the CPD of NO in Fig. 3(b) exposed to the β_2-state of deuterium shows a much larger decrease and a different shape than Fig. 3(a). As seen in Fig. 1, the β_2-state of deuterium is displaced by NO into the β_1-state. Also, for the chemisorption of deuterium on Ir(110) *(17)*, the CPD of deuterium increases by 0.30 eV for the β_2-state and decreases weakly with coverage for the first adsorption sites sampled in the β_1-state. Therefore, the change in the CPD behavior of NO in Fig. 3(b) [β_2-state adsorbed] from Fig. 3(a) [clean] is due to the displacement of deuterium in the β_2-state to the less tightly bound β_1-state.

If this displacement reaction obeys a linear relationship with the coverage

of NO, then the difference between Figs. 3(a) and 3(b) would be a straight line, but this is not the case as can be visualized from the data in Fig. 3. The dispacement of deuterium by NO from its preferred sites as measured by the CPD indicates that either the degree of displacement does not occur linearly with respect to the coverage of NO or that NO and deuterium do not maintain their clean surface dipole moments independent of one another. Both situations are plausible. If the difference between the CPD values in Figs. 3(a) and 3(b) are considered at the saturation coverage of NO, this may give the CPD change for converting deuterium from β_2- to β_1-sites. The value is equal to -0.33 eV and would be equal to -0.40 eV if NO and deuterium acted independently to compete for the β_2-sites. Thus, it is more instructive to view these measurements only as showing that the conversion does occur, verifying the TDS results in Fig. 1.

The CPD of deuterium (or hydrogen) monitored as a function of exposure to a surface with different precoverages of NO provides complementary data to that of Fig. 3, and these results are shown in Fig. 4. In Fig. 4(A), the CPD of deuterium is presented over the exposure range required to saturate the β_2-state, and in Fig. 4(B) the CPD of deuterium is shown over that part of the exposure range pertinent to the β_1-state. Recalling that for the β_2-state of deuterium the CPD increases by 0.30 eV on the clean surface, it is clear that the β_2-adsorption sites are blocked strongly as the coverage of NO increases. For a saturation coverage of NO, the CPD of deuterium does not change [curve (c)] indicating that the β_2-sites of deuterium are blocked completely. Since the adsorption kinetics of deuterium were not measured as a function of the pre-

coverage of NO, the relationship between the coverage of NO and the coverage of deuterium cannot be quantified further. Over the exposure range of the β_1-state of deuterium in Fig. 4(B), NO (qualitatively) blocks these sites as well. Note that the zero in Fig. 4(B) has been shifted to the value of the CPD at 0.25 L D_2 in Fig. 4(A). For an initial coverage of NO equal to 0.23 ML, the CPD of deuterium as a function of exposure is the same as that of the clean surface. For higher coverages of preadsorbed NO, the CPD does not change as strongly with the exposure to deuterium, indicating a decreased probability for chemisorption.

In summary, the co-adsorption of deuterium and NO has been studied with TDS and CPD measurements to gain insight into the competition between the two adsorbates for adsites and to ascertain if the desorption properties of NO, N_2 and D_2 are different from the adsorption of NO and deuterium alone. Saturating a surface that is precovered with the β_2-state of deuterium (0.33 ML) with NO gives the same saturation coverage of NO, but upon desorption more N_2 desorbs (from the dissociation of NO) than from a surface with no deuterium present. The desorption shapes and peak temperatures of NO and N_2 are not perturbed by the presence of deuterium, but the desorption of D_2 is changed strongly from the clean surface in the presence of NO. Saturating the surface with NO does not block the subsequent adsorption of deuterium completely. However, an overlayer saturated with NO and oxygen, a condition that occurs during the steady state reaction at low temperatures (see the following section), completely blocks deuterium from chemisorbing. On a surface free of oxygen, NO displaces deuterium from its preferred sites (β_2) in the missing row

troughs into the less tightly bound sites (β_1) along the (111) microfacets exposed on the Ir(110)-(1x2) surface *(17)*.

4. Steady State Reaction between NO and Deuterium

The reduction of NO with deuterium over Ir(110), as measured by mass spectrometry under steady state conditions, is presented in this section. The procedure used to carry out the steady state experiments was described in Section 2. Under all conditions examined, i.e., partial pressure ratios between 1/2 and 20 ($R = P_{D_2}/P_{NO}$), temperatures between 300 and 1000 K and total pressures between 5×10^{-8} and 1×10^{-6} torr, the partial pressure of D_2 did not vary significantly (< 10%), and no N_2O or NO_2 was observed. Typically, the time required to produce a reaction cycle was between 30 and 60 minutes, where a cycle refers to heating to the maximum temperature desired and cooling to near room temperature. During a reaction cycle, the pressure in the storage bulb (see Section 2) that supplies the reaction mixture to the Ir(110) catalyst decreased by less than 5% in any particular experiment, and this decrease could be accounted for as necessary since the decrease is approximately linear with respect to time. Finally, the gain of the mass spectrometer that was used to monitor the reactants and products during the steady state reaction was measured after each set of reaction cycles in order to compare relative reaction rates between several sets of data.

Reaction cycles corresponding to a set of four ratios of partial pressures (R = 1, 2, 4, 8) at $P_{NO} = 1\times10^{-7}$ torr are shown in Figs 5(A)-5(D), presenting the mass spectrometric intensities of NO, N_2, D_2O and ND_3 [Fig. 5(D) only] as a

function of surface temperature. The intensity has been shifted between each specie for clarity. Arrows on each curve indicate whether the surface temperature is increasing or decreasing. The initial rise in N_2 production near 440 K is seen always in the first reaction cycle for all reaction conditions presented here, but never in succeeding reaction cycles if the surface is not cleaned of oxygen. This rise in N_2 production is not followed by a decrease in the NO intensity or by an increase in the D_2O intensity as required by mass balance. The N_2 peak is due to the surface initially containing a large coverage of NO near room temperature converting to a surface containing a large coverage of oxygen and NO. Thus, the surface conversion causes an *apparent* increase in the steady state rate of N_2 production. Rather, this initial desorption of N_2 is a *nonsteady state conversion* which depends only upon the rate at which the surface is heated. A second maximum in the rate of production of N_2 that occurs near 540 K is seen in most reaction cycles, and this is followed by a decrease in the intensity of NO and an increase in the intensity of D_2O. Consequently, this is due to a steady state reaction condition. However, part of this peak may be due to the surface conversion of some chemisorbed oxygen to a surface oxide which begins to form near this temperature *(20)*, or it may be associated with a peak seen in thermal desorption spectra of NO and N_2 *(16)*.

Returning to Fig. 5, as the surface temperature increases in Fig. 5(A), the N_2 and D_2O production increases with a concomitant decrease in the measured intensity of NO. The temperature was decreased after attaining a maximum value of 980 K, and a slight hysteresis occurred, i.e., a different rate of reaction was measured at the same temperature compared to when the surface was heated.

Below 600 K, the rate of N_2 production did not follow the upward reaction curve for the reason stated earlier concerning the "clean surface" conversion to one which contains a surface oxide as well as chemisorbed oxygen. Succeeding cycles for surfaces not cleaned by annealing to 1600 K follow closely the curve for decreasing temperature in the first cycle.

In contrast to the results for R equal to one in Fig. 5(A), the reaction for R equal to two and four in Figs. 5(B) and 5(C) is quite different at high temperatures. As the temperature increases, a plateau is reached in N_2 production that, once reached, persists at lower temperatures. An abrupt increase in D_2O production occurs at the onset of the N_2 plateau and thereafter maintains a constant value as well. As the temperature decreases further, the rate of N_2 production (NO reduction) decreases and eventually reaches the value observed as the surface temperature increased. Both the onset and the dropoff of the N_2 plateau depend upon the value of R as seen in Figs. 5(B) and 5(C). As P_{D_2} increases the temperature of the onset and the dropoff in the N_2 plateau both decrease. Moreover, the magnitude of the rate increases with P_{D_2}, noting that the reaction curves have been expanded differently. Although a constant rate of D_2O production is seen in Fig. 5(D) as the temperature is decreased, the rate of N_2 production does not remain constant. The decrease in N_2 production is due to the production of ND_3 that competes for nitrogen adatoms. The rate of production of ND_3 reaches a maximum near 560 K.

Doubling the pressure of NO (P_{NO}) for R = 2 inhibits the formation of an N_2 plateau in the rate, as seen in Fig. 6(A). These curves are similar to those in Fig. 5(A) in that neither contains a plateau, but some hysteresis occurs at

high temperature. Thus, the existence of a plateau (high reduction rate) does not depend on R only, but depends also on the absolute value of P_{NO}. Doubling P_{D_2} [compare Figs. 6(B) and 6(A)] causes the N_2 plateau to appear near 840 K, and the curves are similar to those of Figs. 5(B) and 5(C).

The last set of reaction curves is presented in Fig. 7 where the production of ND_3 is maximized by the use of a low pressure of NO and large values of R. For $P_{NO} = 5\times10^{-8}$ torr and R = 8 [Fig. 7(A)], the plateau in the rate of N_2 production occurs near 700 K, accompanied by an abrupt increase in D_2O production, as seen before. As the temperature decreases, the N_2 intensity varies more strongly than was observed in Fig. 5(D) where ND_3 was first detected. In fact, a relative minimum and relative maximum occur in the N_2 curve which is directly associated with the maximum rate of production of ND_3 appearing near 540 K. Once the relative maximum in N_2 production is passed at 520 K, the rate of reaction falls uncontrollably, and the shape of the dropoff depends upon the rate of temperature decrease, i.e., the rate decreases in a smaller temperature range than shown here.

The final reaction cycle, presented in Fig. 7(B), represents the most favorable conditions to produce ND_3 examined on Ir(110), namely, $P_{NO} = 5\times10^{-8}$ torr and R = 20. In Fig. 7(B), the onset of a high rate of reaction does not occur abruptly, as seen previously. Moreover, a small rate of ND_3 production occurs as the temperature increases. As the surface temperature decreases, the competition between N_2 and ND_3 production favors the formation of ND_3 which reaches a maximum near 530 K. This can be seen by a mass balance of ND_3 and N_2 with respect to NO. Again, the rate of N_2 production attains a relative

maximum as the ND_3 production falls to zero.

In summary, Figs. 5-7 provide representative data that may be used to gain insight into the competing processes which are important during the steady state reduction of NO with D_2 (or H_2). It is apparent that the formation of N_2 and ND_3 compete strongly for nitrogen adatoms, provided by the decomposition of NO, when a large excess of D_2 is present in the reaction mixture. Other factors depend strongly on the values of R as well, such as whether or not a plateau in N_2 production is formed, the magnitude of the reduction rate, and the temperature range over which the N_2 plateau is stable. Three reaction regimes are of interest: (1) The reduction reaction in the "unactivated" region regardless of whether or not a plateau exists in the reaction cycle, (2) the plateau in N_2 production, and (3) ND_3 production. Each of these reaction regimes will be examined with respect to the structure of the overlayer and substrate, composition of the adlayer, and the pressure dependences on the reactants for the rate of reduction.

Three N_2 production cycles are shown in Fig. 8 that were presented in the previous figures but are expanded to show clearly the changes caused by varying the partial pressures of the reactants. Increasing P_{NO} at a constant P_{D_2} [Figs. 8(b) and 8(c)] increases the temperature for the onset and dropoff of the N_2 plateau, increases the rate of N_2 production on the plateau, and decreases the rate of N_2 production before the plateau is reached. The latter two observations are for a constant temperature that allows the same reaction regime to be compared. Maintaining P_{NO} constant and increasing P_{D_2} [Figs. 8(a) and 8(b)] decreases the temperature for the onset and dropoff of the N_2 plateau

and increases the rate of N_2 production both on the plateau and before the plateau.

In order to gain insight into the reduction reaction when N_2 is the primary nitrogen-containing product, the dependence of the rate below and on the N_2 plateau and the dependence of the temperature for the onset and dropoff were fit empirically as a power law of the partial pressures of the reactants. For the rate of N_2 production at low rates (T increasing), in the presence or absence of a plateau, the rate may be expressed as

$$R_{N_2} = c P_{NO}^{-1/2} P_{D_2} \tag{1}$$

at a constant temperature. Also, on the N_2 plateau at temperatures where N_2 only is produced, the rate of N_2 production is described by

$$R_{N_2} = c' P_{NO} P_{D_2}^{1/2}. \tag{2}$$

Referring to Fig. 9, the temperature (T_h) and pressure dependences of the onset of the N_2 plateau obey the following relation

$$\ln[P_{NO}^{3/2} P_{D_2}^{-1}] = \frac{\Delta E_1}{k T_h} + \ln A_1 \tag{3}$$

where A_1 is a preexponential factor and ΔE_1, equal to -11.2 kcal-mole^{-1}, is an energy difference between two competing processes. Finally, the empirical expression that fits the temperature dependence of the dropoff (T_l) in the N_2 plateau is

$$\ln[P_{NO}^{3/2} P_{D_2}^{-1/2}] = \frac{\Delta E_2}{k T_l} + \ln A_2$$

(4)

where A_2 is a preexponential factor and ΔE_2, equal to -8.3 kcal-mole^{-1}, is an energy difference between two competing activated processes. Each of these expressions will be discussed in Section 6.

For a given set of partial pressures of D_2 and NO, the rate of reaction of N_2 (below the plateau) as the surface temperature increases may be written as

$$R_{N_2} = \Gamma P_{D_2} P_{NO}^{-1/2} \exp[-E/\ kT], \tag{5}$$

using the empirical expression in Eq. (1), and writing out the term c in Eq. (1) as $\Gamma\exp[-E/\ kT]$. Plotting $ln\ R_{N_2}$ as a function of T^{-1} should give a straight line if this expression holds, and three of these experimental plots are shown in Fig. 10 over the range of conditions observed. All three cases: (1) no N_2 plateau, (2) a N_2 plateau and (3) a N_2 plateau with ND_3 production, are included in Fig. 10. The slope of each straight line in Fig. 10 gives the effective activation energy, E, for the reaction to proceed. In Fig. 10, E varies from 10.3 to 12.6 kcal-mole^{-1}, and all other slopes that were calculated lie in this range. The intercepts of the lines in Fig. 10 are proportional to $\Gamma P_{D_2} P_{NO}^{-1/2}$. Once a calibration is obtained for R_{N_2}, the value of Γ may be calculated, and it was found to be equal to $1\times10^{19\pm1}$ molecules- cm^{-2}-s^{-1}-torr$^{-1/2}$. The error limits are estimates of the bounds due to the averaging of each experimental curve plotted.

Turning to the pressure dependence of ND_3 production at the ND_3 reaction maximum, the rate fits the following relation

$$R_{ND_3} = c'' P_{D_2}^2 P_{NO}^{-1}, \tag{6}$$

including all experimental conditions that produce ND_3. The interpretation of this expression, as for the other empirical rates, will be discussed in Section 6. Several experimental conditions that produce ND_3 in appreciable quantities are shown in Fig. 11. The rate of ND_3 production is shown only as a function of surface temperature for $P_{NO} = 5\times10^{-8}$ torr and R varying from 4 to 20. From Fig. 11, the rate of ND_3 production does not vary with respect to the temperature at which the maximum rate occurs (545 K), and it exhibits asymmetric behavior with a high temperature tail that broadens as R increases.

In summary, experimental reduction reaction cycles have been presented to show the widely different rates in the reduction of NO that occur on Ir(110) as the surface temperature and the partial pressures of the reactants vary. Also, the reduction products containing nitrogen (N_2 and ND_3) are formed in different distributions that depend upon the partial pressures of the reactants and compete between one another strongly for nitrogen adatoms. The dependence of the reaction rate for N_2 and ND_3 on the partial pressures of the reactants has been derived empirically from the experimental curves. The results of this section will be combined with the results that will be presented in the following section, and they will be discussed together in Section 6.

5. XPS, UPS, AES and LEED Results

Several XPS and UPS measurements were performed to determine the chemical composition of the adlayer at various points during the steady state reaction. Also, LEED was used to monitor the order in the adlayer at similar points in the steady state reaction, lending another insight into the reaction.

During the steady state reaction under various conditions the reaction was terminated by suddenly cooling the Ir(110) surface and rotating it away from the reactant flow in the dosing beam. The surface was then analyzed in the N(1s) and O(1s) regions of binding energy by XPS and in the valence region by HeI UPS. In Fig. 12 (XPS) and in Fig. 13 (UPS), three points in the steady state reaction are shown for $P_{NO} = 5\times10^{-8}$ torr: (a) R = 10, quenched at ND_3 reaction maximum (540 K); (b) R = 10, completion of a reaction cycle; and (c) R = 1, completion of a reaction cycle. The N(1s) region in Fig. 12 shows one feature centered at 396.7 eV, which is due to nitrogen adatoms, when the reaction is terminated at the ND_3 reaction maximum. Under the same conditions, the O(1s) shows one low intensity feature centered near 530.5 eV. The corresponding result with UPS [Fig. 13(a)] yields an emission of low intensity between 5 and 6 eV below the Fermi level, E_F, which is due mainly to the nitrogen (2p) orbital. The emission in the O(1s) region of binding energy at 530.5 eV may be caused by hydroxyl groups which exhibit this binding energy on Ir(110) *(21)*. However, no UPS features are observed corresponding to this water fragment, which occur at 11.1 and 7.8 eV on Pt(111) *(22)*. Thus, the assignment of the O(1s) peak in Fig. 12(a) is subject to question, but it is of rather low intensity.

Performing the steady state reaction for R = 10 through a complete reaction cycle and then recording the XP and UP spectra yield the results shown in Figs. 12(b) and 13(b). The N(1s) binding energy region has a single peak with a large high binding energy tail at 400.1 eV which is due to adsorbed NO *(16)*. Also, the O(1s) region has a peak due to adsorbed NO at a binding energy of

531.5 eV. In addition, adsorbed oxygen is present as evidenced by the peak near 528.8 eV. Adsorbed NO is seen as well in Fig. 13(b) for the valence region at 8.5 and 10.4 eV which are emissions from the 1π and 5σ orbitals of molecular NO *(16)*. The emission near 12.8 eV is due to the 4σ orbital but has shifted from its value on the clean surface at low temperature, 13.5 eV. Similar to Fig. 13(a), emission is seen also near 6 eV in Fig. 13(b) which, in this instance, is due to the oxygen (2p) orbital.

The reaction cycle for R = 1, represented in Figs. 12(c) and 13(c) by the XPS and UPS measurements, indicates only one nitrogen-containing species, NO, is present here as for the case of R = 10. However, the concentration of NO is smaller and the concentration of chemisorbed oxygen is larger, as seen in Figs. 12(c) compared to Figs. 12(b). In agreement with this, the valence orbitals (UPS) in Fig. 13(c) are of lower intensity for adsorbed NO, and the O(2p) emission near 6 eV is larger. The orbitals of NO are not perturbed greatly in the reaction cycles compared to the clean surface *(16)*.

The last electron spectroscopy measurement was to record the Auger N-KLL transitions of nitrogen adatoms after terminating the reaction at the ND_3 rate maximum. Two features are seen in Fig. 14 at kinetic energies of 385.7 and 372.5 eV for the N-KLL region. Two features were observed also for nitrogen adatoms on polycrystalline Pd *(23)* at similar kinetic energies. The transition at 385.7 eV involves the N(2p) levels in the Auger process and the transition at 372.5 eV involves both the (2p) and (2s) orbitals of the nitrogen adatoms, as calculated from a simple approximation for the Auger transitions *(24)*.

Finally, LEED observations were made after the reaction was terminated, and the order of the overlayer and substrate was monitored. For low values of R which do not cause a plateau in N_2 production, an imperfect oxygen-c(2x2) overlayer structure is observed as the rate of N_2 production increases with surface temperature and this represents oxygen chemisorbed on the *unreconstructed* (1x1) surface that is stabilized by a surface oxide *(20)*. The degree of order of this LEED superstructure depends upon the reaction conditions. After the termination of the reaction, if the temperature was lower or if R was larger the order in the overlayer was always (qualitatively) less. After the reaction cycle was completed for low values of R and the surface cooled to near room temperature, a (1x2) LEED superstructure was observed with sharp integral order spots and large, diffuse half-order spots. This superstructure does not represent the reconstructed substrate (1x2) pattern since the half-order substrate spots never were large and diffuse, but were streaked in the [001] direction, if the substrate was disordered somewhat. Rather, this overlayer contains approximately 0.5±0.05 ML of both NO and oxygen. It was observed also if an oxygen-c(2x2) superstructure was formed, and then the overlayer was saturated with NO at 300 K *(16)*. Thus, the (1x2) pattern is a superstructure of NO and oxygen co-adsorbed on the Ir(110)-(1x1) surface.

If the value of R is sufficiently large to achieve a plateau in N_2 production, the LEED superstructure is a sharp (1x2) which is a clean and reconstructed substrate pattern. The coverages of NO and oxygen are less than 2% as measured by thermal desorption mass spectrometry. As the surface temperature decreases (with sufficiently large R) and the maximum rate in ND_3 production

is reached, the LEED pattern shows streaks between the substrate spots in the [001] direction with some modulation of intensity, if the reaction is terminated and the surface is cooled to room temperature. From the XPS, UPS and AES results only nitrogen adatoms are present, and this pattern is probably a poorly ordered p(2x2) superstructure on Ir(110)-(1x2). Near the drop-off in N_2 production at low temperature, LEED shows a (1x2) structure with streaking along and between the substrate spots and a higher background than before the dropoff. The streaking along the substrate spots is reminiscent of chemisorbed oxygen *(20)*, and the streaking between the rows is due to both oxygen and nitrogen adatoms. Once the reaction cycle is complete (for large R, > 4), the (1x2) substrate is still observed at room temperature, but the background is quite high as it appears when the surface is saturated with NO at 300 K or below *(16)*.

In the following section, the results of this section and Section 4 will be discussed in terms of understanding microscopically the various stages of the reaction between NO and D_2 over Ir(110). Modelling of the elementary steps will be limited to building qualitatively a conceptual model due to the rather complex competing processes occuring as the reaction proceeds.

6. Discussion

As seen from the data presented in the previous sections, the reduction of NO with D_2 (or H_2) over Ir(110) is quite complex. Depending on the surface temperature and the partial pressure of the reactants the rate of reduction and the product distribution vary considerably. Moreover, the history of the surface (whether the surface is clean or oxidized) during a reaction cycle

influences the rate of reaction. In this section general observations concerning the relative activity of Ir(110) compared to the other transition metals will be discussed. The majority of this section will be devoted to interpreting the observed reaction phenomena for NO + D_2 over Ir(110).

Although hysteresis in the rate of reduction of NO with H_2 over polycrystalline Pt *(1)* was not reported, the distribution of the major products containing nitrogen (N_2 and NH_3) did change in the same way as seen here for Ir(110). Under similar conditions, the maximum rate of ammonia production is near 540 K on Ir(110) compared to 495 K on polycrystalline Pt *(1)*. The temperature at which 50% of the NO is reduced varies for Ir(110), as seen previously, but it is always higher than 445 K which was reported for polycrystalline Pt *(1)*. Also, the ratio of partial pressures (D_2/NO) required to achieve approximately the same fraction of NO converted to ND_3 is (qualitatively) higher for Ir(110) than Pt *(1)*. Thus, the postulate put forth in Section 1 is verified, namely the activity of the Ir catalyst to produce ammonia is lower than that of Pt, and may be related to the observation that NO dissociates more readily on Ir than Pt. Since the reduction reaction has not been studied on Rh under ultra-high vacuum conditions, it cannot be verified further that the activity of Ir is intermediate between Pt and Rh as suggested by the trend in the activity to dissociate NO. From the investigations of the NO/H_2 system on supported metals at atmospheric pressure the trend would at least place the activity of Ir to produce ammonia as less than that of Ru *(4,5)*. This would concur also with the ease of dissociation of NO on Ir *(12-16)* compared to Ru *(9-11)*.

Three regions of interest may be considered separately as suggested by

the steady state reaction cycles. The first region is where N_2 is produced at a lower rate prior to the formation of a plateau (if there is one) and after the rate has passed through a second relative maximum above 500 K as T increases. At this point, the conversion of the surface from one which is relatively free of oxygen to one which is partially covered with oxide and chemisorbed oxygen and NO is completed. The second region is the plateau in N_2 production (and D_2O production by mass balance) which is insensitive to the surface temperature but is dependent upon the partial pressures of the reactants. The third region is the temperature and pressure range under which ammonia production competes strongly with the N_2 production for nitrogen adatoms, i.e., for R > 4 and 470 < T < 630 K, after the surface achieves a high rate of NO reduction. In addition to these three regions, the transitions between the high and low rates of NO reduction will be discussed.

Region 1. Low Rate of N_2 Production

As seen in Figs. 5-7, the rate of production of N_2 is inhibited strongly in the region where the rate is not on a plateau as the temperature increases. The results in Section 2 concerning the adsorption of deuterium on a saturated overlayer of co-adsorbed NO and oxygen showed that deuterium is blocked almost completely from chemisorbing, whereas NO or oxygen alone did not block deuterium completely. In this region, the surface contains approximately a half ML of oxygen, at least a part of which is a surface oxide since the surface has reverted to the (1x1) unreconstructed structure from the (1x2) structure. Also, the surface has a partial coverage of NO which varies as the temperature varies due to the competition between desorption and adsorption

of NO under steady state conditons. As the surface temperature increases, the rate of N_2 production increases. However, N_2 cannot be produced unless the surface is cleaned of oxygen by D_2. The empirical pressure dependence of the rate on the reactants, given by Eq. (1) at a constant temperature, indicates that NO acts as a poison unlike D_2.

The dependence of the rate on P_{D_2} may be visualized by considering the elementary steps involved in producing D_2O,

$$D_2 \underset{k_2}{\overset{S_{D_2}}{\rightleftarrows}} 2D \tag{7}$$

$$D + O \xrightarrow{k_3} OD \tag{8}$$

$$D + OD \xrightarrow{k_4} D_2O_{(g)} \tag{9}$$

where S_{D_2} is the probability of adsorption of deuterium, and the various k_i are the rate coefficients of each elementary reaction. Applying the steady state approximation to adsorbed deuterium implies that

$$2S_{D_2}F_{D_2} - k_2\theta_D^2 - 2k_3\theta_O\theta_D = 0 \tag{10}$$

where F_{D_2} is the impingement flux of D_2 (proportional to P_{D_2}) in the reactant beam, and the fractional coverage of OD, θ_{OD}, is considered small. Under the conditions in this region, $2S_{D_2}F_{D_2}/k_2$ in Eq. (10) is small compared to

$(k_3\Theta_O/k_2)^2$ and Θ_D is given approximately by

$$\Theta_D = \frac{S_{D_2}F_{D_2}}{k_3\Theta_O}. \qquad (11)$$

Substituting Eq. (11) into the expression for the rate of production of D_2O yields

$$R_{D_2O} = S_{D_2}F_{D_2}, \qquad (12)$$

i.e., the proper dependence of P_{D_2} on the rate of production of N_2.

However, understanding the dependence of the rate on NO, $P_{NO}^{-1/2}$, is not so straightforward. It is appealing to think of NO as a poison since oxygen depleted by deuterium is supplied by the dissociation of NO. Moreover, NO will desorb, rather than dissociate, if the coverage of oxygen is sufficiently large. The competition between the removal rate of oxygen (R_{D_2O}), the accumulation rate of oxygen via the dissociation of NO, and the desorption rate of NO govern the rate of N_2 production.

Lastly, Arrhenius plots in Fig. 10 give the effective activation energy (E) for the steady state reaction and it lies between 10.3 and 12.6 kcal-mole^{-1} under all conditions. It may be that this value represents the difference in activation energies for the desorption and the dissociation of NO. This would not be unreasonable since estimates of this difference in energy, in the absence of deuterium, place it near 8 kcal-mole^{-1} *(16)*. However, other elementary reactions are important, so that additional activation energy differences may be embodied in E.

Region 2. Plateau in N_2 Production

For sufficiently large values of P_{D_2} compared to P_{NO} and sufficiently large temperatures, the low rate of N_2 production in Region 1 becomes unstable, and a high rate occurs that does not depend sensitively on temperature, over some temperature range. In this second region, only conditions that produce the N_2 plateau and do not form ND_3 will be considered. As observed by both TDS and LEED, when the reaction is terminated during the steady state reaction on the N_2 plateau, the surface is a clean (1x2) substrate with small coverages of nitrogen and oxygen adatoms, unlike the surface condition in Region 1. Although the oxygen adatoms present on the surface above 700 K are probably in an oxide form *(20)*, they are in low concentration and still react readily with deuterium *(26)*.

As seen in Fig. 8 and quantified by the empirical expression in Eq. (2), both NO and D_2 accelerate the rate in the plateau region. The linear dependence on P_{NO} in Eq. (2) indicates that within the pressure range studied for NO, 5×10^{-8} to 4×10^{-7} torr, the reaction for form N_2 (for a given P_{D_2}) is limited by the rate of dissociation of NO, so long as P_{D_2} is sufficiently large to maintain the plateau behavior. Also, the dependence on P_{D_2} is easily understood in the plateau region by examining the limit in Eq. (10) for $2S_{D_2}F_{D_2}/k_2$ large compared to $(k_3\Theta_O/k_2)^2$ in order to approximate Θ_D in Eq. (11). Substituting this result into the expression for R_{D_2O} gives

$$R_{D_2O} = k_3\left[\frac{2S_{D_2}F_{D_2}}{k_2}\right]^{1/2}\Theta_O \qquad (13)$$

where k_2 and k_3 appear in Eqs. (7) and (8) for the desorption of D_2 and the reaction between deuterium and oxygen to form OD, respectively.

Over the pressure range of D_2 that is accessible (5×10^{-8} to 1×10^{-6} torr), the rate of N_2 formation depends on $P_{D_2}^{1/2}$. However, if larger pressures of D_2 were studied, the rate should reach a limiting value for a give P_{NO}. This rate should be limited by the flux of NO to the surface since the initial probability of adsorption is unity independent of temperature *(16)*. The $P_{D_2}^{1/2}$ dependence in Region 2 indicates that small coverages of oxygen influence the rate of dissociation compared to the rate of desorption of NO.

The two points of instability mentioned in Section 4, termed the "onset" and "dropoff", may be conveniently discussed with Region 2 since they occur at the temperature extremes of the N_2 plateau. Although the onset becomes less sharp in temperature when ammonia is produced (at large R), these data as well as the corresponding data concerning the dropoff may be included since these points occur outside of the temperature range where ND_3 appears.

The onset in the plateau may be defined by a temperature (T_h) at which the plateau occurs and is accompanied often by a spike in D_2O production [e.g. Figs. 5(B), 5(C) and 7(A)]. Moreover, the onset is truly unstable since near T_h the rates of N_2 and D_2O production increase irreversibly to their values at the plateau. The surface reverts from a (1x1) oxide to a (1x2) clean at this point as well. It was shown in Eq. (3) that the onset depends upon $P_{NO}^{3/2}P_{D_2}^{-1}$ as a function of T_h^{-1}. If T_h is at the intersection of the asymptotic rates in Regions 1 and 2, modelled by Eqs. (1) and (2), then the dependence would be $P_{NO}^{3/2}P_{D_2}^{-1/2}$. The

$P_{NO}^{3/2}$ term is correct but the $P_{D_2}^{-1}$ dependence is more like Region 1. This is reasonable since Region 1 dictates *where* in temperature the onset occurs. The energy associated with an Arrhenius plot of Eq. (3) [Fig. 9(a)] is equal to 11.2 kcal-mole^{-1} which is in the same range found for the effective activation energy to produce N_2 in Region 1. It is not apparent, however, that these energies can be compared meaningfully.

As the temperature decreases toward the point at which the rate of NO reduction decreases, oxygen adatoms and NO admolecules begin to accumulate on the surface, seen by TDS and XPS. At some point in coverage, deuterium does not adsorb further to sustain the reaction and the dropoff occurs. At the dropoff, the nitrogen adatoms remaining on the surface are desorbed due to an increasing coverage of NO *(16)*. Once the production of N_2 is inhibited completely below the dropoff, NO and oxygen, only, remain on the surface, as determined by XPS and UPS results. In order to achieve the N_2 plateau again, the temperature must be increased to the onset found previously.

The dropoff in the high rate of NO reduction, whether the products are ND_3 and N_2 or N_2 only, was modelled empirically by Eq. (4). This expression gives the correct dependence, $P_{NO}^{3/2}P_{D_2}^{-1/2}$, on the temperature of the dropoff (T_l) if the asymptotic rates of Eqs. (1) and (2) are considered, as before for T_h. Figure 9(b) shows that $P_{NO}^{3/2}P_{D_2}^{-1/2}$ as a function of T_l^{-1} fits a straight line with E = 8.3 kcal-mole^{-1}, but again it is not clear what significance this value of the energy has in relation to the observed phenomena.

Region 3. Ammonia Production

Ammonia is formed on Ir(110) between 470 and 630 K for values of R greater than four, depending also on the partial pressure of NO. It was found from XPS, UPS and LEED results that the surface is a (1x2) substrate with a partially ordered nitrogen-p(2x2) superstructure near the ND_3 reaction maximum. Since ND_x (x = 1,2) groups are not observed with either XPS or UPS if the reaction is terminated where ND_3 is produced, the rate limiting step to form ND_3 is N + D → ND. The desorption of ND_3 is rapid in the reaction region. This is verified by thermal desorption results for NH_3 on Ir(111) where NH_3 desorbs molecularly near 300 K *(27)*.

Under conditions that produce ND_3 in competition with N_2, the empirical dependence of the rate of ND_3 production on the partial pressures of the reactants is given by $P_{D_2}^{2}P_{NO}^{-1}$ [see Eq. (6)]. As in Region 1 where N_2 is produced at a low rate, NO acts as a poison by supplying oxygen that consumes deuterium which would otherwise react with nitrogen to form ND_3. A squared dependence on P_{D_2} may suggest that diffusion of deuterium adatoms in pairs is important, which was inferred near the rate maximum for CO oxidation on Ir(110) for the squared dependence on the pressure of oxygen *(25)*. Also, the stoichiometry of the reaction between NO and D_2 to form ND_3 and D_2O requires five deuterium adatoms for every NO admolecule and would cause the rate to depend more on P_{D_2} than on P_{NO}, although N + D → ND and O + D → OD are the rate limiting steps as deduced from the data. It should be noted also that a high temperature thermal desorption feature of D_2 appears between 460 and 650 K when NO and deuterium are co-adsorbed (see Figs. 1 and 2). This desorption of D_2

brackets the range where ND_3 is produced (470 - 630 K) and may play a role in the reaction rate for ND_3 production. However, these are postulates only, since the microscopic events occurring on the surface are too complex, with the available data, to predict a priori the observed pressure dependence of the rate of N_2 production on the partial pressure of D_2.

7. Summary

The reaction between NO and D_2 over Ir(110) has been studied under ultra-high vacuum conditions by means of measurements of the steady state rate of NO reduction as a function of the partial pressures of the reactants (5×10^{-8} to 1×10^{-6} torr) and the surface temperature (300 to 1000 K). In addition, co-adsorption studies of NO and deuterium at low temperature were performed to gain insight into the competitive nature of the chemisorption process and to observe the desorption characteristics of the co-adsorbed overlayers as the surface is heated. The results of this investigation may be summarized as follows.

(1) Small precoverages of deuterium do not affect the kinetics of adsorption of NO but do affect the distribution of N_2 and NO that thermally desorbs from the surface. More N_2 desorbs when deuterium is present than in its absence due to the reaction between oxygen (from the dissociation of NO) and deuterium to form D_2O.

(2) The adsorption of deuterium is decreased, relative to the clean surface, when the latter is saturated with NO. However, D_2 is inhibited strongly from adsorbing when the surface is saturated with oxygen and NO, a condition that occurs under some steady state reaction conditions.

(3) Depending on the value of R, under steady state conditions a marked hysteresis occurs in the rate of NO reduction. For certain values of R and T, a plateau in the rate appears that persists as the temperature is decreased. At some temperature, depending upon P_{NO} and P_{D_2}, the rate falls uncontrollably to a new steady state where the reduction reaction is slow.

(4) For large values of R (> 4), ND_3 is produced between 470 and 630 K and competes strongly for nitrogen adatoms with N_2 production.

(5) Three regimes of the steady state reaction were examined separately:

(a) Low rates producing N_2 and D_2O only with an inhibition by NO; (b) High rates with a plateau in the rate producing N_2 and D_2O only; and (c) High rates where N_2 and ND_3 are produced competitively. Tentative explanations of the empirically observed rates were discussed in light of XPS, UPS, TDS and LEED results.

Acknowledgment

The authors are grateful to the National Science Foundation for support of this work (Grant No. CHE77-14976).

References

1. G. Pirug and H. P. Bonzel, J. Catalysis 50,64(1977).

2. R. M. Lambert and C. M. Comrie, Surface Sci. 46, 61(1974).

3. C. T. Campbell and J. M. White, Appl. Surface Sci. 1, 347(1978).

4. T. P. Kobylinski and B. W. Taylor, J. Catalysis 33, 376(1974).

5. K. C. Taylor and R. L. Klimisch, J. Catalysis 30, 478(1973).

6. H. Conrad, G. Ertl, J. Kuppers and E. E. Latta, Faraday Discuss. Chem. Soc. 58, 116(1974).

7. H. Conrad, G. Ertl, J. Kuppers and E. E. Latta, Surface Sci. 65, 235(1977).

8. H. P. Bonzel and G. Pirug, Surface Sci. 62, 45(1977).

9. P. A. Thiel, W. H. Weinberg and J. T. Yates, Jr., Chem. Phys. Letters 67, 403(1979).

10. G. E. Thomas and W. H. Weinberg, Phys. Rev. Letters 41, 1181(1978).

11. E. Umbach, S. Kulkarni, P. Feulner and D. Menzel, Surface Sci. 88, 65(1979).

12. J. Kanski and T. N. Rhodin, Surface Sci. 65, 63(1977).

13. P. A. Zhdan, G. K. Boreskov, W. F. Egelhoff, Jr. and W. H. Weinberg, J. Catalysis 45, 281(1976).

14. P. A. Zhdan, G. K. Boreskov, A. I. Boronin, A. P. Scheplin, W. F. Egelhoff, Jr. and W. H. Weinberg, J. Catalysis 60, 93(1979).

15. J. Kuppers and H. Michel, Surface Sci. 85, 201(1979).

16. D. E. Ibbotson, T. S. Wittrig and W. H. Weinberg, Surface Sci. (submitted).

17. D. E. Ibbotson, T. S. Wittrig and W. H. Weinberg, J. Chem. Phys. 72, 4885(1980).

18. J. L. Taylor, D. E. Ibbotson and W. H. Weinberg, J. Chem. Phys. 69, 4298(1978).

19. C. M. Chan, M. A. Van Hove, W. H. Weinberg and E. D. Williams, Solid State Commun. 30, 47(1979); Surface Sci. 91, 400(1980).

20. J. L. Taylor, D. E. Ibbotson and W. H. Weinberg, Surface Sci. 79, 349(1979).

21. T. S. Wittrig, D. E. Ibbotson and W. H. Weinberg, Surface Sci.(in press).

22. G. B. Fisher and B. A. Sexton, Phys. Rev. Letters(submitted).

23. K. Kunimori, T. Kawai, T. Kondow, T. Onishi and K. Tamaru, Surface Sci. 59, 302(1976).

24. G. G. Tibbetts and J. M. Burkstrand, J. Vacuum Sci. Technol. 15, 497(1978).

25. J. L. Taylor, D. E. Ibbotson and W. H. Weinberg, J. Catalysis 62, 1(1980).

26. D. E. Ibbotson, Ph. D. Thesis, California Institute of Technology, 1981.

27. R. J. Purtell, R. P. Merrill, C. W. Seabury and T. N Rhodin, Phys. Rev. Letters 44, 1279(1980).

Figure Captions

Fig. 1 Thermal desorption spectra from NO adsorbed on the β_2 state of deuterium (0.33 ML) preadsorbed on Ir(110) at 100 K. The desorption products monitored are NO, N_2, D_2 and D_2O with a heating rate of 20 K-s^{-1}.
Under these conditions deuterium was not displaced from the surface as NO was adsorbed.
For comparison, the desorption of the β_2 state of deuterium is shown (×0.5) in the absence of adsorbed NO.

Fig. 2 Thermal desorption spectra of NO, N_2, D_2 and D_2O from 2 L D_2 adsorbed on various surfaces of Ir(110) at 100 K prepared with saturation exposures of NO.
------- Saturated layer of NO adsorbed at 100 K; - - - - Saturated layer of NO adsorbed at 450 K and cooled to 100 K; and ..... Saturated layer of NO adsorbed at 100 K and annealed briefly to 400 K. The heating rate is 20 K-s^{-1}.

Fig. 3 The CPD of NO adsorbed at 100 K on Ir(110) as a function of the fractional coverage of NO. (a) Clean surface; and (b) preadsorbed β_2 state of deuterium (or hydrogen) (0.33 ML).

Fig. 4 The CPD of H_2(or D_2) adsorbed on fractional coverages of NO on Ir(110) at 100 K: (a) 0.23; (b) 0.44; and (c) 1.00.
In (A) the exposure of H_2 is sufficient to saturate the β_2 state, and in (B) the exposure of H_2 includes part of the β_1 state (see text).

The zero in (B) for the CPD is equal to the "saturation" value (at 0.25 L H_2) in (A).

Fig. 5 Steady state reaction for NO + D_2 over Ir(110). $P_{NO} = 1\times10^{-7}$ torr, and R(=P_{D_2}/P_{NO}) equal to: (A) 1; (B) 2; (C) 4; and (D) 8. The intensities monitored in the gas phase are NO, N_2, ND_3, D_2 and D_2O. For all values of R, the intensity of D_2 did not vary appreciably in a reaction cycle, and it is not shown here or in following figures. Arrows pointing to the right (left) indicate the surface temperature is increasing (decreasing). Ammonia (ND_3) production occurs in (D) only.

Fig. 6 Steady state reaction for NO + D_2 over Ir(110). $P_{NO} = 2\times10^{-7}$ torr, and R equal to: (A) 2; and (B) 4. No ND_3 is produced under these conditions.

Fig. 7 Steady state reaction for NO + D_2 over Ir(110) under conditions that favor the production of ND_3. $P_{NO}=5\times10^{-8}$ torr, and R is equal to: (A) 8; and (B) 20. Note that ND_3 and N_2 compete strongly for nitrogen adatoms.

Fig. 8 Steady state rates of N_2 production from Figs. 5 and 6. (a) $P_{NO}=1 \times 10^{-7}$ torr and R = 4;(b) $P_{NO}=1 \times 10^{-7}$ torr and R = 8; and (c) $P_{NO}=2 \times 10^{-7}$ torr and R = 4.

The intensity of N_2 has been expanded by 0.5 in (c).

Note that in (b) some ND_3 is produced near the dropoff in N_2 production, as the temperature is decreased.

Fig. 9 The empirical pressure dependence of (a) the onset, $ln\,(P_{NO}^{3/2}P_{D_2}^{-1})$ and (b) the dropoff, $ln\,(P_{NO}^{3/2}P_{D_2}^{-1/2})$ of the plateau in N_2 production as a function of T^{-1}, inverse of the surface temperature at which they occur.

Fig. 10 The temperature dependence of the rate of N_2 production as the temperature increases but before a plateau is reached (if it is present).

Three different reaction conditions are presented, as noted in the figure, for lnR_{N_2} as a function of T^{-1}.

The slope of each curve is proportional to the effective activation energy for the reaction, which is presented as well.

Fig. 11 Steady state rate of ND_3 production for $P_{NO}=5\times10^{-8}$ torr and R equal to: (a) 4.0; (b) 6.0; (c) 8.0; (d) 10.0; (e) 12.6; (f) 16.0; and (g) 20.0.

Fig. 12 XPS ($h\nu$ = 1486.6 eV) for the N(1s) and the O(1s) regions of binding energy, relative to the Fermi level, at three points in the steady state reaction.

$P_{NO}=5\times10^{-8}$ and (a) R = 10 at the ND_3 reaction maximum; (b) R = 10 after a reaction cycle; and (c) R = 1 after a reaction cycle.

For each spectrum, the reaction was terminated by simultaneously

removing the Ir(110) surface from the reactant gas beam and cooling to near room temperature.

Fig. 13 HeI UPS ($h\nu = 21.2$ eV) of Ir(110) near room temperature for three points in the steady state reaction. The corresponding conditions for (a) - (c) are given in Fig. 12.

Fig. 14 Auger electron spectrum of the N-KLL region of energy. The steady state reaction was terminated for this spectrum at the ND_3 reaction maximum proceeding under the same conditions as in Figs. 12(a) and 13(a).

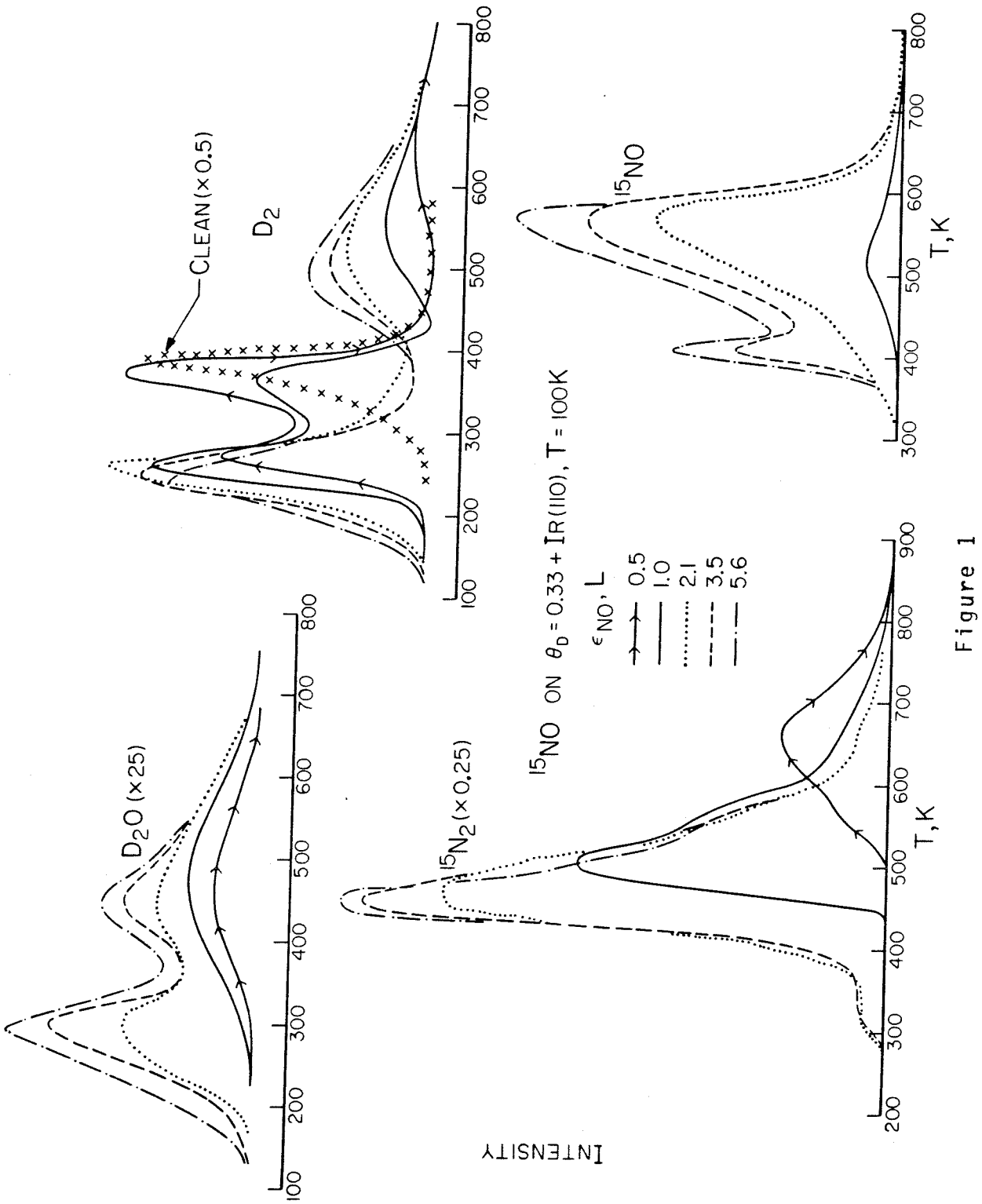
D_2O (×25)
CLEAN (×0.5)
D_2
$^{15}N_2$ (×0.25)
^{15}NO ON θ_D = 0.33 + IR(110), T = 100K
ϵ_{NO}, L
0.5
1.0
2.1
3.5
5.6
^{15}NO
INTENSITY
T, K
T, K

Figure 1

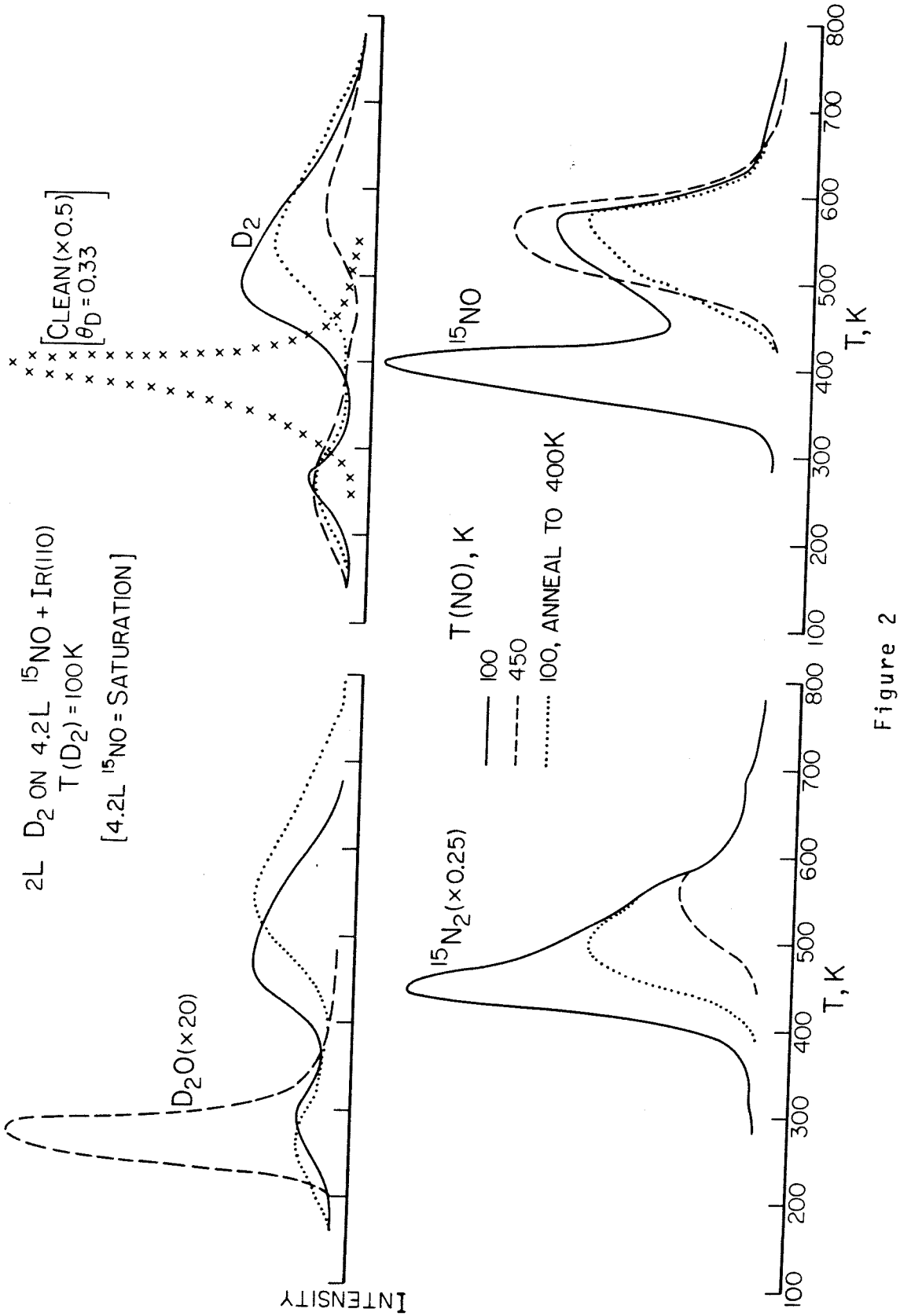
2L D2 ON 4.2L 15NO + IR(110)
T(D2) = 100K
[4.2L 15NO = SATURATION]
[CLEAN(×0.5)
θD = 0.33]
D2
D2O(×20)
15NO
15N2(×0.25)
T(NO), K
100
450
100, ANNEAL TO 400K
INTENSITY
T, K
100
200
300
400
500
600
700
800

Figure 2

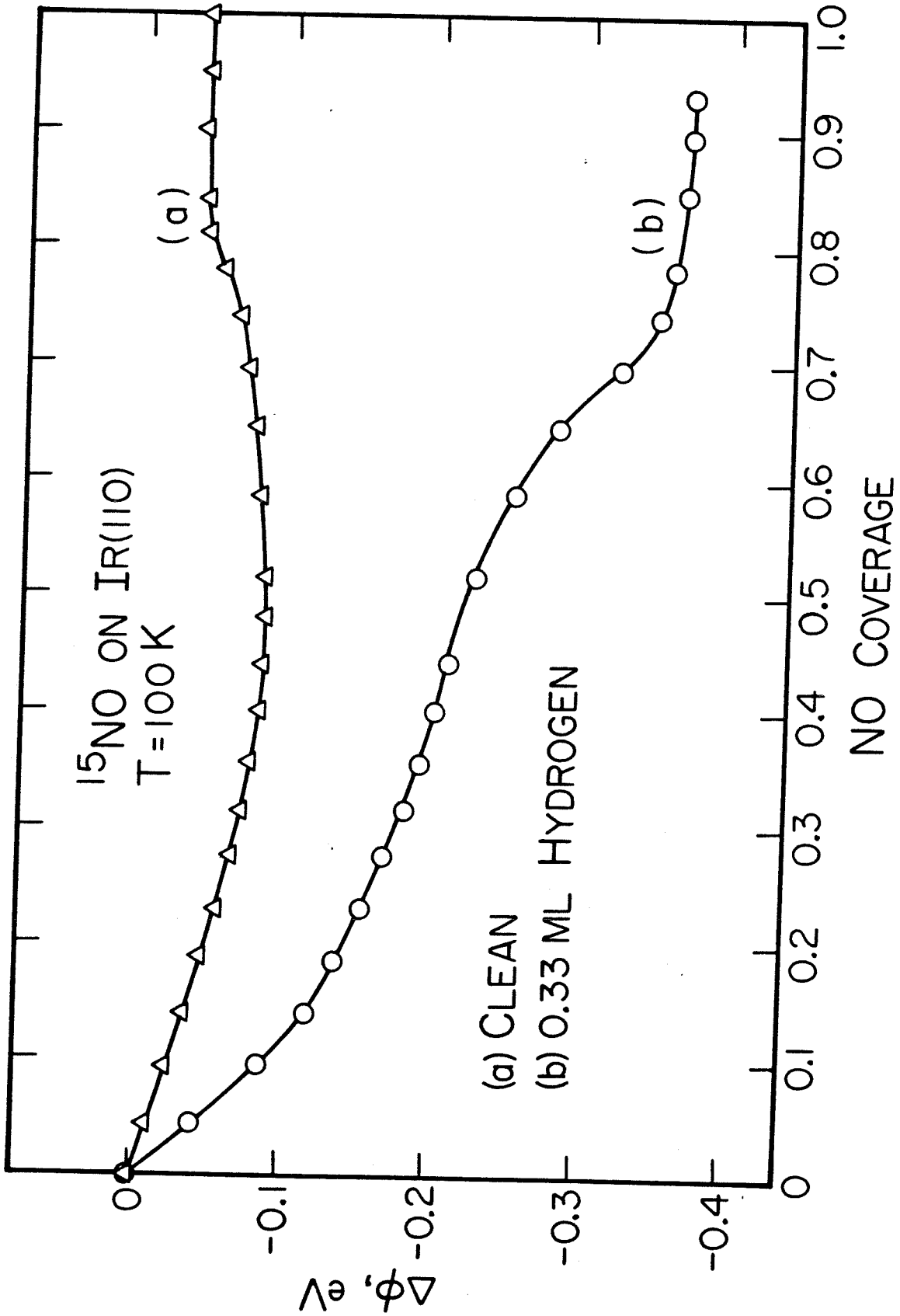
^{15}NO ON IR(110)
T=100 K
(a)
(b)
(a) CLEAN
(b) 0.33 ML HYDROGEN
$\Delta\phi$, eV
0
-0.1
-0.2
-0.3
-0.4
0.1
0.2
0.3
0.4
0.5
0.6
0.7
0.8
0.9
1.0
NO COVERAGE

Figure 3

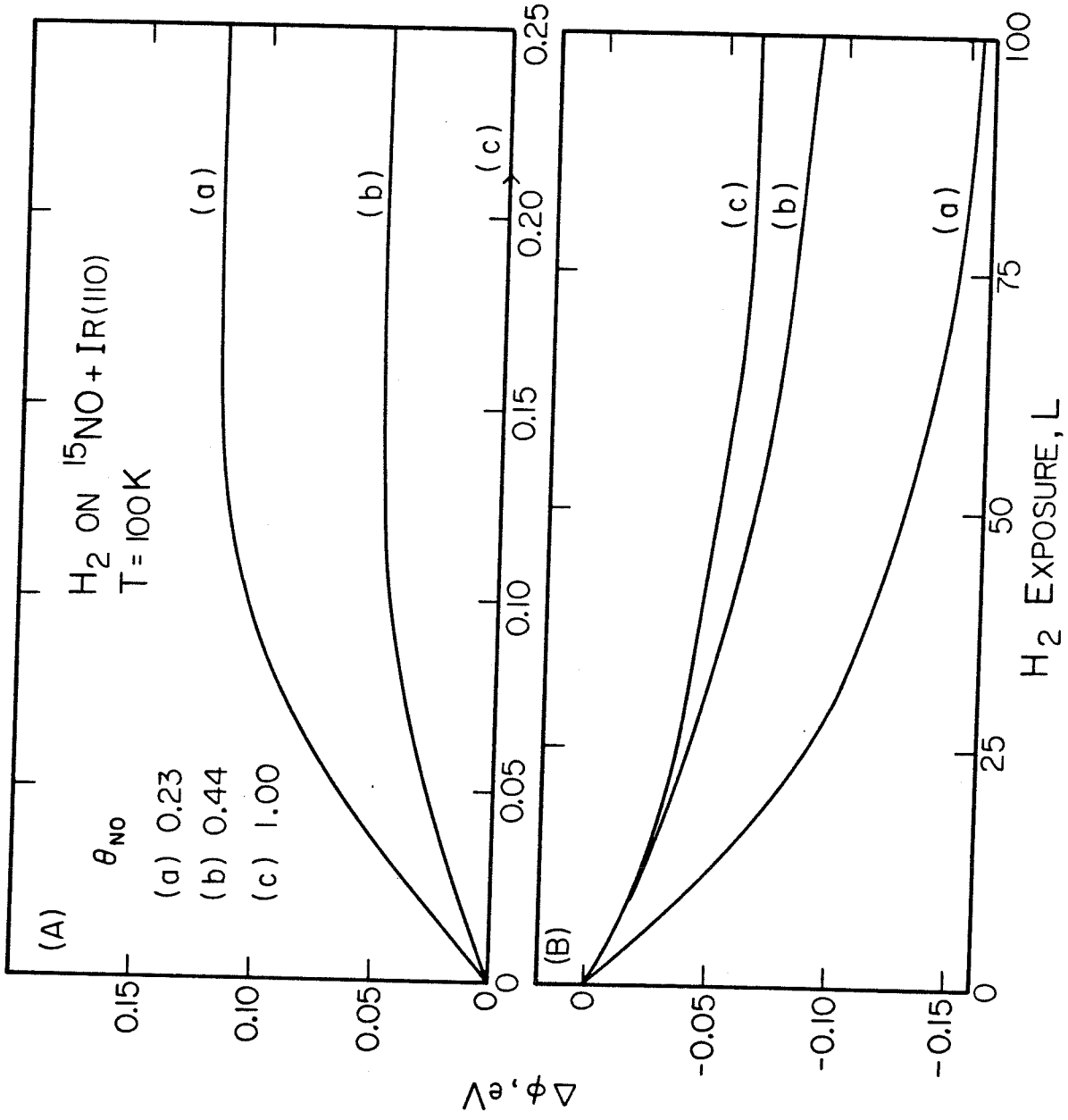
(A)
H_2 ON ^{15}NO + IR(110)
T = 100K
θ_{NO}
(a) 0.23
(b) 0.44
(c) 1.00
(a)
(b)
(c)
(B)
(c)
(b)
(a)
$\Delta\phi$, eV
H_2 EXPOSURE, L
0.25
0.20
0.15
0.10
0.05
0
-0.05
-0.10
-0.15
25
50
75
100

Figure 4

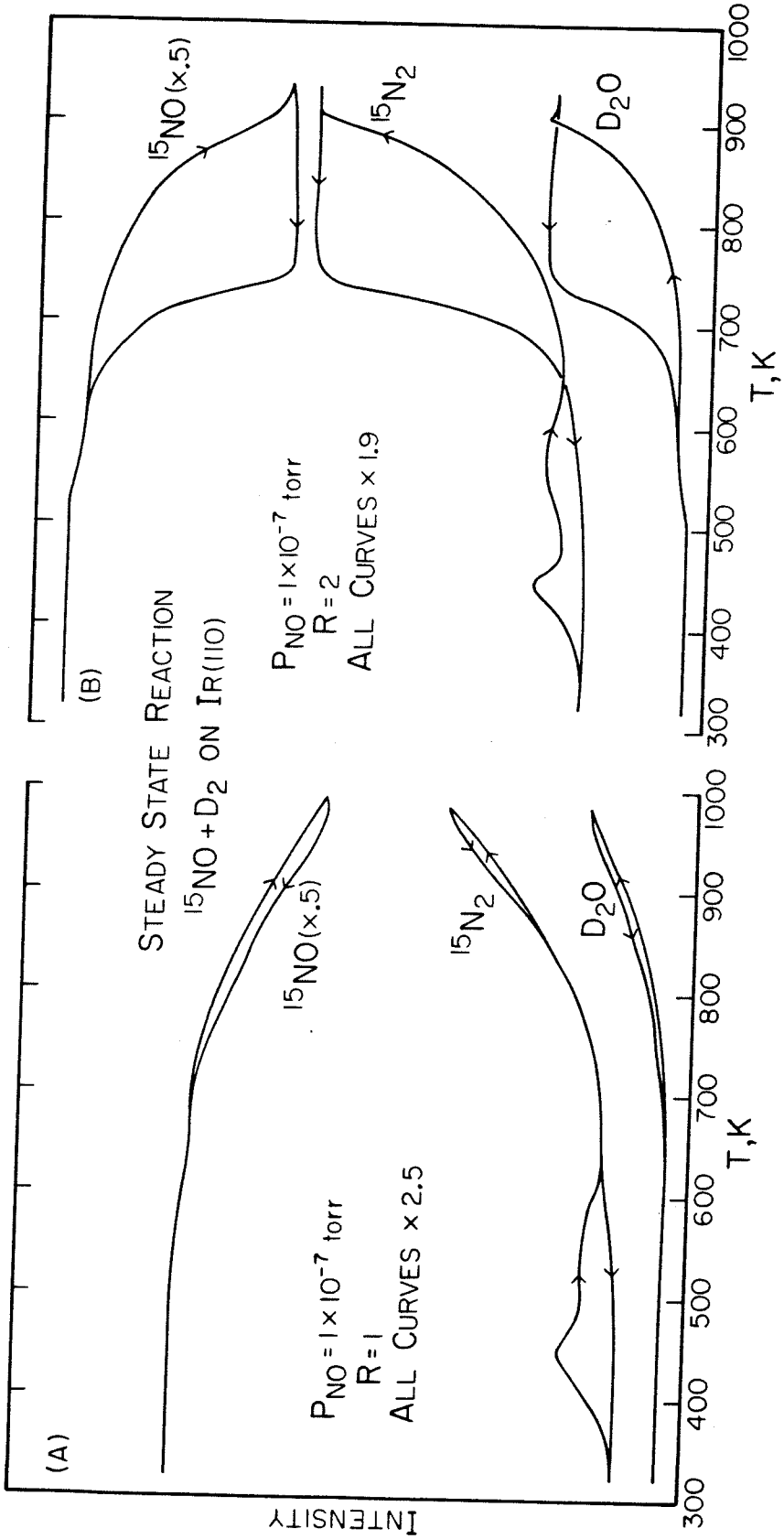
(A)
STEADY STATE REACTION
$^{15}NO + D_2$ ON Ir(110)
$P_{NO} = 1 \times 10^{-7}$ torr
R = 1
ALL CURVES × 2.5
^{15}NO(×.5)
$^{15}N_2$
D_2O
INTENSITY
T, K
300
400
500
600
700
800
900
1000
(B)
$P_{NO} = 1 \times 10^{-7}$ torr
R = 2
ALL CURVES × 1.9
^{15}NO(×.5)
$^{15}N_2$
D_2O
T, K

Figure 5-I

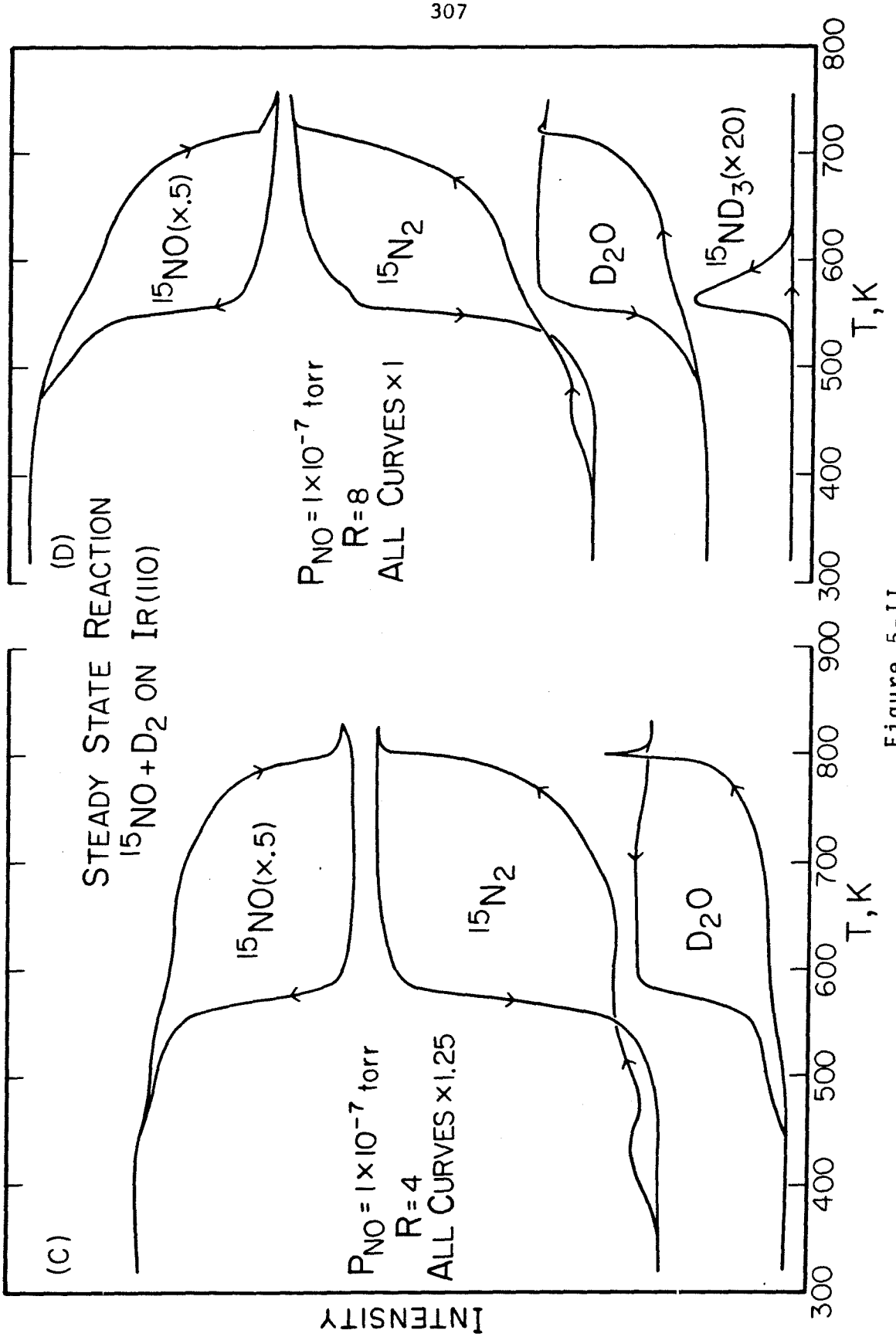
(C)
STEADY STATE REACTION
$^{15}NO + D_2$ ON IR(110)
$P_{NO} = 1 \times 10^{-7}$ torr
R=4
ALL CURVES ×1.25
^{15}NO(×.5)
$^{15}N_2$
D_2O
(D)
$P_{NO} = 1 \times 10^{-7}$ torr
R=8
ALL CURVES ×1
^{15}NO(×.5)
$^{15}N_2$
D_2O
$^{15}ND_3$(×20)
INTENSITY
T, K
300
400
500
600
700
800
900

Figure 5-11

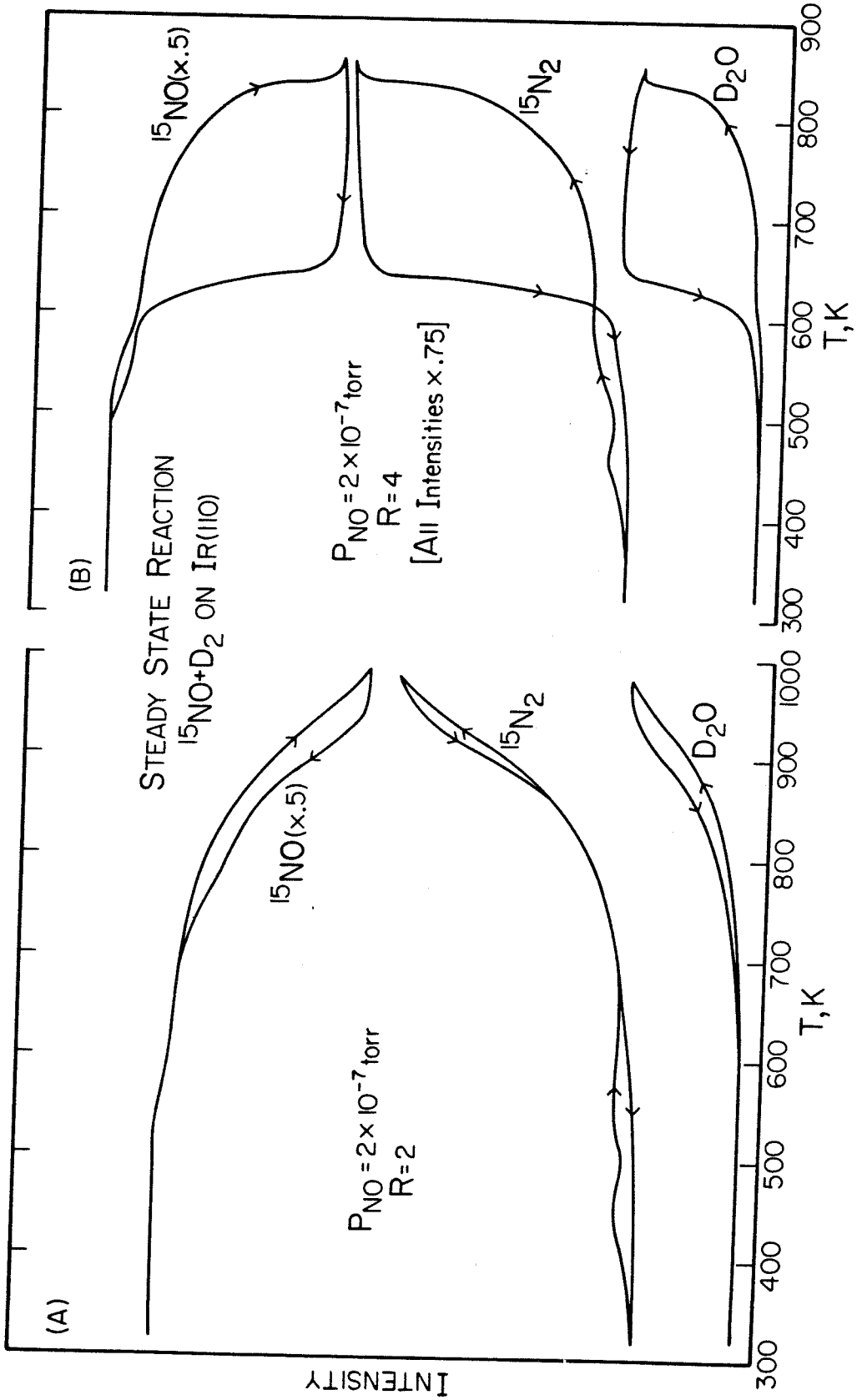
STEADY STATE REACTION
$^{15}NO+D_2$ ON IR(110)
(A)
$P_{NO}=2\times10^{-7}$ torr
R=2
$^{15}NO(\times.5)$
$^{15}N_2$
D_2O
(B)
$P_{NO}=2\times10^{-7}$ torr
R=4
[All Intensities x .75]
$^{15}NO(\times.5)$
$^{15}N_2$
D_2O
INTENSITY
T,K
300
400
500
600
700
800
900
1000

Figure 6

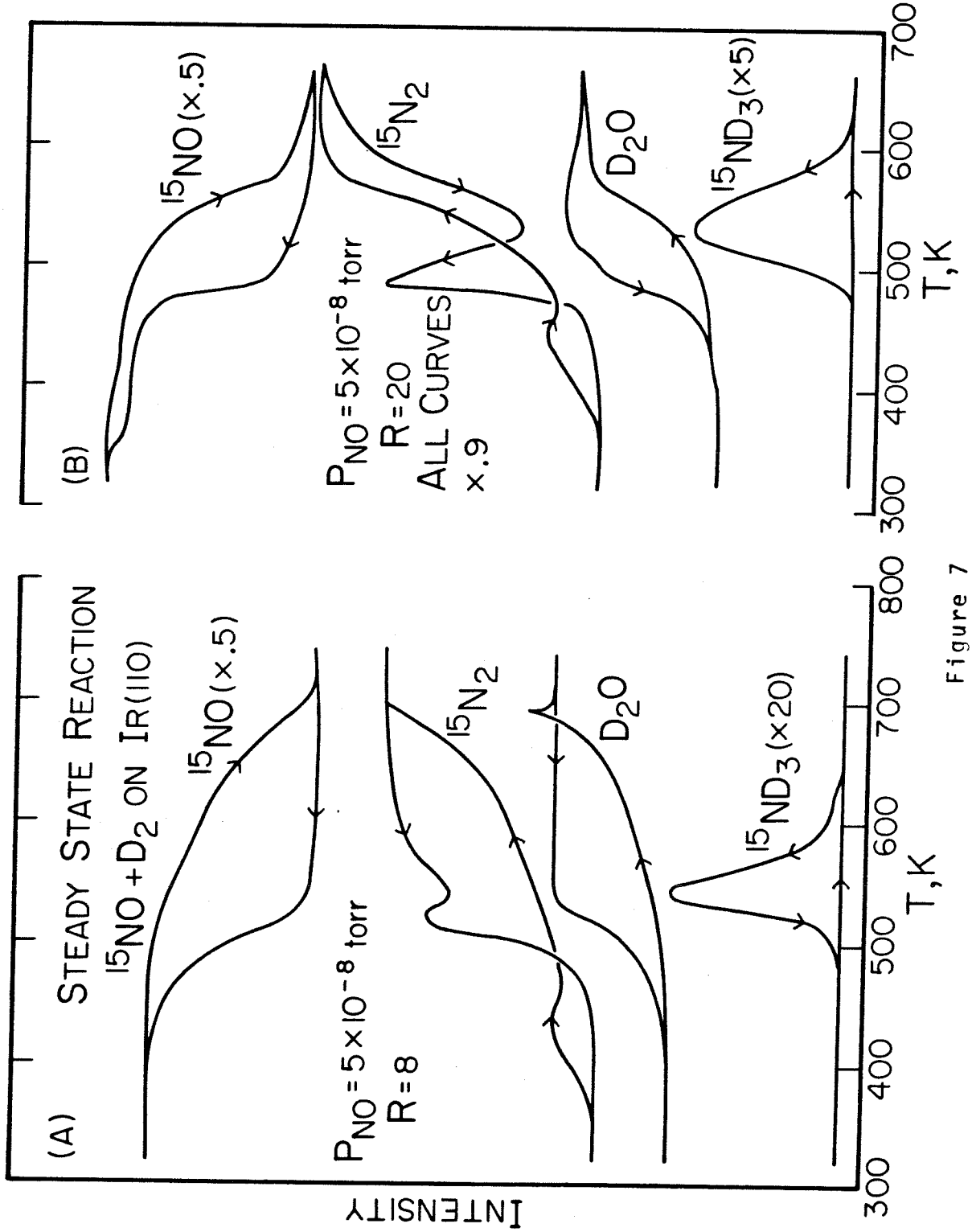
(A)
STEADY STATE REACTION
$^{15}NO + D_2$ ON IR(110)
^{15}NO(×.5)
$P_{NO} = 5\times10^{-8}$ torr
R=8
$^{15}N_2$
D_2O
$^{15}ND_3$(×20)
INTENSITY
300
400
500
600
700
800
T,K
(B)
^{15}NO(×.5)
$P_{NO} = 5\times10^{-8}$ torr
R=20
ALL CURVES
×.9
$^{15}N_2$
D_2O
$^{15}ND_3$(×5)
300
400
500
600
700
T,K

Figure 7

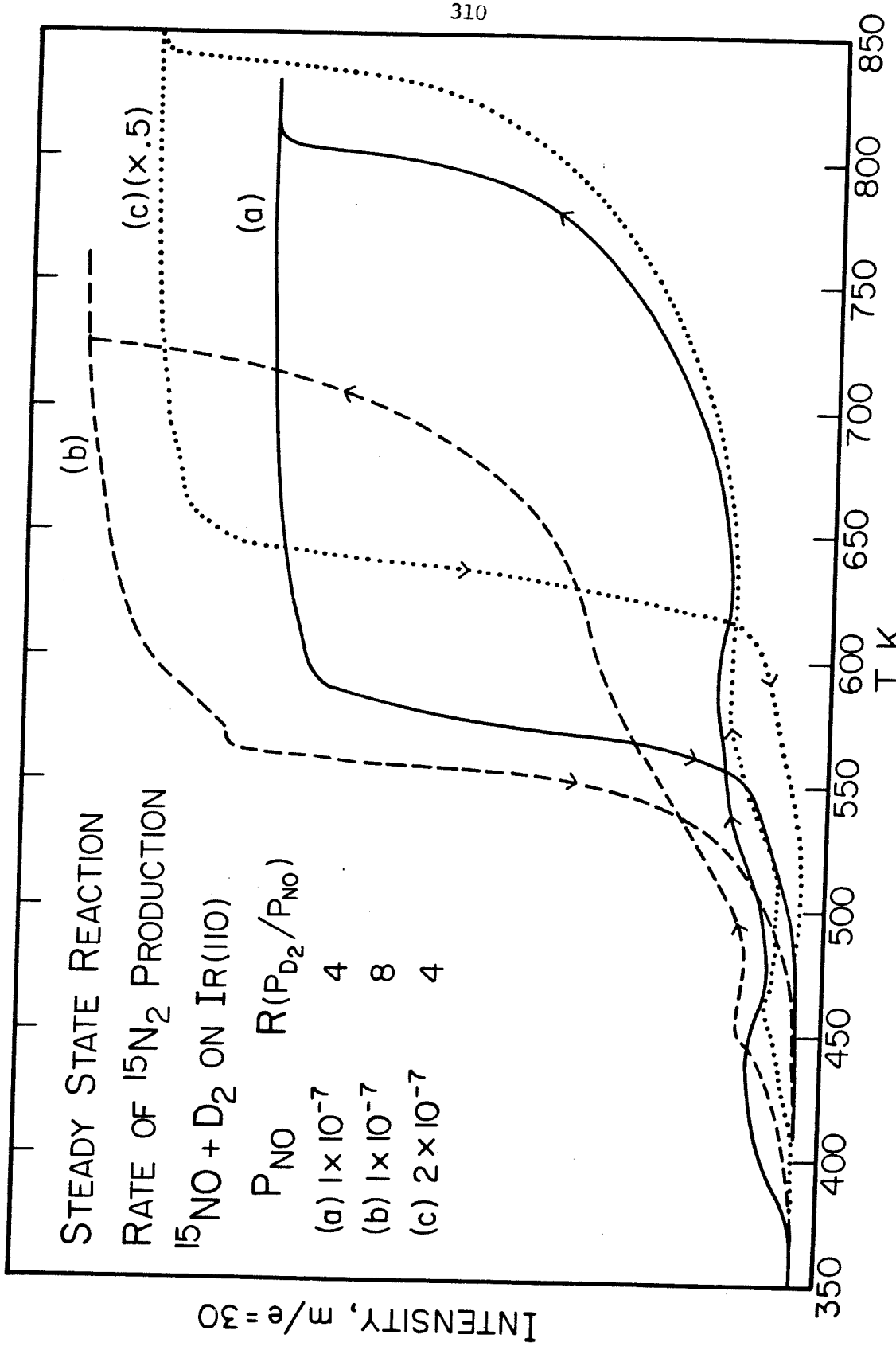
STEADY STATE REACTION
RATE OF $^{15}N_2$ PRODUCTION
$^{15}NO + D_2$ ON IR(110)
P_{NO} $R(P_{D_2}/P_{NO})$
(a) 1×10^{-7} 4
(b) 1×10^{-7} 8
(c) 2×10^{-7} 4
(a)
(b)
(c)(×.5)
INTENSITY, m/e = 30
350
400
450
500
550
600
650
700
750
800
850
T, K

Figure 8

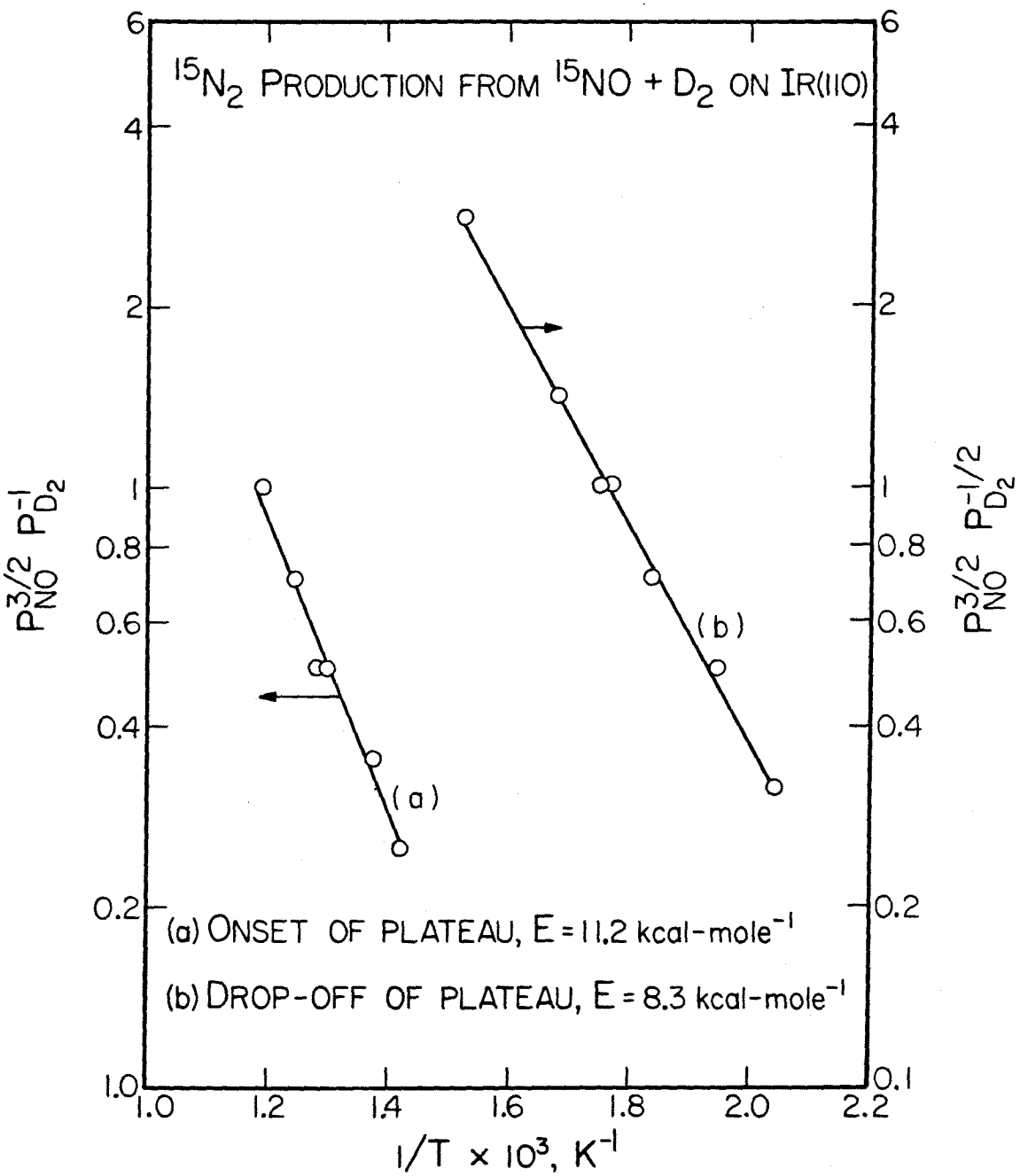
$^{15}N_2$ PRODUCTION FROM $^{15}NO + D_2$ ON IR(110)
$P_{NO}^{3/2} P_{D_2}^{-1}$
$P_{NO}^{3/2} P_{D_2}^{-1/2}$
(a)
(b)
(a) ONSET OF PLATEAU, E = 11.2 kcal-mole^{-1}
(b) DROP-OFF OF PLATEAU, E = 8.3 kcal-mole^{-1}
$1/T \times 10^3$, K^{-1}

Figure 9

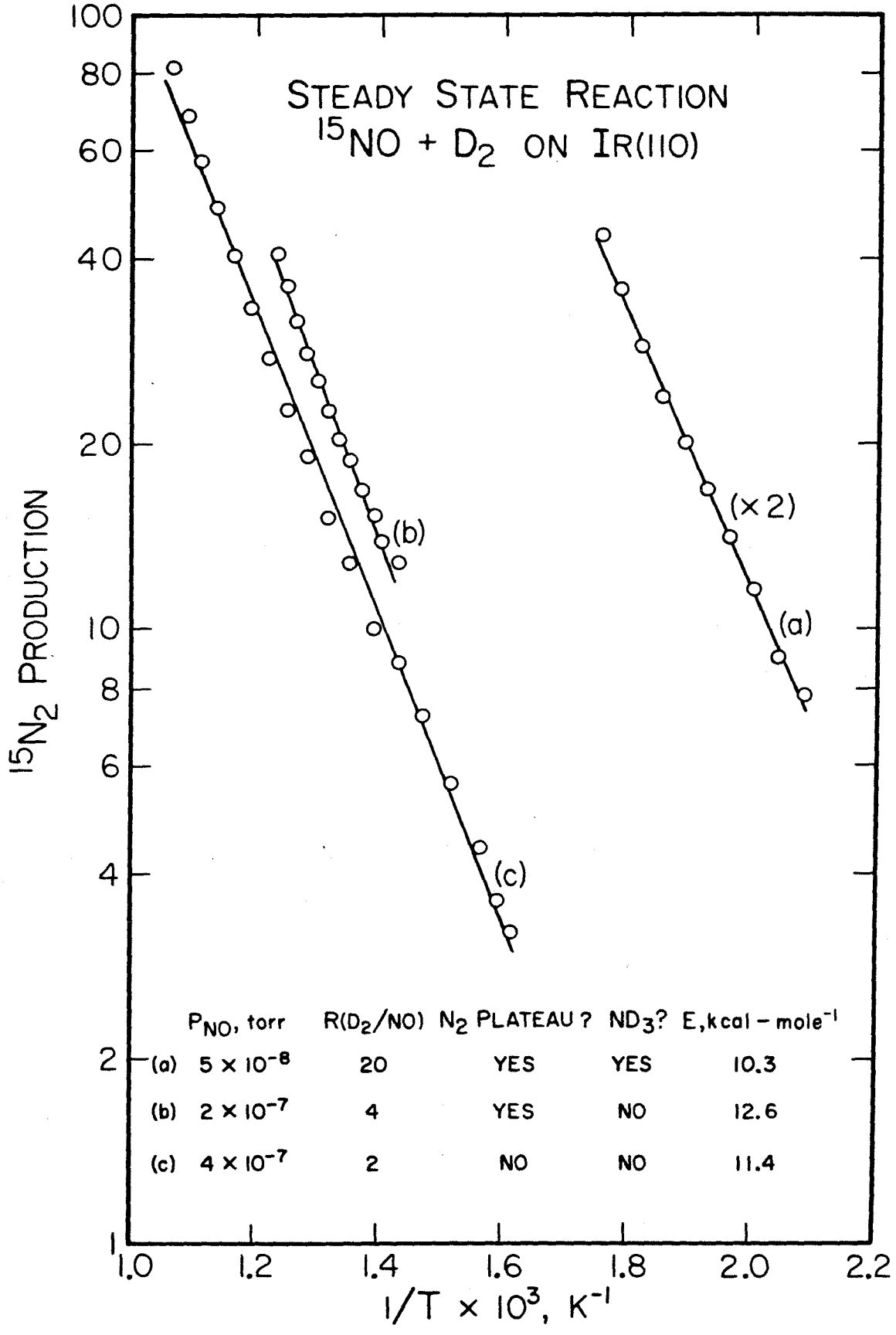
STEADY STATE REACTION
$^{15}NO + D_2$ ON IR(110)
$^{15}N_2$ PRODUCTION
100
80
60
40
20
10
8
6
4
2
1
(a)
(b)
(c)
(×2)
1.0
1.2
1.4
1.6
1.8
2.0
2.2
$1/T \times 10^3$, K^{-1}
P_{NO}, torr
$R(D_2/NO)$
N_2 PLATEAU?
ND_3?
E, kcal − mole^{-1}
(a) 5×10^{-8} 20 YES YES 10.3
(b) 2×10^{-7} 4 YES NO 12.6
(c) 4×10^{-7} 2 NO NO 11.4

Figure 10

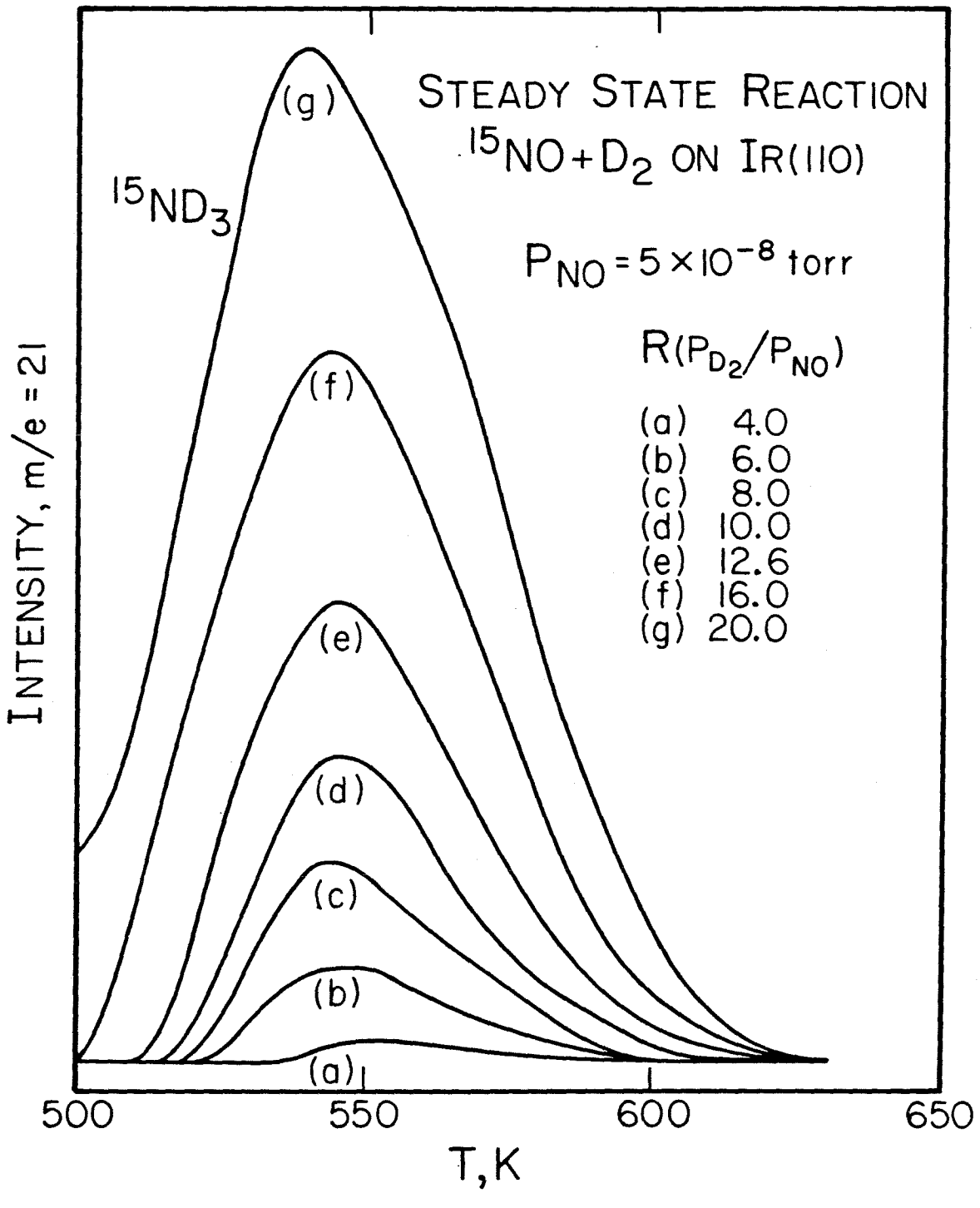
STEADY STATE REACTION
$^{15}NO + D_2$ ON IR(110)
$P_{NO} = 5 \times 10^{-8}$ torr
$R(P_{D_2}/P_{NO})$
(a) 4.0
(b) 6.0
(c) 8.0
(d) 10.0
(e) 12.6
(f) 16.0
(g) 20.0
$^{15}ND_3$
INTENSITY, m/e = 21
500
550
600
650
T, K

Figure 11

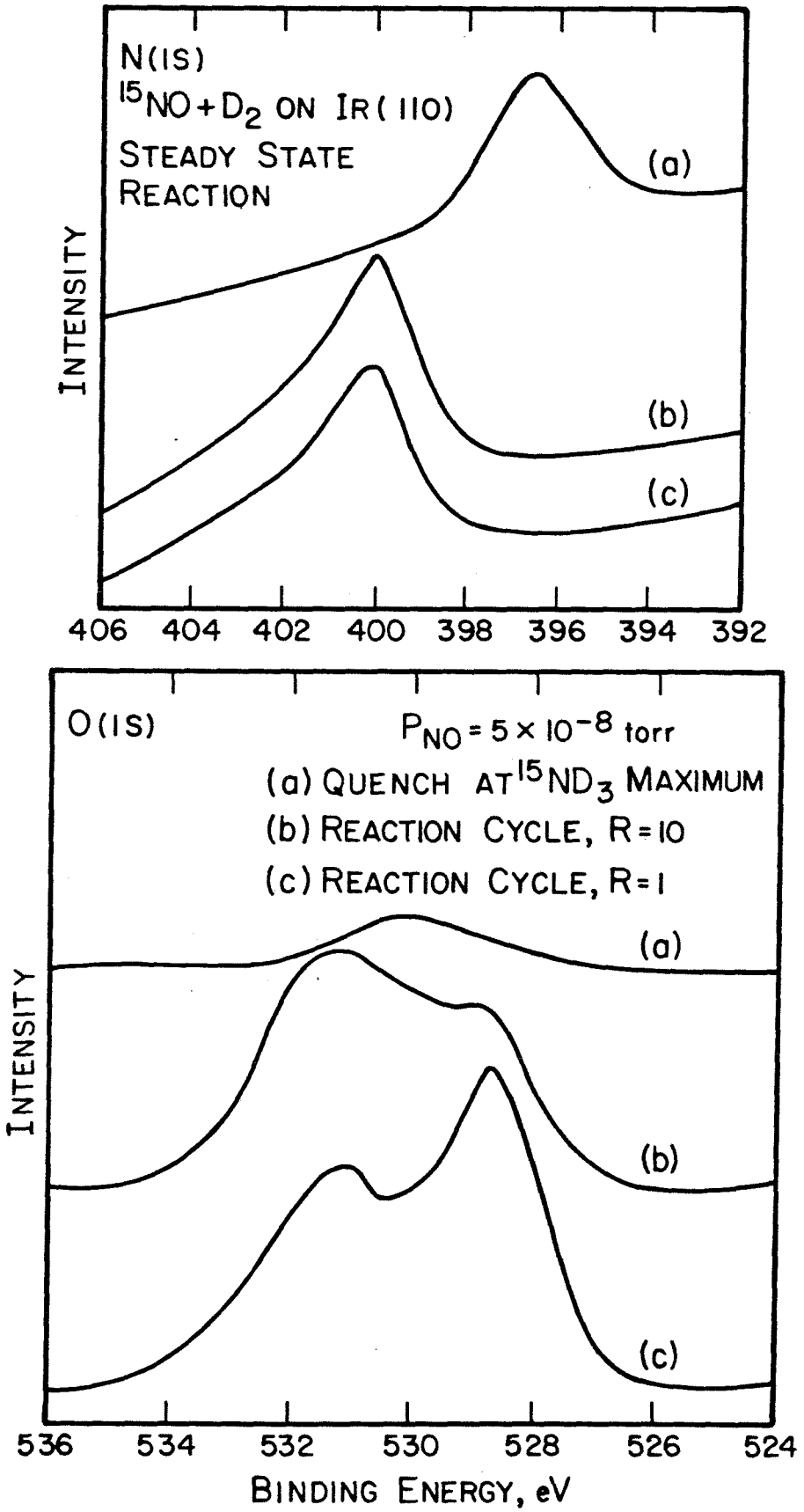
N(1S)
$^{15}NO + D_2$ ON Ir(110)
STEADY STATE
REACTION
(a)
(b)
(c)
INTENSITY
406 404 402 400 398 396 394 392
O(1S)
$P_{NO} = 5 \times 10^{-8}$ torr
(a) QUENCH AT $^{15}ND_3$ MAXIMUM
(b) REACTION CYCLE, R=10
(c) REACTION CYCLE, R=1
(a)
(b)
(c)
INTENSITY
536 534 532 530 528 526 524
BINDING ENERGY, eV

Figure 12

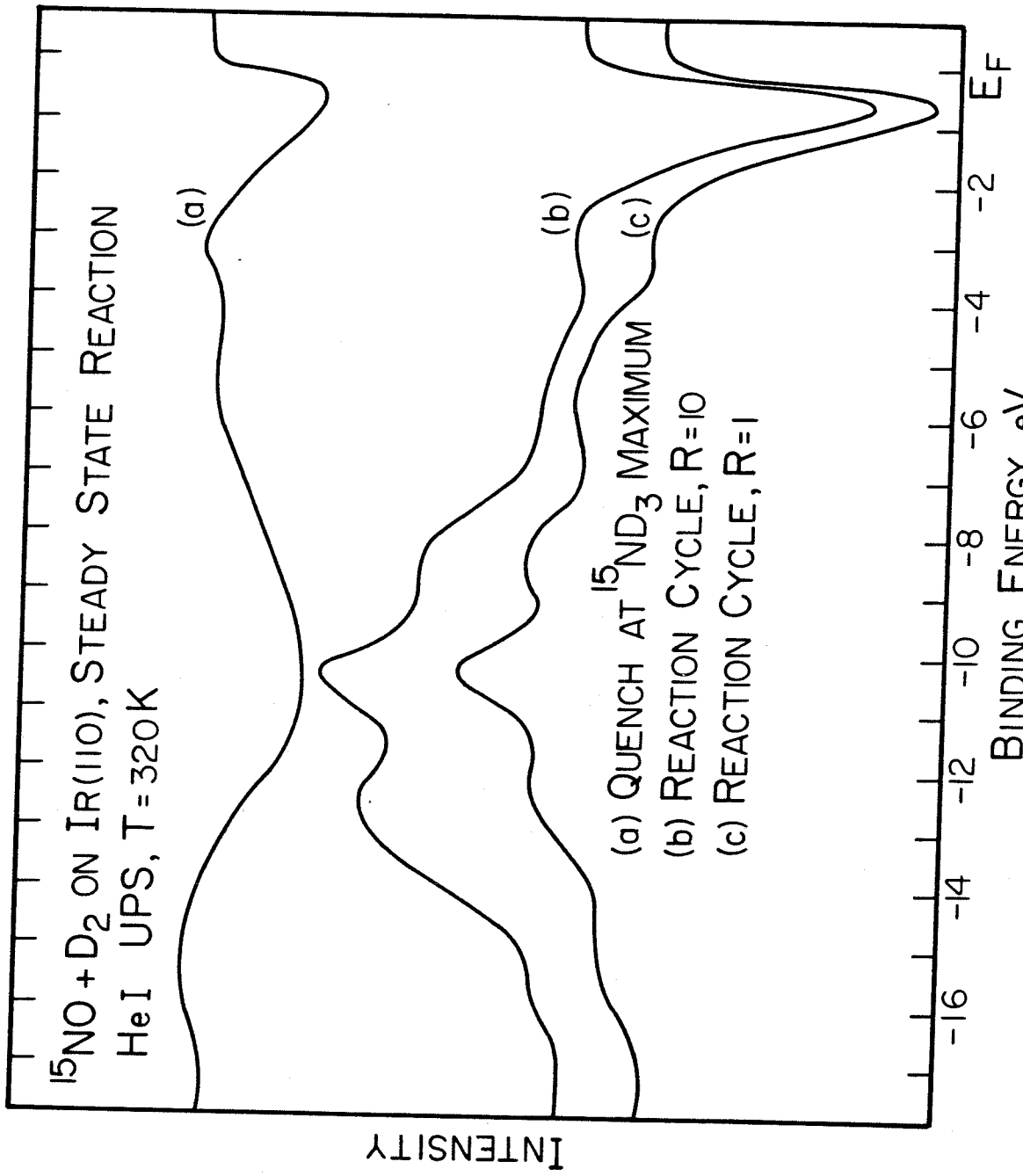
$^{15}NO + D_2$ ON Ir(110), STEADY STATE REACTION
HeI UPS, T = 320K
(a)
(b)
(c)
(a) QUENCH AT $^{15}ND_3$ MAXIMUM
(b) REACTION CYCLE, R=10
(c) REACTION CYCLE, R=1
INTENSITY
-16
-14
-12
-10
-8
-6
-4
-2
E_F
BINDING ENERGY, eV

Figure 13

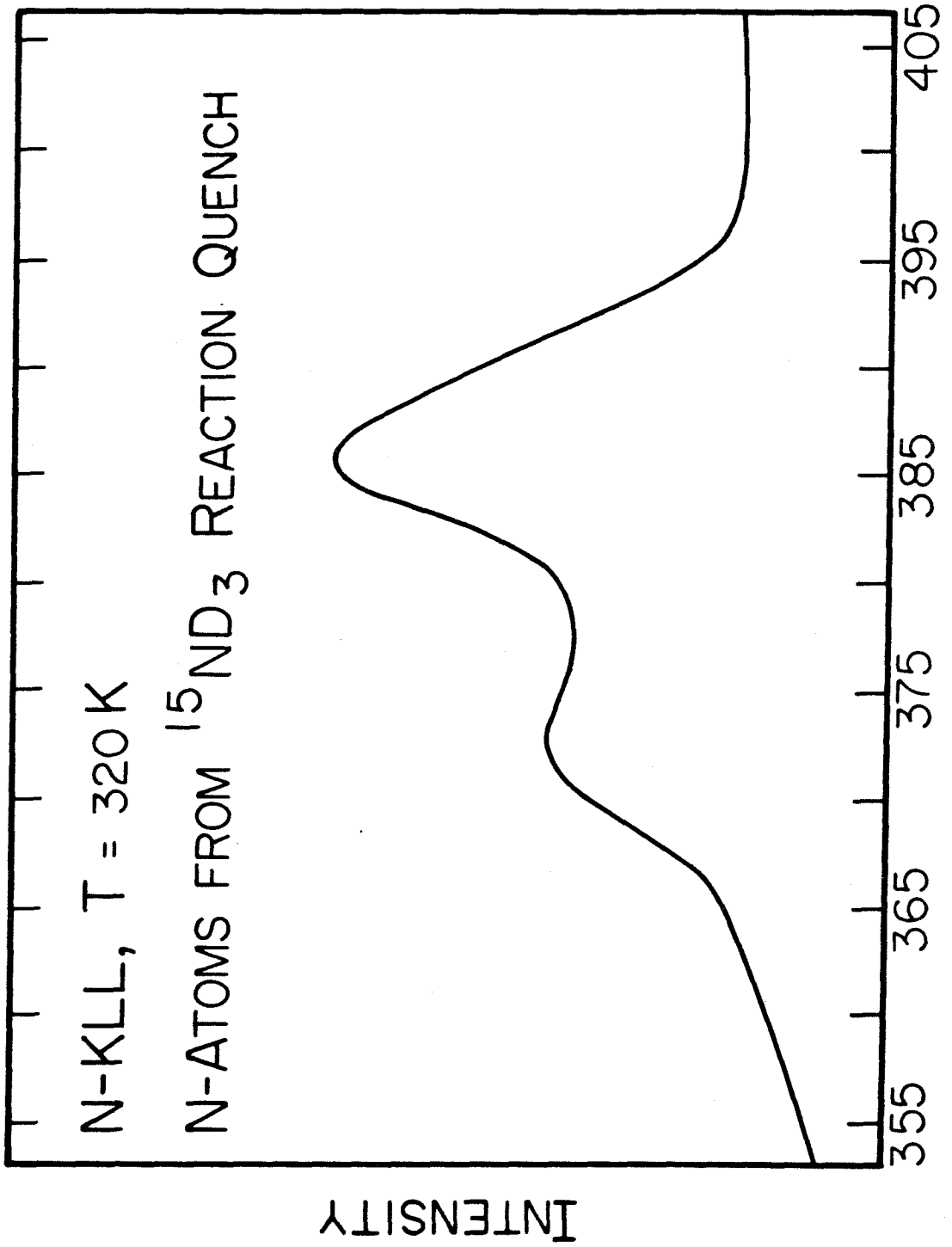
N-KLL, T = 320 K
N-ATOMS FROM $^{15}ND_3$ REACTION QUENCH
INTENSITY
355
365
375
385
395
405
KINETIC ENERGY, eV

Figure 14